Conditions for Stable Propagation of Synchronous Spiking in Cortical Neural Networks

Single Neuron Dynamics and Network Properties

DISSERTATION
zur
Erlangung des Grades
„Doktor der Naturwissenschaften“
an der Fakultät für Physik und Astronomie
der Ruhr-Universität Bochum

von
Markus Diesmann

aus Bochum

Göttingen, Mai 2002

R6

Die Arbeit wurde unter der Verantwortung von Prof. Christoph von der Malsburg am 29.5.2002 bei der Fakultät für Physik und Astronomie der Ruhr-Universität Bochum eingereicht und mit der Disputation am 25.11.2002 angenommen. Die Gutachter waren Prof. Christoph von der Malsburg und Prof. Gregor Schöner.

Acknowledgments

Prof. Ad Aertsen introduced me to the field of theoretical neuroscience almost ten years ago. Since then I have profited from his vast knowledge, unconventional ideas, and personal advice. His style of focusing a complex scientific discourse and untiring ability to provide constructive comments have influenced me immeasurably.

I thank Prof. von der Malsburg and Prof. Schöner for their interest and their helpful comments on this thesis.

The hospitality and support of Prof. Grinvald during my time at the Weizmann Institute of Science is gratefully acknowledged.

I am thankful to Prof. Theo Geisel for his trust and generous support.

Ad Aertsen, Marc-Oliver Gewaltig, Sonja Grün, Alexa Riehle, and Stefan Rotter critically read the text and made numerous comments which helped improving the manuscript.

Many of the treatises in this work are based on ideas set forth in Prof. Moshe Abeles' 1991 monograph. His continuous support and rigorous critique have been of invaluable help.

In always illuminative discussions Prof. George Gerstein explained some of the fundamental problems in spike-time analysis.

Alexa Riehle pointed me to experimentally relevant questions and her experience and intuition helped in interpreting results.

Stefan Rotter's deep mathematical insight and scepticism continue to be a source of inspiration and support in the struggle for clarity.

In the course of the project several people became friends in helping to organize life in new and instable environments, most notably Amos Arieli and Ulrich Egert.

With Marc-Oliver Gewaltig I have shared the major part of my scientific life. His still surprising ways of thinking strongly influence my work and fuel a lasting collaboration and friendship.

My parents Theresia and Otto Diesmann equipped me with the optimism and confidence required for the endeavor.

Every page of this work is inseparably connected to the accompanying adventures of life mastered with the warmth, unlimited energy, and organizational skills of my wife and colleague Sonja Grün.

This work was supported by the German "Bundesministerium für Bildung und Forschung" (BMBF), the "Deutsche Forschungsgemeinschaft" (DFG), the German Israel Foundation (GIF), and the Human Frontier Science Program (HFSP).

Contents

Zusammenfassung **ix**

1 Introduction **1**
1.1 The Cortical Network . . . 1
1.2 Cooperative Effects . . . 2
1.3 Modulations of Spike Time Correlations . . . 3
1.4 The Synfire Model . . . 8
1.5 Focus of the Study . . . 14
1.6 Outline of the Investigation . . . 14

2 Neuron and Network Model **17**
2.1 Membrane Equation . . . 17
2.2 Post-Synaptic Potential . . . 20
2.3 Membrane Potential Fluctuations . . . 21
2.4 Spontaneous Spiking Activity . . . 25
2.5 Classical Transmission Function . . . 27

3 Transmission Function for Transient Input **31**
3.1 Pulse Packets . . . 31
3.2 Reduction to Single Neuron Properties . . . 33
3.3 Quantitative Description of the Response . . . 35

4 State Space of Synfire Activity **41**
4.1 Construction of State Space . . . 41
4.2 Trajectories . . . 44
4.3 Minimal Number of Neurons per Group . . . 47

5 Background Activity **51**
5.1 Background Fluctuations as Bifurcation Parameter . . . 52
5.2 Effect of Spontaneous Activity . . . 57
5.3 Compensation of Background Fluctuations . . . 59

6 Vanishing Noise **61**
6.1 Characteristic Excursions . . . 61
6.2 Transmission Function . . . 65

6.3 Iterative Mapping . . . 66
6.4 Structure of State Space . . . 67
6.5 Transition to Non-Vanishing Fluctations . . . 68

7 Rise Time of the Post-Synaptic Potential 73
7.1 Transmission Function . . . 73
7.2 State Space Portraits . . . 76
7.3 Isoclines . . . 77
7.4 Normalization of PSP . . . 79
7.5 Packet Potential Normalization . . . 84

8 Amplitude of the Post-Synaptic Potential 87
8.1 Relative Group Activation . . . 88
8.2 Reliability of Transmission . . . 90
8.3 Survival Probability . . . 92
8.4 Monte-Carlo Approach to Survival Probability . . . 96

9 Slow Fluctuations Model 101
9.1 Spike Generation on Packet Potential Up-slope . . . 102
9.2 Activation Curves . . . 105
9.3 Output Spread . . . 107
9.4 Vanishing Fluctuations . . . 109
9.5 Relation to Intensity Models . . . 112

10 Discussion 123
10.1 Results and Interpretation . . . 123
10.1.1 Summary of Results . . . 123
10.1.2 Spatio-Temporal Spike Patterns . . . 126
10.1.3 Connection to Subthreshold Dynamics . . . 129
10.1.4 Existence of Feed-Forward Subnetworks . . . 130
10.1.5 Background Activity . . . 132
10.1.6 Subthreshold Oscillations . . . 135
10.1.7 Experimental Determination of the Transmission Function . . . 137
10.2 Open Questions and Outlook . . . 141
10.2.1 Ground State of Synfire Activity . . . 142
10.2.2 High Rate Limit of Synfire Activity . . . 143
10.2.3 Spatial Constraints of Embedding . . . 143
10.2.4 From Random Graphs to Cortical Anatomy . . . 145
10.2.5 Functional Relevance . . . 146

A Exact Integration 147

B List of Symbols 151

Bibliography 153

Lebenslauf 169

Zusammenfassung

Einführung

Die höheren Hirnfunktionen werden dem entwicklungsgeschichtlich jüngsten Teil des Gehirns, dem nur bei Säugern auftretenden Neocortex, zugeschrieben. Die vorliegende Arbeit will einen Beitrag zur Aufklärung der informationsverarbeitenden Prozesse im Neocortex und deren dynamische Eigenschaften liefern.

Es ist allgemein akzeptiert, daß ein wesentlicher Teil der Informationsverarbeitung im Gehirn durch elektrische Aktivität von Nervenzellen getragen wird. Nervenzellen halten eine Potentialdifferenz zwischen dem Zellinneren und dem extrazellulären Medium aufrecht (Membranpotential). Die Wechselwirkung zwischen den Nervenzellen (Neuronen) wird über scharfe Spannungspulse, sogenannte Aktionspotentiale (Spikes), vermittelt. Die Kontaktstellen zwischen Neuronen (Synapsen) sind gerichtet. Erzeugt ein Neuron einen Spike, so löst dies nach einer Zeitverzögerung von einigen Millisekunden in den Zielneuronen eine kleine Auslenkung des Membranpotentials, das postsynaptische Potential (PSP), aus. Stark vereinfacht kann man sich die Dynamik einer Nervenzelle so vorstellen, daß ein Spike emittiert wird, wenn das Membranpotential durch die Überlagerung genügend vieler PSPs einen Schwellwert überschreitet (aktuelle Darstellungen findet man z.B. in Johnston & Wu, 1995; Koch, 1999; Nicholls, Martin, Wallace, & Fuchs, 2001). Direkt nach der Erzeugung eines Spikes kann ein Neuron für einige ms (Refraktärzeit) keinen weiteren Spike emittieren. Diese Beschreibung neuronaler Dynamik wird im weiteren Sinne als „Integrate-and-Fire“ Modell bezeichnet.

Der Verknüpfungsgrad des cortikalen Netzwerkes läßt sich durch folgende Angaben veranschaulichen. In einem Kubikmillimeter Cortex befinden sich ca. 10^5 Neuronen. 80% der Neuronen sind erregend (exzitatorisch), d.h. sie lösen im postsynaptischen Neuron eine Membranpotentialauslenkung in Richtung des Schwellwertes aus, 20% sind hemmend (inhibitorisch). Ein einzelnes Neuron erhält Eingang über etwa 9000 exzitatorische und 2000 inhibitorische Synapsen von Neuronen aus dem lokalen Volumen ($1\,\mathrm{mm}^3$). Zusätzlich besitzt ein Neuron weitere 9000 exzitatorische Synapsen mit presynaptischen Neuronen aus weiter entfernten Bereichen (eine Diskussion der cortikalen Anatomie findet man in Braitenberg & Schüz, 1998; Abeles, 1991).

Der Zeitverlauf des Membranpotentials einzelner Neuronen kann im intakten Tier (*in vivo*) gemessen werden (z.B. Douglas & Martin, 1991b). Dabei zeigen sich starke Fluktuationen des Membranpotentials, die der Überlagerung von ständig auftretenden, exzitatorischen und inhibitorischen synaptischen Ereignissen (Hintergrundaktivität) zugeschrieben werden. In Abwesenheit kontrollierter Stimuli beobachtet man eine geringe Spontanaktivität der Neuronen. Scheinbar zufällig emittieren die Neuronen Spikes mit einer Rate von unter 1 Hz bis

zu wenigen 10 Hz (z.B. Burns & Webb, 1976; Abeles, Vaadia, & Bergman, 1990), also weit unterhalb der durch die Einzelneurondynamik begrenzten maximalen Rate. In jüngerer Zeit ist es gelungen, erste Modelle des lokalen Netzwerkes zu formulieren, in denen eine geringe Spontanaktivität ein stabiler Zustand des Systems, und sowohl Resultat als auch Ursache der Hintergrundaktivität ist (van Vreeswijk & Sompolinsky, 1996; Amit & Brunel, 1997). In diesen Modellnetzwerken ist die Verknüpfung der Neuronen als zufällig angenommen, parametrisiert durch die oben erwähnten Größen aus der statistischen Anatomie.

Die parallele und verteilte Architektur des Cortex legt es nahe, kollektive Eigenschaften des Netzwerkes zu untersuchen. Hebb (1949) formulierte die Hypothese, daß Ensembles von Neuronen die Grundlage neuronaler Prozesse bilden. Die Zugehörigkeit zu einem „Cell Assembly“ soll sich dabei durch die kohärente Aktivität der beteiligten Neuronen ausdrücken. Aufgrund konzeptueller Überlegungen und aufgrund der biophysikalischen Eigenschaften cortikaler Neuronen (von der Malsburg, 1981; Abeles, 1982a; von der Malsburg, 1986a; Gerstein, Bedenbaugh, & Aertsen, 1989; Palm, 1990; Abeles, 1991; Singer, 1993) wurde die Vorstellung entwickelt, daß die geforderte kohärente Aktivität durch die genaue zeitliche Organisation (Korrelation) der Spikezeitpunkte der beteiligten Neuronen realisiert sein könnte.

In elektrophysiologischen Experimenten kann seit einiger Zeit auch die Spikeaktivität mehrerer individueller Neuronen parallel aufgezeichnet werden. Dazu werden mehrere Elektroden in ein kleines Hirnvolumen eingebracht. Aktionspotentiale von Neuronen, die sich in der Nähe des nicht isolierten Bereiches der Elekroden befinden, führen zu charakteristischen Spannungsänderungen an den Elektroden. Diese Experimente können sowohl an anästhesierten als auch an wachen Tieren durchgeführt werden. Im letzten Fall ist es möglich, das Tier in ein Verhaltensexperiment einzubeziehen, sodaß die aufgezeichnete neuronale Aktivität mit der Reizsituation oder dem Verhalten in Verbindung gebracht werden kann. Durch die gleichzeitige Beobachtung der Aktivität mehrerer Neuronen ist es möglich, nicht nur die Aktivität einzelner Neuronen zu charakterisieren, sondern auch kooperative Phänomene zu studieren.

Schon früh wurde die Beziehung der Aktivität zwischen Paaren von Neuronen untersucht, indem die Kreuzkorrelation der Spikefolgen berechnet wurde (Perkel, Gerstein, & Moore, 1967b). Seit einigen Jahren wird auch die Dynamik der korrelierten Aktivität in Abhängigkeit von experimentellen Bedingungen studiert (z.B. Aertsen, Gerstein, Habib, & Palm, 1989; Vaadia et al., 1995). Es konnte gezeigt werden, daß sich die Korrelation in Abhängigkeit von der experimentellen Situation dramatisch ändern kann. Unter Benutzung einer Visualisierungstechnik für Korrelationen zwischen drei gleichzeitig aufgezeichneten Spikefolgen (Perkel, Gerstein, Smith, & Tatton, 1975) beobachtete Abeles (1982a) das Auftreten von bestimmten Spikemustern. In diesen Mustern sind die Spikes der Neuronen mit einer Genauigkeit von wenigen ms plaziert, wobei der zeitliche Abstand der Spikes im Muster bis zu hunderten von ms betragen kann. Die Realisierung eines solchen Ereignisses beeinträchtigt nicht das Auftreten von weiteren Spikes zwischen den zum Muster gehörenden Spikes. In Anbetracht der großen Membranpotentialfluktuationen und der damit verbundenen Variabilität neuronaler Spikefolgen stellt sich die Frage, wie solch hochpräzise Spikemuster zustande kommen können. Die Muster werden als hochpräzise bezeichnet, da ihre zeitliche Unschärfe im Vergleich zu einer weiteren wichtigen Zeitskala neuronaler Dynamik, der Membranzeitkonstante, um eine Größenordnung geringer ist (z.B. Connors, Gutnick, & Prince, 1982).

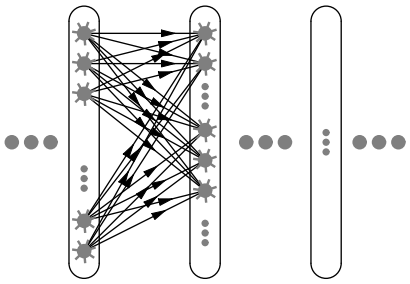

Abbildung 1 Skizze einer Synfire Chain. Gruppen von Neuronen sind zu einer gerichteten kettenartigen Struktur verknüpft, welche als Subnetzwerk eines größeren Netzwerkes aufgefaßt wird. Im einfachsten Fall besitzt jedes Neuron genau eine Verbindung mit jedem Neuron der nächsten Gruppe.

Die Membranzeitkonstate gibt die Zeitskala an, mit der das Membranpotential nach einer Auslenkung passiv auf den Ruhewert relaxiert.

Das Auftreten präziser Spikemuster ist von Interesse, da sie Ausdruck der Aktivierung eines Cell Assemblies sein könnten. Entsprechend den Anforderungen an ein Cell Assembly, ist die Repräsentation verteilt und die Zusammengehörigkeit der Neuronen wird durch zeitliche Beziehungen ausgedrückt. Das Cell Assembly Konzept würde demnach voraussagen, daß Neuronen zu verschiedenen Zeiten und unter verschiedenen experimentellen Situationen Spikemuster mit unterschiedlichen Partnerneuronen aufweisen. Tatsächlich wurden unter Verwendung verschiedener Analysemethoden (Abeles, Bergman, Margalit, & Vaadia, 1993; Riehle, Grün, Diesmann, & Aertsen, 1997; Prut et al., 1998; Grün, Diesmann, & Aertsen, 2002b) Hinweise auf einen Verhaltensbezug und auf ein in der Zeit moduliertes Auftreten von Spikemustern gefunden.

Unabhängig von der funktionellen Bedeutung, beschränken wir uns in dieser Arbeit darauf zu untersuchen, ob ein bestimmtes Netzwerkmodell, welches zur Erklärung der präzisen Spikemuster vorgeschlagen wurde, unter den im Cortex gegebenen Bedingungen plausibel erscheint. In der gleichen Monographie (Abeles, 1982a), in der von Dreierkorrelationen berichtet wird, schlägt Abeles das Modell der „Synfire Chain“ vor, um zeitlich ausgedehnte Spikemuster zu erklären. Die in Fig. 1 gezeigte Netzwerkstruktur geht auf eine Arbeit von Griffith (1963) zurück, der diese Struktur allerdings unter dem Aspekt der Stabilisierung globaler Netzwerkaktivität behandelte. In der Synfire Chain sind exzitatorisch gekoppelte Neuronen zu einer Sequenz von Gruppen organisiert. Die Vorstellung ist nun, daß bei gleichzeitiger Aktivierung der Neuronen einer Gruppe die jeweils nächste Gruppe ebenfalls zuverlässig aktiviert wird. Damit läuft ein Paket synchroner Spikes durch das Netzwerk, wobei eine Neuronengruppe gleichzeitig Empfänger und Erzeuger synchroner Spikeaktivität ist.

Es sollte betont werden, daß die Darstellung einer Synfire Chain (Fig. 1) nicht die anatomische Anordnung der Neuronen repräsentiert, sondern ausschliesslich die sequenzielle Anordnung symbolisiert, in der die Neuronen in der Zeit aktiviert werden. Grundsätzlich können einzelne Neuronen immer wieder in der Kette teilnehmen, wobei ein minimaler Abstand durch die Refraktärzeit vorgegeben ist. Da ein Neuron bei Aktivierung einer Kette nur jeweils einen Spike beiträgt, kann es ohne weiteres an mehreren Ketten teilnehmen.

Werden nun die Spikefolgen zweier Neuronen aufgezeichnet, die sich in einer Gruppe

befinden, wird ein räumliches Muster beobachtet, in dem beide Neuronen mit hoher Präzision gleichzeitig einen Spike emittieren. Nimmt ein Neuron in verschiedenen Gruppen teil, findet man ein rein zeitliches Muster. Zwei Neuronen aus verschiedenen Gruppen erzeugen ein raum-zeitliches Muster, wobei der zeitliche Abstand der Spikes vom Abstand der beiden Neuronengruppen in der Synfire Chain abhängt.

Die strikt vorwärtsverschaltete Synfire Chain wird als ein behandelbares abstraktes Subnetzwerk des Cortex eingeführt. Um eine realistische Hintergrundaktivtät zu modellieren, erhält jedes Neuron in der Synfire Chain zusätzlich Eingang von vielen anderen Neuronen aus dem einbettenden Gesamtnetzwerk. Die Rückprojektion von Neuronen der Synfire Chain in das Gesamtnetzwerk wird hier vernachlässigt. Grundsätzlich stellt sich die Frage, ob divergent/konvergent verschaltete Neuronengruppen ein lokales Organisationsprinzip des Cortex sein können.

Fragestellung

Die vorliegende Arbeit befaßt sich mit der Frage, ob das von Abeles vorgeschlagene Modell der Synfire Chain, unter den im Cortex gegebenen Randbedingungen, tatsächlich in der Lage ist, synchrone Spikeaktivität stabil fortzuleiten. Dazu muß zunächst geklärt werden, in welchem Sinne propagierende synchrone Spikeaktivität einen stabilen Zustand des Systems darstellt, und wie die Robustheit eines solchen Zustandes demonstriert werden kann. Der Mechanismus der Spikesynchronisation soll aufgeklärt und die Bedingungen für die Existenz eines stabilen Zustandes herausgearbeitet werden. Um eine Überprüfung der Konsistenz der Synfire Hypothese mit experimentellen Daten zu ermöglichen, soll im Modell der Zusammenhang zwischen der Präzison der Spikesynchronisation und den Parametern des einzelnen Neurons hergestellt werden.
In einer komplementären Studie (Gewaltig, 2000) wurde die Spikeaktivität in Synfire Chains in Netzwerksimulationen untersucht, und eine kontinuierliche Beschreibung der Aktivitätsausbreitung auf der Ebene von Neuronengruppen entwickelt.

Die Übertragungsfunktion

Die Spikeaktivität in einer Synfire Chain (Fig. 1) ist gekennzeichnet durch die sequentielle Erregung der Neuronengruppen. Dabei sendet jede Gruppe eine Anzahl von Spikes aus, die eine gewisse zeitliche Dispersion aufweisen. Die Entscheidung, ob ein bestimmtes Neuron einen Spike emittiert, und dessen genaue zeitliche Position erscheinen zufällig. Um die Dynamik einer Synfire Chain aufklären zu können, muß untersucht werden, wie ein einzelnes Neuron auf das Eintreffen einer Salve mehr oder weniger synchroner Spikes reagiert. Das Konzept des Pulspakets (Fig. 2 **A**) ermöglicht es, eine Übertragungsfunktion (Fig. 2 **B**) zu definieren (Kapitel 3), die den Zusammenhang zwischen synchron eintreffenden Spikes und der neuronalen Antwort kompakt beschreibt. In dieser Übertragungsfunktion T wird ein Eingangspaket, parametrisiert durch die Anzahl von Spikes und deren zeitliche Unschärfe (a, σ_{in}), abgebildet auf ein Tupel $(\alpha, \sigma_{\text{out}})$, welches die Wahrscheinlichkeit eines Antwortspikes und dessen zeitliche Dispersion angibt. Im Gegensatz zu der „klassischen“ Entladungskurve

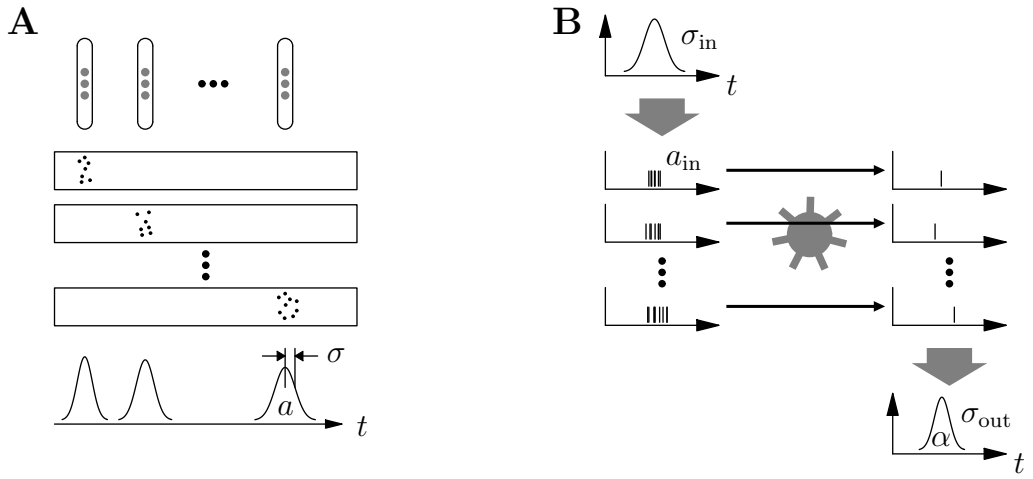

Abbildung 2 Representation (**A**) propagierender synchroner Spikeaktivität durch Pulspakete und Quantifizierung (**B**) des Antwortverhaltens eines einzelnen Neurons auf ein eintreffendes Pulspaket. **A** Skizze des zu untersuchenden Subnetzwerks (oben), angeordnet zu einer Sequenz von Gruppen von Neuronen (1., 2. und eine weitere Gruppe gezeigt, vgl. Fig. 1). Darunter (mittig) ist die typische Spikeaktivität von drei ausgewählten Neuronengruppen gezeigt (*Rasterdiagramm*). Punkte markieren das Auftreten von Spikes in der Zeit (horizontal). Die Netzwerkaktivität wird durch eine Abfolge von Spikepaketen beschrieben (unten), welche durch die Anzahl der enthaltenen Spikes a und einem Maß für die zeitliche Unschärfe σ parametrisiert werden. **B** Ein Modellneuron (mittig, grau) wird wiederholt mit Pulspaketen stimuliert, indem jeweils a_{in} Spikezeitpunkte aus einer Gaußverteilung mit Standardabweichung σ_{in} gezogen werden (links). Um die Hintergrundaktivität im Netzwerk zu berücksichtigen, werden die Pakete in zufällige, exzitatorische und inhibitorische Spikefolgen (nicht gezeigt) eingebettet. Die Antwort des Neurons auf ein eintreffendes Paket besteht typischerweise aus höchstens einem Spike (rechts). Mit einem Histogramm wird die Wahrscheinlichkeit α einen Spike zu emittieren und die zeitliche Unschärfe σ_{out} des Antwortspikes bestimmt. Diese Prozedur definiert die Übertragungsfunktion $(a_{\text{in}}, \sigma_{\text{in}}) \to (\alpha, \sigma_{\text{out}})$.

(discharge curve), die in Kapitel 2 kurz diskutiert werden wird, beschreibt die hier vorgeschlagene Übertragungsfunktion die transiente Antwort des Neurons auf einen transienten Stimulus.

Zustandsraum und Mittelwertsdynamik

In einer vollständig verknüpften Kette mit w Neuronen pro Gruppe ist die erwartete Anzahl von Antwortspikes durch das Produkt der Antwortwahrscheinlichkeit α und der Gruppenbreite w gegeben. Der Strukturparameter w verbindet also die Eigenschaften des einzelnen Neurons mit der im Netzwerk zu beobachtenden Aktivität. Damit kann eine iterative Abbildung T_w (Propagator) angegeben werden, welche die Entwicklung synchroner Aktivität entlang der Kette beschreibt (Kapitel 4).

Die Frage nach dem Auftreten synchroner Aktivität in unserer Netzwerkstruktur reduziert sich auf das Auffinden von Fixpunkten in der iterativen Abbildung. In dieser Sichtweise spannen a und σ den Zustandsraum unseres Systems auf. Unter realistischen Annahmen für die Werte der im Modell enthaltenen Parameter zeigt sich, daß in der Tat ein Attraktor für synchrone Aktivität existiert. Der Attraktor ist umgeben von einem Basin, welches Robustheit gegenüber Störungen garantiert. Ein Sattelpunkt bestimmt den Verlauf von charakte-

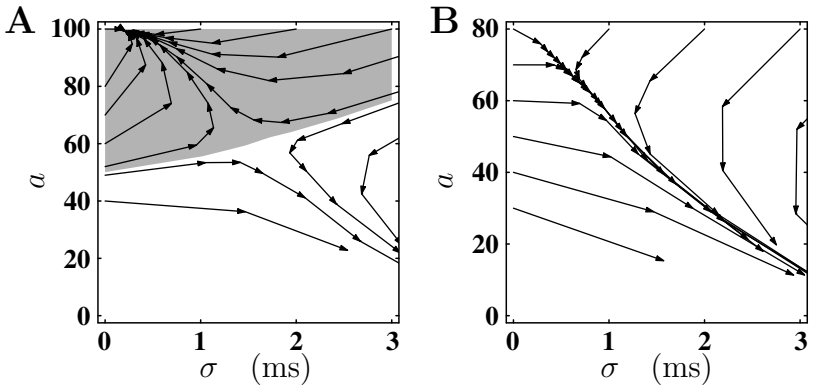

Abbildung 3 Zustandsraum für synchrone Spikeaktivität in einer Synfire Chain und w-Bifurkation. **A** a (vertikal) und σ (horizontal) spannen den Zustandsraum auf. Der Propagator $T_w : (a_i, \sigma_i) \to (a_{i+1}, \sigma_{i+1})$ beschreibt die Fortpflanzung eines Pulspakets von einer Neuronengruppe zur nächsten (Pfeile). Für eine gegebene Anzahl von Neuronen pro Gruppe (hier $w = 100$), ergibt sich der Propagator aus der Übertragungsfunktion (Fig. 2 **B**) durch Identifikation $\sigma_{i+1} = \sigma_{\text{out}}$ und Nutzung der erwarteten Anzahl von Antwortspikes $a_{i+1} = w\alpha$. Die Trajektorien zeigen die Entwicklung eines propagierenden Pulspakets für verschiedene Anfangsbedingungen. Im Attraktorbecken (grau) ist stabile Propagation synchroner Spikeaktivität garantiert. Im Attraktor wird eine nahezu vollständige Aktivierung aller Neuronen einer Gruppe erreicht, wobei eine gewisse zeitliche Unschärfe verbleibt. **B** Gleiche Darstellung wie in **A** für eine Gruppenbreite von $w = 80$. Der Attraktor für synchrone Spikeaktivität ist hier verschwunden, jegliche Anfangsaktivität stirbt aus.

ristischen Trajektorien im (a, σ)-Raum. Die durch die iterative Abbildung vorhergesagten Trajektorien stimmen gut mit Ergebnissen aus Netzwerksimulationen überein. Tatsächlich wurde die nichtmonotone Entwicklung von a und σ für Trajektorien in der Nähe der Separatrix, die das Attraktorbecken begrenzt, erst in Rasterdiagrammen beobachtet, nachdem sie in der iterativen Abbildung gefunden worden war.

Der Einfluß kritischer Parameter für die Fortpflanzung synchroner Aktivität sollte sich in verschiedenen Bifurkationsszenarien im (a, σ)-Raum ausdrücken. Ein offensichtlicher Parameter ist w (Anzahl der Neuronen pro Gruppe), welcher direkt die Anzahl der in einem Paket enthaltenen Spikes skaliert. Es zeigt sich, daß unter Variation von w eine Sattel-Knoten Bifurkation auftritt, in welcher der Attraktor für synchrone Aktivität vernichtet wird (Kapitel 4). Damit existiert eine untere Grenze für die Gruppenbreite, eine Größe, die insbesondere in Überlegungen zur anatomischen Existenz von vorwärtsverschalteten Subnetzwerken von Bedeutung ist (Abeles, 1991; Hehl et al., 2001).

Hintergrundaktivität

In der vorliegenden Studie wird die Dynamik eines einzelnen Neurons als deterministisch angenommen. Große Fluktuationen des Membranpotentials entstehen durch die Einbettung in das cortikale Netzwerk, aus welchem die Neuronen ständig exzitatorische und inhibitorische Eingänge erhalten. Die Stärke der Fluktuationen bestimmt die Spontanaktivität der Neuronen, und als einzige Rauschquelle im System bestimmt sie auch die Streuung der Antwortspikes bei Eintreffen eines Pulspakets. Gleichzeitig stellen die Membranpotentialfluktuationen eine Größe dar, die sich im Laufe eines Experiments ändern kann. Im Kontext

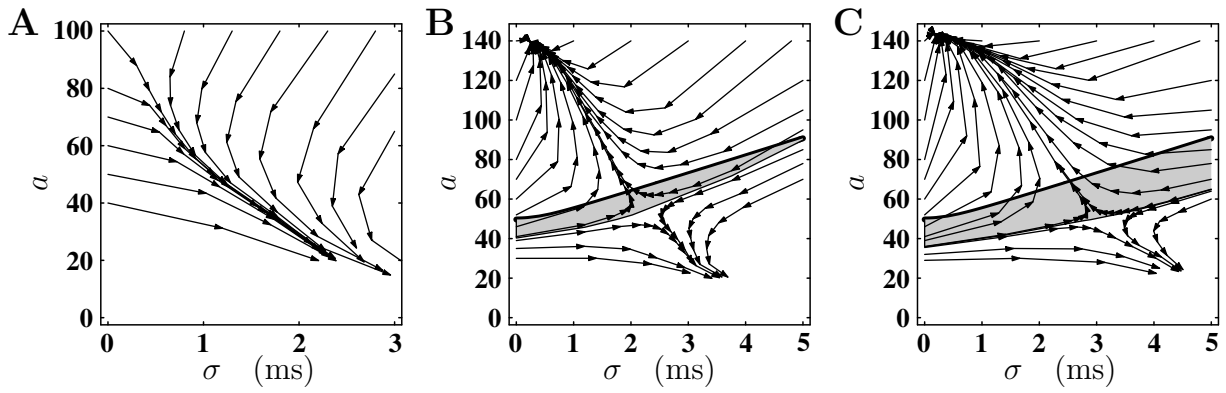

Abbildung 4 Vernichtung des Attraktors für synchrone Spikeaktivität durch erhöhte Membranpotentialfluktuationen und der konstruktive Effekt von Hintergrundaktivität. **A** Gleiche Darstellung und gleiche Anzahl von Neuronen pro Gruppe wie in Fig. 3 **A**. Durch eine Vergrößerung der Amplitude der Membranpotentialfluktuationen (von $\sigma_V = 2.5\,\mathrm{mV}$ auf $4.5\,\mathrm{mV}$) verschwindet der Attraktor für synchrone Spikeaktivität (σ_V-Bifurkation). **B** Gleiche Membranpotentialfluktuationen wie in **A** bei einer auf $w = 140$ erhöhten Anzahl von Neuronen pro Gruppe. Der Attraktor existiert. Die graue Fläche zeigt die Vergrößerung des Attraktorbeckens im Vergleich zum rauschfreien Fall (dicke Kurve). **C** Reduktion von σ_V auf $3.5\,\mathrm{mV}$ bei $w = 140$. Für konstantes w erreicht das Attraktorbecken seine größte Ausdehnung bei einem bestimmten σ_V.

dieser Arbeit wird daher auch die Standardabweichung der Membranpotentialverteilung σ_V als Parameter der Dynamik betrachtet (Kapitel 5).

Es ist also zu untersuchen, wie sich die Dynamik der Synfire Chain in Abhängigkeit von σ_V verändert. Unter Änderung dieses Parameters tritt ebenfalls eine Sattel-Knoten Bifurkation auf, die den Attraktor vernichtet (Fig. 4 **A**). Allerdings ist hier das globale Verhalten komplizierter als bei der w-Bifurkation. Für Gruppenbreiten größer als die minimal erforderliche zeigt sich, daß die Membranpotentialfluktationen einen konstruktiven Effekt auf die synchrone Aktivität ausüben (Kapitel 6). Mit wachsendem σ_V vergrößert sich das Attraktorbasin zunächst (Fig. 4 **C**), sodaß Pakete, die bei kleineren σ_V aussterben würden, in den Attraktor gezogen werden. Bei weiter steigendem σ_V schrumpft das Attraktorbasin wieder zusammen (Fig. 4 **B**). Dieser Effekt lät sich mit der aperiodischen stochastischen Resonanz (Collins, Chow, Capela, & Imhoff, 1996) in Verbindung bringen. Im Kontext der Informationsverarbeitung wird von einigen Autoren die Möglichkeit einer Aktivitätskontrolle durch Hintergrundaktivität diskutiert (z.B. Braitenberg & Schüz, 1998; Boven & Aertsen, 1990). In der hier vorliegenden Arbeit zeigt sich dieser Effekt in einem konkreten Netzwerkmodell.

Auch für kleine Membranpotentialfluktuationen bleibt die generelle Form der Separatrix, die den Zustandsraum in einen Bereich, der Pakete in den Attraktor zieht, von einem Bereich, in dem Pakete aussterben, trennt, erhalten. Bei kleiner werdendem Membranpotential werden allerdings immer weniger Schritte benötigt, um in die Nähe des Attraktors zu gelangen, und die Aktivität bekommt ein schwellwertartiges Verhalten. Dies führt auf die Frage nach dem Verhalten des Systems im rauschfreien Fall, und ob sich verstehen läßt, wie die Struktur des Zustandsraums entsteht.

Der rauschfreie Fall

Im rauschfreien Fall wird die Lage der Separatrix wesentlich von der Form des PSPs bestimmt. Die Erzeugung eines Antwortspikes hängt nur davon ab, ob die durch das Eintreffen eines Pakets ausgelöste Membranpotentialänderung (Paketpotential) den Schwellwert erreicht oder nicht. Wird der Schwellwert erreicht, dann erzeugen alle Neuronen der betreffenden Gruppe gleichzeitig einen Spike. Die Separatrix ist daher gegeben durch die Paare (a, σ), für die das Maximum des Paketpotentials den Schwellwert gerade erreicht. Es stellt sich heraus, daß der Zerfall des Paketpotentials mit wachsender Streuung der Eingangsspikes σ die Lage der Separatrix bestimmt. In Anwesenheit von Rauschen steigt die Antwortwahrscheinlichkeit für schwellennahe Paketpotentiale steil an und erreicht 50% für Paketpotentiale, die gerade die Schwelle erreichen, da die Verteilung der Membranpotentialwerte als symmetrisch angenommen werden kann. Eine Abschätzung der minimalen Gruppenbreite w_* erhält man daher aus der Bedingung, daß eine Neuronengruppe mindestens die Anzahl von Spikes reproduzieren muß, die es an ihrem Eingang erhält. Es werden also zwei mal so viele Neuronen benötigt wie Spikes notwendig sind, um den Schwellwert zu erreichen.

Im Gegensatz zu dem stufenförmigen Anstieg der Antwortwahrscheinlichkeit von 0 auf 1 im rauschfreien Fall, ist der Anstieg in Anwesenheit von Rauschen sigmoidal. Die Steilheit der Schwellencharakteristik wird durch Membranpotentialfluktuationen bestimmt. Während im rauschfreien Fall die Separatrix unabhängig von der Gruppenbreite ist, können durch eine Gruppenbreite größer als w_* im rauschbehafteten Fall auch „unterschwellige“ Pakete ($\alpha < 0.5$) eine Anzahl von Antwortspikes hervorrufen, die größer als die Zahl der Eingangsspikes ist. Somit können auch unterschwellige Pakete in den Attraktor gezogen werden. Dies erklärt den konstruktiven Effekt der Membranpotentialfluktuationen (Kapitel 6).

Anstiegszeit des Potentials

Es ist anschaulich klar, daß die im Attraktor erreichbare Synchronisation der Spikes von der Anstiegszeit der PSPs begrenzt sein muß. Selbst wenn die Eingangsspikes voll synchronisiert sind, bewirkt die endliche Steigung des Paketpotentials am Punkt des Schwellendurchstoßes eine Streuung der Antwortspikes durch Membranpotentialfluktuationen. Damit ist die Anstiegszeit des postsynaptischen Potentials als weiterer relevanter Parameter identifiziert.

Die Untersuchung der Synchronisationsdynamik in Abhängigkeit von der Anstiegszeit τ_0 des PSPs (Chap. 7) zeigt zunächst ein überraschendes Ergebnis. Wie erwartet verschiebt sich mit zunehmender Anstiegszeit die im Attraktor erreichbare Synchronisation zu größeren σ. Die Anzahl der Spikes im Attraktor ändert sich jedoch kaum (Fig. 5 **A**). Auch der Sattelpunkt verschiebt sich zu größeren σ und leicht geringeren Spikezahlen, sodaß sich mit wachsendem τ_0 das Attraktorbecken vergrößert und nicht etwa zusammenschrumpft (Kapitel 7).

Das obige Resultat erhält man, indem die Anstiegszeit des PSPs unter Konstanthaltung seiner Amplitude variiert wird. Dies erscheint zweckmäßig, da wir bereits gesehen haben, daß die Amplitude des PSPs eine wichtige Rolle in der Synchronisationsdynamik spielt. Mit Änderung der Anstiegszeit ändert sich unter Amplitudennormierung zwangsläufig die Fläche F^1 unter dem PSP. Mit wachsendem σ tauschen jedoch die Amplitude des PSPs und dessen Fläche ihre Rollen in Hinsicht auf ihren Einfluß auf die Amplitude des Paketpotentials.

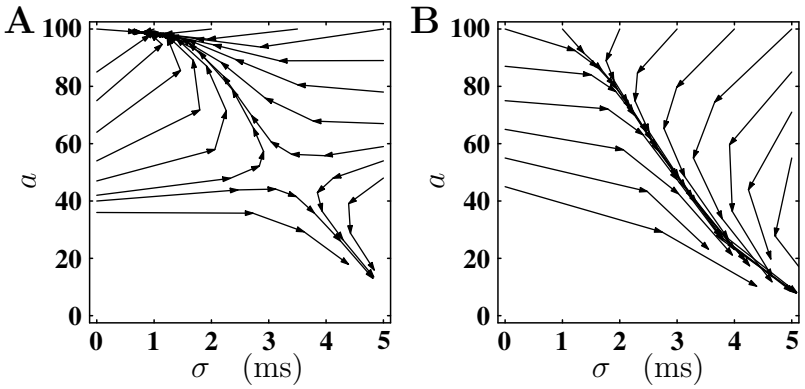

Abbildung 5 Abhängigkeit der im Attraktor erreichbaren zeitlichen Präzision von der Anstiegszeit des postsynaptischen Potentials und Vernichtung des Attraktors bei Vergrößerung der Anstiegszeit des PSPs unter Flächenerhaltung. **A** Gleiche Darstellung und Parameter wie in Fig. 3 **A**. Durch Vergrößerung der Anstiegszeit des PSPs von $\tau_0 = 1.7\,\mathrm{ms}$ auf 6 ms, bei konstanter Amplitude, liegen Attraktor und Sattelpunkt bei größerer zeitlicher Unschärfe. **B** Gleiche Vergrößerung der Anstiegszeit wie in **A**, jedoch unter Konstanthaltung der Fläche des PSPs. Eine stabile Propagation synchroner Spikeaktivität ist hier nicht mehr möglich.

Während bei hoher Synchronisation die Amplitude des Paketpotentials von der Amplitude des PSPs bestimmt wird, so wird sie bei großer Streuung der Spikes von F^1 bestimmt. Eine große Anstiegszeit des PSPs führt zu einer Verschiebung der Fixpunkte hin zu größerer zeitlicher Streuung, gleichzeitig nimmt die Amplitude des Paketpotentials mit wachsendem σ jedoch weniger schnell ab als bei kleinerer Anstiegszeit des PSPs. Dieser Effekt stabilisiert die Dynamik bei größerem σ.

Untersuchen wir jedoch die Änderung der Synchronisationsdynamik bei Änderung von τ_0 unter Flächennormierung, ergibt sich ein vollständig anderes Bild. Der Attraktor verschiebt sich weiterhin zu größeren σ. Der Sattelpunkt kann jedoch nicht mehr zu größeren σ vordringen, die erforderliche Anzahl von Spikes nimmt jedoch zu, sodaß das Attraktorbecken schrumpft, bis sich die beiden Fixpunkte vernichten (Fig. 5 **B**).

Zusammenfassend kann man über den Einfluß der Anstiegszeit des postsynaptischen Potentials sagen, daß sie die erreichbare zeitliche Präzision der Spikes bestimmt, nicht aber das Auftreten stabiler Spikesynchronisation selbst. Sollte allerdings eine größere Anstiegszeit mit einer kleineren Amplitude gekoppelt sein, beispielsweise durch die Forderung des Erhalts der durch ein einzelnes PSP transportierten Ladung, ergibt sich eine kritische Anstiegszeit, oberhalb derer keine Spikesynchronisation mehr möglich ist (Kapitel 7).

Variabilität von Einzelrealisierungen

Durch die Konstruktion einer Mittelwertsdynamik konnten die dynamischen Eigenschaften der zu untersuchenden Netzwerkstruktur in einer zweidimensionalen iterativen Abbildung zusammengefaßt werden. Dieses Vorgehen ermöglicht es, den Effekt der für die Synchronisationsdynamik wesentlichen Parameter zu studieren: Anzahl der Neuronen pro Gruppe w, Amplitude der Membranpotentialfluktuationen σ_V, und Anstiegszeit des postsynaptischen Potentials τ_0. In Zusammenhang mit der Untersuchung des rauschfreien Falls wurde

klar, daß die Amplitude des PSPs $\widehat{u}$ und der Abstand des mittleren Membranpotentials zur Spikeschwelle nicht als eigenständige Parameter untersucht werden müssen, da sich alle Spannungsgrößen skaliert auf diesen Abstand betrachten lassen.

Es konnte gezeigt werden, daß für die Amplitude der Membranpotentialauslenkung, die ein Neuron bei Eintreffen eines Pakets erfährt, nur das Produkt $(w\alpha)\widehat{u}$ relevant ist. Daraus ergibt sich ein Skalierungsgesetz, nach welchem die Synchronisationsdynamik unverändert bleiben sollte, wenn die Gruppenbreite w um einen Faktor κ vermindert und gleichzeitig die PSP Amplitude um $1/\kappa$ erhöht wird. Mit der Reduktion der Anzahl von Neuronen pro Gruppe wächst allerdings der Beitrag jedes einzelnen Spikes am Paketpotential. Es stellt sich dann die Frage, wie gut die Mittelwertsdynamik noch die Aktivität in einzelnen Realisationen beschreibt. Die Existenz des Attraktorbeckens sichert eine gewisse Robustheit gegen Fluktuationen in der Anzahl der Spikes und deren zeitlicher Streuung. Eine einzelne Realisation der Netzwerkaktivität wird sich nur dann qualitativ von der Vorhersage der Mittelwertsdynamik unterscheiden, wenn in der Propagation von einer Neuronengruppe zur nächsten die Separatrix des deterministischen Modells überschritten wird. Aus diesem Grund wird die Variabilität einzelner Realisationen in einer neuen Größe, der Überlebenswahrscheinlichkeit $\mathcal{S}(a, \sigma)$, zusammengefaßt. Sie ist definiert als das Verhältnis der Anzahl der am Ort (a, σ) gestarteten Trajektorien, die den Attraktor erreichen, zur Gesamtzahl der gestarteten Trajektorien. Im deterministischen Fall ist diese Größe im Attraktorbecken 1 und fällt an der Separatrix instantan auf 0 ab. Indem wir die deterministische iterative Abbildung um geeignete probabilistische Komponenten für a und σ erweitern, können wir einen Eindruck davon gewinnen, wie gut die deterministische Beschreibung die wirkliche Dynamik erfaßt. Die Überlebenswahrscheinlichkeit kann jetzt für verschiedene w und skalierte $\widehat{u}$, also Situationen in denen die deterministische Dynamik unverändert bleibt, untersucht werden.

Unter Variation von w wird der scharfe Übergang der Überlebenswahrscheinlichkeit an der Separatrix aufgeweicht. Mit kleiner werdendem w wird der Übergang weniger steil. Selbst bei einer Gruppenbreite von 10 bleibt jedoch eine Umgebung um den Attraktor erhalten, in der die Überlebenswahrscheinlichkeit praktisch 1 ist. In der Nähe der Separatrix können jedoch Trajektorien, die in der Mittelwertsdynamik den Attraktor erreichen, durchaus aussterben. Auch der gegenteilige Fall kann auftreten: Trajektorien, die nach der Mittelwertsdynamik aussterben, können in der Einzelrealisierung in das Attraktorbecken springen.

Die probabilistische Erweiterung der iterativen Abbildung sagt voraus, daß die Mittelwertsdynamik eine gute Beschreibung für die Aktivität von Einzelrealisationen liefert (Kapitel 8). Dieser Befund läßt sich in Netzwerksimulationen bestätigen (Gewaltig, Diesmann, & Aertsen, 2001b).

Herkunft der Übertragungsfunktion

Durch die Einführung der Übertragungsfunktion für transiente Eingangsaktivität (Kapitel 3) konnte ein realistisches Neuronenmodell untersucht, und der Einfluß von physiologisch interpretierbaren Parametern auf die Synchronisationsdynamik studiert werden. Der Frage, wie sich die Übertragungsfunktion aus dem konkreten Neuronenmodell ergibt, kommt keine zentrale Bedeutung zu, da sie durch das beschriebene Konstruktionsverfahren für arbiträre Neuronenmodelle erzeugt werden kann. Selbst wenn für ein bestimmtes Neuronenmodell die

Übertragungsfunktion in geschlossener Form vorliegen würde, liefert nur die Analyse des Zustandsraumes eine Erklärung für den Mechanismus der Spikesynchronisation.

Allerdings wäre ein geschlossener Ausdruck für die Übertragungsfunktion wünschenswert, um ein besseres Verständnis der Parameterabhängigkeit der Übertragungsfunktion selbst zu erreichen. Um einen Einblick in das Entstehen der Übertragungsfunktion zu bekommen, erweitern wir einen Ansatz von Abeles (1991), der sich auf eine Abschätzung der Streuung der Spikezeitpunkte bezieht, sodaß auch Antwortwahrscheinlichkeiten kleiner 1 berücksichtigt werden können (Kapitel 9). Dadurch erhalten wir einen Ansatz, der beide Variablen (a, σ) und alle diskutierten Parameter enthält. Einige grundlegende Eigenschaften der so erhaltenen Übertragungsfunktion und die Abweichungen vom vollständigen Modell können somit diskutiert werden. Der Zusammenhang mit Intensitätsmodellen (z.B. Rotter, 1994; Gewaltig, 2000), die für eine weitere Behandlung vielversprechend erscheinen, wird diskutiert. Es wird gezeigt, daß die Ableitung des Paketpotentials nach der Zeit wesentlich in die Intensität eingeht.

Ergebnisse

Auf der Grundlage des Integrate-and-Fire Modells für das einzelne Neuron konnte gezeigt werden, daß die stabile Fortpflanzung synchroner Spikeaktivität in vorwärtsverschalteten Subnetzwerken unter den physiologischen Randbedingungen des Cortex möglich ist. Um die Analyse durchzuführen, wurde eine neue Übertragungsfunktion definiert und eine zweidimensionale iterative Abbildung konstruiert, welche die Dynamik im vorliegenden Netzwerk erfaßt. Mit Hilfe der eingeführten Werkzeuge konnte die Abhängigkeit der Dynamik von drei unabhängigen Parametern –Anzahl der Neuronen pro Gruppe, Amplitude der Membranpotentialfluktuationen und Anstiegszeit des postsynaptischen Potentials– studiert werden. Es zeigt sich, daß alle drei Größen Bifurkationsparameter der Dynamik darstellen, die den Attraktor für synchrone Spikeaktivität vernichten können. Allerdings steht für alle drei Größen ein Intervall im physiologischen Bereich zur Verfügung, in dem der Attraktor existiert. Jeder Parameter hat spezifische Auswirkungen auf die zu beobachtende Netzwerkaktivität.

Ausblick

Die Übertragungsfunktion ist im Prinzip auch experimentell zugänglich. Zunächst können in einem *in vitro* Experiment die synaptische Aktivität, sowohl für eintreffende Pakete als auch für die Hintergrundaktivität, durch Strominjektion nachgebildet werden (Rodriguez et al., 2001). Aus diesen Experimenten erwarten wir Erkenntnisse darüber, in wieweit das hier verwendete Neuronenmodell das Antwortverhalten eines cortikalen Neurons für transiente Stimuli beschreibt.

In der vorliegenden Arbeit wurden zwei Beschreibungsebenen cortikaler Aktivität miteinander verbunden: einerseits das Auftreten raum-zeitlicher Spikemuster, beruhend auf Daten von parallelen extrazellulären Ableitungen individueller Spikeaktivitäten vieler Neuronen, und andererseits unterschwellige Membranpotentialfluktuationen sowie Parameter einzelner postsynaptischer Potentiale, wie sie aus intrazellulären Einzelneuronableitungen gewonnen

werden können. Wenn nun Daten vorlägen, in denen die Spikeaktivität vieler Neuronen aufgezeichnet und gleichzeitig die unterschwellige Aktivität einzelner Neuronen beobachtet wurde, ließe sich die Konsistenz des Modells überprüfen.

In der durchgeführten Analyse wurde vorausgesetzt, daß das cortikale Netzwerk einen stabilen Grundzustand einnimmt, in dem die Neuronen bei niedrigen Raten unkorreliert aktiv sind, und daß dieser Zustand durch die Existenz des vorwärtsverschalteten Subnetzwerks nicht gestört wird. Die Stabilität des Grundzustands ist Gegenstand gegenwärtiger Forschung (Tetzlaff, Geisel, & Diesmann, 2001).

Bei der Konstruktion der iterativen Abbildung wurden die zeitlichen Aspekte der Dynamik eliminiert. Die Abbildung liefert keine Information darüber, nach welcher Zeit eine bestimmte Neuronengruppe aktiviert wird. Netzwerksimulationen haben jedoch gezeigt, daß bei Stimulation mit schwachen Paketen der Aktivierungszeitpunkt einer bestimmten Neuronengruppe um einige ms schwanken kann. Diese Unschärfe in der Kopplung an den Stimulus baut sich bereits in den ersten Neuronengruppen auf. Sobald der Attraktor erreicht ist, bleibt die Präzision der Kopplung praktisch stationär (Gewaltig, Diesmann, & Aertsen, 2001b). In experimentellen Daten treten raum-zeitliche Spikemuster allerdings nur lose gekoppelt an den Stimulus auf, mit einer Unschärfe von ca. $10 - 100$ ms. In ersten Simulationen (Grün, 1996) konnte gezeigt werden, daß ein vorwärtsverschaltetes Subnetzwerk, welches durch eine Ratenerhöhung in einer Reihe von aufeinanderfolgenden Neuronengruppen aktiviert wird, einerseits Aktivität aufweist, die sich zu synchronen Paketen organisiert und dann stabil propagiert wird, andererseits aber keine scharfe Kopplung an den Stimulus existiert. Der Mechanismus dieses Übergangs von asynchroner Aktivierung zu synchroner Aktivität muß noch geklärt werden und wird in aktuellen Arbeiten untersucht.

Die oben beschriebenen weitergehenden Fragestellungen bewegen sich alle im Rahmen des Ansatzes, der in dieser Arbeit vorgestellt wurde. Ein Subnetzwerk wird isoliert vom Gesamtnetzwerk betrachtet, um einer Analyse zugänglich zu sein. Über den Grundzustand von Zufallsnetzwerken ist inzwischen viel bekannt (van Vreeswijk & Sompolinsky, 1996; Amit & Brunel, 1997) und ebenso über die Dynamik vorwärtsverschalteter Subnetzwerke. Daher erscheint es an der Zeit, die beiden extremen Modelle zusammenzuführen. Netzwerke der erforderlichen Größe können inzwischen mit vertretbarem Aufwand simuliert werden (Mehring et al., 2003). Ist das einbettende Netzwerk nicht vollständig zufällig verknüpft, stellt sich die Frage nach der räumlichen Anordnung der Neuronen einer Synfire Chain (Hehl et al., 2001).

Mit dem letzten Absatz eng verbunden ist die Frage nach der richtigen Nullhypothese für die Suche nach raum-zeitlichen Spikemustern in experimentellen Daten (siehe z.B. Grün, Diesmann, & Aertsen, 2002b). Die angemessene Modellierung eines Cortexvolumens wird es erlauben, Analyseverfahren anhand der Spontanaktivität des Netzwerkes zu kalibrieren.

Möchte man die Möglichkeit des Cortex, synchrone Spikeaktivität in vorwärtsverschalteten Subnetzwerken stabil zu transportieren, nicht nur als mögliche Dynamik auffassen, die eventuell nur als Nebeneffekt in Erscheinung tritt, so besteht eine große Herausforderung darin, eine funktionelle Verwendung dieses Mechanismus zu finden. Ein plausibles Netzwerkmodell, das vorwärtsverschaltete Subnetzwerke nutzt, um eine bestimmte Leistung zu vollbringen und Vorteile gegenüber anderen Lösungen demonstriert (siehe z.B. die Ansätze in Abeles et al., 1993b; Bienenstock, 1995), würde eine starke Unterstützung der „Synfire“-Hypothese bedeuten und eventuell neue Vorhersagen für experimentelle Studien liefern.

Chapter 1

Introduction

The present work seeks to contribute to our understanding of the dynamical properties of the mammalian brain, specifically the neocortical network. The first section of this chapter introduces the basic structure and dynamics of the mammalian cortex. The following section briefly reviews experimental results and theoretical concepts on the dynamics of the cortical network. Sec. 1.3 concentrates on the study of correlations in the activity of nerve cells which motivated the present work. A specific subnetwork architecture, the "synfire chain", was proposed to explain a certain type of correlations, "spatio-temporal spike patterns", in the experimental data. Sec. 1.4 introduces the model and illustrates its typical dynamics. The network model has raised a number of questions regarding its dynamical properties and its plausibility given the conditions in the cortex. The focus of the present study, described in Sec. 1.5, is derived from the need to gain an understanding of fundamental properties of this system. The last section provides an outline of the investigation.

1.1 The Cortical Network

The mammalian brain contains a large number of nerve cells (10^{14} in humans). It is commonly accepted that information processing in the brain is primarily based on the electrical activity of this specific class of cells, also called neurons. Neurons maintain a potential (membrane potential) difference across their membrane, separating the intracellular from the extracellular medium. The interaction between neurons is mediated by the occurrence of sharp voltage transients (duration 1 ms), called action potentials or spikes, in individual neurons. The contacts between neurons, called synapses, are directed. A spike in the presynaptic neuron causes, after a fixed time delay of a few ms, a small membrane potential excursion (post-synaptic potential, PSP) in the post-synaptic neuron. In a strongly simplified view of neuronal dynamics, an action potential is emitted when the superposition of a sufficient number of post-synaptic potentials reaches a certain voltage threshold (for recent introductory texts see e.g. Kandel, Schwartz, & Jessel, 1991; Johnston & Wu, 1995; Koch, 1999; Nicholls, Martin, Wallace, & Fuchs, 2001). The generation of an action potential is followed by a period of refractoriness in which no further spike can occur. A cortical neuron is the target site of about $20,000$ connections. 80% percent of the synapses are excitatory, the remaining ones inhibitory (Braitenberg & Schüz, 1998). Inhibitory synapses drive

the membrane potential away from spike threshold. The action potential itself is strongly driven by the internal dynamics of the neuron and, hence, does not depend on the details of the membrane potential excursion causing the spike. Thus, in this simplified picture, the sequence of spike times determines the state of the network.

In electrophysiological experiments, one or more microelectrodes are inserted into the brain (e.g. Abeles, 1982a; Gerstein, Bloom, Espinosa, & Evanczuk, 1983; Kandel, Schwartz, & Jessel, 1991; Nicolelis, 1998; Nicholls, Martin, Wallace, & Fuchs, 2001). Spikes of neurons in the neighborhood of the unisolated tip of an electrode are seen as potential fluctuations compared to a reference electrode. Because of volume conductance and the different morphological structure of neurons, spikes from a few individual neurons can often be identified by data processing of the action potential wave shapes (for a recent review see Lewicki, 1998). It should be noted, however, that many problems remain and the quality of spike sorting is debated and an active field of research.

1.2 Cooperative Effects

Being able to record the electrical activity of neurons in the intact animal (anesthetized or awake) allowed researchers to directly study the dynamics of the neural network. The principal tools are to correlate neural activity with stimulus or behavioral events, and to correlate the activity of different recorded neurons amongst each other (Perkel & Bullock, 1968).

Initially, recording techniques were limited to recordings from one channel at a time. Here, the recording was optimized to obtain the spikes from a single neuron only, or the spikes where left unidentified (e.g. in recordings from nerve fibers). Due to this limitation and also guided by early considerations about the integrative properties of the neuron (Sherrington, 1906; Eccles, 1957) researchers concentrated on reproducible changes in the spike rate. Adrian (1928) observed that the spike rate of neurons is related to changes in the environment and concluded that the intensity of sensation is proportional to sensory spike rates. Single neurons with their specific characteristics became the building blocks of cortical processing (Barlow, 1972; Barlow, 1992, for reviews see Martin, 1994; Martin, 2000). This approach led to fundamental insights into the neuronal mechanisms of brain function (e.g. Lettvin, Maturana, McCulloch, & Pitts, 1959; Hubel & Wiesel, 1968) and to important theoretical works on information processing by neuronal networks (McCulloch & Pitts, 1943). The influential book by Minsky and Papert (1988) pointed out the limitation of this concept (see also von der Malsburg, 1986b).

The parallel and distributed architecture of the cortex suggested the investigation of the collective properties of neural networks. Hebb (1949) proposed that ensembles of neurons, "cell assemblies", constitute the units of neuronal processing. In this view, functional groups are formed by the coherent activity of the participating neurons. This hypothesis provided the conceptual framework for successful theoretical work on neural networks (e.g. Hopfield, 1982; Rummelhart, McClelland, & the PDP Research Group, 1986; Amit, 1989; Amit & Brunel, 1997). These models exhibit multiple attractor states, the attractors being groups of neurons with elevated spike rates. A prominent example from the experimental literature demonstrating the representation of information by ensembles of neurons is (Georgopoulos,

Kettner, & Schwartz, 1988; Georgopoulos et al., 1989).

In parallel, however, conceptual difficulties of the representation of assembly membership by spike rate were pointed out (von der Malsburg, 1981; von der Malsburg, 1986a). The notion was developed that, alternatively, assembly membership could be expressed in the temporal organization of spiking activity (von der Malsburg, 1981; Abeles, 1982a; von der Malsburg, 1986a; Palm, 1990; Abeles, 1991; Gerstein, Bedenbaugh, & Aertsen, 1989; Singer, 1993). Consequently, neuronal processing should be reflected in dynamical changes of spike time correlation.

Dynamic modulations of spike correlation at various scales of precision have, in fact, been observed in different cortical areas: visual (Eckhorn et al., 1988; Gray & Singer, 1989) for reviews see (Engel, König, Schillen, & Singer, 1992; Aertsen & Arndt, 1993; Singer & Gray, 1995; Roelfsema, Engel, König, & Singer, 1996; Singer et al., 1997; Singer, 1999b), auditory (Ahissar, Ahissar, Bergman, & Vaadia, 1992; Eggermont, 1992; deCharms & Merzenich, 1996; Sakurai, 1996), somato-sensory (Laubach, Wessberg, & Nicolelis, 2000; Nicolelis, Baccala, Lin, & Chapin, 1995; Steinmetz et al., 2000), motor (Murthy & Fetz, 1992; Sanes & Donoghue, 1993; Riehle, Grün, Diesmann, & Aertsen, 1997; Hatsopoulos, Ojakangas, Paninski, & Donoghue, 1998), and frontal (Aertsen et al., 1991; Abeles, Bergman, Margalit, & Vaadia, 1993; Vaadia et al., 1995; Prut et al., 1998; Grün, Diesmann, & Aertsen, 2002b).

Fujii et al. (1996) provides an extensive review on the conceptual framework of the cell assembly hypothesis with a focus on its implementation by spike time correlation. A review of the various aspects of the electrophysiological data supporting the different concepts of neuronal processing can be found in (Vaadia & Aertsen, 1992). More recent reviews on neural coding are (Shadlen & Movshon, 1999; Singer, 1999a; Salinas & Sejnowski, 2001).

1.3 Modulations of Spike Time Correlations

Searching for correlations as a signature of cooperative phenomena in the brain, researchers found that, indeed, the spiking activity recorded on different channels may be correlated. The signals of two channels are classified as being correlated if channel 2 reports a spike at certain delays after (or before) the occurrence of a spike in channel 1 more often than expected assuming independence. In order to detect the activity of cell assemblies and their interactions, simultaneous recordings should be obtained from as many neurons as possible. Recording from awake animals involved in a behavioral paradigm enables the experimenter to observe the correlation structure while the neurons are carrying out computational tasks.

Cross-Correlation Studies

An important first step was to demonstrate that the correlation between neurons may be context dependent. Gray, Singer, Eckhorn, and their co-workers showed that, depending on the stimulus, neurons in the visual cortex exhibit changes in the correlation of the spiking activity (Gray & Singer, 1987; Eckhorn et al., 1988; Gray & Singer, 1989; Gray, König, Engel, & Singer, 1989). In these findings, the pronounced oscillatory structure of the cross-correlogram with a central peak was interpreted as evidence that the neurons entered a synchronous oscillatory state. The correlations observed in neuronal data cannot be attributed

to the underlying network structure alone (Aertsen, Gerstein, Habib, & Palm, 1989; Aertsen et al., 1991). Parameter changes seem to be able to drive the network into different dynamical regimes or activate different subnetworks.

Having established stimulus and behavioral dependence of spike time correlations, the next step in the investigation of cortical processing was to study the dynamics of correlations. New tools like the Joint-PSTH (Aertsen, Gerstein, Habib, & Palm, 1989, based on earlier work, Gerstein & Perkel, 1969) allowed for an analysis of the dynamics of spike time correlation of two neurons with respect to a stimulus or behavioral event. Thus, Vaadia et al. (1995) reported changes in correlations within fractions of a second. Under different experimental conditions a different time course of the correlation is exhibited.

Still, the tools presented so far are restricted to the simultaneous analysis of only two neurons. With state of the art technology, experimenters are now able to record the individual spiking activity of in the order of 10-100 of the 10^5 neurons in a local volume. Thus, to increase chances to uncover the nature of cortical dynamics and to exploit the available data, methods are desired which analyze as many channels as are available as a whole, rather than as a collection of single units or pairs of units.

Analyzing Multiple Single Neuron Recordings

The method of "gravitational clustering" (Gerstein & Aertsen, 1985) expresses the correlation between neurons by the distances between abstract particles in N-space. The dynamics of the correlation structure is mapped onto the relative movements of the particles. Here, for the first time, the correlation dynamics of a population of neurons could be analyzed and visualized. If neurons of a functional group exhibit correlated activity for a period of time long enough for the "gravitation" to become effective, the subset of neurons composing the group forms a cluster. Different functional groups activated at different times should give rise to different clusters at the corresponding times. The common membership of a neuron in several functional groups could result in movements of the corresponding particle from one cluster to the other. However, the interaction between particles is a two-body interaction, therefore strict statements about higher-order correlation could not be made. Two uncorrelated particles may approach each other because they are both correlated to a third one. At the same time, three neurons firing in synchrony more often than expected may not particularly attract each other because the pairwise synchrony does not exceed expectation (Baker & Gerstein, 2000 discuss 3-particle interaction). A further limitation is that the attractive force has to be specified by a temporally restricted interaction kernel depending on the distance between spikes. Therefore, the interaction kernel determines the type of correlation which is searched for. Usually an interaction kernel with a center of mass close to zero is chosen. This is consistent with the finding that most cross-correlations with significant contributions show high amplitudes close to the origin (see Vaadia & Aertsen, 1992 for a review).

A clear signature of the activation of a functional group of neurons should be the occurrence of higher-order correlations under specific behavioral conditions. The reasoning here was that membership in a functional group might be expressed by the contribution of single well placed spikes, not necessarily at zero delay to other spikes. Using a visualization technique for triple correlations (Gerstein & Perkel, 1972; Perkel, Gerstein, Smith, & Tat-

ton, 1975), Abeles (1982a) found that in sets of three neurons particular spike constellations $(i, j, k; t_1, t_2)$ occur much more often than expected by chance. These triplets are events where following a spike in neuron i, neuron j generates a spike at delay t_1, which is at delay t_2 followed by a spike of neuron k.

The timing of spikes in the triplets was found to be at ± 1 ms precision. Surprisingly, the time delays often spanned hundreds of ms. In principle, reflections of such spike patterns should be visible in the classical (two neuron) cross-correlogram, assuming they occur often enough to stand out against the background level. However, narrow delayed peaks are only seldomly observed. Abeles (1991) explained this finding by the view that neurons are engaged in a large number of different processes. The process which generates the specific pattern that both neurons are involved in occurs only occasionally. Therefore, the specific time-locked activity is buried in the spikes generated by other processes. By having available the data of three or more neurons, involved in the same process, chances are much better to be able to distinguish the specific spike constellation from uncorrelated activity. It should be noted here that the absence of indications for precise spike patterns in the pairwise cross-correlograms does not imply that the correlograms are flat.

Spatio-Temporal Spike Patterns

In the same book (Abeles, 1982a) reporting the spike triplets, Abeles introduced the model of a "synfire chain" to explain the occurrence of temporally extended spike patterns. The dynamical properties of the synfire chain model and its plausibility are the focus of the present work. Before we describe the synfire model in detail in the next section (Sec. 1.4), let us briefly review the experimental evidence for spike patterns along with the further development of tools for their analysis. With our current knowledge we cannot separate the experimental evidence from the available and applicable analysis tools, because different experimental situations have required different analysis tools, and different analysis tools highlight different aspects of cortical activity.

Thus, giving up the dynamical aspects of spike time correlation, Abeles and Gerstein (1988) designed an algorithm to search N parallel spike trains for the occurrence of spatio-temporal spike patterns. The term "spatio-temporal pattern" indicates the two domains of a spike pattern: the temporal domain and the domain of neuron identifiers. A purely spatial pattern consists of spikes from different neurons occurring simultaneously, a purely temporal pattern consists of consecutive spikes from a single neuron. A number of studies has demonstrated that precise spatio-temporal spike patterns do occur in the experimental data. Confirming the 1982a finding, spike patterns often exhibit spike time delays of up to several hundred ms. In addition, patterns occur related to the behavioral context. A particular pattern might occur in one experimental condition but not in another. Typically, patterns are only weakly time-locked to external stimuli (Abeles, Vaadia, & Bergman, 1990; Villa & Abeles, 1990; Abeles et al., 1993b; Abeles, Bergman, Margalit, & Vaadia, 1993; Abeles et al., 1993a; Abeles, Prut, Bergman, & Vaadia, 1994). Fig. 1.1 exemplifies the typical appearance of a spatio-temporal firing pattern in neuronal data.

Concentrating on triplets, Prut (1995) designed a statistical test, demonstrating that the precise temporal patterns found in the experimental data could not be explained by pairwise correlations. Prut et al. (1998) provides a detailed study on the properties of spatio-temporal

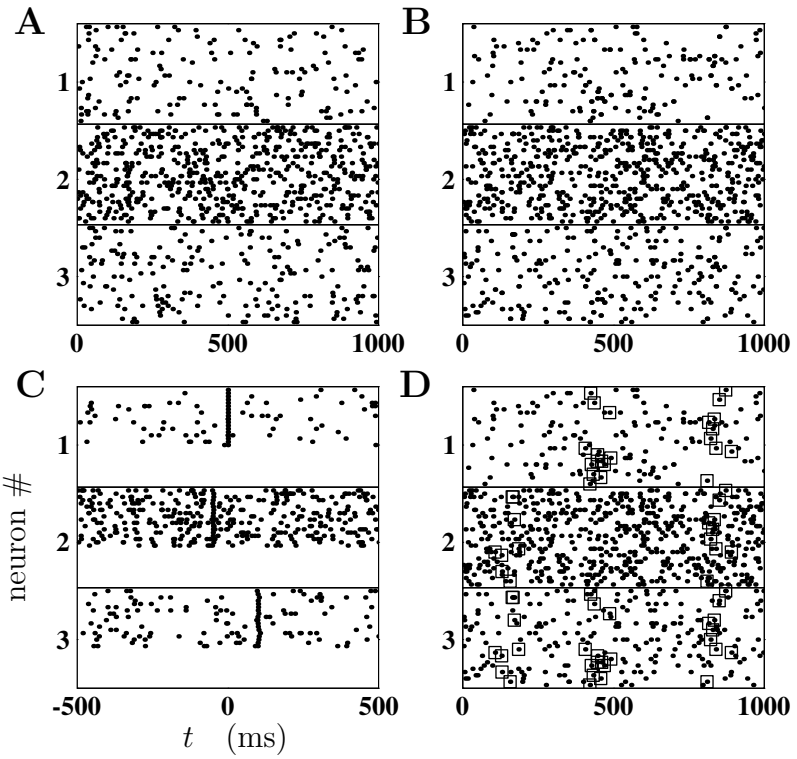

Figure 1.1 Typical appearance of spatio-temporal spike patterns in the dot display. **A** Dots in boxes labeled 1 to 3 represent spike times of three simultaneously recorded neurons. In each box, one vertical position is reserved for every repetition (30 trials) of the experiment. Time t is advancing along the horizontal axis. The spike data displayed are generated from independent Poisson processes with rates 5 Hz (box 1), 20 Hz (2), and 7 Hz (3). Parallel processes are observed for 1000 ms starting at an arbitrary point in time (0 ms). A spatio-temporal spike pattern $(2, 1, 3; 50\,\text{ms}, 100\,\text{ms})$ is injected into the data homogeneously distributed over an interval ± 200 ms around $t = 500$ ms at a rate of 3 Hz. In addition each spike time in a pattern is subject to a Gaussian distributed temporal jitter of 1.5 ms standard deviation. A constant spike rate of individual neurons is maintained by correcting the independent base rates for the additional spike rate caused by the pattern in the corresponding time intervals. **C** Same data as in **A**. Only the trials in which the injected pattern occurred at least once are shown. Here, trials are aligned on the spike neuron 1 contributes to the first occurrence of the pattern in the trial ($t = 0$ ms). Compared to **A**, vertical positions of the trials are reorganized. Trials containing the pattern occupy the top vertical positions to visualize their proportion (18 of 30). Alignment of the spikes of neuron 1 at $t = 0$ ms is perfect by definition. Spikes of neuron 2 and 3 appear aligned at $t = -50$ ms, and $t = 100$ ms respectively, exhibiting the internal jitter in the pattern. **B** Same spike rates and procedure as in **A**, different realization. Three purely spatial patterns are injected at different points in time: $(2, 3; 0\,\text{ms})$ at rate 4 Hz homogeneously distributed in an interval ± 50 ms centered at $t = 150$ ms, $(1, 3; 0\,\text{ms})$ with 4 Hz at $t = 450\,\text{ms} \pm 50\,\text{ms}$, $(1, 2, 3; 0\,\text{ms}, 0\,\text{ms})$ with 3 Hz at $850\,\text{ms} \pm 50\,\text{ms}$. **D** Same data as in **B**. Using an analysis window of 100 ms and requiring a significance level of 0.01, the injected coincidences appear as significant in UE-analysis (binwidth 1 ms). Here, spikes belonging to an injected pattern are marked by squares. UE-analysis would, in addition, mark chance coincidences surrounding the injected patterns. For early experimental data displayed as in **C** see Abeles (1982a) and for recent results Prut et al. (1998), for **D** see e.g. Riehle, Grün, Diesmann, and Aertsen (1997) and Grün, Diesmann, and Aertsen (2002b).

patterns, and their relation to behavior. She also showed that the patterns were not generated by slow temporal changes of correlation, such that identification of a pattern would critically depend on the significance threshold. In comparison to spike constellations with slightly different time delays, a dramatic increase in significance was observed. Spatio-temporal patterns classified as significant remain significant for almost arbitrarily high thresholds.

The search for spatio-temporal patterns revealed that temporally extended precise correlations do exist. However, in contrast to the JPSTH and gravitational clustering, the dynamics of correlations cannot be studied. This is basically due to the fact that long pieces of continuous data are needed for the identification of the patterns. If a pattern occurs non-homogeneously distributed over time, the number of occurrences can be non-significant although it would be significant in a specific time interval of the experiment. If, however, a pattern occurs homogeneously distributed, but the spike rate of the neurons is changing in time, a pattern may be significant in one time interval of the experiment, but not in another. In addition, the observation of changes in pattern constellation in a time resolved manner may provide information about the nature of neuronal processing.

An independent motivation to return to a time resolved measure are technical considerations on the computation of reliable expectations (see Grün, Diesmann, & Aertsen, 2002b and the references cited therein). By restricting the analysis to purely spatial patterns, so called "unitary events" (UEs), Grün (1996) was able to define a measure, the joint-surprise, that indicates the presence of an unexpected spike constellation in short windows in the order of 100 ms. In contrast to Prut (1995), the method is designed for a large number of parallel processes, and can analyze the data for all possible patterns simultaneously. Sliding the analysis window over the data, conspicuous spike patterns can be marked at the point of their occurrence in time. The result is a visualization of the correlation structure of the data as a function of time. The appearance and disappearance of spike patterns can be compared with the stages of the experimental protocol. The time course of pattern occurrence can also be compared to the time course of other time varying features of the data, such as the spike rate.

Analyzing data from monkey primary motor cortex, we found (Riehle, Grün, Diesmann, & Aertsen, 1997) that unitary events appear at points in time where the animal could expect a stimulus to occur, without the stimulus actually being presented. Here, typically no change in spike rate was observed. By contrast, when unitary events occurred in relation to external events such as a stimulus or a behavioral event, they were typically accompanied by changes in spike rate. The composition of the unitary events was different for different movement directions. No strict locking of unitary events to stimuli, expected events, or behavioral events was observed. However, typically unitary events appeared clustered in time. Analysis of data from frontal cortex (Grün, 1996; Grün, Diesmann, & Aertsen, 2002b) showed that the appearance and composition of unitary events is task dependent. A particular neuron generated a unitary event with one neuron in a first task, and formed a unitary event with another neuron in a second task. It was also observed that during the course of an experiment, neurons formed unitary events with different partners.

However, in the light of the methodological difficulties (see e.g. Brody, 1999b; Brody, 1999a; Grün et al., 1999; Roy, Steinmetz, & Niebur, 2000; Pauluis & Baker, 2000; Baker & Gerstein, 2000; Baker & Gerstein, 2001; Grün, Riehle, & Diesmann, 2001; Gütig, Aertsen,

& Rotter, 2002), the search for cooperative phenomena in multiple single unit recordings and the development of appropriate analysis tools remains a challenging field of research. In the next section we will discuss how spike synchronization and the occurrence of temporally extended spike patterns may be explained in a consistent framework.

1.4 The Synfire Model

Classically (Sherrington, 1906; Eccles, 1957), the mode of operation of a neuron is described as that of an integrator. This is also suggested by our description of the basic dynamics of a neuron in Sec. 1.1: synaptic inputs are integrated until a threshold is reached and a spike is emitted. However, in his 1982a monograph Abeles demonstrated that under the conditions prevailing in the cortex, neuronal dynamics allows for a different interpretation. The effect of the activation of a single excitatory synapse on the post-synaptic neuron is small in the sense that the probability of spike generation in response to that input is low. However, the effect of a single synapse is not so small if the amplitude of the post-synaptic potential is considered. The superposition of a few tens of post-synaptic potentials is sufficient to elevate the membrane potential from its mean to spike threshold. Let us assume that the response probability to a single input is 0.001, and that 50 spikes are needed to reach spike threshold, both representing realistic numbers. In this case, 500 asynchronous input spikes are required to expect 0.5 output spikes, whereas 50 spikes are sufficient in the synchronous case. According to this consideration, synchronous input is about 10 times more effective than asynchronous input. Thus, Abeles (1982a) concluded that the cortical neuron can act as a coincidence detector. In a quantitative analysis (Abeles, 1982b; Abeles, 1991) it could be shown that in the parameter regime of interest, synchronous activity is more effective in adding spikes to the post-synaptic spike train than the corresponding asynchronous activity (see Murthy & Fetz, 1993; Bernander, Koch, & Usher, 1994; Murthy & Fetz, 1994 for the limiting case where more spikes are synchronized than required to elicit an output spike, "overcrowding" reduces the output spike rate).

The delay between a pre-synaptic spike and a post-synaptic response spike is in the order of a few ms. Abeles (1982a) pointed out that if the occurrence of a spike pattern spanning hundreds of ms should be explainable by a flow of activity from a neuron early in the pattern to a later one, many synaptic stages would have to be involved. However, because of the weak coupling mediated by a single synapse, a chain of hundreds of neurons connected by single synapses cannot explain the strong coupling expressed in the spike patterns. As we have seen above, an effective way to cause a neuron to generate a response spike is to supply it with a large enough number of synchronous input spikes. Such input can be provided by a group of neurons projecting to the target neuron (Fig. 1.2 **A**). Thus, the occurrence of synchronous spikes in neuronal data could be regarded as an indication that, consecutively, other neurons in the system might be reliably activated. If two neurons receive the same input, they will tend to generate spikes at the same points in time. Hence, synchronous activity can be the result of common input (Fig. 1.2 **B**). In this view the occurrence of synchronous spikes in neuronal data is explained by the presence of common input.

The combination of the two principles: (1) convergent input from a group of source neurons (Fig. 1.2 **A**), and (2) common input to a group of target neurons (Fig. 1.2 **B**) leads to

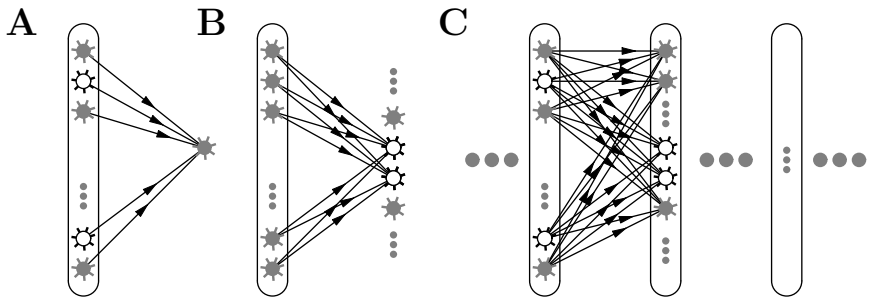

Figure 1.2 Propagation of synchronous spiking in locally feed-forward arrangements of cortical neurons. **A** Effect of tight spike correlation by convergence onto a target neuron. **B** Generation of tight spike correlation among target neurons by shared input activity. Two simultaneously recorded neurons are indicated by highlighting. **C** Combination of arrangements **A** and **B** leads to a volley of coincident spikes which, by repeating the arrangement, is propagated from one group of neurons to the next: a "synfire chain". Depending on neuron and network properties and on the initial spike volley configuration, such propagation can either be maintained in stable fashion or become instable (cf. Fig. 1.3).

a local network structure in which synchronous activity in one neuron group is the generator of synchronous activity in another neuron group (Fig. 1.2 **C**). This structure is called a divergent/convergent link. Connectivity is divergent from the point of view of a source neuron and convergent from the point of view of a target neuron. Now, the target group reproduces the synchronous activity of the source group. Hence, the target group can act as the source to yet another neuron group. By repeating this arrangement, long chains of groups of neurons can be formed. In the simplest case, each neuron establishes exactly one synapse with each neuron of the preceding group. At each stage, synchronous activity occurring in the preceding group is reproduced. Thus, if the neurons in the first group spike in synchrony a volley of spikes travels through the network activating one neuron group after the other. The use of groups of neurons instead of individual ones overcomes the weak synaptic coupling between individual neurons. This feed-forward arrangement of groups of excitatory neurons allowing the propagation of volleys of synchronous spikes is called "synfire chain" (Abeles, 1982a).

The occurrence of spatio-temporal spike patterns can now be explained by assigning the neurons contributing to a pattern appropriate locations in a synfire chain. A spatial pattern is generated by neurons that are members of the same neuron group. A temporal pattern with long time intervals between the spikes times is generated by neurons located in distant neuron groups. The number of intermediate neuron groups is proportional to the temporal delay between the spikes. In the experimental data, spatio-temporal spike patterns are embedded in spiking activity which seems to be uncorrelated to the process generating the pattern. Therefore, it is an essential property of the synfire chain that on each activation the participating neurons are contributing only a single spike. Between activations of a specific chain, a neuron can take part in many other processes. The participation of a neuron in several different patterns is explained by the membership of the neuron in several, partly overlapping chains.

It should be pointed out that we are here facing a cooperative effect. Membership of a neuron in a synfire chain cannot be deduced by observation of the spike train of the single

neuron. If activation of the chain is not strictly locked to an event under the control of the experimenter, the single spike contributed by the activation of the chain is indistinguishable from other spiking activity. The occurrence of a spike in experimental data not contributing to any pattern does not mean that the spike is not generated by synfire activtity. It may just mean that we have missed to record from the appropriate partner neurons. We have seen above that the number of neurons we can record from is small compared to the total number of neurons in the local volume. Since every neuron may participate in many different processes, and since there is a large number of potential partner neurons available, it is unlikely that our sample of neurons is sufficient to resolve all the neuronal processes. An extreme view would require all spiking activity to be generated by synfire activity (see Chap. 10).

The concept of a synfire chain does not require intra-chain synapses to be stronger than other synapses in the network. Assume that we are recording from two neurons from two successive neuron groups. If the pre-synaptic neuron is individually stimulated in some way (e.g. current injection), the cross-correlation between the two shows only a weak coupling between the neurons. If the source neuron group is activated, the coupling will suddenly appear to be strong. Whether activation of the synfire chain is noticeable in the cross-correlation depends on the number of these activations compared to the uncorrelated spikes of the neurons. If the synfire chain is repeatedly active (in time or across trials) in one phase of the experiment and not in a different phase, the cross-correlation would exhibit dynamical changes.

Analysis of the spatio-temporal spike patterns occurring in experimental data revealed (Abeles, Bergman, Margalit, & Vaadia, 1993; Prut et al., 1998) that often an individual neuron is contributing several spikes to the pattern. The synfire model explains this phenomenon by the participation of a neuron in several successive neuron groups (Abeles, 1982a). The sparse reoccurrence of neurons in later groups does not perturb the propagation of synchronous activity along the chain. The type of activity exhibited by a network structure which is locally feed-forward, supporting the propagation of synchronous activity from one neuron group to the next, but on a more global scale has recurrent structure, is termed "synfire reverberation" (Abeles, Bergman, Margalit, & Vaadia, 1993). Under certain conditions, activity may re-excite itself while still supporting precise spike patterns. Properties of synfire reverberations and implications are studied using network simulations in (Abeles et al., 1993b; Abeles, Prut, Bergman, & Vaadia, 1994).

The discussion in the previous paragraph made clear that the graphical representation of a synfire chain (Fig. 1.2 **C**) should not be understood as a visualization of the anatomical arrangement of the neurons in the cortex. The feed-forward arrangement of neuron groups from left to right solely symbolizes the order in which the neurons are activated. According to this graph-like model, the location of the neurons in the cortex is arbitrary. The graph like-model of a synfire chain describes a distributed system (Rummelhart, McClelland, & the PDP Research Group, 1986), not restricted by cortical space (see Hehl et al., 2001 for a discussion of spatial constraints). We would like to speak of neuron groups rather than "layers", to avoid confusion with the anatomical layers of the cortex and the distinct meaning of a layer in artifical neural networks (e.g. Haykin, 1998). Abeles also uses the terms "nodes" (Abeles, 1991) and "pools" (Abeles et al., 1993b). In the foregoing we assumed that

the chain is fully connected in the sense that each neuron in the source group projects to each neuron in the target group. Griffith (1963) discussed such structures in the context of stability of network activity and termed a fully connected chain a "complete transmission line". He noticed that a chain-like structure should allow for the reliable transport of excitation through a network without excitation of the whole system. The preferential mode of activity being synchronous volleys of spikes (see also Beurle (1956) for an early study on the propagation of activity in excitatory networks).

Anatomical considerations suggest that, at least locally in a 1mm^3 volume, the cortical network has the properties of a random graph (Braitenberg & Schüz, 1998; Hellwig, 2000). The probability of two nearby neurons having (direct) synaptic contact is about 0.3. Assuming that network connectivity is random was also successful in uncovering fundamental properties of the dynamics of large spiking neural networks at low spontaneous firing rates (van Vreeswijk & Sompolinsky, 1996; van Vreeswijk & Sompolinsky, 1998; Amit & Brunel, 1997; Brunel & Hakim, 1999; Brunel, 2000). It is therefore a natural question to ask whether the cortex would allow for the existence of synfire structures. The answer is twofold. Complete (i.e. fully connected) chains are very unlikely to exist. However, incomplete or diluted chains in which only a fraction (about 1/3) of the possible connections is realized are likely to exist (Abeles, 1991; Hehl et al., 2001). The dynamics of an incomplete chain can be expected to be comparable to that of a complete chain if the number of neurons per group is scaled up to keep the number of inputs to individual neurons constant (Hehl, Aertsen, & Diesmann, 2001a). Therefore, we can concentrate on complete chains when analyzing the fundamental dynamical properties of such feed-forward type structures.

Evidence from Single Neuron Dynamics

The argument of Abeles (1982a) that synchronous input is more effective than asynchronous input is based on assuming deterministic dynamics of the single neuron. Also the assumed property in the synfire model that neurons receiving the same input will synchronously generate spikes is based on deterministic single neuron dynamics. In both cases, the stochastic element is introduced by the large fluctuations of the membrane potential caused by the excitatory and inhibitory activity coming in from the many thousands pre-synaptic neurons in the remainder of the network. In a locally feed-forward architecture these fluctuations would be overcome by the large current transients caused by synchronously arriving spikes. An incoming volley of synchronous spikes drives the membrane potential to spike threshold, making the spike generation and the timing of the response spike quasi-independent of the ongoing fluctuations. In this view, synchronous activity is at the same time the result (Fig. 1.2 **B**) and the generator (Fig. 1.2 **A**) of sharp transients in membrane potential.

Thus, independent evidence for the idea that synchronous activity is a natural mode of operation of the cortex can be provided by appropriate single neuron studies. A demonstration that the cortical neuron has the required dynamical properties evidently cannot show that synfire chains exist and are used by the brain. However, it delivers strong support for the claim that synfire activity constitutes a possible mode of activity. In contrast to the search for spatio-temporal firing patterns in multiple single neuron recordings, dynamical properties of single neurons can be investigated without the need for advanced statistical tools and data processing (however, see early reports e.g. Calvin & Stevens, 1968; Bryant &

Segundo, 1976 for the efforts required in those days), and the corresponding difficulties in interpretation.

An early study on the sources of variability in spike timing was performed by Calvin and Stevens (1968). These researchers performed a study on spinal motoneurons in the either decerebrated or anesthetized cat. By comparing intracellular recordings under the injection of a constant (DC) current with simulations of a neuron model with deterministic spike generation, they concluded that the major source of variability in spike timing comes from synaptic activity. A later *in vitro* study (Bryant & Segundo, 1976) in aplysia neurons investigated the neuronal response to Gaussian white noise current (in the absence of synaptic activity). It could be shown that the neurons emit a highly reproducible spike train in response to repetitions of the same piece of noise current realization ("frozen noise"). Preferentially, the neurons responded to transients in the input current. A simple model with a deterministic threshold was sufficient to explain most of the results. The main effect is carried by the amplitude of the current, however, also slope and acceleration contributed. Mainen and Sejnowski (1995) reconsidered the older studies and could clarify some of the confusion on the precision of spike timing in intracellular studies (see also Nowak, Sanchez-Vives, & McCormick, 1997). In an *in vitro* preparation of rat neocortical slice, the spiking activity was recorded in response to DC current and to filtered Gaussian white noise. In the DC protocol, spikes were initially locked to the onset of the current, however, locking was lost for later spikes, and spike timing became unpredictable on repetitions of the experiment. If, however, a frozen noise current was injected into the same neuron, the results of Bryant and Segundo (1976) were reproduced. Now the spike trains were almost identical on repetition of the stimulus.

We can conclude that cortical neurons exhibit a low intrinsic noise level in spike generation. Under static, supra-threshold input conditions, this jitter builds up from spike to spike leading to unpredictable spike timing (see Rotter, 1994 and the many references therein for a description of variability in the absence of synaptic input). Under the influence of strongly fluctuating input, spikes are generated by excursions of the membrane potential. Spikes in repetitive trials are synchronized up to some residual jitter, spike timing becomes independent of the time of the last spike. We can think of the first situation (DC current injection) as having a set of imperfect identical clocks, which progressively show different readings after an initial synchronization. In the second case (frozen noise current injection), the set of clocks is enslaved by an external (aperiodic) reference signal, basically rendering clock ticks independent of the internal dynamics.

Let us now introduce the typical form of activity occurring in a synfire chain. Fig. 1.3 shows four examples of activity occurring in the same network for four different initial conditions. Details of the model are given in Chap. 2. Here, we concentrate on the qualitative results. At least for a specific setting of model parameters, the synfire chain indeed supports stable propagation of synchronous activity (Fig. 1.3 **A**). However, synchronous activity is only evoked by certain initial conditions. In the absence of temporal spread, only a small number spikes is needed (Fig. 1.3 **A**). By contrast, at considerable temporal spread only a large number of spikes is sufficient (Fig. 1.3 **B**). The network structure has a stabilizing effect on synchronous activity with respect to two different qualities. In Fig. 1.3 **B**, the synchronization reached in the final group is better than the initial synchronization. In Fig. 1.3 **A**,

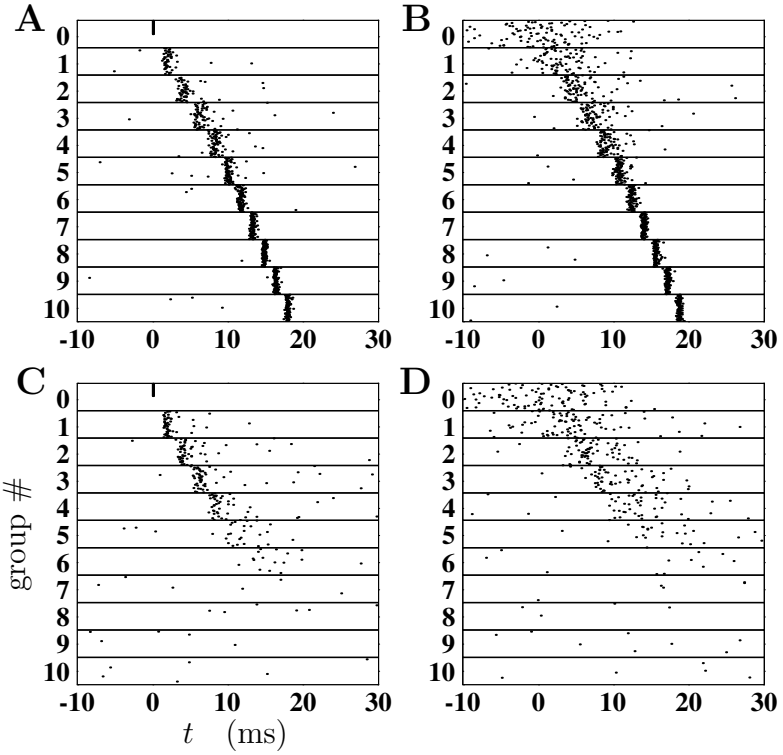

Figure 1.3 Four qualitatively different developments of spiking activity in a complete synfire chain. Panels **A** to **D** show spiking activity in the same network for different initial conditions. The synfire chain consists of 10 consecutive groups with 100 neurons per group. In addition to the input from the preceding group, each neuron independently receives excitatory and inhibitory input from a large number of synapses, modeling the membrane potential fluctuations observed *in vivo*. All synapses have the same strength. Dots in boxes 1 to 10 represent individual spike times of all neurons. Labeling corresponds to group number. In each box one vertical position is reserved for every neuron of the group (100 positions). Time (t) is advancing along the horizontal axis. The first group (1) is stimulated by a packet of spikes drawn from a Gaussian distribution. Time zero is the center of this spike time distribution. A synaptic delay of 1 ms is assumed for all synapses (incl. the synapses mediating the stimulus). The spike times of the stimulus are shown in box 0. In panels **A** and **C**, stimulus spikes are fully synchronized. Spikes occupy the top vertical positions to visualize the relative activation of the virtual group. **A** 51 perfectly synchronized spikes elicit a packet of spikes traveling through the network. While gaining spikes, activity initially spreads out in time, however synchronizes again in later groups. **B** With 100 dispersed ($\sigma = 4.8$ ms) stimulus spikes, activity is able to synchronize under an intermediate loss in the number of spikes in the packet. **C** Lower number of spikes than in **A** (47). The packet maintains activity for a few stages and spreads out in time. At later stages, further spreading is combined with a loss in spike number. Synchronous activity vanishes before the end of the chain is reached. **D** Larger temporal spread than in **B** ($\sigma = 5.8$ ms). The packet synchronizes, however, under a steady loss in spike number. Eventually, synchronous activity ceases to exist. The neurons are spontaneously active (dots occurring before the arrival of the packet) because of membrane potential fluctuations. Spontaneous activity appears to be reduced after the packet has passed because the neurons are synchronously refractory.

the final number of spikes is larger than the number of spikes in the stimulus. Historically, the non-monotonic development in the two qualities was discovered only after it had been observed in an iterative mapping (Diesmann, Gewaltig, & Aertsen, 1999) which we introduce in Chap. 4. Fig. 1.3 **C** and Fig. 1.3 **D** represent cases in which synchronous activity cannot be sustained. Note that the speed at which the spike volley propagates through the network (measured in number of successively activated groups per unit time) increases with the synchronization of the spikes in the volley.

1.5 Focus of the Study

The network simulations presented in the previous section illustrate the occurrence of synchronous spiking activity in a feed-forward network, depending on initial conditions. Thus, the "synfire chain" model of Abeles is in principle able to generate volleys of synchronous spiking, and therefore can be the origin of spatio-temporal spike patterns. Whether this is a suitable mode of operation for the cortex depends on the compatibility of the model assumptions with the conditions in the cortex. The central topic of the present work are the synchronization dynamics and the conditions under which stable synchronous spiking can occur. In order to gain insight into the system's dynamics and the parameter dependence we have to answer the following questions:

- In which sense does a propagating volley of synchronous spikes represent a stable state (attractor) of the system?
- How can we demonstrate robustness of this state and what are conditions for its existence?
- How does the temporal spread depend on single neuron and network parameters?
- Is the temporal spread predicted by the model consistent with that found in experimentally observed spike patterns?

1.6 Outline of the Investigation

The investigation is organized in 10 chapters. The introduction is followed by 3 chapters providing the tools to study the synchronization dynamics. The next 5 chapters exploit these tools to answer the questions stated above. The last chapter discusses the results.

Neuron and Network

The next chapter (**Chap. 2**) introduces the network and neuron model used throughout the study. The parameters determining subthreshold dynamics of the membrane potential and synaptic events are introduced. On the basis of the neuron model, the properties of cortical neurons are described.

Transmission Function

The following chapter (**Chap. 3**) introduces a pair of variables to describe a volley of synchronous spikes. A new transmission function, is defined which characterizes a neuron's response to such input packets. Here, we discuss a specific neuron model, however, the definition of the transmission function is model independent.

State Space

The transmission function allows for the construction of a two-dimensional iterative mapping, describing the propagation of a packet of spikes from one neuron group to the next (**Chap. 4**). With the above tools at hand and using the methods of non-linear dynamics, we demonstrate that an attractor for synchronous activity can exist. The attractor is surrounded by a basin providing robustness against perturbations. The number of neurons per group is shown to constitute a bifurcation parameter of the system.

Background Activity

The language developed in the preceding chapters will now be used to discuss the role of several physiologically relevant parameters. In **Chap. 5** the effect of membrane potential fluctuations on the synchronization dynamics is investigated. Large membrane potential fluctuations consistent with *in vivo* conditions can be tolerated, and can even be helpful. However, at a certain amount of fluctuations a bifurcation occurs and the attractor is destroyed.

Vanishing Noise

The case of vanishing membrane potential fluctuations (**Chap. 6**) allows us to investigate the origin of the most prominent structure in state space: the border (separatrix) between the basin of attraction for the synchronous state and the regime in which initial activity ceases. The separatrix is largely determined by the shape of the post-synaptic potential. Analysis of the transition to finite membrane potential fluctuations shows that fluctuations can increase the basin of attraction and, thus, exhibit a constructive effect on the synchronization dynamics.

Rise Time of the Potential

The next chapter (**Chap. 7**) discusses the rise time of the post-synaptic potential as a parameter of the dynamics. Rise time is strongly influencing the temporal spread in the attractor. Depending on the normalization of the post-synaptic potential, different effects on the basin of attraction are observed. Under amplitude normalization, the basin increases with increasing rise time. Area normalization leads to a bifurcation in which the attractor is destroyed.

Variability

The reduction of network activity to two variables was possible by considering only the dynamics of the mean. To obtain an estimate of the variability in single realizations of network activity, we introduce in the next chapter (**Chap. 8**) the survival probability of synchronous activity. It turns out that the system behaves quasi-deterministically. The survival probability exhibits a sharp transition from 0 to 1 at the border of the basin of attraction. However, the slope of the transition depends on the number of neurons per group. For the dynamics of the mean, a scaling law predicts that narrow groups exhibit the same dynamics as broader groups, provided that the amplitudes of the post-synaptic potentials are adjusted such that the product of group size and PSP amplitudes remains constant. In such narrow groups with rescaled PSP amplitudes, the dynamics becomes less deterministic. However, down to a group size of some ten neurons, the attractor is still surrounded by a neighborhood in which the survival probability is practically unity.

Origin of the Transmission Function

The definition of the transmission function is independent of the neuron model. This allows us to compute the transmission function for a realistic neuron model and to study the dependence of synchronization dynamics on physiologically relevant parameters without further approximations. However, up to this point it is unclear how critically the transmission function used in the present work depends on our particular choice of neuron model. Some intuition on how the transmission function originates from the properties of the neuron model is required to judge its robustness against model structure. We therefore conclude our investigation (**Chap. 9**) with a simplified model for the origin of the transmission function, still containing all parameters. The relationship with models based on an instantaneous spike intensity is discussed.

Discussion

In the final chapter (**Chap. 10**) we summarize the results and critically review the model assumptions. Two types of experiments are proposed to verify the predictions of the present work and to exploit the relationship between the parameters of the subthreshold dynamics and the synchronous spiking for consistency checks. The chapter closes with a discussion of open questions and directions for further research.

Chapter 2

Neuron and Network Model

The preceding chapter introduced the basic abstractions used in the description of the structure of the cortical network and the interaction of its elements. In the present chapter we motivate and specify the model of single neuron dynamics we will use. The neuron model is a variant of the leaky integrate-and-fire model, a standard model in the study of the dynamics of neuronal networks. As an extension, a finite rise-time of the post-synaptic potential is included. Later chapters demonstrate that this rise-time is an important constraining parameter of spike synchronization. Comparison of the statistical properties of the membrane potential in the *in vitro* and *in vivo* preparation shows that the feed-forward structures subject to the present study cannot be studied in isolation. The structures need to be investigated in their embedding in a large network in order to obtain realistic results. A simple and self-consistent model of "background activity" providing such embedding is introduced.

2.1 Membrane Equation

The time course of the membrane potential of a cortical neuron looks very different in the *in vitro* and *in vivo* preparations. In the *in vitro* preparation, recordings are obtained from a thin brain slice (for details see e.g. McCormick, Connors, Lighthall, & Prince, 1985; Sherman-Gold, 1993; Nicholls, Martin, Wallace, & Fuchs, 2001) which can be sustained in a dish for several hours. In the *in vivo* preparation, recordings are obtained from the intact brain (for details see e.g. Douglas & Martin, 1991b; Bringuier, Chavane, Glaeser, & Frégnac, 1999; Azouz & Gray, 1999; Lampl, Reichova, & Ferster, 1999; Nicholls, Martin, Wallace, & Fuchs, 2001). Fig. 2.1 contrasts the typical time courses of the membrane potential in the two preparations (taken here from simulations). In the *in vitro* preparation the membrane potential fluctuates around a resting potential V_0. Fluctuations are small compared to the distance from resting level to spike threshold θ. These fluctuations are caused by thermal noise, spontaneous ion channel openings, and few synaptic events (e.g. Katz, 1966; Johnston & Wu, 1995). In the *in vivo* situation, however, the mean of the membrane potential is elevated by some value η. Fluctuations around this mean are large compared to the distance from η to spike threshold. The variability is attributed to the ongoing *synaptic bombardment* of the cell with excitatory and inhibitory synaptic events (e.g. Calvin & Stevens, 1968; Holt, Softky, Koch, & Douglas, 1996). It is assumed that the cell is silent in the *in vitro*

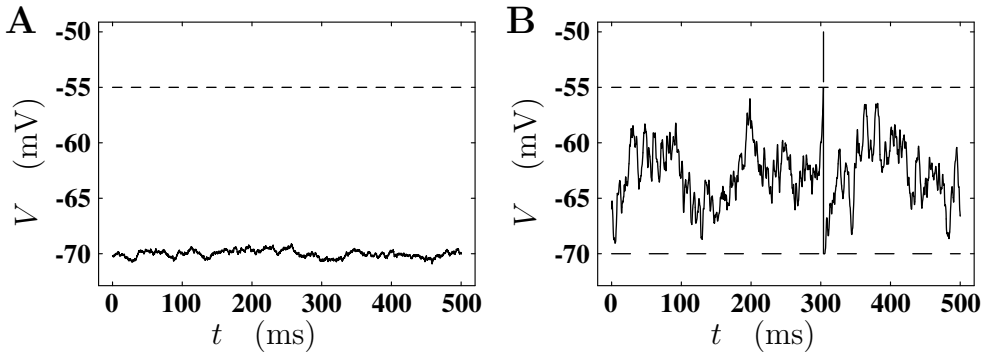

Figure 2.1 Sketches of typical membrane potential time courses *in vitro* (**A**) and *in vivo* (**B**) in the absence of specific stimuli. **A** Membrane potential V (ordinate) as a function of time (abscissa). V exhibits small fluctuations around a resting level V_0 (here, $-70\,\mathrm{mV}$). The dashed horizontal line indicates the potential $V_0 + \theta$ (here, $\theta = 15\,\mathrm{mV}$) at which an action potential could be elicited. Typically, in this situation action potentials do not occur. **B** Same display as in **A**. The mean $V_0 + \eta_V$ of the membrane potential is elevated from resting level (here, $\eta_V = 7.95\,\mathrm{mV}$). Fluctuations (here, $\sigma_V = 2.85\,\mathrm{mV}$) fill the space from V_0 (long dashed line) to spike threshold (short dashed). Action potentials (spikes) are generated at a low rate (here, 2 Hz), occurrence of a spike at $t = 300\,\mathrm{ms}$ (arbitrary origin of t) indicated by vertical line above short dashed line). Panels show simulated data.

preparation because neurons in the slice have lost most of their connections and, thus, the residual network cannot sustain spontaneous activity.

The leaky integrate-and-fire model can be motivated by an experiment performed on the *in vitro* preparation. Fig. 2.2 **A** shows membrane potential traces as they would typically be recorded in an electrophysiological experiment during short epochs of DC current injection. A positive current *depolarizes* the membrane and, provided the membrane potential remains subthreshold, a new stationary voltage is approached. A negative current *hyperpolarizes* the membrane, again up to a new stationary value. In both cases the membrane potential starts to decay to resting level as soon as the external current is switched off. This subthreshold behavior of the cell can well be described by an RC circuit or "leaky integrator": a capacitance with a parallel (leak) resistance (Fig. 2.2 **B**). The resting potential V_0 observed with no external current applied is generated by ion-pumps, maintaining constant concentration gradients (see e.g. Nicholls, Martin, Wallace, & Fuchs, 2001; Johnston & Wu, 1995). In the model circuit, V_0 can be expressed by a battery in series to the resistor. However, in a model neuron where V_0 merely represents a constant offset to the time course of the membrane potential $V(t)$, V_0 is usually assumed to be zero. It is the relationship between membrane potential $V(t)$ and external current $I(t)$ which is described by the leaky integrator equation

$$\dot{V} + \frac{1}{\tau_\mathrm{m}} V = \frac{1}{C} I. \tag{2.1}$$

C is the membrane capacitance. Membrane time constant $\tau_\mathrm{m} = RC$ depends on both resistance R and capacitance C.

In the *leaky integrate-and-fire* model, the mechanisms which generate an action potential (AP) and the following after-hyperpolarization (AHP) are represented by a threshold operation. Once the membrane potential reaches a certain threshold θ, the information that the model just generated an action potential is made available to the observer and poten-

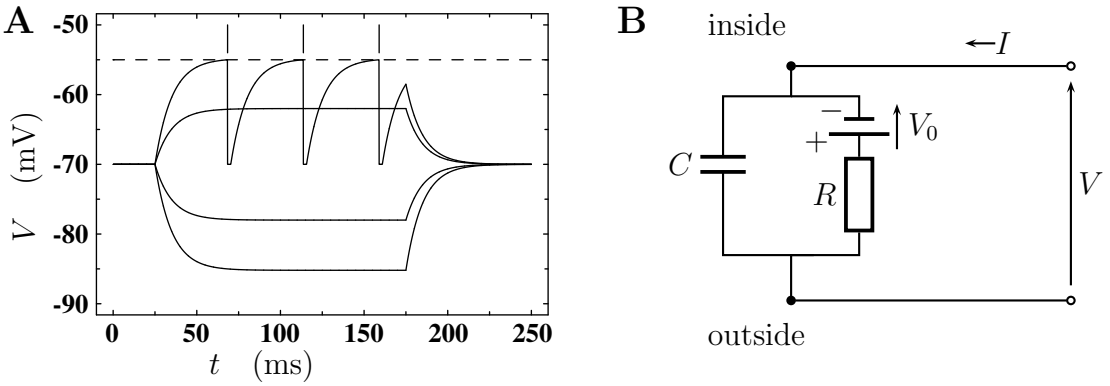

Figure 2.2 Characterization of the isolated neuron. **A** Sketch of typical membrane potential (V) traces of a cortical neuron in the *in vitro* preparation subject to current injection. Fluctuations are assumed to be zero (V_0 and θ as in Fig. 2.1). Curves show voltage responses for four DC currents applied for 150 ms starting at $t = 25$ ms (from bottom to top $I = -380$, -200, 200, and 380 pA). Only for the largest current applied the threshold is reached and a sequence of spikes is emitted (indicated by vertical lines above dashed line, see Fig. 2.7 **A** for I-dependence of spike rate). At threshold, V is reset and clamped to V_0 for $\tau_r = 2$ ms (caricature of after-hyperpolarization (AHP), no adaptation in this model). **B** Equivalent circuit of the biological membrane (leaky integrator model) describing the subthreshold dynamics. Membrane capacitance C (250 pF) and resistance R (40 MΩ) define the membrane time constant $\tau_m = RC$ (10 ms). The resting potential of the cell is represented by a battery (V_0). I is a, potentially time dependent, current injected into the cell. V measures the voltage across the membrane.

tially other neurons in the network. The membrane potential is instantaneously reset to resting level. For a period of absolute refractoriness τ_r the neuron is short-circuited, and the membrane potential is clamped to V_0. After-hyperpolarization and relative refractoriness are both expressed in the neuron model's recovery from reset, governed by the membrane time constant τ_m. The effect of this sequence of events on $V(t)$ is visualized in the membrane potential time course for the largest input current in Fig. 2.2 **A**. Equation (2.1) for the subthreshold dynamics combined with variants of the threshold operation described above constitute the leaky integrate-and-fire model, or Lapicque model in the older literature (e.g. Lapicque, 1907; Eccles, 1957; Stein, 1965; Knight, 1972; MacGregor, 1987; Tuckwell, 1988a; Koch, 1999). A simulation scheme for networks of such units is described in Appendix A. In the present study the term "I&F model" is used interchangeably with "leaky integrate-and-fire model", a perfect integrator is not considered. The phenomenology of Fig. 2.2 **A** is utilized to motivate the neuron model. No attempt is made to derive the model from more detailed biophysical descriptions of the membrane potential and the (Hodgkin-Huxley type) mechanisms of action potential generation (see Hodgkin & Huxley, 1952; Cronin, 1987; Tuckwell, 1988a; Tuckwell, 1988b; Kandel, Schwartz, & Jessel, 1991; Johnston & Wu, 1995; Koch, 1999).

Some studies use normalized variables where τ_m is unity and voltage is normalized by the distance from resting potential 0 to spike threshold to demonstrate qualitative model properties. Central to the present work is the question whether stable propagation of synchronous spiking is possible in a physiologically plausible range of parameter values. Therefore, we refrain from general normalization of variables to facilitate comparison with physiological data and interpretation of the model results at all stages of the argument.

2.2 Post-Synaptic Potential

In the preceding section, we have constructed a model for the neuron's response to a general time dependent input current $I(t)$. We now have to specify how a pre-synaptic spike arriving at the synapse is converted into a post-synaptic potential (PSP). In the context of I&F models, synaptic events are often modeled by a small (compared to the distance from membrane potential mean to spike threshold) instantaneous increment in membrane potential (e.g. Tuckwell, 1988a; Amit & Brunel, 1997; Brunel, 2000). The choice is justified by the fact that the time constant governing the rise time of the synaptic currents typically is an order of magnitude smaller than the membrane time constant. Physiologically measured post-synaptic potentials have rise times from fractions of a millisecond to several milliseconds, which is considerably smaller than the membrane time constant (e.g. Fetz, Toyama, & Smith, 1991; Mason, Nicoll, & Stratford, 1991; Matsumura et al., 1996). However, the spike synchronization to be studied occurs at the millisecond time scale, and we will see later (Chap. 7) that the rise time of the PSP is indeed an important parameter of the synchronization dynamics. Therefore, a more detailed model allowing for a finite rise time of synaptic currents is needed. A function commonly used to describe the time course of synaptic currents or conductance changes is the so called α-function (e.g. Jack, Noble, & Tsien, 1983; Bernard et al., 1994)

$$\iota(t) = \widehat{\iota} \cdot \frac{e}{\tau_\alpha} t e^{-t/\tau_\alpha}, \quad t \geq 0. \tag{2.2}$$

Apart from the amplitude of the synaptic current $\widehat{\iota}$, (2.2) introduces a new time constant τ_α, the rise time of the post-synaptic current (PSC). (2.2) is a solution of a time-invariant linear system of two differential equations. Thus, the total current coming in from an arbitrarily large number of such synapses can be described by only two state variables. Appendix A shows how the properties of the α-function can be exploited to incorporate this model of synaptic currents into an accurate and efficient simulation scheme suitable for large networks (Rotter & Diesmann, 1999; Diesmann, Gewaltig, Rotter, & Aertsen, 2001). The post-synaptic potential generated when the leaky integrator equation (2.1) is subject to a post-synaptic current (2.2) can be written in closed form

$$u(t) = \widehat{\iota} \cdot \frac{1}{C} \frac{e}{\tau_\alpha} \left(\frac{e^{-t/\tau_\mathrm{m}} - e^{-t/\tau_\alpha}}{(1/\tau_\alpha - 1/\tau_\mathrm{m})^2} - \frac{t e^{-t/\tau_\alpha}}{1/\tau_\alpha - 1/\tau_\mathrm{m}} \right), \quad t \geq 0. \tag{2.3}$$

Equation (2.3) is easily obtained by convolving (2.2) with the impulse response

$$\frac{1}{C} e^{-t/\tau_\mathrm{m}}, \quad t \geq 0$$

of (2.1). The detailed shape of (2.3) will become relevant in later chapters, but it is of no importance for the purpose of the present chapter, where only certain integrals of $u(t)$ are exploited (the time course of the PSP is visualized in Fig. 6.2 on page 63). The fact that the generator of (2.3) is a time-invariant linear system of differential equations has an interesting consequence. At any given point in time, the value of the neuron's membrane potential is completely described by the linear superposition of the post-synaptic potentials

that occurred in the past. It should be pointed out that this property is neither a prerequisite in the definition of the state space for synchronous activity (Chap. 3, Chap. 4), nor for its numerical analysis (Chap. 4, Chap. 5, Chap. 7). However, linearity is exploited in many aspects of the analytical work (e.g. Sec. 2.3 and Chap. 6). Limitations of the model of synaptic effects presented above are discussed in Chap. 10.

2.3 Membrane Potential Fluctuations

Fluctuations of the membrane potential of a single neuron observed *in vivo* are caused by the synaptic bombardment (see Sec. 2.1). We can now combine knowledge of the statistical properties of the membrane potential fluctuations (Fig. 2.1) with our model of a single post-synaptic potential (2.3) to relate the single neuron dynamics to network structure. Let us assume that N neurons, independently spiking at rate λ, are projecting to the same post-synaptic neuron, and that all input spikes generate an identical excitatory PSP. For sparsely firing neurons in the cortex, it is a reasonable approximation to describe spike generation by a Poisson process (e.g. Gerstein & Mandelbrot, 1964; Stein, 1972; Tuckwell, 1988b; Abeles, 1991; Softky & Koch, 1993; Shadlen & Newsome, 1998). Details of the individual processes are, however, washed out in the superposition of a large number of independent processes (Cox & Isham, 1980). Thus, we can replace the N independent processes by a single Poisson process of rate $N\lambda$. In this situation, the membrane potential fluctuations resulting from the superposition of the individual PSPs elicited by the point events impinging on the neuron are called *shotnoise* (Campbell, 1909; Rice, 1944; Goldstein, 1960; Papoulis, 1991). Campbell's theorem (e.g. Papoulis, 1991) states that mean η_V and standard deviation σ_V of the shotnoise process are given by

$$\eta_V = N\lambda F^1 \tag{2.4}$$

$$\sigma_V^2 = N\lambda F^2. \tag{2.5}$$

The F^k are form factors which depend on the amplitude and shape of the post-synaptic potential

$$F^k = \int_{-\infty}^{\infty} u^k(t)dt. \tag{2.6}$$

F^1 describes the area under the post-synaptic potential, and F^2 is a measure of its peakedness. For (2.3) we obtain

$$F^1 = \frac{\tau_\mathrm{m}}{C} \cdot \widehat{\imath e}\tau_\alpha \tag{2.7}$$

$$F^2 = \frac{\tau_\mathrm{m}^2}{C^2} \cdot \frac{\tau_\alpha\left(\tau_\alpha + 2\tau_\mathrm{m}\right)}{\left(\tau_\alpha + \tau_\mathrm{m}\right)^2} \cdot \frac{1}{4}\widehat{\imath}^2 e^2 \tau_\alpha. \tag{2.8}$$

Let us now check if this model of the background activity received by a cortical neuron can explain the measured membrane potential. Fig. 2.3 **A** shows the dependence of η_V and σ_V on background rate λ for a realistic set of further parameters. Before σ_V reaches realistic values above 1 mV, η_V has already entered the supra-threshold regime. Thus, a model of

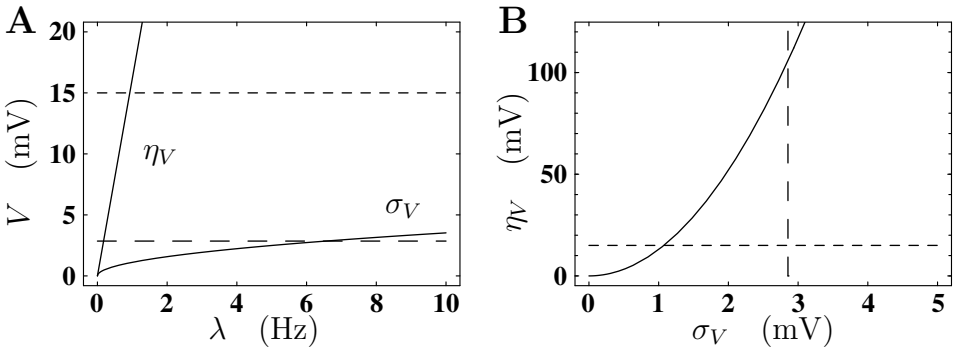

Figure 2.3 Membrane potential fluctuations generated by purely excitatory input spike trains. **A** Mean η_V (neglecting the offset V_0) and standard deviation σ_V of membrane potential as a function of input spike rate λ. The total input to the neuron is composed of 10,000 independent excitatory Poisson spike trains of rate λ. The amplitude of an individual post-synaptic potential (PSP) is 0.14 mV with a rise-time of 1.7 ms, further parameters as in Fig. 2.2). The location of spike threshold θ is indicated by the short dashed line, and a realistic level of membrane potential fluctuations by the long dashed line (cf. Fig. 2.1 **B**). **B** Quadratic relationship of mean η_V (ordinate) and standard deviation σ_V (abscissa) of the membrane potential fluctuations specified in **A** (λ eliminated). The two reference values indicated by dashed lines in **A** are now located on separate axes.

background activity which assumes purely excitatory inputs is inconsistent with the large fluctuations and at the same time low firing rate observed *in vivo*. The model neuron would compensate the supra-threshold input current with a high firing rate, resulting in a regular firing pattern. Consequently, the membrane potential distribution would strongly deviate from a Gaussian distribution. (2.5) can be used to eliminate λN from (2.4)

$$\eta_V = \sigma_V^2 \cdot \frac{F^1}{F^2} \tag{2.9}$$

demonstrating the quadratic dependence of η_V on σ_V. This relationship is visualized in Fig. 2.3 **B**. For realistic PSP shapes the ratio of PSP area F^1 and peakedness F^2 is much larger than unity (here, $F^1/F^2 \approx 10\,\mathrm{mV}^{-1}$). We have to conclude that for realistic PSP shapes, excitatory processes alone cannot explain the membrane potential statistics. However, this conclusion is based on the assumption, that the N processes are sufficiently independent. If the input to a neuron is considerably more structured, the argument does not apply (e.g. Levitan, Segundo, Moore, & Perkel, 1968; Kuhn, Rotter, & Aertsen, 2002; Tetzlaff, Buschermöhle, Geisel, & Diesmann, 2003).

It is known that about 80% of the synapses a neuron receives are excitatory and about 20% are inhibitory (Braitenberg & Schüz, 1991; Abeles, 1991). Up to now we have only considered excitatory post-synaptic potentials (EPSPs), i.e. synaptic events that drive the membrane potential into the direction of spike threshold. We define inhibitory post-synaptic potentials (IPSPs) as synaptic events that drive the membrane potential away from threshold. Following physiological *in vivo* data (Matsumura et al., 1996), it is assumed that IPSPs have the same shape as EPSPs, with only the sign of the membrane potential excursion reversed. Thus, (2.3) also holds for the IPSP, with $\widehat{\iota}_- = -\widehat{\iota}_+$.

It should be noted that in more detailed neuron models, the labels "excitatory" and "inhibitory" specify the functional role of the synapse in the typical range of membrane

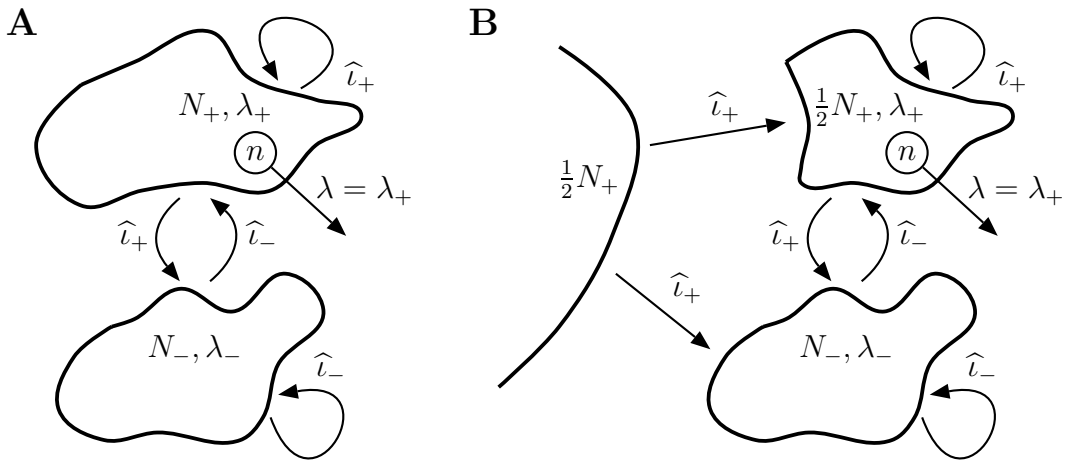

Figure 2.4 Embedding of an individual neuron in the recurrent cortical model network. **A** The excitatory (+) neuron under consideration (n), as any other neuron, receives N_+ randomly selected inputs from a large ($\gg N_+$) population (contour enclosing symbol) of excitatory neurons and N_- inputs from an inhibitory population (single neuron spike rates λ_+, λ_-). The spike rate λ of n (straight arrow) should be consistent with λ_+. The curved arrows indicate the four possible combinations of pre- and post-synaptic neuron type. In the model, the amplitude of the synaptic current ($\widehat{\iota}_+$, $\widehat{\iota}_-$) depends only the pre-synaptic neuron type. **B** More detailed model of network structure as in **A**. Neurons receive about 50% of the excitatory inputs from local sources. Nonlocal sources (curve) are not affected by the recurrent local dynamics.

potential values, not the sign of the membrane potential excursion. In that case, synaptic currents $\iota(t) = g(t)(E - V)$ are described by specific conductances g and reversal potentials E, depending on the type of the synapse. In general, depending on the sign of the difference between the membrane potential V of the cell and the reversal potential E, an inhibitory synapse can either cause a negative or a positive current. The same is true for an excitatory synapse. These considerations also show that the amplitude of the PSP depends on the membrane potential. This effect is stronger for inhibitory synapses, because their reversal potential is closer to the typical regime of the membrane potential (see Tuckwell, 1988b; Johnston & Wu, 1995; Kandel, Schwartz, & Jessel, 1991; Nicholls, Martin, Wallace, & Fuchs, 2001 for detailed discussions).

Fig. 2.4 sketches a network model where the neuron under consideration receives excitatory inputs from N_+ neurons with individual firing rate λ_+ and inhibitory inputs from N_- neurons with individual firing rate λ_-. The contribution of the N_+ excitatory inputs to the membrane potential is again described by equations (2.4) and (2.5), with the total number of inputs N replaced by N_+. Also the joint effect of the inhibitory inputs can be described by the same set of equations, with $F_-^1 = -F_+^1$ but $F_-^2 = F_+^2$. Therefore, we now have two contributions to the mean and variance of the membrane potential. As a direct consequence of the statistical properties of the sum of two independent random variables (e.g. Papoulis, 1991) we have

$$\eta_V = \eta_{V+} + \eta_{V-} \tag{2.10}$$

$$\sigma_V^2 = \sigma_{V+}^2 + \sigma_{V-}^2. \tag{2.11}$$

Note that the two contributions to the mean of the membrane potential have opposite sign and therefore can partly cancel each other. The variances, however, are both positive and,

thus, add up to a larger total variance. We can rewrite equations (2.10) and (2.11) in matrix form

$$\begin{bmatrix}\eta_V\\ \sigma_V^2\end{bmatrix} = \begin{bmatrix}F^1N_+ & -F^1N_-\\ F^2N_+ & F^2N_-\end{bmatrix}\cdot\begin{bmatrix}\lambda_+\\ \lambda_-\end{bmatrix}. \tag{2.12}$$

Form factors do not carry a label specifying the type of synapse, because absolute values are identical. The sign of the matrix elements is made explicit. The matrix can be decomposed into

$$\begin{bmatrix}F^1N_+ & -F^1N_-\\ F^2N_+ & F^2N_-\end{bmatrix} = \begin{bmatrix}F^1 & 0\\ 0 & F^2\end{bmatrix}\cdot\begin{bmatrix}1 & -1\\ 1 & 1\end{bmatrix}\begin{bmatrix}N_+ & 0\\ 0 & N_-\end{bmatrix}. \tag{2.13}$$

A scaling matrix which weighs λ_+ and λ_- by the number of corresponding inputs is followed by a $\pi/4$ rotation into the new coordinates with an additional isotropic scaling of $\sqrt{2}$. Finally, another scaling matrix weighs the new coordinates by the appropriate form factors of $u(t)$. The three transformations are invertible and, hence, so is (2.12):

$$\begin{bmatrix}\lambda_+\\ \lambda_-\end{bmatrix} = \begin{bmatrix}\frac{1}{2F^1N_+} & \frac{1}{2F^2N_+}\\ -\frac{1}{2F^1N_-} & \frac{1}{2F^2N_-}\end{bmatrix}\cdot\begin{bmatrix}\eta_V\\ \sigma_V^2\end{bmatrix}. \tag{2.14}$$

For any combination (η_V, σ_V^2), we can now find a combination of generating background rates (λ_+, λ_-). This is in contrast to the situation in (2.4), (2.5). (2.14) is only limited by the constraint that firing rates are bound to be non-negative. In the context of the present study, we are particularly interested in the ability to control the fluctuations (σ_V^2) while keeping the membrane potential mean (η_V) at a constant distance from spike threshold. The study of the dependence of spike synchronization on membrane potential fluctuations presented in Chap. 5 exploits this scaling property. The lower row of (2.14) immediately shows that fluctuations cannot be reduced to 0 for a given non-zero mean. λ_- would need to be negative in a situation where σ_V^2 vanishes and η_V has a finite positive value. The minimal σ_V^2, obtained for $\lambda_- = 0$, is given by

$$0 = -\frac{1}{2F^1N_-}\eta_V + \frac{1}{2F^2N_-}\sigma_{V0}^2 \tag{2.15}$$

$$\sigma_{V0}^2 = \frac{F_2}{F_1}\cdot\eta_V. \tag{2.16}$$

This is the result we already obtained in (2.9). At $\lambda_- = 0$, only the excitatory shotnoise is contributing to the fluctuations. The minimal fluctuations are obtained if only the excitatory shotnoise is present. For a higher mean η_V, a larger σ_{V0} has to be tolerated. The minimal rate λ_{+0} needed to sustain η_V is obtained from the upper row of (2.14) by insertion of the minimal σ_V (2.16)

$$\lambda_{+0} = \frac{1}{F^1N_+}\eta_V. \tag{2.17}$$

The dependence of background firing rates on membrane potential fluctuations is illustrated in Fig. 2.5. Smaller fluctuations can only be generated if an additional current from an external source contributes to the mean (cf. Fig. 2.5 **B**, see also van Vreeswijk & Sompolinsky, 1996; Amit & Brunel, 1997; van Vreeswijk & Sompolinsky, 1998).

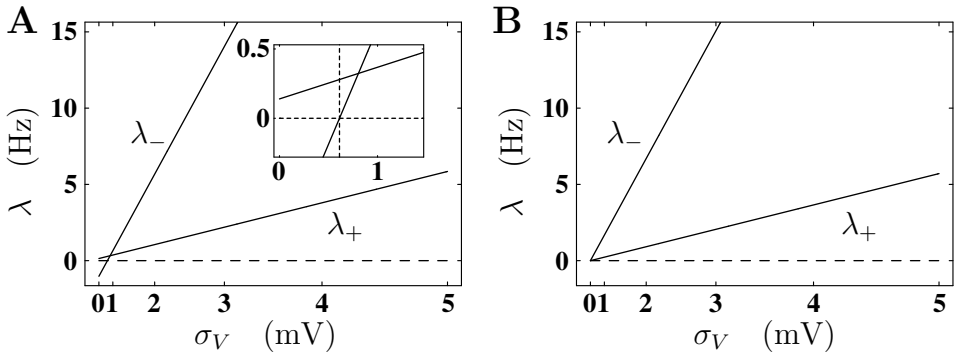

Figure 2.5 The combination of background spike rates generating membrane potential fluctuations σ_V at a given membrane potential mean $V_0 + \eta_V$. **A** Spike rates (ordinate) of the excitatory (λ_+) and inhibitory (λ_-) background neurons as a function of the standard deviation σ_V (abscissa) of the membrane potential. Quadratic scaling is used on the abscissa (the linear measure on this axis is the variance σ_V^2). The elevation from the resting potential V_0 caused by the background rates is held constant at $\eta_V = 7.95\,\mathrm{mV}$ ($N_+ = 17600$ (88%) of all synapses, $N_- = 2400$ (12%), PSPs as in Fig. 2.3 with reversed sign for inhibitory synapses). The dashed horizontal line indicates the minimal allowed input spike rate (0 Hz). The inset shows an enlargement of the region (identical units) where λ_+ and λ_- approach the origin. The requirement of non-negative spike rates defines the minimal standard deviation σ_{V0} (dashed vertical line) of the membrane potential. At this value λ_- is zero and λ_+ has a finite value λ_{+0}. **B** Same curves as in **A** for $\eta_V = 0\,\mathrm{mV}$. Membrane potential fluctuations vanish at vanishing background spike rates $\lambda_+ = \lambda_- = 0\,\mathrm{Hz}$.

2.4 Spontaneous Spiking Activity

The most important use of (2.12) is that it relates network activity to the membrane potential statistics of an individual neuron. Thereby, (2.12) provides the bridge connecting the model of spike generation obtained from *in vitro* studies to a model for the neuron's embedding in a large neural network under *in vivo* conditions. Now, two levels of description of neuronal dynamics can be checked for consistency: (1) the statistics of membrane potential fluctuations and (2) the statistics of the generated spike trains.

Let us find a self-consistent solution, where the spike rate of the neuron equals the low spike rate assumed for the excitatory neurons in the remainder of the network:

$$\lambda_+ = \lambda(\lambda_+, \lambda_-), \tag{2.18}$$

where λ denotes the (output) spike rate of our model neuron. It turns out that (2.18) can easily be fulfilled by adjusting the inhibitory background rate λ_- using simulations. Approximative analytical expression for (2.18) are available (e.g. Amit & Brunel, 1997; Ricciardi, Di Crescenzo, Giorno, & Nobile, 1999; Tetzlaff, Geisel, & Diesmann, 2002). The following table summarizes model parameters and the resulting membrane potential statistics at the self-consistent rates

N_+	17600 (88%)	$\lambda = \lambda_+$	2.0 Hz	η_V	7.95 mV
N_-	2400 (12%)	λ_-	12.61 Hz	σ_V	2.85 mV

for a particular choice of N_+ and N_- (further parameters specified in Fig. 2.6). Note that the inhibitory spike rate is higher than the excitatory firing rate, compensating for the lower number of inhibitory inputs. The assumed excitatory spike rate is well within the

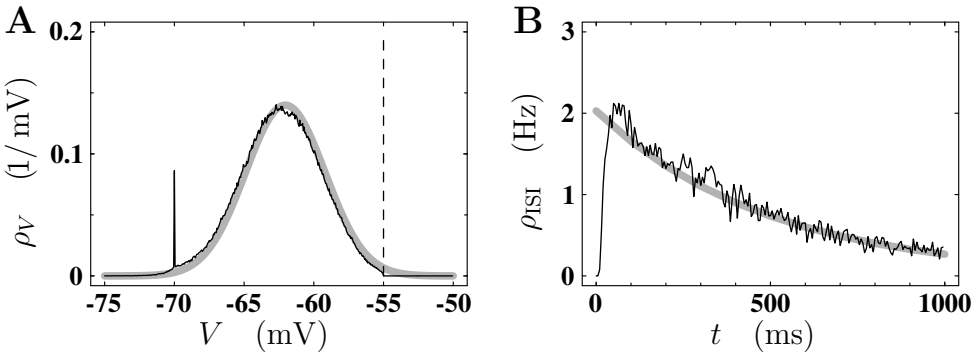

Figure 2.6 Membrane potential distribution and spike interval distribution. **A** Distribution ρ_V of membrane potential values V in the presence of background activity (black curve, simulation time 100 s, step size 0.1 ms, bin size 0.05 mV). V does not exceed $V_0+\theta$ (position indicated by dashed vertical line, cf. Fig. 2.1). Clamping of V at resting potential $V_0 = -70\,\mathrm{mV}$ for the absolute refractory period $\tau_{\rm r} = 2\,\mathrm{ms}$ following the generation of a spike causes the peak at V_0 (spike rate 2 Hz). The gray curve represents ρ_V not perturbed by spike generation. The Gaussian is parameterized by mean $\eta_V = 7.95\,\mathrm{mV}$ (shifted by V_0) and standard deviation $\sigma_V = 2.85\,\mathrm{mV}$ of the fluctuations caused by background activity: $\lambda_+ = 2\,\mathrm{Hz}$, $\lambda_- = 12.61\,\mathrm{Hz}$ (cf. Fig. 2.5, corresponding to voltage trace Fig. 2.1 **B**). **B** Inter-spike interval (ISI) distribution (black curve) of the situation described in **A**. The lack of short intervals t is explained by the absolute and relative refractory period (noisy appearance due to the limited simulation time of 10, 000 s, bin size 5 ms). For comparison, the gray curve shows the exponential $\rho_{\rm ISI}$ of a Poisson process with parameter $\lambda = 2\,\mathrm{Hz}$.

physiological *in vivo* regime (e.g. Burns & Webb, 1976; Abeles, Vaadia, & Bergman, 1990). The fact that the spike rate of inhibitory neurons is higher than the spike rate of excitatory neurons is consistent with the literature (e.g. Connors & Gutnick, 1990). Alternatively, we can enforce $\lambda_+ = \lambda_-$ and achieve self-consistency by adjusting the amplitude of the inhibitory post-synaptic potentials ($F_-^k \neq F_+^k$ Amit & Brunel, 1997). Also, for this type of scaling, support can be found in the experimental literature. However, the main result of the discussion above is that the membrane potential statistics, resulting from the adjusted spike rates, appears to be consistent with the experimental *in vivo* literature (e.g. Douglas & Martin, 1991b), as are the rates. The distribution of membrane potential values is close to a Gaussian (Fig. 2.6 **A**). In addition, the interval distribution (*inter-spike interval* (ISI), see Perkel, Gerstein, & Moore, 1967a; Tuckwell, 1988b; Koch, 1999) of the spike trains generated by the model neuron approximates the interval distribution of a Poisson process, the type of process assumed for neurons providing input to the model neuron (Fig. 2.6 **B**).

Recently, van Vreeswijk and Sompolinsky (1996) and also Amit and Brunel (1997) investigated the stability of random networks of excitatory and inhibitory model neurons at low spike rates. For the present purpose, the central finding in both studies is that with only few and plausible additional assumptions about network structure, a state of independent irregular spiking at low rates is not only consistent with the parameters, but is also stable. At the same time the quiescent state can be made unstable. This finding constitutes a significant achievement because earlier network models required some form of global inhibition which is probably physiologically not realistic. van Vreeswijk and Sompolinsky (1996) used a binary (formal) neuron model, whereas Amit and Brunel (1997) used a neuron model very similar to the model used in the present study. Both studies assume that neurons receive a large number of inputs, which is however small compared to the total number of neurons in the

network. Only part of the excitatory input to a neuron is assumed to come from the local recurrent network (Fig. 2.4 **B**, Braitenberg & Schüz, 1998; Abeles, 1991). The large fluctuations are generated in the local network, the non-local input can be assumed non-fluctuating. In the steady state, the mean of the excitatory input and the mean of the inhibitory input closely balance each other. Stable irregular spiking at low rates is achieved within a deterministic neuron model and without the need for "artificial" sources of noise. Simple and plausible relationships between the strength of excitatory and inhibitory synapses guarantee that the activity in the network is stable at low spike rates. The relative adjustment of time constants of the excitatory and inhibitory neurons is not necessary (see van Vreeswijk & Sompolinsky, 1998; Brunel & Hakim, 1999; Brunel, 2000 for a detailed analysis of these systems).

However, in the present study we are not concerned with the stability of firing rate in recurrent random networks itself. The question under study is whether synchronous activity in feed-forward structures can be sustained under the conditions of an embedding in a large random network (the *in vivo* situation). A possible interaction from synchronous activity in the feed-forward structure back onto the asynchronous network activity is neglected here. In this view, the random network provides the "background activity", against which the dynamics of synchronous activity is studied. The next two chapters (Chap. 3, Chap. 4) describe this approach in detail. The material presented in this section insures us that we can construct a simple and consistent model of background activity. The presence of background activity explains the large fluctuations of the membrane potential. The model allows us to control the amount of membrane potential fluctuations, which turn out to be an important parameter of the synchronization dynamics (Chap. 5). Clearly, the distinction between irregular background activity and synchronous activity in feed-forward sub-networks is an artificial one, motivated mainly by theoretical tractability. We return to approaches pursuing an integration of the different types of activity within a common framework in the discussion (Chap. 10).

2.5 Classical Transmission Function

Since the early studies of neuronal physiology, researchers have tried to summarize the response properties of neurons in "transmission functions" (e.g. Adrian, 1928). In accordance with the approach of systems theory (e.g. Wiener, 1948), some output variable is plotted as a function of an input variable under the control of the experimenter. Transmission functions yield a compact characterization of neuronal dynamics, allow for a fit of neuron models to experimental data, and can connect single neuron properties to network dynamics. We have already seen one example of a transmission function in (2.18). It allows for a stability analysis of spike rate in a recurrent neural network. However, this transmission function is experimentally of little relevance, because the rate of synaptic inputs can usually not be controlled in quantitative fashion and independently of output spike rate (but see Hentschke & Antkowiak, 1999). The analysis of spike synchronization in feed-forward networks developed in the next chapters is based on a new neuronal transmission function which is introduced in Chap. 3. Therefore, it is instructive to first introduce the "classical" case, and use our neuron model as an example. The success of the integrate-and-fire model of a cortical neuron

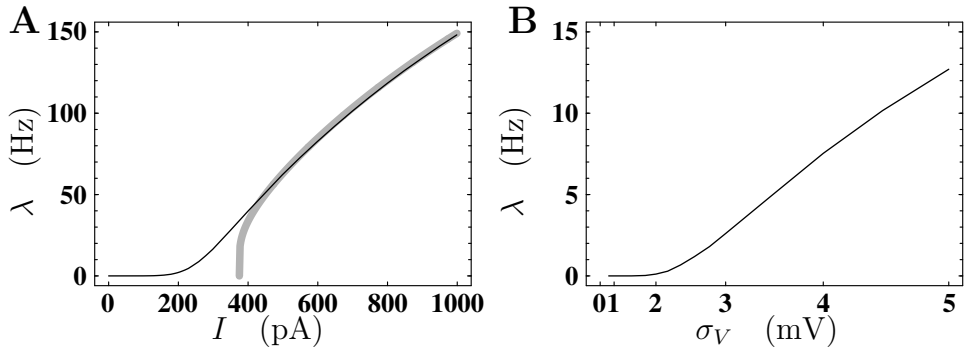

Figure 2.7 Discharge curve for the leaky integrate-and-fire model with and without membrane potential fluctuations. **A** Spike rate λ (ordinate) as a function of a DC input current I (abscissa). In the absence of membrane potential fluctuations, spike rate (gray curve) is 0 until a critical current I_θ is reached (here 375 pA, further model parameters see Fig. 2.2). In the presence of fluctuations (corresponding to Fig. 2.6), spike rate increases smoothly (black curve). For comparability, in the latter case I specifies the total injected current, including the mean current $(\tau_\mathrm{m}/C)\eta_V = 198.66\,\mathrm{pA}$ contributed by the background activity. **B** Spike rate (ordinate) as a function of membrane potential fluctuations σ_V (abscissa) at constant mean η_V. Variables σ_V and η_V specify the "free" membrane potential statistics, ignoring the threshold process (cf. Fig. 2.6 **A**). Quadratic scaling of the abscissa (cf. Fig. 2.5). Different ranges of ordinates in **A** and **B**.

is partly based on the fact that it accurately reproduces the classical neuronal transmission function. Deviations of the basic models predictions from the experimental data are well understood (e.g. Connors, Gutnick, & Prince, 1982; Connors & Gutnick, 1990) and appropriate additional mechanisms can be integrated into the model (see Koch, 1999 for a recent summary on models of spike rate adaptation and relative refractoriness). The classical transmission function is the so called *frequency-current curve*, *f-I curve*, or *discharge curve* (λ-I curve in our variables). It describes the stationary firing rate as a function of the amplitude of an applied constant current (Lapicque, 1907; Agin, 1964; Stein, 1967a; Jack, Noble, & Tsien, 1983; Tuckwell, 1988a). Here, it is assumed that the neuron does not receive additional input, as it is true in the slice preparation (Sec. 2.1). Fig. 2.7 **A** (gray curve) shows the λ-I curve for our neuron model. There is no spiking activity below a certain threshold current

$$I_\theta = \frac{C}{\tau_\mathrm{m}}\theta \tag{2.19}$$

because the membrane potential saturates at a subthreshold value. I_θ is called the *rheobase*. For supra-threshold currents, the membrane is charged until the threshold θ is reached. A spike is emitted and the membrane potential is reset, eliminating all the charge. For a time period τ_r the input current is shunted before the membrane is charged up to threshold level again. Thus, at supra-threshold currents, the spike rate λ is given by

$$\lambda(I) = \frac{1}{\tau_\mathrm{r} - \tau_\mathrm{m} \ln\left(1 - \frac{\theta C}{I\tau_\mathrm{m}}\right)}. \tag{2.20}$$

In this mode of operation, where the input current to the cell is supra-threshold, the stationary state can be described by an equilibrium between the charge transported into the cell during an inter-spike interval, and the charge transported out of the cell (or shunted) due

to the after-spike effects. The distribution of membrane potential values is not Gaussian (as it would result from shotnoise input) and mainly reflects the repolarization and after-spike effects. Note that in our model, the generated spike train is periodic with period $1/\lambda$ from the first spike on. This is due to the absence of noise and the strict reset of the membrane potential to resting level. Firing rate is limited by $1/\tau_{\mathrm{r}}$, a rate which can only be reached at unphysiologically high input currents. The black curve in Fig. 2.7 **A** represents the λ-I curve in the presence of large membrane potential fluctuations. Now, we observe a low spontaneous activity at subthreshold DC input currents (cf. Stein, 1967b).

With increasing current, the spike rate rises smoothly (effect known as *stochastic linearization* (Stemmler, 1996)) in a sigmoidal fashion. This relationship motivates the sigmoidal activation function commonly used in abstract neural network models (e.g. Hopfield, 1984, see Dayan & Abbott, 2001 for a recent review). At low input currents, the output spike train is irregular. Spike generation is mainly driven by the shotnoise input, before the neuron reaches threshold again, the reset following the preceding spike is "forgotten". At high input current, the regularity of the output spike train becomes more pronounced. Fig. 2.7 **B** shows for comparison the dependence of output spike rate on the standard deviation of the membrane potential fluctuations. Here, the mean of the input current remains constant at a subthreshold value. Fluctuations are generated using (2.12).

The classical transmission function describes the stationary part of the neuronal response to a stationary stimulus. The next chapter (Chap. 3) shows that in order to understand the dynamics in feed-forward networks, the complementary relationship is needed: the transient neuronal response to a transient stimulus. We conclude this chapter with the remark that the λ-I curve of the integrate-and-fire neuron is in good agreement with the experimental literature. Whether the same neuron model also successfully predicts experimental results for the new transmission function is the subject of ongoing experimental research (Chap. 10).

Chapter 3

Transmission Function for Transient Input

The synfire model (Sec. 1.4) states that the cortical network can sustain synchrony in propagating volleys of spikes. In order to understand the synchronization dynamics and the conditions under which synchronization can occur, we introduce collective variables describing the development of activity in the network and characterize the relevant single neuron properties. The analysis is based on the conditions in the cortical network discussed in the preceding chapter (Chap. 2). We have already described in Sec. 1.4 that in a locally feed-forward network, spike volleys are at the same time the generator and the result of transients in the neuronal input. The first section of the present chapter (Sec. 3.1) introduces the notion of a *pulse packet* to quantify the degree of synchrony in a propagating spike volley. Sec. 3.2 identifies the single neuron's response to transient input as the basis for understanding the network dynamics. The concept of pulse packets allows for the construction of an appropriate single neuron simulation experiment. The last section (Sec. 3.3) introduces a two-dimensional transmission function to represent neuronal response properties in compact form. In contrast to the "classical" transmission function (Sec. 2.5), the new transmission function characterizes the transient neuronal response to transient input. Properties of the transmission function are illustrated for the specific neuron model (Chap. 2) used throughout the present study. However, the definition of the transmission function is independent of the choice of the neuron model. The next chapter (Chap. 4) combines the characterization of single neuron properties derived in the present chapter with a description of the network structure, allowing for an analysis of synchronization dynamics.

3.1 Pulse Packets

In Sec. 1.4 the synfire chain was introduced as a model for the occurrence of spatio-temporal spike patterns in neuronal data. In such subnetworks groups of neurons are connected in a feed-forward manner. In the simplest case each neuron in group i receives input from all neurons in group $i-1$ and projects to all neurons in group $i+1$ (cf. Fig. 1.2). The typical spiking activity in these subnetworks are volleys of spikes emitted by successive neuron groups. We have seen examples of this activity in Fig. 1.3. Changing our perspective from

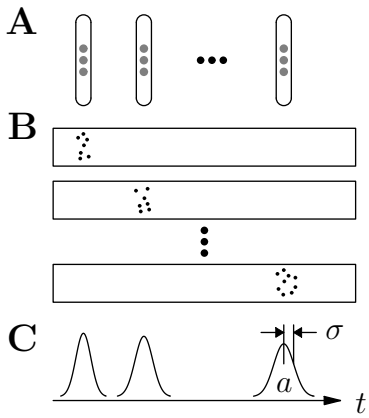

Figure 3.1 Pulse packet representation of a propagating volley of synchronous spikes. **A** Sketch of the subnetwork organized in a sequence of groups of neurons (cf. Fig. 1.2). The first, the second and a group at a position further in the chain are shown as representatives. **B** Sketch of activity in the network. Each box indicates the spiking activity of a corresponding neuron group. The horizontal arrangement of neuron groups in **A** is translated into the vertical arrangement of boxes. Dots within boxes indicate individual spike times. In each box one vertical position is reserved for any neuron of the group (cf. Fig. 1.3). Time is advancing along the horizontal axis. **C** Activity in the network is represented as a sequence of packets parameterized by the number of spikes a in the corresponding spike volley (**B**) and by a measure of the temporal spread of spike times σ. The tuple (a, σ) specifies a pulse packet.

the individual neuron group to the network level we can also describe the development of activity as a single volley of spikes traveling through the network. On its path through the network the volley undergoes transformation of its shape at each neuron group. Typical developments of the volley are the four cases shown in Fig. 1.3. Here, different initial conditions lead to qualitatively different spiking activities. The most prominent effect is that the number of spikes a in the volley is not constant. The number of spikes can grow (Fig. 1.3 **A**) as well as decline (Fig. 1.3 **D**). The other immediately observable effect is that also the temporal spread of spikes in the volley is subject to change. Temporal spread can grow (Fig. 1.3 **C**) as well as decline (Fig. 1.3 **B**). A direct measure for the temporal spread in the volley is the standard deviation σ of the spike times. Our strategy now is to express network activity in terms of a and σ, and to try to gain an understanding of synfire dynamics in terms of these collective variables.

The approach is depicted in Fig. 3.1. The individual configuration of spikes arriving at a neuron group is collectively described by just two variables $(a_{\text{in}}, \sigma_{\text{in}})$: the input packet. In response the group will itself emit a pulse packet $(a_{\text{out}}, \sigma_{\text{out}})$, again in this picture the detailed timing of the individual response spikes is ignored. Alternatively, we can say that the neuron group transforms the incoming packet $(a_{\text{in}}, \sigma_{\text{in}})$ to the outgoing packet $(a_{\text{out}}, \sigma_{\text{out}})$. Thus, we would like to describe the dynamics of a neuron group by a propagator for pulse packets

$$(a_{\text{in}}, \sigma_{\text{in}}) \to (a_{\text{out}}, \sigma_{\text{out}}). \tag{3.1}$$

Doing so we have reduced the problem of understanding synfire dynamics to the construction and analysis of a propagator for a two-dimensional iterative system (Strogatz, 1994; Kaplan & Glass, 1995; Elaydi, 1999). Obviously, it may still turn out that the reduction to two variables is not sufficient to describe the effects observed in network simulations. Before we

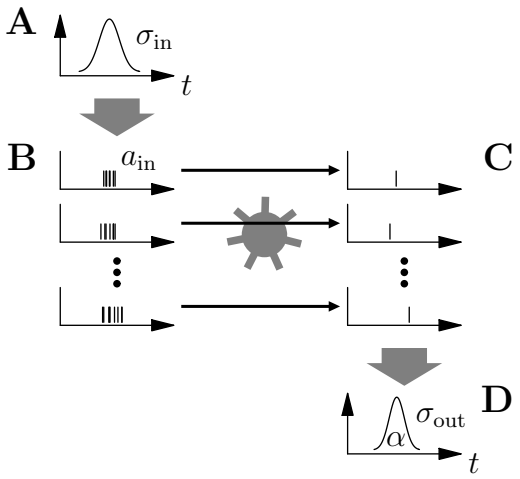

Figure 3.2 Illustration of the procedure quantifying the neuronal response to pulse packet input. A cortical model neuron (center, gray) is stimulated with a pulse packet (upper graph in **B**) by drawing a_{in} spike times (vertical bars) from a gaussian probability density function (**A**) with standard deviation σ_{in}. The pulse packet is embedded in random excitatory and inhibitory spike trains (not shown), mimicking the ongoing synaptic bombardment due to background activity. The response (upper graph in **C**) of the neuron to such pulse packet input typically consists of at most one spike (vertical bar), the timing of which depends on the realizations of background activity and the incoming pulse packet. The process is repeated many times (indicated by vertical sequence of graphs in **B** and **C**) to obtain a histogram (**D**) of the neuronal spike response to pulse packets parameterized by $(a_{\text{in}}, \sigma_{\text{in}})$. The probability α to observe a response spike is determined by the net area of the output distribution, the temporal spread σ_{out} is measured by the standard deviation.

can construct the propagator in the next chapter we first have to analyze the single neuron's response to an incoming pulse packet.

3.2 Reduction to Single Neuron Properties

In a complete synfire chain every neuron of a particular neuron group receives exactly the same pulse packet from the preceding group. Let us assume that all the neurons in a group are identical and differ only in their independent dynamical state. In this situation, having a quantitative description of the single neuron's response to an incoming pulse packet (a, σ) should be sufficient to predict the group response. In the case of a stationary input current, neuronal response properties are successfully captured by the "classical" transmission function. The so called λ-I curve (cf. Fig. 2.7) neglects all details of spike timing. The λ-I curve is a model-free compact description of neuronal dynamics. This transmission function therefore allows direct comparison of experimental results with a neuron model and in addition the comparison of different neuron models. Following this line of thought, we will now try to construct a transmission function suitable for the case of transient input.

First we need to design a method to average over individual pulse packet realizations, because in our approach pulse packets with identical (a, σ) should be equivalent with respect to their effect on a target neuron. However, the detailed neuronal response will, obviously, depend on the configuration of spike times in the incoming pulse packet realization. Let us

assume that pulse packets are well described by a gaussian shape. This is a shape completely specified by its standard deviation σ. The mean of the temporal distribution of input spikes is arbitrary because we assume homogeneous synaptic delays. Therefore, we can define the origin of the temporal axis as the point in time where the mean of the gaussian distribution "arrives" at the target neuron. Thus, for the purpose of the construction of an appropriate transmission function we refine the definition of a pulse packet as follows: A pulse packet (a, σ) is a volley of a spikes individually drawn from a gaussian spike time distribution with standard deviation σ. In order to suppress details of individual spike timing, we define the response to an input packet (a, σ) as the neuronal response averaged over all possible realizations.

The feed-forward structure is assumed to be embedded in a large cortical network. Each neuron is subject to an ongoing synaptic bombardment with excitatory and inhibitory inputs (background activity). Consequently, the membrane potential exhibits large fluctuations on the mV scale. We can assume that because of the structure and the dynamics of the embedding balanced network (Chap. 2), the membrane potential time courses of the neurons in the feed-forward subnetwork are independent. Thus, although the single neuron dynamics is assumed to be deterministic, the neuronal response to an incoming pulse packet exhibits variability because of the random nature of thousands of input channels. The synapses connecting a neuron with the preceding group constitute only a small fraction of the neuron's total number of post-synaptic sites. When studying the neuronal response to pulse packet input this fact has to be taken into account. Fig. 3.2 (Diesmann, Gewaltig, & Aertsen, 1996a; Aertsen, Diesmann, & Gewaltig, 1996; Diesmann, Gewaltig, & Aertsen, 1999) illustrates the single neuron simulation experiment suggested by our considerations. Here, we simultaneously average over realizations of membrane potential time courses and realizations of pulse packets. While the former capture the variability of the dynamical states of the neurons in a group receiving the packet, the latter are only due to our definition of a pulse packet. In the propagation of a pulse packet from one neuron group to the next, the identical configuration of spike times is received by all the neurons of the target group. It turns out, however, that membrane potential fluctuations are the predominant source of variability in this system (Chap. 5, Chap. 8). Therefore, the additional variability introduced by pulse packet realizations does not perturb the results.

The neuronal response to an incoming pulse packet typically consists of not more than a single spike. This is due to the refractory period of the neuron. When the neuron recovers from refractoriness the excitation caused by the input packet has already substantially decayed and, therefore, no further spike is generated. In addition, part of the input current is lost due to the increased conductance following the onset of spike dynamics (modeled in Chap. 2 by clamping the membrane potential to the resting level during the absolute refractory period). The response spikes can be recorded in a peri-stimulus time histogram (PSTH) triggered to the mean of the distribution the input spikes are drawn from. Thus, by normalizing the response histogram by the number of trials performed, the area of the histogram can be interpreted as the probability α of the neuron to emit a spike in response to an incoming pulse packet $(a_{\text{in}}, \sigma_{\text{in}})$. The standard deviation σ_{out} of the output distribution is a measure for the temporal jitter in neuronal response to an input packet $(a_{\text{in}}, \sigma_{\text{in}})$. Hence, by comparing σ_{in} with σ_{out} we can directly determine whether the timing of the neuronal

response is more ($\sigma_{\text{in}} < \sigma_{\text{out}}$) or less ($\sigma_{\text{in}} > \sigma_{\text{out}}$) precise than the spike timing at its input. While σ_{out} is a measure for the temporal precision, α is a measure for the reliability of the neuronal response. To investigate the parametric dependence of the spike response distribution on the degree of input synchrony, we can now repeat the experiment for a range of values of input parameters a_{in} and σ_{in}, and in each case determine the associated response parameters $(\alpha, \sigma_{\text{out}})$. In summary, we have defined a new transmission function T characterizing the transient response of a single neuron to transient input

$$(\alpha, \sigma_{\text{out}}) = (T^{\alpha}(a_{\text{in}}, \sigma_{\text{in}}), T^{\sigma}(a_{\text{in}}, \sigma_{\text{in}})) \tag{3.2}$$

$$= T(a_{\text{in}}, \sigma_{\text{in}}), \tag{3.3}$$

where T^{α} and T^{σ} denote the two output components of T. In contrast to the λ-I curve, where a scalar variable is mapped to a scalar, T maps a pair of input variables to a pair of output variables.

There is a third parameter which can directly be extracted from the response histograms: the mean response time. In general, also this parameter is dependent on the input pair $(a_{\text{in}}, \sigma_{\text{in}})$. Thus, the speed of propagation of synchronous activity is determined by the constant synaptic delay and a dynamic component depending on the state of the system. In the process of computing the transmission function from the collection of histograms, the mean response time can be determined without additional costs. However, the next chapter (Chap. 4) demonstrates that time can be eliminated from the dynamics of synchronous activity and that for stability analysis it is sufficient to analyze an iterative mapping. Therefore, an analysis of the mean response time is outside the scope of the present study. Elsewhere (Gewaltig, Diesmann, & Aertsen, 2001b) we have investigated the speed of propagation using network simulations, additional information can be found in (Wennekers & Palm, 1996). The remainder of the present work makes no reference to the mean response time. The next section discusses quantitative aspects of the transmission function (3.3) and its graphical representation.

3.3 Quantitative Description of the Response

The preceding section outlines how the histograms obtained by the protocol (Fig. 3.2) defining the transmission function (3.3) are reduced to two parameters $(\alpha, \sigma_{\text{out}})$. Fig. 3.3 shows response histograms for four extreme choices of input variables $(a_{\text{in}}, \sigma_{\text{in}})$ and explains the details of parameter extraction (Diesmann, Rotter, Gewaltig, & Aertsen, 1996). Response parameters cannot directly be obtained from the raw histograms because of the presence of spontaneous spiking activity and the limited amount of data available. The reduction to variables α and σ_{out} requires some criterion to separate the "response" from spontaneous activity. Clearly, the histograms cannot simply be described by the superposition of a homogeneous (unperturbed) distribution and a bell shaped response. Observe the reduction of the activity level in the top left panel of Fig. 3.3 around $t = 10\,\text{ms}$ compared to the spontaneous level for $t < 0$. (even more pronounced in Fig. 9.4 on page 112). In any case, consistent results are obtained by subtracting the spontaneous level from the histograms and by computing α and σ_{out} from the remainder. The histograms contain only a finite amount of data

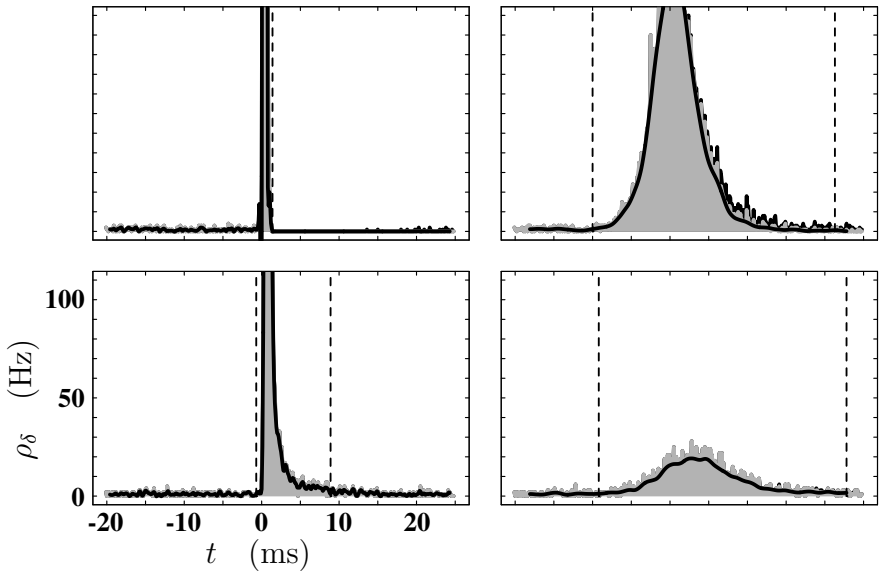

Figure 3.3 Response of the integrate-and-fire model to pulse packet input. Panels showing data for extreme input packets (a, σ) are arranged as follows: a vertical, bottom (45) to top (115) and σ horizontal, left (0 ms) to right (5 ms). The origin of the temporal axes (horizontal) is defined by the center of mass of the distribution the input spikes are drawn from (cf. Fig. 3.2). The gray area represents the distribution of the neuronal spike response estimated over 10,000 repetitions as a histogram with temporal resolution 0.1 ms. The histogram is normalized by the number of repetitions and temporal resolution, expressing the response (vertical axes) in units of spike rate. The black curve shows the same data smoothed by a symmetrical Savitzky-Golay filter (left column: carrier ± 0.5 ms, order 4; right column: carrier ± 2 ms, order 2). The negativity at the onset of the up-slope in the top left panel is an artefact of filtering. Peak values of histograms shown truncated are: 470 Hz (bottom left), 2600 Hz (top left), and 135 Hz (top right). Histogram counts (gray bars) falling below the black curve are not visible due to the finite linewidth of the graphical representation. Dashed vertical lines indicate the points in time where, viewed from the peak, the up-slope and the down-slope of the smoothed histogram intersect $\lambda_0 + \varepsilon$ for the first time. Raw histograms are computed on a $[-20\,\text{ms}, +25\,\text{ms}]$ carrier (observe reduction on both ends by filtering). When there is no intersection in the interval, the corresponding limit is used (e.g. lower right panel). λ_0 is the spontaneous spike rate (here: 1 Hz at $\sigma_V = 2.5$ mV, $\eta_V = 8$ mV), and ε an arbitrary offset (0.2 Hz). The left vertical line defines the onset of the response (line not distinguishable from up-slope in upper left panel) . To the right of the onset only the first spike is included in the gray histogram. At the given parameter settings, second spikes are only rarely observed (dark gray bars on the down-slope of upper right and around $t = 20$ ms in upper left panel). Response probability α and temporal spread (standard deviation) of the response σ_{out} are computed on the interval enclosed by vertical lines, using the smoothed histogram with λ_0 subtracted. Details of neuron model and unspecified parameters as in Chap. 2. See Fig. 9.4 on page 112 for example data at $\sigma_V = 4.5$ mV.

(spike times) and are, therefore, subject to statistical fluctuations. Robustness is achieved by smoothing the histograms and extracting the peak region as described in Fig. 3.3.

We are interested in the temporal spread of the response. Therefore, any operation on the data corrupting the peak width of the histogram or restricting the measure of temporal spread in any other way has to be avoided. Savitzky-Golay smoothing filters (Savitzky & Golay, 1964; Ziegler, 1981; Press, Teukolsky, Vetterling, & Flannery, 1992) are ideally suited for our purposes because they conserve the second moment and, depending on the order of the filter, also higher moments of the data. This is in contrast to the moving window average or boxcar filter, preserving only the zeroth moment (area) and the mean response time (provided the filter is symmetric). The idea of Savitzky-Golay filtering is to fit a polynomial to the data points in the moving window, and then to evaluate that polynomial at the central position. The reduction in noise level achieved by filtering can be observed in the peak region of the data in the bottom right panel of Fig. 3.3. The smoothed histogram (black curve) exhibits little remaining fluctuations and crosses through the erratic gray bars representing the raw data. Note that this does not indicate a degradation of the peak value of the histogram. The fluctuations in the gray histogram leading to values below the black curve are not visible because in the graphical representation the gray bars are overlapping. The extreme input conditions in Fig. 3.3 demonstrate two potential sources of error in the estimation of response parameters. First, if the filter cannot follow an abrupt change in spike density (gray), an excursion to negative spike rates may be generated, leading to an underestimation of the temporal extent of the peak region (black curve drops below zero at the onset of the response in top left panel). Second, if the response fails to drop back to the spontaneous level in the time interval spanned by the histogram, the temporal extent of the peak region may be underestimated (positioning of the right vertical line in bottom right panel). Fig. 3.3 illustrates that neuronal responses cover a wide range of shapes, from needle-like excursions of high amplitude to broad and shallow bumps. Unfortunately, the necessary compromise between sufficient smoothing and accurate description of the data requires the use of different filters for different shapes of the response. Filter parameters are adjusted by visual comparison of the filter results with the raw histograms (see Press, Teukolsky, Vetterling, & Flannery, 1992 and the references therein for more advanced methods). It turns out that three sets of filter parameters are sufficient to achieve reliable results. The choice of filter parameters should not be made dependent on the input variables $(a_{\text{in}}, \sigma_{\text{in}})$ to avoid the danger of a predetermination of the results of later analysis. Anyway, the filter parameters applied are organized, here, in terms of the input variable σ_{in} for clarity: $0 \leq \sigma_{\text{in}} \leq 0.5\,\text{ms}$: $(\pm 0.5\,\text{ms}, 4)$, $0.5 < \sigma_{\text{in}} \leq 2.5\,\text{ms}$: $(\pm 1\,\text{ms}, 2)$, $2.5 < \sigma_{\text{in}} \leq 5\,\text{ms}$: $(\pm 2\,\text{ms}, 2)$, where the first parameter in the parentheses is the symmetric half-width of the filter and the second parameter is the order of the polynomial. Filter parameters are kept constant throughout the present study. For responses to $a_{\text{in}} < 15$ a larger filter width is required. However, subsequent chapters show that this regime is of no relevance for our purposes. In two other studies (Gewaltig, Diesmann, & Aertsen, 2001b; Hehl, Aertsen, & Diesmann, 2001b) we have used different methods of parameter estimation leading to results consistent with the present work. The histograms are computed by performing a constant number of repetitions of the simulation experiment (Fig. 3.2). Therefore, the histograms for input packets causing a broad response profile or having low response probability exhibit a larger relative variability

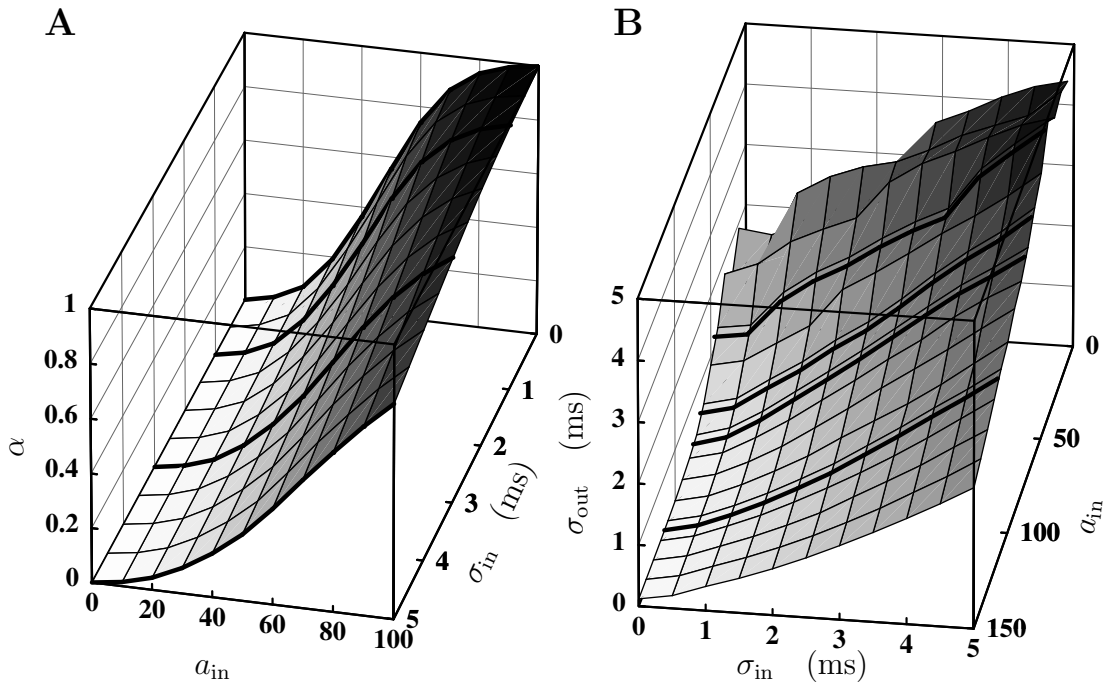

Figure 3.4 Two-dimensional transmission function for pulse packet input. Dependence of the two output variables on the two input variables $(a_{\text{in}}, \sigma_{\text{in}})$. Each output variable is a function of the two input variables. Data are represented by two simultaneous three-dimensional surface plots, one for each of the output variables α (**A**) and σ_{out} (**B**). The grid (lines of constant a_{in} and σ_{in}, respectively) is shown for orientation. Simulations are performed on a grid with spacing $\Delta a_{\text{in}} = 10$ and $\Delta\sigma_{\text{in}} = 0.25\,\text{ms}$. Linear interpolation is used for input pairs $(a_{\text{in}}, \sigma_{\text{in}})$ not corresponding to sample points. Thick curves indicate the location of four characteristic sections of the transmission function (σ_{in} = const in **A**, a_{in} = const in **B**) used throughout the study (cf. Fig. 3.5). Gray shading of surface indicates value of output variable (same information as vertical axis). A different range of a_{in} is used in **A** and **B**. Fluctuations observable in **B** at low a_{in} are due to the limited accuracy of parameter estimation. Parameters and neuron model as in Fig. 3.3.

of neighboring bins. Independent of input parameters $(a_{\text{in}}, \sigma_{\text{in}})$, a more advanced simulation scheme would use an adaptive number of repetitions to achieve a predefined accuracy goal.

The two surface plots in Fig. 3.4 constitute a complete representation of the transmission function (3.3). The complexity of the matrix of histograms obtained by simulation has been reduced here to a continuous two-dimensional map. As expected, the response probability α (Fig. 3.4 **A**) increases with the number of input spikes a_{in}. For a fixed temporal spread of the input σ_{in}, α depends on a_{in} in sigmoidal fashion. With increasing temporal jitter in the input packet, the slope of the sigmoid becomes less steep and the point of inflection moves to larger a_{in}. At perfect synchronization of the input spikes ($\sigma_{\text{in}} = 0\,\text{ms}$), the interval from 0 to 100 input spikes exploits the full range from vanishing α to a response probability approaching unity. While the response probability reaches zero for vanishing a_{in} independent of input synchrony, the number of input spikes required to reach saturation at the upper limit of the response probability depends on σ_{in}. α is restricted to the unit interval. Note that a_{in}, σ_{in}, and σ_{out} are defined on the positive half of the real axis (a_{in} restricted to integers). Thus, the lower limit of the range of values considered for a_{in} and σ_{in} is well defined. At this stage the upper limit of a_{in} and σ_{in} in Fig. 3.4 appears to be arbitrary. However, the next chapter

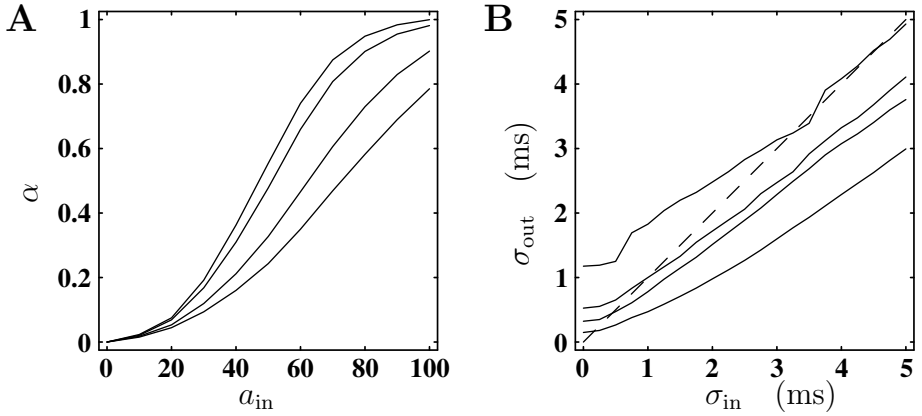

Figure 3.5 Compact representation of the transmission function (Fig. 3.4) used in the remainder of the study. **A** Response probability as a function of the number of input spikes $\alpha(a_{\mathrm{in}})$ for constant temporal spread σ_{in} of the input. From left to right: $\sigma_{\mathrm{in}} = 0, 1, 3, 5\,\mathrm{ms}$. Same data as thick curves in Fig. 3.4 **A**. **B** Temporal spread of the response as a function of input synchrony $\sigma_{\mathrm{out}}(\sigma_{\mathrm{in}})$ for a constant number of input spikes a_{in}. From top to bottom: $a_{\mathrm{in}} = 45, 65, 75, 115$. Same data as thick curves in Fig. 3.4 **B**. The dashed line indicates the diagonal.

demonstrates that the regime relevant for an analysis of the dynamics of synchronous activity in feed-forward networks is fully covered.

Fig. 3.4 **B** shows the dependence of the temporal spread of the response spike σ_{out} on the temporal spread in the input packet σ_{in} and the number of input spikes a_{in}. Compared to Fig. 3.4 **A**, the orientation of the axes of the surface plot spanning the (a_{in},σ_{in})-plane are exchanged to suggest a correspondence between input and output variables: $\sigma_{\mathrm{in}} \rightarrow \sigma_{\mathrm{out}}$, $a_{\mathrm{in}} \rightarrow \alpha$. The temporal spread of the response distribution increases with increasing σ_{in} and decreasing number of input spikes a_{in}. Even for perfect synchronization of input spikes $\sigma_{\mathrm{in}} = 0\,\mathrm{ms}$, a finite spread of the response spikes remains, reflecting the influence of background activity. The magnitude of this residual jitter depends on the number of synchronous input spikes. Interestingly, at a given a_{in} the slope of $\sigma_{\mathrm{out}}(\sigma_{\mathrm{in}})$ is smaller than unity: the output jitter increases slower than the input jitter. The combination of the two features, residual jitter at $\sigma_{\mathrm{in}} = 0\,\mathrm{ms}$ and a slope below 1, implies that for any a_{in} there is a a critical input spread above which the synchronization of the output is better than the synchronization in the input. Below the critical input spread, the neuronal response is less precise than the jitter of the input: synchronous input is desynchronized. Fig. 3.5 constitutes a further reduction of the representation in Fig. 3.4. Fig. 3.5 **A** is constructed from Fig. 3.4A by projecting the three-dimensional data points into the facing plane, collapsing the dimension extending into the depth of the page. Fig. 3.5 **B** is constructed analogously. For clarity, only curves for four representative values of the collapsed dimension are shown. We call Fig. 3.5 **A** the α-section of the transmission function. The curves for constant σ_{in}, resembling the well-known sigmoid activation function (e.g. Amit, 1989), are called *activation curves*. The limiting character of perfect synchronization of the input is now apparent. No input packet can exceed the response probability of the topmost curve in Fig. 3.5 **A**. Due to the saturation of response probability for vanishing a_{in} as well as for large a_{in}, the effect of input spread on the response probability is most pronounced at intermediate a_{in}. We call Fig. 3.5 **B** the σ-section of the

transmission function and $\sigma_{\text{out}}(\sigma_{\text{in}})$ the *dispersion curves*. Having identical physical units on both axes allows us to discuss the location of the dispersion curves with respect to the diagonal. The intersection of a dispersion curve with the diagonal defines the critical σ_{in} proposed above. The slope of $\sigma_{\text{out}}(\sigma_{\text{in}})$ is only weakly dependent on a_{in}; the number of input spikes merely controls an offset in output jitter.

Our neuron model contains a number of physiologically relevant parameters like the rise-time of the post-synaptic potential and the magnitude of membrane potential fluctuations. The remainder of the present work utilizes the α- and σ-sections (Fig. 3.5) of the transmission function to document and to compare the basic effects of various parameters.

To conclude, in the presence of large membrane potential fluctuations the cortical neuron is able to emit spikes with a temporal precision exceeding the precision of spike timing in its input. The temporal precision that can be reached is limited. A situation where the spread of the output equals the spread in the input would be a point on the diagonal of Fig. 3.5 **B**. Given a limited number of neurons emitting the input packet (say, 100) there is a maximal number of input spikes a_{in}. Having these spikes available would, in principle, permit a fixpoint temporal precision σ in the sub-millisecond range. However, the transmission function does not reveal whether such a state exists and whether it is stable. Further considerations beyond the single neuron level are required. The next chapter relates the transmission function to network structure, providing the desired propagator (3.1) and the tools for an analysis of the stability of synchronous spiking.

Chapter 4

State Space of Synfire Activity

The preceding chapter (Chap. 3) introduced variables to describe synchronous spiking activity and a new transmission function to characterize the single neuron dynamics. Here, we combine the transmission function with a parameter characterizing network structure to construct an iterative mapping determining the propagation of synchronous activity in a synfire chain (Sec. 4.1). The state space introduced in this chapter provides a general framework for an analysis of the dependence of the synchronization dynamics on the parameters of the system. It turns out that within this framework the question whether the cortical neuron supports precise spike timing can meaningfully be stated and addressed. Now, the tools are available to derive the central result of the present study (Sec. 4.2). On the basis of our neuron and network model (Chap. 2), we demonstrate that there is an attractor for synchronous activity governing the synchronization dynamics. Within the basin of attraction, synchronous spiking activity can propagate in stable fashion. Different initial conditions lead to qualitatively different trajectories. The last section (Sec. 4.3) demonstrates that the number of neurons per group w is a bifurcation parameter of the system. At a minimal w the attractor for synchronous activity vanishes. In three following chapters (Chap. 5, Chap. 7, Chap. 8) we will exploit the techniques developed here to investigate the dependence of synchronization dynamics on various physiologically relevant parameters. Chap. 6 and Chap. 9 explore the origin of parameter dependence.

4.1 Construction of State Space

The transmission function introduced in the preceding chapter shows that the temporal jitter of a single neuron's response to pulse packet input can be smaller than the temporal spread of the input packet (cf. Fig. 3.5 **B**). Since each neuron typically responds to an incoming pulse packet with only a single spike (Fig. 3.3), stable propagation of synchronous volleys of spikes inevitably requires the activation of successive, large enough groups of neurons (cf. Fig. 1.2 **C**). For a group of identical, otherwise independent neurons, the temporal distribution of the group's response spikes to an input pulse packet is identical to the response distribution for a single neuron (cf. Fig. 3.1). Hence, the temporal spread of the group's response spikes equals the single neuron's response dispersion σ_{out}. Similarly, the expected number of response spikes a_{out} in a group of w neurons equals the single neuron response

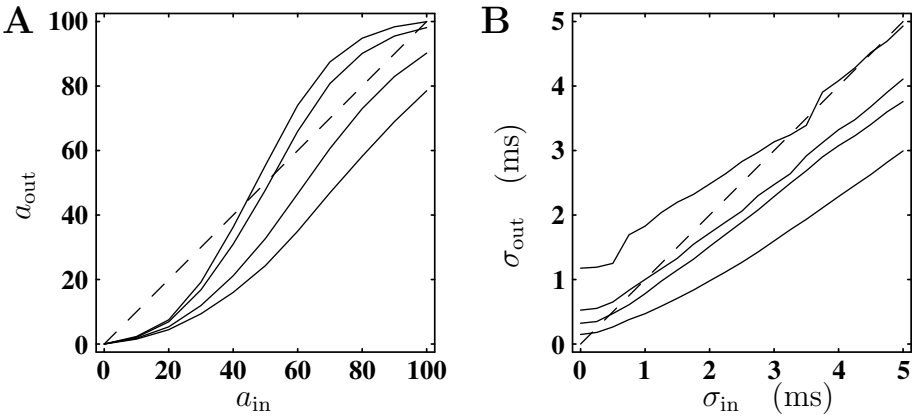

Figure 4.1 Input-Output relation T_w describing pulse packet transmission by a group of $w = 100$ neurons. **A** Number of output spikes $a_{\rm out}$ as a function of the number of input spikes $a_{\rm in}$. Curves are for constant temporal spread of the input packet: $\sigma_{\rm in} = 0, 1, 3, 5\,{\rm ms}$ (left to right). The graph is constructed from Fig. 3.5 **A** by multiplying values on the ordinate with w. **B** Temporal spread $\sigma_{\rm out}$ of the output packet as as function of the temporal spread in the input packet $\sigma_{\rm in}$. The panel is identical to Fig. 3.5 **B**. The dashed lines indicate the diagonals.

probability α (Fig. 3.5A), multiplied by the group size w. Thus, concentrating on expectation values, we can write the propagator asked for in (3.1) in terms of the single neuron transmission function (3.3):

$$T_w = (wT^\alpha, T^\sigma). \tag{4.1}$$

The variability of the group response is discussed in Chap. 8. Fig. 4.1 shows T_w for a particular choice of group size $w = 100$. Now, the output of a neuron group is described in terms of the same variables as the input. Note that to achieve this goal, a parameter describing network architecture (w) enters the mapping. In Fig. 3.5 **B** we discussed the neuronal ability to decrease the temporal spread of an incoming pulse packet by comparing the dispersion curves to the diagonal of the σ-section of T. The same analysis can now be carried out for the number of spikes in the pulse packet. In contrast to Fig. 3.5 **A**, Fig. 4.1 **A** has a meaningful diagonal (same physical units on both axes). Clearly, there is a regime where the number of response spikes $a_{\rm out}$ exceeds the number of input spikes $a_{\rm in}$. Provided that the temporal spread in the input packet is sufficiently small, the neuron group can increase the number of spikes in a propagating pulse packet. Thus, the two properties, reduction of temporal spread and elevation of spike count, already indicate that the network has the potential to sustain synchronous spiking. However, the two variables are not independent. A positive gain for the number of spikes is only observed for a limited range of input jitter. Likewise, a reduction in temporal spread can only be achieved if a sufficient number of input spikes is available. The observations made above for the individual sections of the mapping (4.1) are necessary requirements for stable propagation of synchronous activity, but are not sufficient. The two sections have to be treated simultaneously as a single dynamical system.

Assuming that our system is fully described by the two variables (a, σ), the dynamics is specified by a two-dimensional iterative mapping

$$(a_{i+1}, \sigma_{i+1}) = T_w(a_i, \sigma_i). \tag{4.2}$$

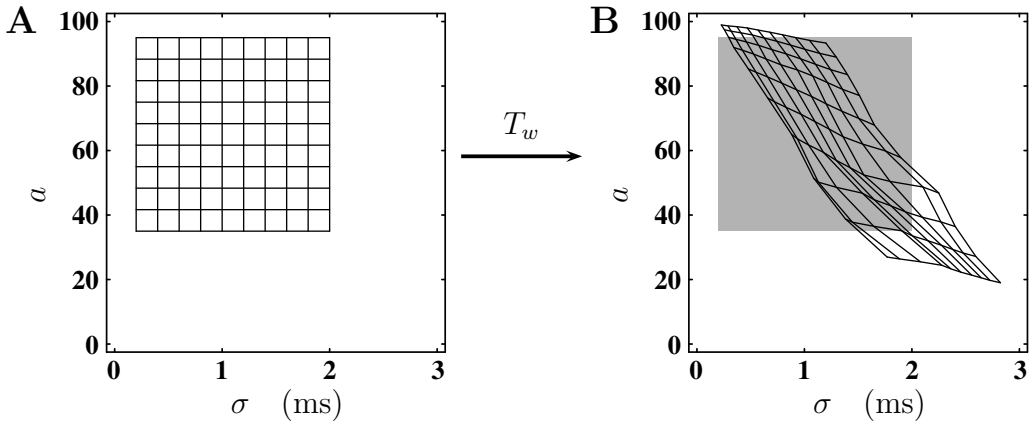

Figure 4.2 Simultaneous operation of the iterative mapping T_w on variables a and σ spanning the state space of synchronous spiking activity. **A** Graphical representation of the state space. By convention, the first component (number of spikes) of the tuple (a, σ) spans the vertical axis and the second (temporal spread) the horizontal axis. Lattice sites indicate an arbitrary subset of possible initial conditions (a, σ). The spacing of the lattice in σ-direction is $\Delta\sigma = 0.2\,\text{ms}$, $\Delta a = 100/3\,\text{ms} \cdot \Delta a$ is adjusted to yield a visually identical spacing in both directions at the particular aspect ratio of this graph. The lower left coordinate of the lattice is $(35, 0.2\,\text{ms})$. **B** Deformation of the lattice in a single iteration step (T_w of Fig. 4.1 applied once to each lattice site). Gray area indicates initial position of the lattice for comparison.

A pulse packet (a_i, σ_i) emitted by neuron group i causes neuron group $i + 1$ to respond with (a_{i+1}, σ_{i+1}). Variables a and σ span the two-dimensional state space of our system. Fig. 4.2 **A** is a representation of state space. This is the orientation of axes used throughout the present work. Due to the limited group size w, there is a natural lower (0) and upper (w) bound for a. In contrast, σ only has a lower (0 ms) bound. The finite range shown in Fig. 4.2 **A** is arbitrary. The simultaneous operation of the mapping on both coordinates can be visualized by the deformation of a lattice in Fig. 4.2**.** It is immediately observable that the mapping exhibits considerable overall smoothness. Neighboring lattice sites remain neighbors in (a, σ)-space. No folding occurs. The lattice undergoes a compression in σ-direction to intermediate values of σ. Lattice sites at low dispersion move to larger temporal spread and strong broad packets are synchronized. In addition the lattice is tilted: at large a synchronization dominates, and at low a the increase in dispersion. At the same time there is a downward as well as an upward expansion of the lattice spacing in a-direction at intermediate values of a. The lattice sites concentrate at large a. We do not observe this at low a, due to the restricted range of the initial lattice. Roughly, the lattice deformation is explained by the slopes of the intersections of the a-section (Fig. 4.1 **A**) and the σ-section (Fig. 4.1 **B**) with their respective diagonal. While the nature of the intersections is attractive in Fig. 4.1 **B**, it is repelling in Fig. 4.1 **A**. It seems that there is a region of state space at low σ and large a where the mapping has a constructive effect, simultaneously in both variables. In order to obtain a more detailed picture of the dynamics of the system, the next section turns to individual trajectories.

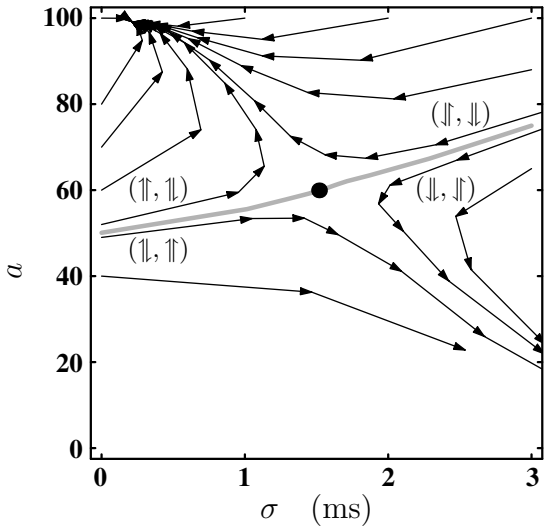

Figure 4.3 State space portrait for a propagating pulse packet (a, σ). Trajectories (sequences of arrows) for different initial conditions on the rim of the region of state space (introduced in Fig. 4.2 **A**) show the development of (a, σ) as the spike volleys move from one neuron group to the next. The four labeled trajectories enclosing the saddle point (central black dot, $(60, 1.5\,\text{ms})$) exhibit the non-monotonic evolution of the two variables. $(\Uparrow, \Uparrow)$ is a trajectory where a continuously increases ($\Uparrow$) and σ initially increases ($\uparrow$) before it declines again ($\downarrow$), other combinations encoded respectively for further reference. A separatrix (gray curve) divides state space into a regime (above gray curve) where synchronous spiking stabilizes (attractor at $(99, 0.2\,\text{ms})$) and a regime (below gray curve) where any initial activity eventually vanishes. The labeled trajectories correspond to the network simulations shown in Fig. 1.3, where the relative location of the trajectories in state space defines the arrangement of the panels.

4.2 Trajectories

In the last section we have studied the deformation of an initial state space volume under a single application of the propagator for pulse packets. Applying the iterative mapping (4.2) repeatedly, starting with some initial condition (a_0, σ_0), we can describe the evolution of synchronous activity on its path through the cortical network. The history of spiking activity, hopping from neuron group to neuron group, is recorded in the sequence

$$\{(a_0, \sigma_0), (a_1, \sigma_1), (a_2, \sigma_2), \ldots, (a_i, \sigma_i), \ldots\}\,, \tag{4.3}$$

defining a *trajectory* in state space. (a_i, σ_i) specifies the pulse packet emitted by the ith neuron group. The smoothness of the mapping suggests that a few characteristic trajectories might be sufficient to reveal the overall structure of state space. Fig. 4.3 shows the resulting state space portrait of our system. The prominent and most important feature is that, indeed, there is an attractor for synchronous spiking governing the synchronization dynamics. The attractor is surrounded by a *basin of attraction*. A spike volley starting anywhere inside this regime rapidly (i.e. after only a few stages) reaches the vicinity of the attractor. Thus, we have demonstrated that pulse packets with sub-millisecond precision recruiting nearly all the neurons of a group can stably propagate through the network. A saddle point controls the part of the border of the basin of attraction not predetermined by the definition of the

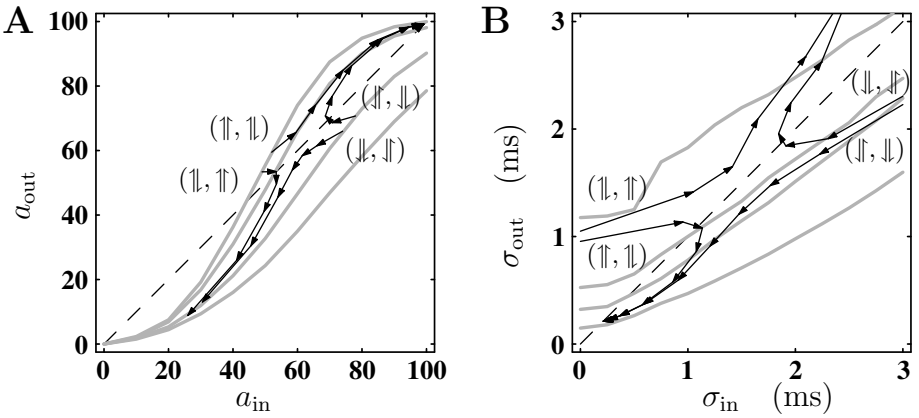

Figure 4.4 Projection of trajectories into the a-section and the σ-section of the iterative mapping. Gray curves are identical to the curves in Fig. 4.1 (σ restricted to 3 ms to increase resolution). Trajectories and labeling correspond to the four labeled trajectories of Fig. 4.3. The starting point of a trajectory indicates the particular initial condition (a_0, σ_0). One coordinate can be read of from the horizontal axis, the other is specified by the gray curve the starting point is located on (for clarity trajectories with large σ_0 start at $\sigma = 3$ ms). In **A** the arrangement of the trajectories with respect to the saddle seen in Fig. 4.3 remains unchanged. In **B** the vertical arrangement is exchanged, the horizontal one preserved. The attractor for synchronous spiking is projected to the upper right corner of **A** and the lower left corner of **B**.

variables ($0 \leq a \leq w$ and $\sigma \geq 0$). We call the set of states (a, σ) reaching the saddle for $i \to \infty$, the *separatrix* of the system. The $i \to -\infty$ separatrix is of no special relevance in the remainder of the present work. At larger initial spread more input spikes are required to reach the attractor. Spike volleys starting outside the basin decay after only a few stages: synchronous activity which is too weak (few spikes) or too dispersed rapidly dies out. The "trivial" attractor for vanishing activity is not of interest for the scope of the present study. We return to this point in the discussion (Sec. 10.2). If not stated otherwise, by *attractor* we refer to the attractor guaranteeing stable propagation of synchronous spiking.

Note that neither a nor σ alone describe the dynamics of the system. This is particularly clear from the non-monotonic way in which each of them evolves along a trajectory (Fig. 4.3, labeled curves). An initial increase in temporal spread may still lead to stable propagation, provided that the number of spikes in the initial volley was large enough ($\Uparrow, \Downarrow$). If, however, this number is too small, the volley dies out, in spite of the initial increase in spike number ($\Downarrow, \Uparrow$). Conversely, an initial decrease in the temporal spread may still lead to vanishing synchronous activity ($\Downarrow, \Downarrow$). If, however, the initial number of spikes in the volley is large enough, the volley survives ($\Downarrow, \Downarrow$). Thus, neither the relation between numbers of input and output spikes (Fig. 4.1 **A**), nor the relation between input and output jitter (Fig. 4.1 **B**) alone determine whether synchronous activity survives; the evolution to the stable fixpoint is governed by the interaction of the two state variables (Fig. 4.3). Careful visual inspection of Fig. 1.3 reveals that the non-monotonicity predicted by our iterative mapping can indeed be observed in individual realizations of (simulated) network activity.

Let us conclude the discussion of individual trajectories by projecting them back into our representation of the iterative mapping (Fig. 4.1). Fig. 4.4 shows projections of the four labeled trajectories of Fig. 4.3 into the a-section (Fig. 4.4 **A**) and the σ-section (Fig. 4.4 **B**) of T_w. In a fixpoint of the iterative mapping we have $(a_{\text{out}}, \sigma_{\text{out}}) = (a_{\text{in}}, \sigma_{\text{in}})$. Thus, fixpoints are

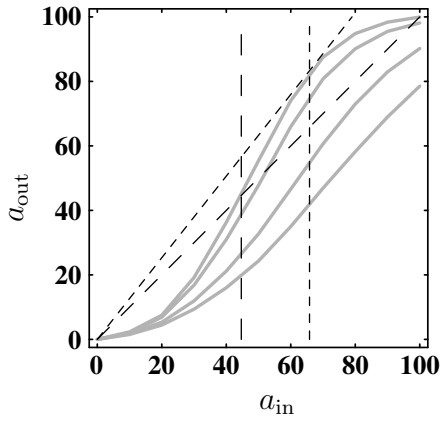

Figure 4.5 Threshold packet and condition for the existence of an attractor for synchronous spiking activity. The gray curves show the a-section of the iterative mapping (Fig. 4.1 **A**). The intersection of the diagonal (long dashed) with the activation curve for perfect synchronization (top gray) defines the threshold packet. Pulse packets with fewer spikes (threshold a indicated by long dashed vertical line) cannot survive. The location of the diagonal relative to the activation curves is determined by group size w (here, 100). At a certain minimal w (79, new diagonal short dashed) all activation curves run below the diagonal (point of contact with ($\sigma_{\mathrm{in}} = 0$)-curve indicated by short dashed vertical line): stable propagation of synchronous spiking is excluded.

simultaneously located on the diagonals of the a-section ($a_{\mathrm{out}} = a_{\mathrm{in}}$) and the σ-section ($\sigma_{\mathrm{out}} = \sigma_{\mathrm{in}}$). The two trajectories starting on the curve for perfect synchronization of the input in Fig. 4.4 **A** both have an initial number of spikes above the diagonal. Nevertheless, one of the trajectories reaches the attractor, the other one crosses the diagonal and activity decays. The curve for $\sigma_{\mathrm{in}} = 3\,\mathrm{ms}$ in Fig. 4.4 **A** runs completely below the diagonal. Nevertheless, one of the two trajectories started here reaches the attractor. Although the sigmoidal activation curves strongly shape the overall appearance of the trajectories, the variable a is not sufficient to describe the dynamics (e.g. by the usual cobweb construction). Propagation involves shifting to other activation curves. Similar statements can be made for the variable σ. Trajectory ($\Uparrow, \Downarrow$) in Fig. 4.4 **B** would converge to temporal spread $> 1\,\mathrm{ms}$ in a one-dimensional consideration. However, the diagonal is crossed from above and the attractor for synchronous spiking is reached. Trajectory ($\Downarrow, \Uparrow$) starts on a dispersion curve leading to low temporal spread if Fig. 4.4 **B** is considered as a one-dimensional mapping. Nevertheless, the diagonal is crossed from below and temporal spread starts to grow again.

The present section shows that an additional parameter w describing network structure has to be incorporated into the transmission function T before the question whether the cortical neuron supports precise spike timing can be answered. For the examples in this section we decided for the arbitrary value of $w = 100$ (in fact, Chap. 6 demonstrates that given the single neuron parameters, this is a canonical choice). Consequently, the next section has to analyze the role of parameter w for the synchronization dynamics.

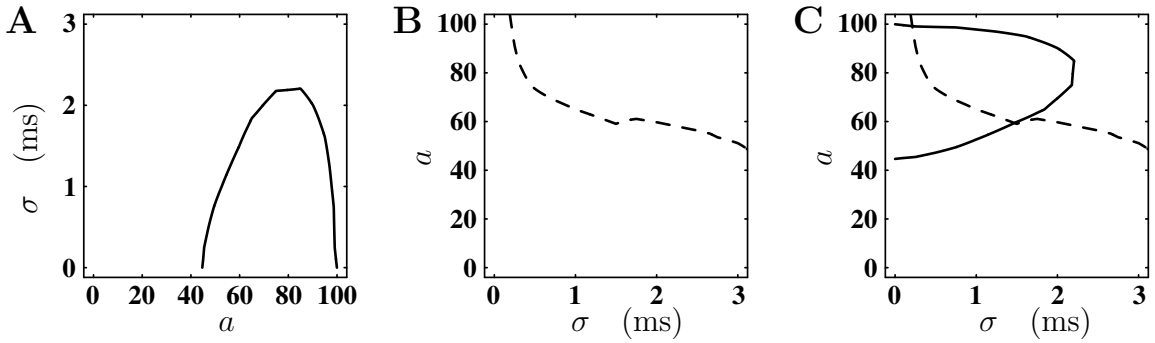

Figure 4.6 The isoclines of the iterative mapping. **A** The temporal spread σ (ordinate) of a pulse packet required for a given number of spikes a (abscissa) to be invariantly transmitted by a neuron group (constructed using Fig. 4.1 **A**). There is a lower and an upper limit of the interval of a in which invariant transmission is possible. **B** The number of spikes a (ordinate) of a pulse packet required for a given temporal spread σ (abscissa) to be invariantly transmitted by a neuron group (constructed using Fig. 4.1 **B**). The minimal σ for which invariant transmission is possible is given by the maximum value of a ($= w$). **C** Projections of the two curves into the (a, σ) state space define the a-isocline (**A**, solid) and the σ-isocline (**B**, dashed) of the system. Intersections of the two isoclines are fixpoints of the dynamics (cf. Fig. 4.3).

4.3 Minimal Number of Neurons per Group

Evidently, the number of neurons per group w should influence the evolution of synchronous activity. Consider again the a-section of the iterative mapping (Fig. 4.5). The activation curves cross the diagonal in two points (apart from the trivial crossing at the origin 0). Here, the number of output spikes equals the number of input spikes. The lowest of these intersections occurs with the curve for perfectly synchronized input defining a lower bound for the number of spikes required to reach the attractor. For a_{in} below this threshold, we necessarily have $a_{\text{out}} < a_{\text{in}}$. Independent of temporal spread, pulse packets with fewer spikes cannot survive, since for all other activation curves the number of output spikes is even smaller. Decreasing the group size rotates the diagonal counter-clockwise around the origin (illustrated in Fig. 4.5). As a consequence, the intersection points with a given activation curve move closer together, and the number of spikes in the threshold packet increases. For lower w, more curves fall below the diagonal, until, at a certain value of w, even the curve for fully synchronized input only touches the diagonal in a single point. At smaller neuron group sizes, all curves run below the diagonal: the attractor vanishes and stable propagation of synchronous spiking is no longer possible. Thus, variation of w causes a structural change in state space. We have derived a lower bound on group sizes potentially supporting synchronous spiking. In order to determine how many neurons are, in fact, needed to guarantee that their synchronous activity survives in the network, we have to examine how the structure of the (a, σ) state space depends on the group size.

The *isocline* for the state variable a is defined as the collection of states for which the number of spikes in a volley does not change from one iteration to the next, irrespective of the behavior of σ. This set can be constructed by traveling along the diagonal of the a-section of the iterative mapping Fig. 4.1 **A** and recording the σ_{in} of the activation curve intersection with the diagonal at the current a for all points on the diagonal. The resulting curve is shown in Fig. 4.6 **A**. Obviously, the a-isocline is only defined for the regime of a

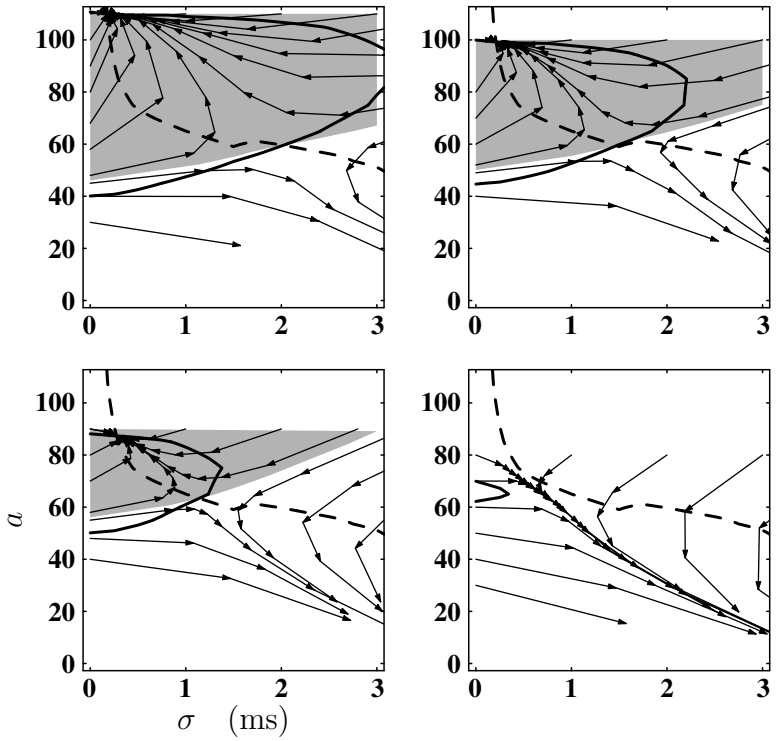

Figure 4.7 Dependence of spike synchronization on neuron group size. The panels show state space portraits (cf. Fig. 4.3) for four group sizes w (110, 100, 90, and 80, decreasing from top left to bottom right panel). The basin of attraction for synchronous spiking is indicated by the gray area. The region of state space shown is arbitrarily restricted to a maximum temporal spread of 3 ms. The upper (large a) boundary of the basin of attraction is defined by the group size ($a \leq w$). The a-isocline and the σ-isocline (cf. Fig. 4.6) are represented by the thick solid curve and the thick dashed curve, respectively. The σ-isocline is identical in all panels. At $w = 80$ the isoclines do not intersect. Fixpoints are given by the intersections of the two isoclines.

where the activation curve for perfect synchronization runs above the diagonal. Similarly, the σ-isocline contains all states which maintain their temporal spread, irrespective of a. The curve constructed using Fig. 4.1 **B** is shown in Fig. 4.6 **B**. Finally, the position of the two isoclines in state space is shown in Fig. 4.6 **C**. By definition, the isoclines are the loci of horizontal (a-isocline) and vertical (σ-isocline) flow, respectively. The fixpoints, defined by the requirement that neither a nor σ changes as the activity propagates, are given by the intersections of the two isoclines. Thus, we have a method at hand to determine the fixpoints of the dynamics directly from Fig. 4.1, not involving the use of test trajectories as in Fig. 4.3. Temporal spread of the response spike is a single neuron property (cf. Fig. 4.1 **B**) and, therefore, independent of w. Thus, the σ-isocline remains unchanged under variation of w. The situation is different for the a-isocline of the mapping. Here, the isocline changes as the diagonal rotates with respect to the activation curves.

Fig. 4.7 shows the state space portrait for four values of w. The qualitative change caused by w is immediately visible. Starting from our reference value of $w = 100$ (top right panel), increasing w moves the two fixpoints further apart, increasing the basin of attraction. As a result, the regime over which synchronous spiking is able to survive in the network increases.

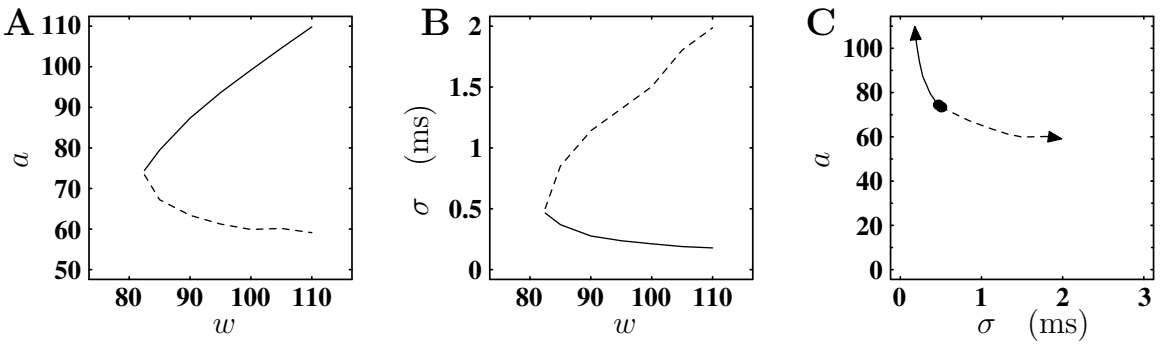

Figure 4.8 Bifurcation diagram for parameter neuron group size w. The graphs are constructed by computing the isoclines (cf. Fig. 4.6) for each value of w and recording only the coordinates of their intersections. **A** a-projection of the w-bifurcation. The a components (ordinate) of the attractor (solid) and the saddle point (dashed) are shown as a function of w (abscissa). Fixpoints are born at $w = 85$ with an initial number of spikes of $a = 75$ and separate with increasing w. **B** σ-projection of the w-bifurcation. The σ components (ordinate) of the two fixpoints as a function of w (abscissa). The temporal dispersion in the initial fixpoint is $\sigma = 0.5\,\text{ms}$. **C** Trace of the two fixpoints in state space following w-bifurcation (fixpoints created at dot, arrows indicate direction of increasing w). While the attractor gains more and more spikes, the saddle point moves out into the regime of larger temporal spread.

By contrast, for smaller numbers of neurons per group, the two fixpoints move closer together, until at some critical value the attractor and the saddle-point annihilate each other. Below this critical value, no fixpoint exists and all trajectories lead to extinction. Thus, the group size w acts as a bifurcation parameter, controlling the existence and separation of fixpoints in state space. A minimum of some 90 neurons per group is required to reliably maintain precise spike synchrony.

The isoclines reveal the mechanism of the bifurcation. As discussed above, in the w-bifurcation the σ-isocline remains unchanged. However, the a-isocline depends on w. The range of a over which the a-isocline is defined shrinks with decreasing w. Simultaneously, the a-isocline withdraws from the regime of large temporal spread. In this process the intersection points of the isoclines approach each other along a path prescribed by the static σ-isocline. Eventually, the a-isocline contacts the static σ-isocline only in a single point, with a further decrease in w the contact is lost. Continuing reduction of w finally abolishes the a-isocline (see Fig. 4.5). Fig. 4.8 reduces the relative movement of isoclines to a description of the movements of the fixpoints with the help of bifurcation diagrams. While Fig. 4.8 **A** and Fig. 4.8 **B** illustrate the explicit dependence of the state space coordinates of the fixpoints on parameter w, Fig. 4.8 **C** presents their locations in the two-dimensional state space as an implicit function of w. The same sequence of graphs is also used in later chapters (Chap. 5, Chap. 7) to document the dependence of state space structure on further parameters of the dynamics. In Chap. 10 the bifurcation diagrams are compared, uncovering the specific contribution of each parameter to the structure of state space.

Taken together, the results of the present chapter suggest that the answer to the question whether the cortical neuron supports precise spike timing is positive. However, it turns out that the question can not meaningfully be stated on the basis of single neuron properties alone (Chap. 3). Single neuron properties have to be combined with network structure. The concept of pulse packets allows us to demonstrate that there is an attractor

for synchronous activity governing the synchronization dynamics. The attractor describes a stationary configuration of activity in the (a, σ)-space. At the same time, it describes a dynamic configuration of activity in neuron space, with different groups of neurons, one after the other, contributing single spikes to the propagating pulse of activity. The attractor is characterized by a relatively large fraction (about 90%) of activated neurons per group, firing at sub-millisecond synchrony. Convergence into the vicinity of the attractor typically takes only a few successive group firings. The stable state is surrounded by a basin of attraction, the extent of which depends on the group size. The basin of attraction guarantees robustness of the propagating synchrony against perturbations of various sorts, which might affect the spike time distribution and/or the number of responsive neurons per group by an amount which exceeds the response variability accounted for by the transmission function. Perturbations such as temporal dispersion due to differences in axonal or dendritic delays, fluctuations in synaptic transfer properties, or correlated background fluctuations will not destroy the synchronous transmission as long as they do not push the network outside its basin of attraction. Essentially all the spikes of a volley in the stable state fall within a window of 1-2 ms. This temporal precision is consistent with the high accuracy of experimentally observed spike patterns in cortical recordings, both *in vivo* (e.g. Abeles, Bergman, Margalit, & Vaadia, 1993; Riehle, Grün, Diesmann, & Aertsen, 1997 and *in vitro* (e.g. Mainen & Sejnowski, 1995). Thus, in contrast to other model studies (e.g. Shadlen & Newsome, 1994), we conclude that highly precise synchronous firing of cortical neurons is indeed feasible, in spite of the large membrane time constant of 10 ms or more. Further interpretation and literature are given in Chap. 10.

Chapter 5

Background Activity

In the preceding chapters we have studied pulse packet transmission for a fixed level of membrane potential fluctuations ($\sigma_V = 2.5\,\mathrm{mV}$). These fluctuations are assumed to arise from the superposition of excitatory and inhibitory post-synaptic potentials, caused by the continuous synaptic bombardment. The value of σ_V was chosen to describe a realistic setting in the living brain in agreement with the physiological data (see Chap. 2 and Chap. 3). We now have to study how the observed effects depend on the magnitude of membrane potential fluctuations in the physiologically accessible range of fluctuations. First, we demonstrate that at a certain level of background activity the attractor for synchronous activity vanishes and discuss the properties of this bifurcation. The spontaneous activity of a neuron is a function of background activity. Sec. 5.2 analyzes the contribution of spontaneous spiking to the destruction of the attractor. At large σ_V the attractor can be recovered by increasing the number of neurons per group w (Sec. 5.3). The next chapter describes how the state space structure for finite σ_V develops from the noise-free case. It turns out that under certain conditions, background activity can increase the basin of attraction (Chap. 6). A simple model for the noise dependence of the transmission function is introduced in Chap. 9.

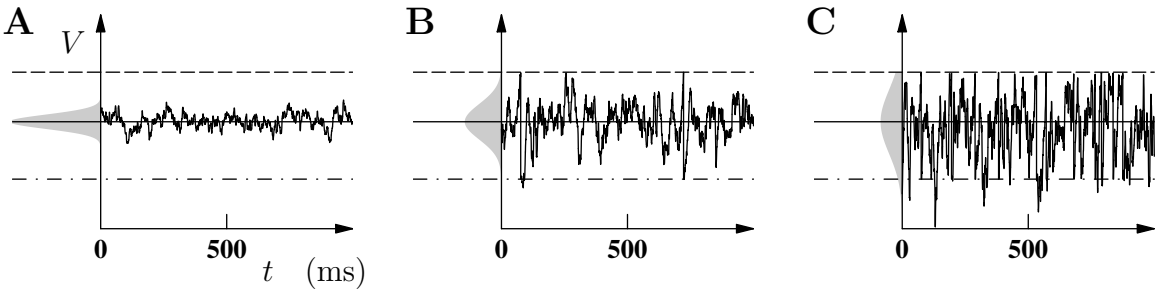

Figure 5.1 Example traces of simulated membrane potential fluctuations. The standard deviation of the fluctuations $\sigma_V = 1.0, 2.5, 4.5\,\mathrm{mV}$ is increasing from left to right. Traces of 1000 ms duration are recorded in a situation where the mean η_V (solid horizontal line) of the membrane potential V has reached a steady state. The dashed horizontal line indicates spike threshold ($\theta - \eta_V = 7\,\mathrm{mV}$), the dash-dotted horizontal line the resting potential. A Gaussian distribution (truncated at threshold) with mean and standard deviation corresponding to the fluctuations is plotted to the left of the ordinate (area shaded gray).

5.1 Background Fluctuations as Bifurcation Parameter

Fig. 5.1 shows three example traces obtained from single neuron simulations as described in Chap. 2. The standard deviation of the membrane potential is controlled by simultaneous changes in excitatory and inhibitory background spike rate, leaving the mean of the membrane potential unchanged (see Chap. 2). The spike threshold constitutes an upper bound for the membrane potential (our model does not describe the action potential itself). A Gaussian amplitude distribution with the same mean and standard deviation as the free membrane potential (without the threshold boundary) is a good approximation for this shot-noise process. The distribution is truncated at spike threshold and renormalized. Panel **B** represents our standard situation at $\sigma_V = 2.5\,\mathrm{mV}$ and low spontaneous activity. In panel **C** the standard deviation is increased to $\sigma_V = 4.5\,\mathrm{mV}$. Here, the fluctuations already fill the physiologically available range, the distance between mean and spike threshold being

$$\theta - \eta_V < 2 \cdot \sigma_V . \tag{5.1}$$

In the latter case, the spontaneous activity is already about 10 Hz. In panel **A**, fluctuations ($\sigma_V = 1.0\,\mathrm{mV}$) are reduced close to the minimal fluctuations caused by the excitation needed to overcome the distance from resting potential to the required mean (see Chap. 2). The distribution of membrane potential values is well separated from spike threshold and spontaneous activity is practically zero. Let us now investigate how the transmission function for synchronous activity depends on the membrane potential fluctuations. Fig. 5.2 shows the $\alpha(a_{\mathrm{in}})$ and $\sigma_{\mathrm{out}}(\sigma_{\mathrm{in}})$ sections of the transmission function introduced in Chap. 3 for four different levels of membrane potential fluctuations ($\sigma_V = 1.5, 2.5, 3.5, 4.5\,\mathrm{mV}$). We first concentrate on the changes observed in the $\sigma_{\mathrm{out}}(\sigma_{\mathrm{in}})$ curves. Starting from our original magnitude of fluctuations 2.5 mV (second row from top) with decreasing σ_V the curves drop to lower values of σ_{out}. However, increasing σ_V does not have a large influence on the spread of response spikes σ_{out}. Only for strong input packets $a_{\mathrm{in}} = 115$ the output spread increases by a small amount. The fluctuations in the σ_{out} curves for weak input packets $a_{\mathrm{in}} = 45$ are probably caused by the parameter estimation. In the case of small membrane potential fluctuations $\sigma_V = 1.5\,\mathrm{mV}$ and weak input packets a new effect appears far away from the diagonal which brings the σ_{out}-curves close together. We will come back to this effect in Chap. 9. More pronounced changes can be observed in the α-curves. For constant σ_{in} the activation curves exhibit a sigmoidal shape. At $\sigma_V = 2.5\,\mathrm{mV}$, the point of inflection is close to the number of input spikes a_θ where for a fixed σ_{in} the maximum $\widehat{U}$ of the membrane potential excursion caused by the incoming packet just overcomes the distance from mean to threshold

$$\theta - \eta_V = \widehat{U}\,(a_\theta, \sigma_{\mathrm{in}})\,. \tag{5.2}$$

For the example curves shown the values (rounded to integers, see also Fig. 6.7) are

$\sigma_{\mathrm{in}}/\mathrm{ms}$	0	1	3	5
$a_\theta(\sigma_{\mathrm{in}})$	50	55	73	91

.

It turns out that the behavior of $\widehat{U}\,(a_\theta, \sigma_{\mathrm{in}})$ is crucial for the structure of the (a, σ) state space. We will come back to this function and the assumption needed to define it in Chap. 6.

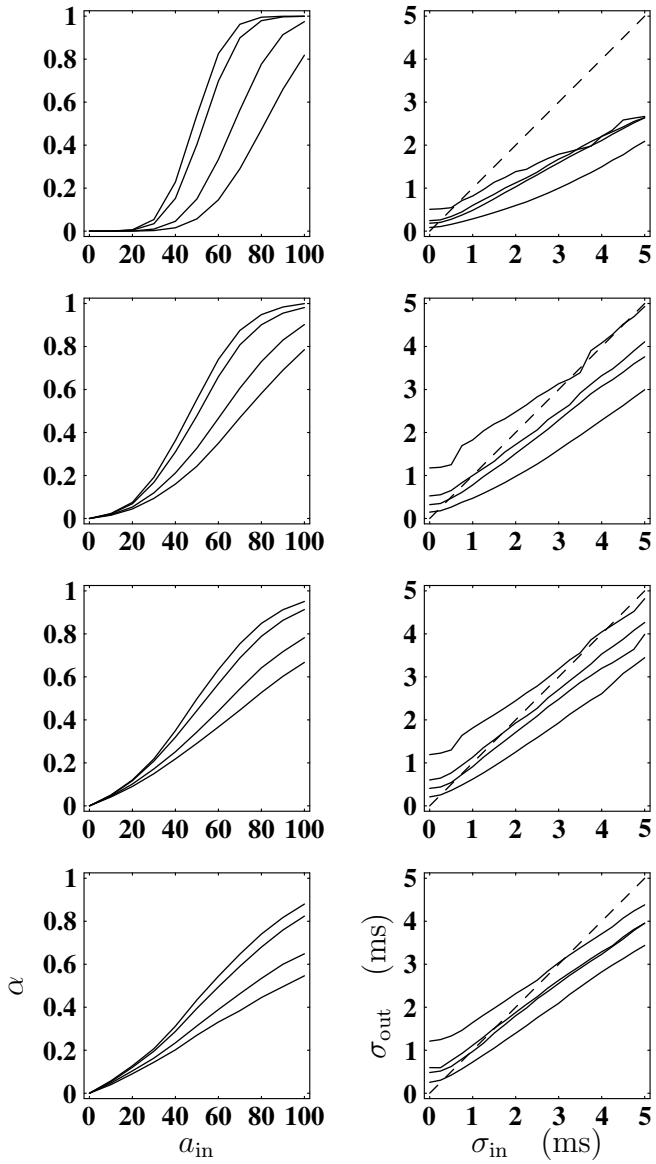

Figure 5.2 Dependence of transmission function on membrane potential fluctuations. The standard deviation of the fluctuations is increasing from top to bottom $\sigma_V = 1.5, 2.5, 3.5, 4.5\,\mathrm{mV}$ (four rows). The left column displays the $\alpha(a_{\mathrm{in}})$ section of the transmission function. The four curves represent different constant input spread $\sigma_{\mathrm{in}} = 0, 1, 3, 5\,\mathrm{ms}$ (from left to right). The right column displays the $\sigma_{\mathrm{out}}(\sigma_{\mathrm{in}})$ section of the transmission function. The four curves represent different constant input activity $a_{\mathrm{in}} = 45, 65, 75, 115$ (from top to bottom). The dashed line indicates the diagonal.

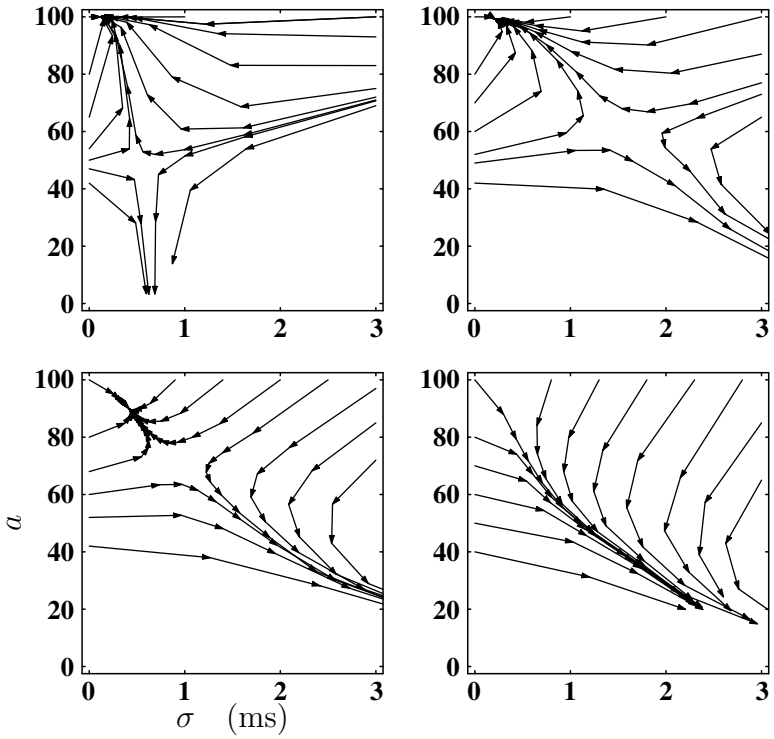

Figure 5.3 Dependence of state space structure on magnitude of membrane potential fluctuations. Four portraits of (a, σ) state space (σ horizontal, a vertical). The number of neurons per group is identical in all four cases ($w = 100$). Fluctuations σ_V are increasing from left to right and from top to bottom $1.5, 2.5, 3.5, 4.5\,\mathrm{mV}$. Selected trajectories starting at the border of the displayed region of state space indicate the position of fixpoints. Arrows depict the development of activity along a chain from one neuron group to the next. A structural change occurs between $\sigma_V = 3.5\,\mathrm{mV}$ and $4.5\,\mathrm{mV}$: the two fixpoints present in the first three portraits disappear, and all trajectories flow to the trivial attractor.

Response probability at the point of inflection is about 0.5 (larger for larger σ_{in}). The sigmoids become steeper with decreasing σ_{in}. The curve for $\sigma_{\mathrm{in}} = 0\,\mathrm{ms}$ represents a limiting curve. No $\alpha(a_{\mathrm{in}}, \sigma_{\mathrm{in}} = \mathrm{const})$ is steeper and reaches higher response probabilities than the one for $\sigma_{\mathrm{in}} = 0\,\mathrm{ms}$. When σ_V is decreased all activation curves become steeper leaving the point of inflection at about the same value of a_{in}. Thus, for particular a_{in} the difference between the response probabilities for different σ_{in} increases. With increasing σ_V the response probability at the point of inflection drops to a lower value. The sigmoidal shape now becomes asymmetrical: at $a_{\mathrm{in}} = 0$ the response probability is still zero, however to the right of the point of inflection the range of a_{in} shown in the graphs now covers only a part of the sigmoid. Even for the maximal a_{in} shown in the graph and full synchronization the upper saturation level is no longer reached.

The resulting state space structures for groups of $w = 100$ neurons is shown in Fig. 5.3. Again, we start the description with $\sigma_V = 2.5\,\mathrm{mV}$ (upper right), the situation which we already discussed in Chap. 4. When the membrane potential fluctuations are decreased ($\sigma_V = 1.5\,\mathrm{mV}$, upper left) both fixpoints move. The attractor moves to lower spread and larger activity. Only small changes can be observed in the position of the separatrix. The saddle point basically moves along the separatrix to lower temporal spread. Comparing

corresponding trajectories with the case of $\sigma_V = 2.5\,\mathrm{mV}$, the system is somewhat faster now (the effect increases for smaller σ_V). When the membrane potential fluctuations are increased to $\sigma_V = 3.5\,\mathrm{mV}$ (lower left), the change is dominated by a shift of the separatrix to higher activities and a stronger bend, such that no stable trajectories exist for temporal spread larger than 2 ms and the basin of attraction is considerably reduced. Surprisingly (but in consequence of the separatrix) the increased fluctuations move the saddle point back to lower temporal spread. At the same time, the saddle point is moved to larger activity and comes closer to the attractor, which itself is moved to a lower activiy and only slightly larger spread. Similarly to the w-bifurcation studied in Chap. 4, a further increase of σ_V to 4.5 mV leads to a dramatic change in state-space structure. The two fixpoints vanish, and synchronous activity cannot survive anymore. The local picture of this bifurcation is the same as for the w-bifurcation. However, globally the movement of the fixpoints is more complicated. In the w-bifurcation, the two fixpoints separate monotonously. With increasing w, the saddle point consistently moves to lower activity and higher temporal spread, the attractor moves in the opposite direction. Observe that in the w-bifurcation the separatrix does not change its position much. Under variation of σ_V, the separatrix shows little change for large σ_V, the regime in which the bifurcation occurs. However, for low σ_V it turns to low temporal spread, even for small activities. The determination of α and σ_{out} in our simulation study is difficult and, accordingly, imprecise for input packets with only a small number of spikes and large temporal spread. Here results may depend on the method of parameter estimation employed. Further work will be needed to explore the precise dynamics in the instable regime. No attempt will be made in the present study to describe this regime in detail. However, for vanishing membrane potential fluctuations we obtain some results in Chap. 6. A perspective is given in the discussion.

Let us now turn to the movement of the isoclines under variation of σ_V to understand how the σ_V-bifurcation occurs and how it differs from the w-bifurcation. Fig. 5.4 shows the isoclines correspondig to the four values of σ_V shown in Fig. 5.3. As in the w-bifurcation, the parabolic shape of the a-isocline contracts when the bifurcation parameter is changed into the direction where the stability is finally lost (here increasing σ_V). The a-isocline starts at a large activity value and zero spread. With decreasing a, the temporal spread on the isocline increases until a maximal spread is reached. For further decreasing a, the temporal spread decreases again, until at a certain activity value the limiting zero spread is reached again. With increasing σ_V the amplitude of this excursion into the direction of larger σ decreases. As in the w-bifurcation, the decrease in amplitude is combined with a decrease of the distance between the two activity levels where the a-isocline hits the $\sigma = 0$ axis. For small membrane potential fluctuations σ_V, the shape of the a-isocline becomes asymmetrical. The upper branch (for large a) approaches the σ-axis (horizontal line in our representation) at full activation (here $a = 100$). Interestingly, the lower branch (for low a) seems to approach the separatrix. In contrast to the w-bifurcation, σ_V cannot extend the a-isocline to values below a_θ. In Sec. 6.5 we will see why these effects occur. For a discussion on the σ-isocline we return to our reference situation ($\sigma_V = 2.5\,\mathrm{mV}$). With increasing σ_V, the isocline does not change much. For a given a it moves to slightly larger σ with increasing σ_V. The effect seems to be strongest for intermediate values of a. In this regime of large fluctuations the situation is comparable to the w-bifurcation where the σ-isocline is invariant, because

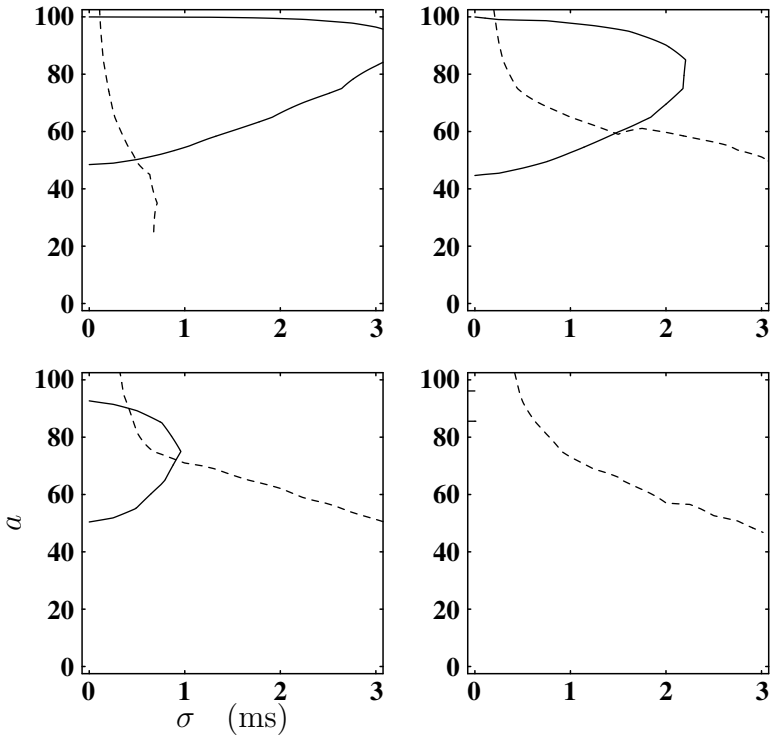

Figure 5.4 Dependence of isoclines on membrane potential fluctuations. The four graphs correspond to the $(a,\ \sigma)$ state space portraits shown in Figure 5.3 (σ horizontal, a vertical). Fluctuations σ_V are increasing from left to right and from top to bottom $1.5, 2.5, 3.5, 4.5\,\mathrm{mV}$. The solid curve represents the a-isocline, the set of points in state space for which in the next iteration the number of spikes does not change (the loci of horizontal flow). The dashed curve is the σ-isocline, the set of points in state space for which in the next iteration the temporal spread remains unchanged (the loci of vertical flow). Fixpoints occur at the intersections of the two isoclines (no flow). As for $\sigma_V = 2.5, 3.5\,\mathrm{mV}$ (upper right and lower left) the a-isocline is a continuous curve at $\sigma_V = 1.5\,\mathrm{mV}$ (upper left). The maximal extend in σ direction is not visible due to the arbitrary restriction of the region of state space shown to $\sigma \leq 3\,\mathrm{ms}$. The σ-isocline is not computed for a values below 40 because of insufficient smoothness of the estimate of the underlying transmission function determined by simulations. At $\sigma_V = 4.5\,\mathrm{mV}$ the number of response spikes a_{out} is always smaller than a_{in} no a-isocline exists.

w operates exclusively on the a_{out} component of the map (see Chap. 4). However, with decreasing σ_V the σ-isocline changes dramatically. For low background activity the isocline bends to lower temporal spread. Comparing the cases $\sigma_V = 2.5\,\mathrm{mV}$ (upper right in Fig. 5.4) and $\sigma_V = 1.5\,\mathrm{mV}$ (upper left in Fig. 5.4), the change in the isocline considerably moves the saddle point to lower temporal spread. For $\sigma_V = 1.5\,\mathrm{mV}$, the σ-isocline is vertically oriented. Together with the fact that it represents the loci of vertical flow, this explains the vertical orientation of the instable trajectories. Because under variation of σ_V both isoclines move, the picture is more complicated than in the case of the w-bifurcation.

We are now in a position to summarize the movement of the fixpoints with the help of the isoclines. Starting at small and continuously increasing membrane fluctuations, the attractor moves to larger temporal spread because of the bending of the σ-isocline. At larger fluctuations the shrinkage of the a-isocline becomes dominant and the attractor moves to lower activity with only a small increase in temporal spread. The saddle point moves to

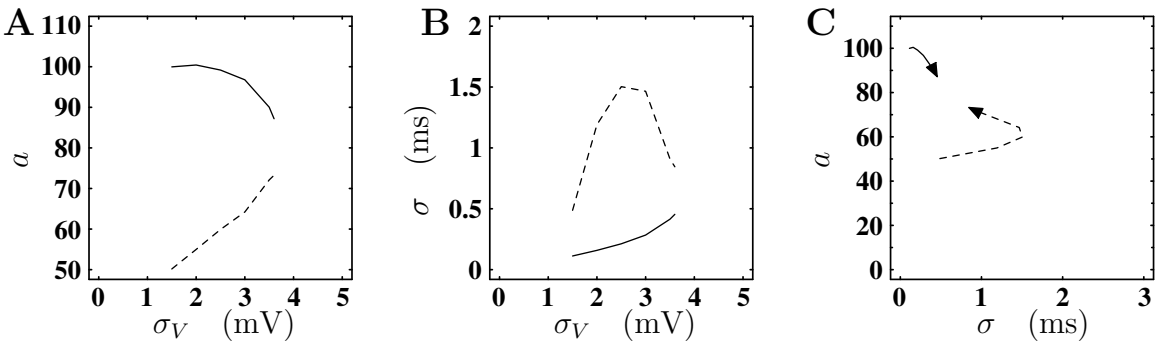

Figure 5.5 Bifurcation diagram for the parameter membrane potential fluctuations σ_V at $w = 100$ (attractor: solid line, saddle: dashed line). **A** a-projection of the σ_V-bifurcation. **B** σ-projection of the σ_V-bifurcation. **C** Trace of the two fixpoints in state space in σ_V-bifurcation. With increasing membrane potential fluctuations, the attractor and saddle approach an intermediate a. Temporal spread in the attractor increases moderately. By contrast, the temporal spread of the saddle exhibits a non-monotonous behavior. Initially, the temporal spread increases, reaches a maximum of 1.5 ms at $\sigma_V = 2.5$ mV, and then shrinks again until the two fixpoints collide (point of collision not shown).

larger temporal spread and larger activity, mainly by the increasing bend of the σ-isocline. At larger membrane potential fluctuations, the σ-isocline becomes stationary and the now considerably shrinking a-isocline moves the saddle point back to lower temporal spread, at still increasing activity, until it collides with the attractor. In Fig. 5.5 we summarize the complex movement of the fixpoints in a bifurcation diagram. While we lose the information how the isoclines contribute to the movement, the general behavior of the system is now very simple to describe. The construction of the diagrams is the same as for the w-bifurcation in Fig. 4.8.

5.2 Effect of Spontaneous Activity

An increase in membrane potential fluctuations naturally leads to an increase in so called "spontaneous" activity. While the spontaneous activity is about 1 Hz at $\sigma_V = 2.5$ mV, it has increased to 10.3 Hz at $\sigma_V = 4.5$ mV (see Chap. 2 for a calibration curve). In the neuron model we use, the threshold crossing is followed by a period of absolute refractoriness, during which the membrane potential is clamped to resting level. Under continuous fluctuations it now recovers to its mean with the time constant of the membrane. Clearly, the ability of the neuron to respond to an incoming pulse packet is reduced in this period. The effect increases with increasing spontaneous spike rate, because the probability that an incoming pulse packet strikes a neuron shortly after it spontaneously generated a spike increases. We have to conclude that the precise effect of spontaneous activity on pulse packet transmission may depend on the details of our model of the after-hyperpolarization. Therefore, it would be instructive to learn how the transmission function we measured at large membrane potential fluctuations (say $\sigma_V = 4.5$ mV) is influenced by the spontaneous activity. It is not obvious whether at this level of fluctuations the refractory effects already dominate the picture, or if it is still largely determined by the statistics of the membrane potential fluctuations.

The naive approach would be to prohibit the generation of spontaneous spikes and to

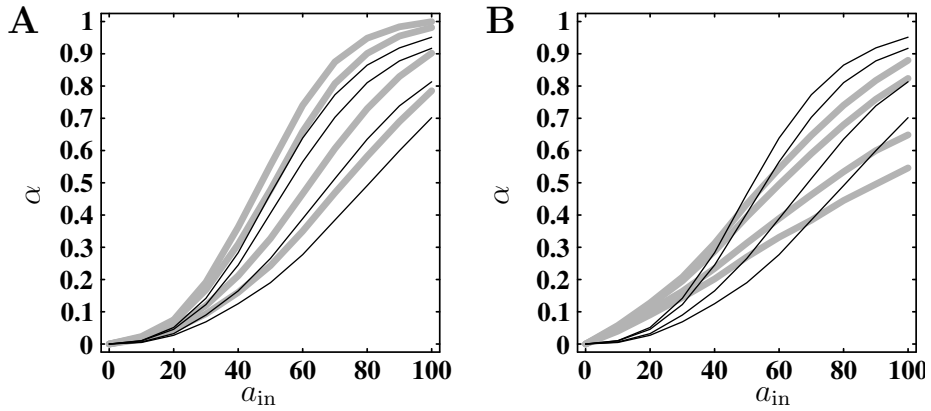

Figure 5.6 Effect of spontaneous activity on response probability. Gray curves in **A** represent the $\alpha(a_{\mathrm{in}})$ section of the transmission function for fluctuations $\sigma_V = 2.5\,\mathrm{mV}$ and corresponding spontaneous rate 1 Hz ($\sigma_{\mathrm{in}} = 0, 1, 3, 5\,\mathrm{ms}$, compare Fig. 5.2 second row). Superimposed solid curves are obtained under same conditions with spontaneous firing rate raised to 10.3 Hz by eliciting additional spikes at random times. Gray curves in **B** represent $\alpha(a_{\mathrm{in}})$ for $\sigma_V = 4.5\,\mathrm{mV}$ and corresponding spontaneous rate 10.3 Hz (Fig. 5.2 bottom row). Solid curves are identical to the solid curves in **A** (10.3 Hz, but $\sigma_V = 2.5\,\mathrm{mV}$).

compare the result with the original simulation. However, this turns out to be problematic. Increasing the threshold value prevents the generation of spontaneous spikes, but at the same time influences the response to an incoming pulse packet. A more elaborate scheme which prevents firing until the first spike of the pulse packet reaches the neuron is no cure to the principal problem. Because the neuron has never fired before, the spontaneous firing probability is high when spiking is first allowed, and from there on declines to a stationary level. In the response to an incoming pulse packet the above described non-stationarity will be present and, hence, perturb the estimation of $(\alpha, \sigma_{\mathrm{out}})$. Depending on the parameters, the spike probability density may even be bimodal.

Fortunately, there is an alternative approach which does not suffer from the problems described above. Instead of eliminating spontaneous spikes in the case of large fluctuations, we introduce additional spontaneous spikes in a simulation with small membrane potential fluctuations. Fig. 5.6 shows the original $\alpha(a_{\mathrm{in}})$ curves for $\sigma_V = 2.5\,\mathrm{mV}$ (**A**) and $\sigma_V = 4.5\,\mathrm{mV}$ (**B**) as gray curves. Superimposed as solid curves in both **A** and **B** are the results of a simulation at $\sigma_V = 2.5\,\mathrm{mV}$, but with the spontaneous activity artificially raised to the level of spontaneous activity in the case of $\sigma_V = 4.5\,\mathrm{mV}$. This was achieved by eliciting, in addition to the spikes naturally occuring at $\sigma_V = 2.5\,\mathrm{mV}$, spikes in the neuron at random points in time, irrespective of the value of the membrane potential at that point. Let us first concentrate on panel **A**. As expected, the increase in spontaneous activity leads to a decrease in the responsiveness of the neuron. The overall shape of the activity curves remains the same. However, a detailed comparison shows that the gray curves can neither be transformed into the solid curves by multiplication with a scalar, nor by the addition of a constant. Multiplication with a scalar would be equivalent to assuming an effective absolute deadtime. It describes the deviations between the two sets of curves well in the regime where they do not approach saturation at high values of a_{in}. In the saturation regime, however, the amplitude of the packet potentials is much larger than the distance from mean membrane potential to spike threshold. Therefore, a reduced mean of the membrane

potential in some distance from the last (spontaneous) spike does not considerably affect the response probability, whereas for weaker packets the distance from the last spike can decide between being sub- or supra-threshold.

Panel **B** illustrates the difference between the two sets of curves obtained at the same spontaneous rate. The gray curves apply in the regime of large membrane potential fluctuations $\sigma_V = 4.5\,\mathrm{mV}$, the solid curves at smaller fluctuations $\sigma_V = 2.5\,\mathrm{mV}$. Clearly, the fluctuations determine the shape of the activation curves, and not the level of spontaneous activity. We have seen in the discussion of panel **A** that part of the reduction in response probability for large input activity can be explained by the increase in spontaneous activity. However, if the level of spontaneous activity is held constant, the activation curves for $\sigma_V = 4.5\,\mathrm{mV}$ at large input activities still run below the corresponding curves for $\sigma_V = 2.5\,\mathrm{mV}$.

We conclude that in the regime where the σ_V-bifurcation occurs, the change in the transmission function caused by the increased membrane potential fluctuations is the dominating effect, not the increased spontaneous activity. Hence, the details of our model of after-hyperpolarization are of minor importance for this issue.

5.3 Compensation of Background Fluctuations

We have seen in Chap. 4 that in our system the number of neurons per group is a bifurcation parameter. Above a certain number of neurons the two fixpoints appear, and with further increasing group size the basin of attraction increases. The question arises whether in a situation where stability is lost because of large fluctuations (bifurcation parameter σ_V), we can possibly recover the fixpoints by increasing the number of neurons per group (bifurcation parameter w).

Fig. 5.7 shows the isoclines and state space structure at large membrane potential fluctuations $\sigma_V = 4.5\,\mathrm{mV}$ for two different group sizes, 115 (upper row) and 130 (lower row) neurons per group. In both cases stability is recovered. The group size w provides the transformation from response probability α to the number of output spikes a_{out}. At $\sigma_V = 4.5\,\mathrm{mV}$ and $a_{\mathrm{in}} = 100$, the response probability reaches a value of 0.9 (compare Fig. 5.6 **B**). Therefore, a group size of 115 already constitutes a strong compensation for the reduced response probability. For 100 completely synchronized input spikes we now expect $115 \cdot 0.9 = 103$ response spikes. The resulting state space structure is comparable to the case of smaller fluctuations at $\sigma_V = 3.5\,\mathrm{mV}$ (compare Fig. 5.7 upper right panel with Fig. 5.3 lower left panel). The saddle point is at approximately the same position, leading to a comparable basin of attraction. The attractor is located at similar temporal spread, however, the stable activity level is somewhat higher for the parameter set $(\sigma_V = 4.5\,\mathrm{mV}, w = 115)$ than for $(\sigma_V = 3.5\,\mathrm{mV}, w = 100)$. We already observed above that the σ-isocline for large fluctuations only weakly depends on σ_V. In addition, the σ-isocline does not depend on w. Thus, it is approximately the same for the two parameter sets. Upscaling of w has recovered the a-isocline for $\sigma_V = 4.5\,\mathrm{mV}$. Its comparable extension into the σ direction explains the correspondence of the positions of the saddle points. There is, however, a characteristic difference. Because the slope of the activation curves is less steep for $\sigma_V = 4.5\,\mathrm{mV}$, the interval of a over which the a-isocline exists is larger. Upper and lower limits of the interval are defined by the intersections of the activation curve for $\sigma_{\mathrm{in}} = 0\,\mathrm{ms}$ with the diagonal. The effect is more

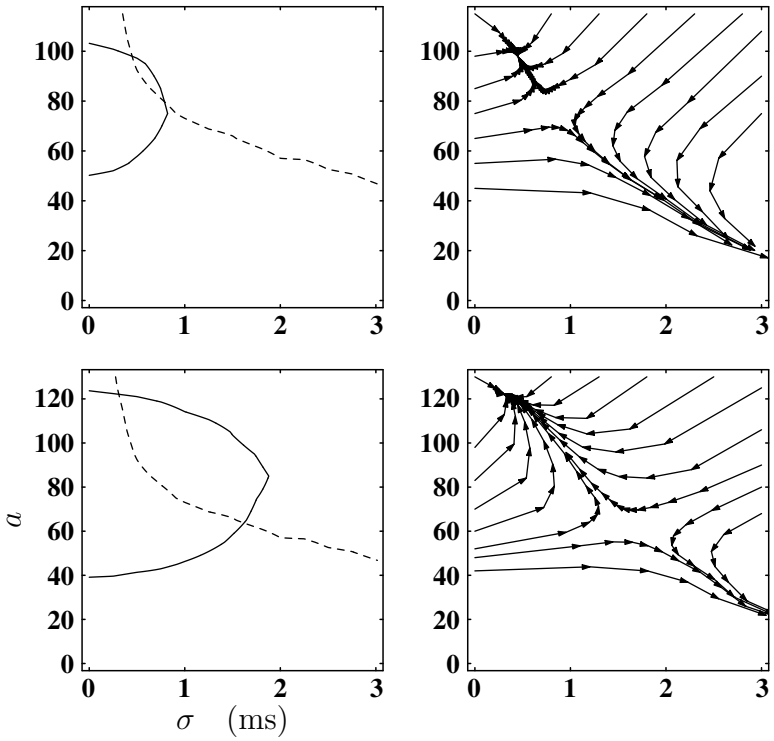

Figure 5.7 Interchangeability of bifurcation parameters σ_V and w. Isoclines (left column, graphs as in Fig. 5.4) and state space portrait (right column, graphs as in Fig. 5.3) at large membrane potential fluctuations $\sigma_V = 4.5\,\mathrm{mV}$. Number of neurons per group is $w = 115$ in the upper row and $w = 130$ in the lower row. In contrast to $w = 100$ (Fig. 5.3, lower right panel) at $w = 115$ the attractor for synchronous activity (upper intersection of isoclines) exists and the basin of attraction is increased for $w = 130$. Scaling of a-axes (vertical) different from scaling in Fig. 5.4 and Fig. 5.3.

pronounced for large a, where the activation curves approach saturation, than for smaller a, where the activation curves are steep. Therefore the attractor is moved to larger activities in the case of $\sigma_V = 4.5\,\mathrm{mV}$, compared to $\sigma_V = 3.5\,\mathrm{mV}$. The σ-isocline runs almost vertically in this regime, thus the temporal spread in the attractor is the same. The description given above still holds if the group width is further increased to $w = 130$. Now the state space structure is comparable to membrane potential fluctuations $\sigma_V = 2.5\,\mathrm{mV}$ (compare Fig. 5.7 lower right panel with Fig. 5.3 upper right panel). Again the saddle point is at a comparable location and the attractor appears at a larger activity. The interval over which the a-isocline is defined now also extends to lower a for $(\sigma_V = 4.5\,\mathrm{mV}, w = 130)$ compared to $(\sigma_V = 2.5\,\mathrm{mV}, w = 100)$.

We conclude that in a situation where the attractor for synchronous activity is lost due to large membrane potential fluctuations, stable propagation can be recovered by an increased number of neurons per group. Possible limitations of this compensation are described in Chap. 10.

Chapter 6

Vanishing Noise

In the preceding chapter we described the dependence of the structure of state space on the fluctuations of the membrane potential. When the fixpoints exist, the basin of attraction exhibits a characteristic shape. The dominant feature is the separatix, running from low activity at small temporal spread to large activity at large temporal spread, dividing the state space into the basin of attraction and the regime where activity dies out. The basin of attraction grows or shrinks, depending on the two bifurcation parameters w and σ_V we isolated. The overall shape, however, remains characteristic for the system under consideration. In the present chapter we study the case of vanishing fluctuations to uncover the origin of the shape of the separatrix. The transition to finite membrane potential fluctuations (Sec. 6.5) shows that background activity can have a constructive effect on the synchronization dynamics.

6.1 Characteristic Excursions

Vanishing background activity is a situation where the total input current a neuron receives from the network is constant. To achieve a state comparable to our model of *in vivo* fluctuations, the membrane potential should be equal to the mean of the shot-noise potential. The expression for the time course $u(t)$ of a PSP (2.3) shows that PSP amplitude scales linearly with the amplitude $\widehat{\iota}$ of the corresponding PSC. We can therefore define $\widehat{\iota}_0$ as the PSC amplitude at which the amplitude of the PSP $\widehat{u}$ equals unity

$$\widehat{\iota}_0 = \widehat{\iota} : \widehat{u}(\widehat{\iota}) = 1. \tag{6.1}$$

The resulting PSP of unit amplitude is called $\upsilon_0(t)$, where the meaning of index 0 will become clear below. Thus, the PSP can be decomposed into an amplitude factor and a function characterizing its time ourse

$$u(t) = \widehat{u} \cdot \upsilon_0(t). \tag{6.2}$$

With (2.6) it is easy to see that we can write the form factors F^1 (2.7) and F^2 (2.8) as

$$F^1 = \widehat{u} \cdot F^1_0 \tag{6.3}$$

$$F^2 = \widehat{u}^2 \cdot F^2_0, \tag{6.4}$$

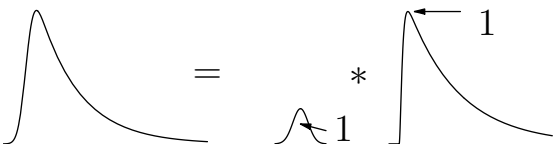

Figure 6.1 Characteristic membrane potential excursion caused by an incoming pulse packet. The characteristic excursion υ_σ (leftmost graph) is given by the convolution of a Gaussian of unit area g_σ (center graph) and a PSP of unit amplitude $u/\widehat{u}$ (rightmost graph). For a given input packet (a, σ) the actual membrane potential excursion can be computed by multiplying the characteristic excursion υ_σ with the product of the number of incoming spikes a and the amplitude of a single PSP $\widehat{u}$.

where F_0^1 and F_0^2 are the form factors of $\upsilon_0(t)$. Mean and variance of the membrane potential under shot-noise conditions are given by

$$\eta_V = K\widehat{u} \cdot \lambda F_0^1 \tag{6.5}$$

$$\sigma_V^2 = K\widehat{u}^2 \cdot \lambda F_0^2. \tag{6.6}$$

For simplicity we assume only one type of input (excitatory or inhibitory) here (see (2.12) for the full model). K is the number of inputs, and λ the firing rate of a single (input) neuron. In the limit

$$\lim_{\substack{K\to\infty \\ K\widehat{u}=c}} \sigma_V^2 = \lim_{\substack{K\to\infty \\ K\widehat{u}=c}} \frac{1}{K} c^2 \cdot \lambda F_0^2 \tag{6.7}$$

η_V is constant and the standard deviation tends to zero with $1/\sqrt{K}$, c denotes a constant equal to some intitial product $K'\widehat{u}'$. The only source of randomness that remains and would therefore become dominant at very small membrane potential fluctuations is the fact that different pulse packet realizations (with identical (a, σ)) cause different membrane potential excursions (see Sec. 10.2). However, if we assume that the synapses connecting the neurons in a synfire chain and the synapses delivering background activity are equally strong, the effect of one neuron group on the next will decrease with decreasing $\widehat{u}$. Using the same argument as for the background activity, namely that the total input should remain constant in the limit of vanishing $\widehat{u}$, we have to up-scale the group width accordingly: $w \cdot \widehat{u} = \text{const}$. Now all pulse packet realizations cause identical membrane potential excursions. Thus, using the same limit as in (6.7) in which we down-scale the amplitude of the post-synaptic potentials and hold the product of participating neurons and PSP amplitude constant, we have rendered our system completely deterministic. We call this the *limit of small PSPs*.

In this limit, evidently for a given pulse packet (a, σ) there are only two possible outcomes: either the packet potential reaches spike threshold and elicits a spike precisely at the same point in time in each trial, or it remains subthreshold and the response probability is zero. To compute the membrane potential excursion caused by an incoming pulse packet, we can now replace the sum of the post-synaptic potentials starting at individual input spike times by the convolution of a Gaussian input spike density of area a with a single PSP of amplitude $\widehat{u}$:

$$U(t) = a\,\widehat{u} \cdot (g_\sigma * \frac{1}{\widehat{u}} u)(t) \tag{6.8}$$

$$= a\,\widehat{u} \cdot (g_\sigma * \upsilon_0)(t). \tag{6.9}$$

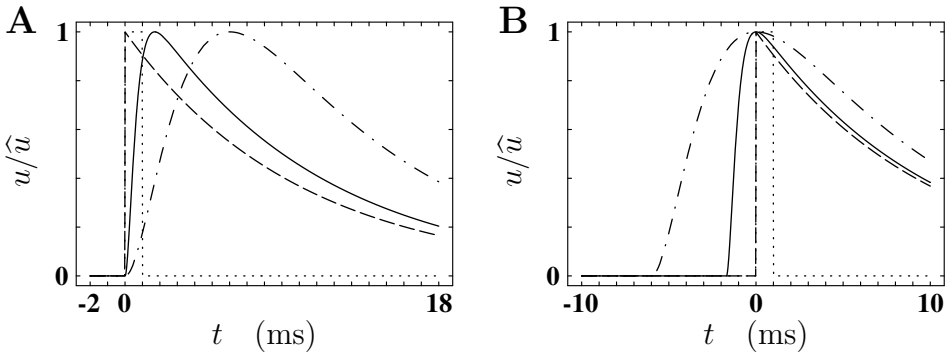

Figure 6.2 Four different post-synaptic potential shapes of unit amplitude. **A** The different shapes are aligned at the onset of the membrane potential excursion. The curves with finite rise times (solid 1.7 ms, dot-dashed 6 ms) are used as a realistic model for a PSP, the assumed post-synaptic current is an α-function $\widehat{\imath}(e/\tau_\alpha)te^{-t/\tau_\alpha}$ ($\tau_\alpha = 0.33$ ms, 1.73 ms respectively). The truncated exponential (dashed) is the limiting case of vanishing rise time. In all three cases the decay of the membrane potential excursion is dominated by a membrane time constant τ_m of 10 ms. A rectangular potential shape (dotted) of duration 1 ms is shown for comparison. **B** The same shapes aligned at their maximum.

$ag_\sigma(t)$ is the Gaussian spike density and we have substituted (6.2). Because the convolution is linear, a and $\widehat{u}$ can immediately be taken out of the integral. The remaining convolution represents the characteristic, normalized membrane potential excursion, illustrated in Fig. 6.1:

$$\upsilon_\sigma(t) = (g_\sigma * \upsilon_0)(t). \tag{6.10}$$

At vanishing temporal spread $\sigma = 0$ ms, $\upsilon_\sigma(t)$ reduces to a PSP of unit amplitude which is therefore denoted as $\upsilon_0(t)$ (cf. (6.2)). The maximum $\widehat{\upsilon}(\sigma)$ of $\upsilon_\sigma(t)$ only depends on the shape of the PSP (see example shapes in Fig. 6.2 and Chap. 2 for details of the PSP model) and σ. Therefore, the function $\widehat{\upsilon}(\sigma)$ is characteristic for a given PSP shape (see Fig. 6.3 **A**).

We now have to relate the packet potential to the spike threshold to see under which conditions a response spike is generated. Consider a situation where a certain packet potential is subthreshold. Clearly, if the membrane potential excursion is increased by an arbitrary change in the parameters of the packet potential, it will reach threshold first at its maximum value. Let $\bar{\theta}$ denote the difference in membrane potential from the mean η_V to spike threshold θ. For a given threshold the lowest number of spikes a at which the threshold is crossed is given by

$$a \cdot \widehat{u} \cdot \widehat{\upsilon}(\sigma) = \bar{\theta} \tag{6.11}$$

$$\Rightarrow a = \frac{\bar{\theta}}{\widehat{u} \cdot \widehat{\upsilon}(\sigma)}. \tag{6.12}$$

The next task is to define variables independent of a specific choice of θ. We express the membrane potential in units of the threshold value, and define u_θ as the relative input potential and u_a as the relative input strength

$$u_\theta = \frac{1}{\bar{\theta}} \cdot u \tag{6.13}$$

$$u_a = a \cdot u_\theta. \tag{6.14}$$

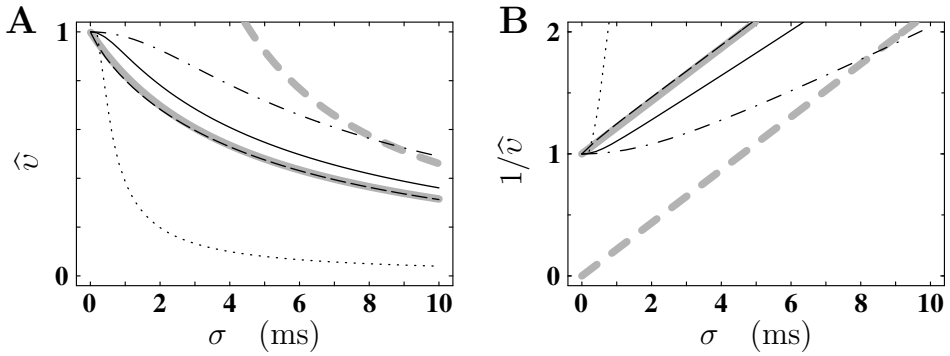

Figure 6.3 Characteristic amplitude $\widehat{v}\,(\sigma)$ **A** and minimal relative input strength $\widehat{u}_a\,(\sigma)$ **B** as a function of input spread. PSP shapes, parameters, and notation as in Fig. 6.2. **A** By definition $\widehat{v}\,(\sigma)$ is unity at full synchronization. With increasing temporal spread, the characteristic amplitude declines. Curves for finite rise time (solid, dot-dashed) approach the maximum with vanishing slope in a concave manner, the point of inflection is determined by the rise time. At a given spread, curves for larger rise time maintain a higher characteristic amplitude. After a brief plateau, the amplitude for the rectangular PSP of duration 1 ms (dotted) rapidly decays compared to the other curves (membrane time constant $\tau_m = 10$ ms). **B** By definition, $\widehat{u}_a\,(\sigma)$ is unity at full synchronization. With increasing temporal spread a larger minimal input strength is required to reach threshold. Curves for finite rise time (solid, dot-dashed) approach the minimum with vanishing slope in a convex manner. At a given spread, curves for larger rise time afford a lower relative input strength. The rectangular PSP (dotted) rapidly requires a large relative input strength. Curves in **B** simply constitute the reciprocal values of the data shown in **A**. Gray curves represent approximations (dashed (6.17) and solid (6.18) for PSP with rise-time 1.7 ms) of the σ dependence of $\widehat{v}\,(\sigma)$.

In these variables, the threshold condition reads

$$\widehat{u}_a \cdot \widehat{v}\,(\sigma) = 1 \tag{6.15}$$

and we define

$$\widehat{u}_a\,(\sigma) = \frac{1}{\widehat{v}\,(\sigma)}. \tag{6.16}$$

Thus, the minimal relative input strength needed to reach threshold is inversely proportional to the characteristic amplitude $\widehat{v}\,(\sigma)$. Fig. 6.3 **B** illustrates the relationship for different PSP shapes. For any input packet (a, σ), we can obtain from this graph whether it elicits a response spike or not, using (6.16).

For large σ, the Gaussian input distribution dominates the convolution with the post-synaptic potential. The maximum of the normalized Gaussian is $1/(\sigma\sqrt{2\pi})$. Thus, in the limit of large σ we can approximate the characteristic amplitude by

$$\widehat{v}(\sigma) \approx \frac{F_0^1}{\sqrt{2\pi}} \cdot \frac{1}{\sigma}. \tag{6.17}$$

Fig. 6.3 illustrates the approximation as the dashed gray curve in both panels. Large deviations are observed for small σ, here $\widehat{v}(\sigma)$ is dominated by the amplitude normalized PSP. A better approximation can be achieved when the divergence at $\sigma = 0$ ms is removed by addition of the appropriate constant

$$\widehat{v}(\sigma) \approx \frac{F_0^1}{\widehat{u}\sqrt{2\pi}} \cdot \left(\frac{F_0^1}{\widehat{u}\sqrt{2\pi}} + \sigma \right)^{-1}. \tag{6.18}$$

The result is shown in Fig. 6.3 as the solid gray curve in both panels. Although (6.18) well describes the overall decay of $\widehat{v}\,(\sigma)$, the plateau at small σ introduced by PSP rise-time is not captured.

In the present section we have seen that it is sufficient to consider a post-synaptic potential of unit amplitude to describe the characteristic decay of the amplitude of the packet potential with increasing input spread. When the influence of changes in PSP shape on the stability of synchronous activity is discussed in Chap. 7, we will see that we have to distinguish between amplitude and area normalization to understand the effects of the rise time of the PSP.

6.2 Transmission Function

The results obtained in the section above allow us to construct the transmission function for the case of zero noise. The neuron emits a spike if and only if the packet potential reaches threshold. There are no fluctuations in the background activity, and the packet potential is completely deterministic. Thus, the temporal spread of the output spikes is 0. If the packet potential remains subthreshold, the output spread is not defined, as there are no response spikes. However, in our simulation study at small membrane potential fluctuations we have seen that the outspread tends to zero also for small input packets (Chap. 5). To achieve a picture consistent with finite levels of noise, we define the output spread to be zero in case the input packet generates a subthreshold response and, thus, no output spike is emitted. Evidently, for the study of the synchronization dynamics the detailed position of the attrator for vanishing activity is of no importance (see Sec. 10.2 for discussion) because the system can never regain activity.

The transmission function then simply reads

$$T\big(\widehat{u}_a,\ \sigma\big) = \begin{cases} \big(1,\ 0\big), & \widehat{u}_a \cdot \widehat{v}\,(\sigma) \geq 1 \\ \big(0,\ 0\big), & \text{else} \end{cases} . \tag{6.19}$$

Fig. 6.4 displays the transmission function in our standard representation, introduced in Chap. 3. Because we use maximum relative input strength $\widehat{u}_a$ instead of a_{in} here, the graphs are independent of the specific choice of spike threshold and of the amplitude of the post-synaptic potential. The sigmoidal shape of $\alpha(a_{\text{in}})$ we observe for finite noise has now reduced to a Heaviside function. At full synchronization of the input, $\widehat{v}$ obtains its maximal value 1. Therefore, the minimal input strength at which an output spike can be genereated is unity. With increasing input spread, the transition from response probability 0 to 1 occurs at larger relative input strengths. We now understand the non-equidistant transistion points (for equidistant σ) we already observed in the simulations at finite noise (e.g. compare Fig. 5.2). The distance between transition points is determined by the characteristic amplitude $\widehat{v}\,(\sigma)$ and, hence, by the shape of the post-synaptic potential. However, σ_{out} is always 0. The arrows in the $\sigma_{\text{out}}(\sigma_{\text{in}})$ graph (Fig. 6.4B) indicate the points where for a given $\widehat{u}_a$ the spike probability drops from 1 to 0. Again, the spacing is non-equidistant because, reversing the argument, an equidistant spacing $\widehat{u}_a(\sigma)$ leads to a non-equidistant spacing of the corresponding values of σ. The spacing becomes equidistant for large σ, because $1/\widehat{v}\,(\sigma)$

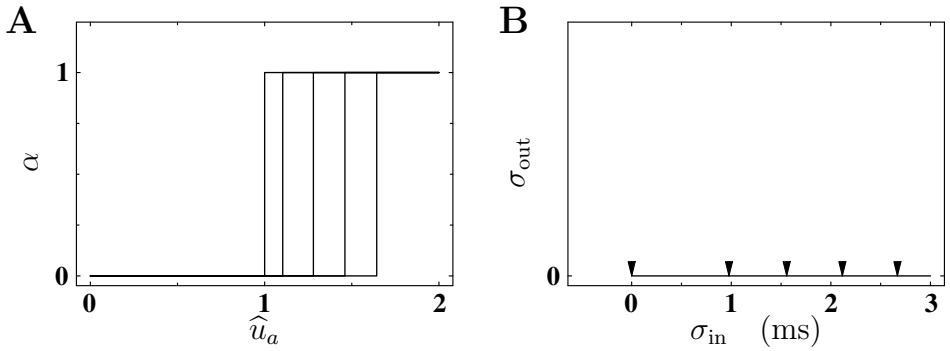

Figure 6.4 Transmission function in the noise-free case. **A** $\alpha(a_{\text{in}})$ section of the transmission function. $\widehat{u}_a$ (product of number of input spikes and amplitude of a single PSP divided by spike threshold) is used for labeling the abscissa. Depending on $\sigma_{\text{in}} = 0, 1, 2, 3, 4\,\text{ms}$ (from left to right) response probability jumps from 0 to 1 at increasing values of $\widehat{u}_a$ (here for the PSP with rise time 1.7 ms described in Fig. 6.2). **B** $\sigma_{\text{out}}(\sigma_{\text{in}})$ section of the transmission function. Output spread is 0 for supra-threshold packet potentials and defined to be also 0 for subthreshold packet potentials. Arrows indicate input spread σ_{in} at which for a given $\widehat{u}_a = 1.0, 1.1, 1.2, 1.3, 1.4$ (from left to right) the corresponding packet potential transits from the supra- to the subthreshold regime.

then approaches a straight line. (6.18) gives an estimate for the slope of $1/\widehat{v}\,(\sigma)$, see also Sec. 7.4 for the dependence on the rise-time of the PSP.

6.3 Iterative Mapping

As in the case of non-vanishing noise, we can use the transmission function (6.19) in the zero-noise case to construct an iterative mapping T_w, enabling us to study the development of activtiy in a synfire chain. The iterative mapping T_w is constructed from (6.19) by multiplying the firing probability with the number of neurons per group w:

$$T_w(a,\sigma) = \begin{cases} \big(w,\ 0\big), & a \cdot \widehat{u}_\theta \cdot \widehat{v}\,(\sigma) \geq 1 \\ \big(0,\ 0\big), & \text{else} \end{cases} . \tag{6.20}$$

Here, we used (6.14) to make the (a, σ) dependence of the threshold condition explicit. Let us now study the dynamics of this system. From an arbitrary initial state (a, σ), the system jumps into one of two possible output states $\{(w, 0), (0, 0)\}$ in one step:

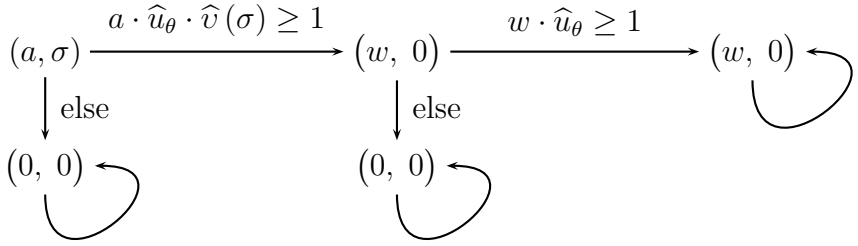

. (6.21)

In (6.21) we have for generality not assumed that $a \leq w$, as it is necessarily the case for activity inside a chain. One can imagine a situation where the first group of a chain of width

w receives input from a group of considerably more than w neurons. If (a, σ) fulfills the threshold condition, the system goes into $(w, 0)$. However, activity can only survive if also $(w, 0)$ fulfills the threshold condition $w \cdot \widehat{u}_\theta \geq 1$ ($\widehat{v}\,(0) = 1$). Clearly, stable transmission of activity is only possible if $w \cdot \widehat{u}_\theta \geq 1$. Both, $(w, 0)$ and $(0, 0)$ are fixpoints of T_w, and they both are stable. From small perturbations, the system will always return to its original state, unless the perturbation changes the result of the threshold condition from one direction or the other. We can solve the threshold condition $w \cdot \widehat{u}_\theta = 1$ for the minimal w for which stable transmission of activity is possible:

$$w_\mathrm{b} = \frac{1}{\widehat{u}_\theta} = \frac{\bar{\theta}}{\widehat{u}}. \tag{6.22}$$

Here, w_b is the chain width at which in the case of zero noise the bifurcation occurs. It is equal to the number of input spikes needed to reach threshold at full synchronization. Note, that for $w = w_\mathrm{b}$ the attractor for non-vanishing activity is only stable from one side. Any perturbation which decreases the packet potential will throw the system into the quiescent state. A discussion of the iterative map should be performed in terms of the number of spikes a. However, we have already seen that the quantity relevant for the threshold condition is the product $a \cdot \widehat{u}_\theta$. Thus, our result still depends on the amplitude of the post-synaptic potential. Using (6.14) and (6.22), we can express the number of spikes in units of the minimal group size

$$a_{w_\mathrm{b}} = a \cdot \frac{1}{w_\mathrm{b}} = \widehat{u}_a. \tag{6.23}$$

Fortunately, we can identify this value to be $\widehat{u}_a$. Thereby, we have removed the amplitude of the post-synaptic potential from the iterative map

$$T_w(a_{w_\mathrm{b}}, \sigma) = \begin{cases} (\frac{w}{w_\mathrm{b}}, 0), & a_{w_\mathrm{b}} \cdot \widehat{v}\,(\sigma) \geq 1 \\ (0, 0), & \text{else} \end{cases}. \tag{6.24}$$

6.4 Structure of State Space

Fig. 6.5 **A** illustrates the $a_\mathrm{out}(a_\mathrm{in})$ relation (in units of w_b) for a relative group width of $w/w_\mathrm{b} = 2$. This ratio is typical for a chain in which, in the presence of fluctuations, stable propagation of activity is possible, e.g. $\{\widehat{u} = 0.14\,\mathrm{mV},\ \bar{\theta} = 7\,\mathrm{mV},\ w = 100\}$. Panel **B** displays the state space of this system. The minimal relative input strength (6.16), naturally expressed in units of w_b

$$a^\mathrm{s}_{w_\mathrm{b}} = \frac{1}{\widehat{v}\,(\sigma)}, \tag{6.25}$$

is unity at $\sigma = 0\,\mathrm{ms}$, and requires larger activity with increasing input spread. Thus, $a^\mathrm{s}_{w_\mathrm{b}}$ is the separatrix. All initial activity above the separatrix reaches the attractor in one step, all activity below the separatrix vanishes in the next iteration step. We conclude that the state space structure is dominated by the shape of the post-synaptic potential. The PSP determines the border between the stable and the instable regime. The state space itself is limited to the first quadrant by the restriction of our variables to positive values. In

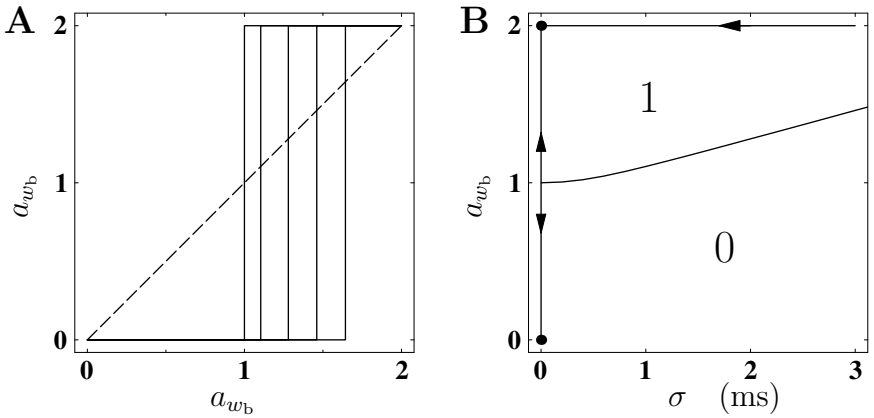

Figure 6.5 State space in the noise-free case. **A** Number of output spikes as a function of number of input spikes in units of the minimal group size w_b for a chain of width $w = 2w_\mathrm{b}$ (other parameters as in Fig. 6.4 **A**). Diagonal (dashed) for orientation. **B** (a, σ)-space (a vertical in units of w_b and σ horizontal) resulting from parameters in **A**. Black dots mark fixpoints: the attractor for synchonous activity $(2,\ 0)$ and the attracting quiescent state at $(0,\ 0)$. Minimal relative input strength $1/\widehat{v}\,(\sigma)$ (center curve) separates the basin of attraction for synchronous activity (marked "1") from the regime where activity dies out (marked "0"). The horizontal line at $a_{w_\mathrm{b}} = 2$ is the a-isocline (trivial a-isocline for $a = 0$ not considered), the vertical line at $\sigma = 0\,\mathrm{ms}$ is the σ-isocline. Arrows indicate the direction of flow. The region of state space shown is arbitrarily restricted to temporal spread below 3 ms (compare solid curve in Fig. 6.3 **B**).

addition, the number of spikes is limited by the group width, thus only the lower part of the first quadrant is accessible. The state space is open only into the direction of increasing σ. However, the basin of attraction is limited also in this direction. The shape of the PSP determines the maximal input spread from which the attractor can be reached. This value can be computed by solving (6.25) for σ at maximal group activation w/w_b:

$$\sigma_w = \widehat{v}^{\,-1}\left(\frac{w_\mathrm{b}}{w}\right). \tag{6.26}$$

For the parameters used in Fig. 6.5, the maximally allowed spread in the basin of attraction is about $\sigma_w = 6.5\,\mathrm{ms}$ (compare solid curve in Fig. 6.3 **B**). Apart from 0, w is the only allowed activity value. The activity w is kept as long as the initial state (w, σ) fulfills $\sigma \leq \sigma_w$. The σ-isocline is the vertical line from $(0, 0)$ to $(w, 0)$: temporal spread is always equal to zero. Note that for a group size of $w = 100$ we find a remarkable agreement between the basin of attraction in the noise-free case and at considerable membrane potential fluctuations (see Fig. 6.6). This effect will be explained in the next section.

6.5 Transition to Non-Vanishing Fluctations

Let us now study how the isoclines we observed at non-vanishing background activity emerge from the noise-free situation. The fact that the basin of attraction is limited to small σ already demonstrates the asymmetry of the activation curves with respect to the two limiting activity levels 0 and w. Activity level 0 can be reached from any temporal spread, whereas activity level w can only be reached from a certain σ range. We already discussed the asymmetry of the activation curves in the case of non-vanishing noise in Sec. 5.1. The

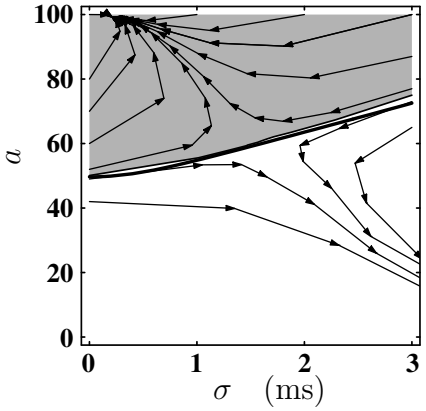

Figure 6.6 Comparison of state space structure with and without background activity. State space portrait for a group size of $w = 100$ and membrane potential fluctuations $\sigma_V = 2.5\,\mathrm{mV}$ (same data as in Fig. 5.3 upper right). The basin of attraction is shaded in gray. For comparison the separatrix in the corresponding noise-free case is shown as a thick curve (cf. Fig. 6.5 **B**).

a-isocline is constructed by undertaking a journey along the diagonal in the $(a_{\mathrm{in}}, a_{\mathrm{out}})$ graph (Fig. 6.5 **A**), and collecting the set of points (a, σ) where a is the current position on the diagonal and σ is the temporal spread of the activation curve which crosses the diagonal at this a. At zero noise all activation curves meet the diagonal at w (Fig. 6.5 **A**). However, at non-vanishing noise the activation curves do not reach $a_{\mathrm{out}} = w$ at $a_{\mathrm{in}} = w$. Instead, depending on σ_{in}, each one crosses the diagonal at a different a. The larger the temporal spread σ_{in}, the larger the input activity a_{in} at which the diagonal is crossed. Activation curves for large σ_{in} reaching threshold in the case of zero noise can now fall below the diagonal. Thus, the upper branch of the a-isocline observed at finite background fluctuations emerges from the horizontal line at $a = w$ extending from $\sigma = 0$ to the limiting temporal spread σ_w given by (6.26). With increasing σ_V, the extent into σ direction decreases, and the a-isocline is bent downwards.

Fig. 6.7 compares the activation curves in the noise-free case with the activation curves for finite membrane potential fluctuations. The curves for corresponding σ_{in}-values cross each other close to the point of inflection of the curve for finite σ_V (gray). At zero noise the transition from 0 to 100% response probability for a given σ_{in} occurs when the maximum of the packet potential reaches threshold. Thus, the point of inflection for finite σ_V is located at the number of input spikes a_{in} where in the noise-free case the packet potential reaches threshold. A simple model for this effect is introduced in Chap. 9. At the point of inflection, the response probability is about 50% for narrow input packets (small σ_{in}) and larger for broad packets. In Fig. 6.7 **A**, the group size was chosen to be $w = 100$. We have seen above that about 50 fully synchronized spikes are needed to reach threshold. At $(a_{\mathrm{in}} = 50, \sigma_{\mathrm{in}} = 0\,\mathrm{ms})$ the activation curve is at the point of inflection, and the response probability is $\alpha = 50\%$. With $a_{\mathrm{out}} = w \cdot \alpha$ we expect 50 response spikes. Thus, at full synchronization the number of output spikes equals the number of input spikes at the point of inflection. This situation is depicted in Fig. 6.7 **A**, where the diagonal intersects the activation curve for $\sigma_{\mathrm{in}} = 0\,\mathrm{ms}$ at the point of inflection. For larger σ_{in} the point of inflection falls below the diagonal. Above we discussed how with increasing σ_V, the upper branch of the

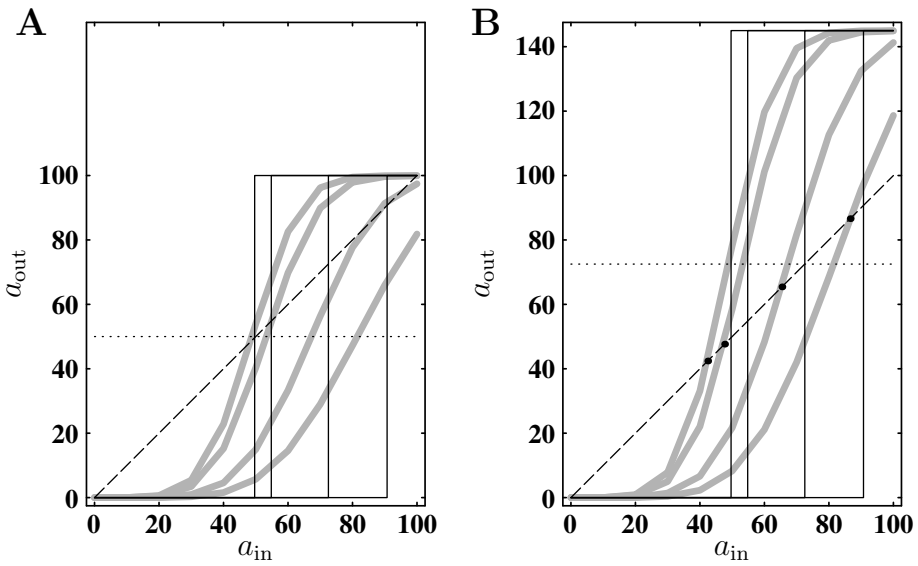

Figure 6.7 Comparison of activation curves $a_{\text{out}}(a_{\text{in}})$ for zero and non-vanishing noise. **A** Group width $w = 100$. Each set of four curves is obtained at input spreads (from left to right) $\sigma_{\text{in}} = 0, 1, 3, 5\,\text{ms}$. Black solid curves represent the noise-free case (cf. Fig. 6.4), gray curves are for membrane potential fluctuations of $\sigma_V = 2.5\,\text{mV}$ (cf. Fig. 5.2 second row). Other parameters as in Fig. 6.4 **A**. Dashed line marks the diagonal on which the number of output spikes equals the number of input spikes. Dotted horizontal line indicates the 50% response probability level. **B** Same graph as **A** for a group size of $w = 145$. Thick dots mark points where for non-vanishing noise the number of output spikes equals the number of input spikes.

a-isocline develops from a straight line at $a = w$. Now we also understand the emergence of the lower branch: The combinations $(a_{\text{in}}, \sigma_{\text{in}})$ at which the response probability jumps from 0 to 1 define the separatrix in the case of $\sigma_V = 0\,\text{mV}$. The intersections of the diagonal with the activation curves in the case of finite σ_V, however, define the a-isocline. In the discussion of Fig. 5.2 we have seen that the position of the point of inflection does not depend on σ_V. At a group size of 100, the lower branch of the a-isocline is close to the separatrix. With decreasing σ_V, it approaches the separatrix, until in the limit $\sigma_V = 0\,\text{mV}$ the two curves merge and the lower branch of the a-isocline ceases to exist. We conclude that the lower part of the a-isocline emerges from the separatrix for the noise-free case. The saddle point observed at non-vanishing σ_V is born at $\big(1,\ 0\big)$, when the activation curve obtains a finite slope at the intersection with the diagonal and, hence, allows for the existence of a fixpoint. With increasing σ_V the σ-isocline rapidly moves and bends to considerable values of σ and drags the saddle point along the a-isocline to larger temporal spread. We will come back to the properties of the temporal spread of response spikes in Chap. 9.

The group size $w = 100$ is a "magic" number in the sense that only at this value the diagonal intersects the activation curve at the point of inflection (for small σ_{in}) and, thus, makes the lower part of the a-isocline only weakly dependent on σ_V. Knowing that at the point of inflection the response probability is 50%, and using (6.22) we can write

$$w_* = 2 \cdot \frac{\bar{\theta}}{\widehat{u}} \tag{6.27}$$

as the condition for the "magic" w. This is the value used to create Fig. 6.5. We now have

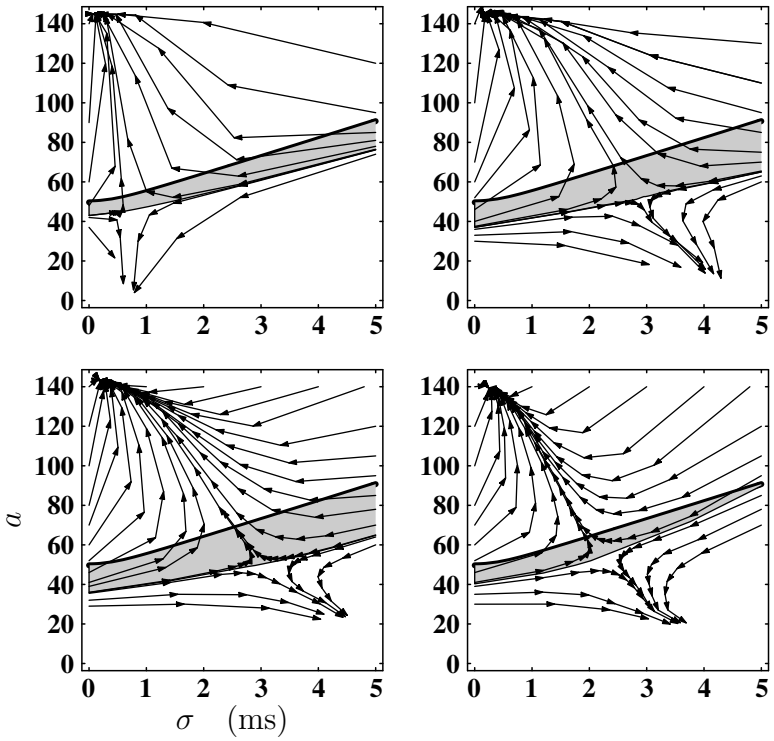

Figure 6.8 Constructive effect of background activity. State space portraits for four different levels of membrane potential fluctuations $\sigma_V = 1.5, 2.5, 3.5, 4.5\,\mathrm{mV}$ increasing from left to right and from top to bottom. Group size $w = 145$ is the same as in Fig. 6.7**B**, larger than $2w_\mathrm{b}$. The separatrix for the noise-free case is shown for comparison as a thick curve. The enlargement of the basin of attraction compared to the noise-free case is shaded in gray. With increasing σ_V, the basin of attraction first increases and then decreases again. Compare with Fig. 5.3, same data and arrangement but for $w = 100 = 2w_\mathrm{b}$.

to investigate how critical the correspondence discussed above depends on the specific choice of w. Panel **B** of Fig. 6.7 is the same graph as panel **A**, only the group size is increased to $w = 145$. Clearly, the intersection with the diagonal and the point of inflection do no longer coincide. The intersection with the diagonal now occurs already at a lower number of input spikes (dots on the activation curves in panel **B**). Hence, a larger regime of input activity is accessible for the a-isocline. However, let us assume that σ_V is continuously decreased. The activation curves become steeper and, consequently, the intersections with the diagonal approach the value where in the case of zero noise the threshold crossing occurs (intersection of dashed diagonal with solid vertical lines). Thus, for small σ_V, the a-isocline becomes independent of w. As a consequence, the a-isocline which is determined by the separatrix of the noise-free case remains characteristic for the system for group sizes which do not precisely fulfill (6.27). Essential in this argument is that the separatrix does not depend on the group size in the noise-free case (compare position of solid vertical lines in panels **A** and **B** of Fig. 6.7 and (6.25)). Increasing the group size does not extend the basin of attraction to lower number of input spikes. However, if the group size is larger than the "magic" group size w_*, finite noise can increase the extent of the a-isocline to lower numbers of input spikes. In particular, packet potentials which are subthreshold in the case of zero noise can elicit more response spikes than there are spikes in the input packet (Fig. 6.7 **B** the

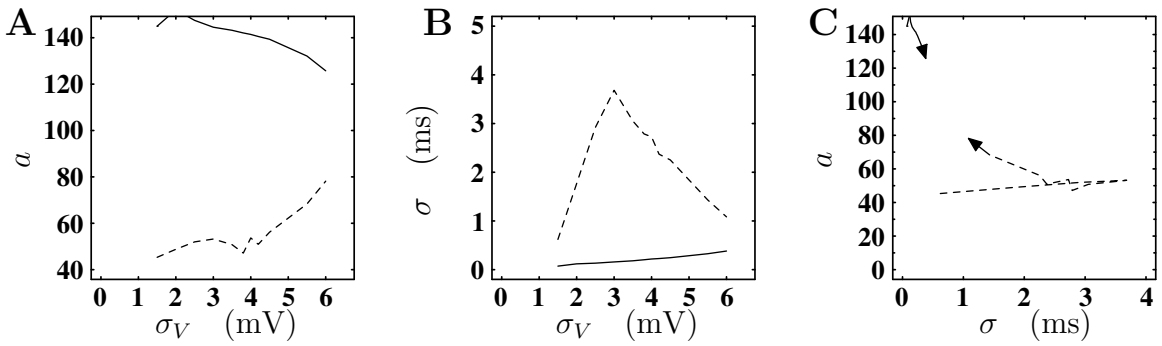

Figure 6.9 Bifurcation diagram for parameter membrane potential fluctuations σ_V at $w = 145$ (attractor: solid line, saddle: dashed line). **A** a-projection of the σ_V-bifurcation. **B** σ-projection of the σ_V-bifurcation. **C** Trace of the two fixpoints in state space in σ_V-bifurcation. With increasing membrane potential fluctuations, the attractor and saddle approach an intermediate a. Temporal spread in the attractor increases slightly. Temporal spread of the saddle increases until a maximum is reached at $\sigma_V = 3\,\mathrm{mV}$, and then shrinks again until the two fixpoints collide (point of collision not shown). Fluctuations seen in the trajectory of the saddle point at small a are due to the limited precision of the transmission function obtained from simulation data.

regime between leftmost dot on the diagonal and leftmost solid vertical line). An increase in background noise σ_V increases this regime. Therefore, an increase in noise can increase the basin of attraction. Eventually, when the noise becomes too large, the overall response probability drops, and the basin of attraction must decrease again. Already for $w = 145$ (the value used in Fig. 6.7 **B**) the effect can clearly be observed. Fig. 6.8 illustrates the increase of the basin of attraction, compared to the zero-noise case, as a function of the magnitude of the membrane potential fluctuations. We can relate this effect to an aperiodic version of *stochastic resonance*, an effect recently observed in several systems including I&F neuron models (see Sec. 10.1.5 and the corresponding references there). Note the qualitative difference between Fig. 5.3 ($w = w_*$) and Fig. 6.7 ($w > w_*$). In the first case, the basin of attraction decreases and is lost at $\sigma_V = 4.5\,\mathrm{mV}$, in the second case, the noise increases the basin of attraction, and at $\sigma_V = 4.5\,\mathrm{mV}$ it is still bigger than in the case of zero noise.

The bifurcation scenario at $w = 145$ is depicted in Fig. 6.9. Compared to Fig. 5.5, the domain covered by trajectories of the fixpoints appears enlarged in a and in σ direction. The fact that the saddle point initially stays at approximately the same a and moves out into the direction of larger temporal spread results in an increase of the basin of attraction.

Chapter 7

Rise Time of the Post-Synaptic Potential

In the preceding chapters we have studied pulse packet transmission for a fixed shape of the post-synaptic potential under the influence of different levels of membrane potential fluctuations. At a critical amount of fluctuations the system undergoes a bifurcation, beyond which the attractor for synchronous activity has vanished. However, an analysis of the noise-free case revealed that the shape of the PSP determines typical features of the structure of the state space. In particular, the separatrix depends on the decay of the amplitude of the packet potential with increasing input spread. This decay is different for different PSP shapes. The temporal spread remaining in the attractor, vanishing in the noise-free case, depends on the up-slope of the PSP. Physiological data show that the rise time of the PSP can vary, depending on the type of synapse, typical values ranging from 1 to 6 ms (e.g. Fetz, Toyama, & Smith, 1991; Mason, Nicoll, & Stratford, 1991; Matsumura et al., 1996). The down-slope is dominated by the time constant of the membrane, and is not as critically determined by the synaptic current as the rise time is. In the present chapter we investigate how the state-space structure depends on the rise time of the post-synapic potential. With increasing rise time, the attractor moves to larger temporal spread. Surprisingly, though, an increase in rise time does not necessarily destabilize the system. We demonstrate that different normalizations are appropriate in different regions of the state space. It depends on the choice of the normalization whether the PSP rise time acts as a bifurcation parameter.

7.1 Transmission Function

Let us now investigate how the transmission function for synchronous activity depends on the rise time of the post-synaptic potential. Fig. 7.1 shows the $\alpha(a_{\mathrm{in}})$ and $\sigma_{\mathrm{out}}(\sigma_{\mathrm{in}})$ sections of the transmission function introduced in Chap. 3 for four different rise times τ_0. The rise time of the PSP is adjusted by changing the time constant τ_α of the post-synaptic current using the methods introduced in Chap. 2, while holding the amplitude constant at the standard value. We first concentrate on the changes observed in the $\sigma_{\mathrm{out}}(\sigma_{\mathrm{in}})$ curves (right column). The top panel shows the result for the original rise time 1.7 ms. With increasing rise time, changes are most pronounced for highly synchronized input spikes, whereas for less

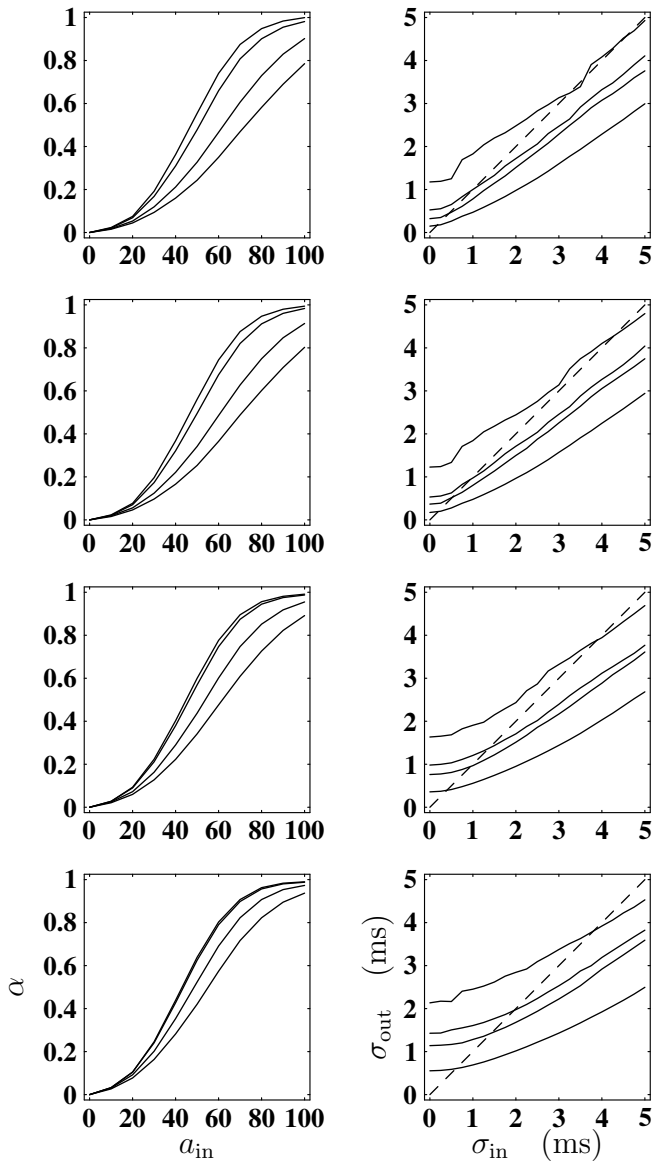

Figure 7.1 Dependence of the transmission function on the rise time of the post-synaptic potential. The rise time is increasing from top to bottom $\tau_0 = 1.7, 2.0, 4.0, 6.0\,\mathrm{ms}$ (four rows), respectively . The left column displays the $\alpha(a_{\mathrm{in}})$ section of the transmission function. In each panel, the four curves represent different constant input spread $\sigma_{\mathrm{in}} = 0, 1, 3, 5\,\mathrm{ms}$ (from left to right). The right column displays the $\sigma_{\mathrm{out}}(\sigma_{\mathrm{in}})$ section of the transmission function. The four curves represent different constant input activity $a_{\mathrm{in}} = 45, 65, 75, 115$ (from top to bottom). The dashed line indicates the diagonal. Fluctuations of membrane potential are $\sigma_V = 2.5\,\mathrm{mV}$ in all cases.

synchronized input spikes the curves remain largely unchanged. Here, the rise time of the packet potential is dominated by the Gaussian input, and the specific value of the rise time of the individual PSP has little influcence. However, the amplitude of the packet potential decreases less fast with increasing σ_{in} for larger PSP rise times (see Fig. 6.2). The effect on σ_{out} is small. It can best be observed for the bottom curve ($a_{\text{in}} = 115$). At $\sigma_{\text{in}} = 5\,\text{ms}$ (largest σ_{in} in panels), the output spread declines from 3 ms for a rise time of 1.7 ms to 2.5 ms for a rise time of 6 ms. We come back to this effect later in this chapter. For input spread below 2 ms, the transmission curves move upwards to larger temporal spread of the output spikes. The larger the rise time of the PSP, the larger the temporal spread of the response spikes. For a fixed input spread, a larger number of input spikes is required to reach the regime where the output spread is smaller than the input spread (i.e. where synchronization occurs). We discussed in Chap. 3 that a lower bound for the precision of synchronization achieved in the stationary situation is given by the intersection of the curve for the maximal number of input spikes w with the diagonal. Thus, from the sequence of panels in Fig. 7.1 we can already conclude that if the attractor for synchronous spiking exists at all, it moves to larger temporal spread with increasing rise time of the PSP. As judged from these graphs, the lower bound approximately is $\sigma = 0.3\,\text{ms}$ for a rise time of 1.7 ms, and $\sigma = 1\,\text{ms}$ for a rise time of 6 ms, in each case assuming a group size $w = 100$. Indeed, these results are in excellent agreement with the corresponding simulations (cf. Fig. 7.2).

Let us employ a relationship derived in a later chapter to give a direct interpretation of the above results. In Sec. 9.3 we introduce an approximation relating the output spread to the membrane potential fluctations and the slope of the packet potential in the case of strong input packets. Here, we can verify that this approximation gives accurate results under variation of the rise time of the PSP and, thereby, of the slope of the packet potential. In the regime $\sigma_{\text{out}} > \sigma_{\text{in}}$, the slope of the transmission curve $\sigma_{\text{out}}(\sigma_{\text{in}})$ is practically zero for strong input packets. To obtain the intersection with the diagonal for $w = 100$ we can therefore replace the rise time of the packet potential by the rise time of the PSP, and use (9.21) to compute the lower bounds:

$$\frac{1.7\,\text{ms}}{100 \cdot 0.14\,\text{mV}} \cdot 2.5\,\text{mV} = 0.30\,\text{ms} \tag{7.1}$$

$$\frac{6.0\,\text{ms}}{100 \cdot 0.14\,\text{mV}} \cdot 2.5\,\text{mV} = 1.07\,\text{ms}. \tag{7.2}$$

We now turn to the activation curves (left column in Fig. 7.1). Whereas the effect of PSP rise time on the $\sigma_{\text{out}}(\sigma_{\text{in}})$ curves (right column) is large for small σ_{in} and small for large σ_{in}, the situation is reversed for the $\alpha(a_{\text{in}})$ curves (left column). Here, the effect is small for small σ_{in} and large for large σ_{in}. The curve for $\sigma_{\text{in}} = 0\,\text{ms}$ (top curve) is essentially identical for the four PSP rise times shown. In the slow noise model (Chap. 9) we show that the response probability is mainly determined by the amplitude of the packet potential and not by its rise time. At $\sigma_{\text{in}} = 0\,\text{ms}$, however, the amplitude of the packet potential is independent of the rise time of the PSP (see Fig. 6.3). Thus, the response probability is independent of the PSP rise time. For larger input spread, however, the effect of increasing rise time is considerable. The curves for constant σ_{in} approach the limiting activation curve ($\sigma_{\text{in}} = 0\,\text{ms}$) from below. At a rise time of 6 ms (bottom panel), the activation curve for the

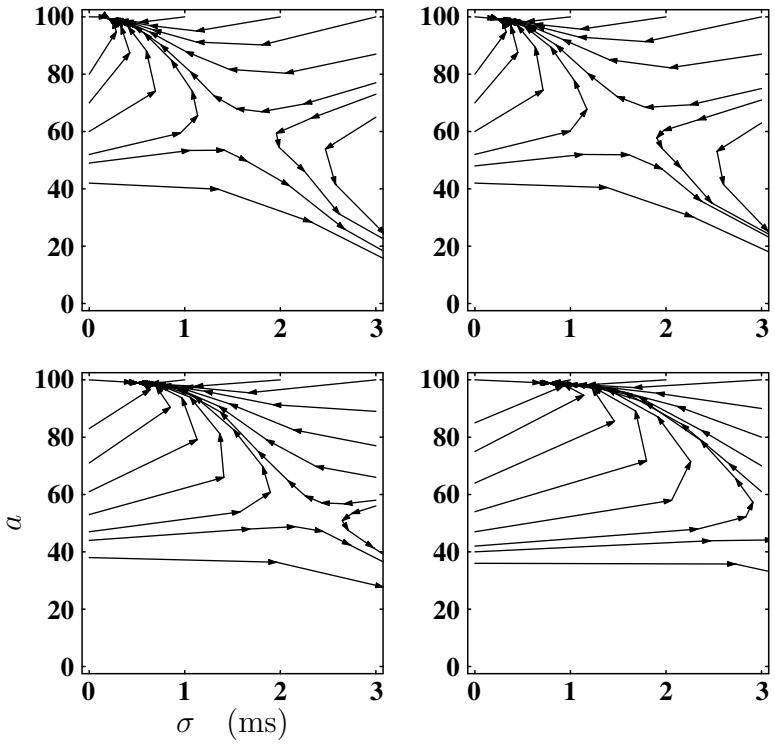

Figure 7.2 Dependence of state space structure on PSP rise time. Four portraits of (a, σ) state space (σ horizontal, a vertical). The number of neurons per group is identical in all four cases $w = 100$. Rise time of the post-synaptic potential is increasing from left to right and from top to bottom $\tau_0 = 1.7, 2.0, 4.0, 6.0\,\text{ms}$. Selected trajectories starting at the border of the displayed region of state space indicate the position of fixpoints. Arrows depict the development of activity along a chain from one neuron group to the next. No structural change occurs in the parameter range of interest.

largest input spread $\sigma_{\text{in}} = 5\,\text{ms}$ shown (bottom curve) is close to saturation at $a_{\text{in}} = 100$. Thus, as the curve for vanishing spread, it fully exhibits the sigmoidal shape in the range of available spikes in a system with 100 neurons per group. This property allows for the existence of fixpoints at much larger temporal spread compared to the situation with a rise time of 1.7 ms (top panels). Assume that the α-axis is scaled with the group size $w = 100$, then for large σ_{in} the bottom panel curves have a regime above the diagonal, whereas in the top panel they run below the diagonal. Again, we can use Fig. 6.3 to explain the effect. For $\sigma_{\text{in}} > 0$, the amplitude of the packet potential depends on the rise time of the PSP. The amplitdue decreases much slower with incresing σ_{in} for PSPs with a larger rise time.

7.2 State Space Portraits

The state space structure for a group size of $w = 100$ resulting from the transmission functions discussed above is shown in Fig. 7.2. As predicted from the transmission function, with increasing rise time the attractor moves to larger temporal spread. The activity level reached in the attractor is not impaired by the rise time. However, the prominent property of the state space portraits is that the basin of attraction is increasing in the direction of larger

temporal spread. Although the neuronal response is less precise for larger rise times, the gain in response probability due to the slower decay of packet potential amplitude leads to an increase of the basin of attraction, especially in the direction of larger temporal spread. We have seen in Fig. 5.2 that at $\sigma = 0$, the response probability is practically identical in all four cases, whereas output spread is increasing. Nevertheless, the separatrix is shifted to lower number of input spikes also for $\sigma = 0$. This is explained by the following mechanism. In the sequence of three iteration steps $(a_0, 0) \to (a_1, \sigma_1) \to (a_2, \sigma_2)$, the number of response spikes a_2 is considerably larger for larger rise times, despite the larger loss in timing precision σ_1 in the preceding step. The trajectories in Fig. 7.2 show that the number of iteration steps needed to reach the vicinity of the attractor does not change with rise time. The overall picture of the deformation of state space has the appearance of an inhomogeneous scaling of the σ-axis. This observation is in contrast with the results for the σ_V-bifurcation (Fig. 5.3). Here, increasing membrane potential fluctuations have the effect of slowing down the development of activity in the system. The different behavior under variation of the parameters σ_V and τ_0 is explained by the parameter dependence of the activation curves $a_{\text{out}}(a_{\text{in}})$. The slope of $a_{\text{out}}(a_{\text{in}})$ becomes less steep with increasing σ_V, in particular for $\sigma_{\text{in}} = 0\,\text{ms}$, limiting the change of variable a in one iteration step. Variation of τ_0 does not change the slope of $a_{\text{out}}(a_{\text{in}})$ for $\sigma_{\text{in}} = 0\,\text{ms}$, while for $\sigma_{\text{in}} > 0\,\text{ms}$ an increase in τ_0 moderately increases the slope of $a_{\text{out}}(a_{\text{in}})$.

At large rise times, the separatrix loses its dependence on σ_{in}, and bisects the state space almost horizontally (constant a). The decline in packet potential amplitude $\widehat{\nu}_\sigma$ with increasing σ is small (cf. Fig. 6.3 **A**), the activation curves $a_{\text{out}}(a_{\text{in}})$ for different σ_{in} approach the curve for $\sigma_{\text{in}} = 0\,\text{ms}$. Therefore, the position of the separatrix is mainly determined by the minimal number of input spikes needed at full synchronization to achieve a larger number of response spikes (Fig. 7.2, lower right panel).

7.3 Isoclines

The isoclines corresponding to the state space portraits in Fig. 7.2 are shown in Fig. 7.3. The origins of the two branches of the a-isocline at $\sigma = 0\,\text{ms}$ practically do not change with increasing rise time. This is explained by the fact that the activation curve for $\sigma_{\text{in}} = 0\,\text{ms}$ does not change. The maximal σ for which the number of output spikes equals the number of input spikes, however, increases with rise time. This is caused by the above discussed effect that the activation curves $a_{\text{out}}(a_{\text{in}})$ for increasing τ_0 approach the activation curve for $\sigma = 0\,\text{ms}$ and, thus, the activation curve which just touches the diagonal $a_{\text{out}} = a_{\text{in}}$ occurs at a larger σ_{in}. The behavior of the a-isocline under variation of τ_0 differs from the behavior under variation of σ_V (Fig. 5.4). While the origin of the upper branch moves to smaller a for increasing σ_V, it remains unchanged under variation of τ_0. The lower branch approaches a horizontal line for large τ_0, whereas the limiting curve in the case of σ_V depends on the shape of the PSP. Let us compare the separatrices in the two cases before we come back to the isoclines. In Sec. 6.5 we demonstrated that at $\sigma_V = 0\,\text{mV}$, the lower branch of the a-isocline coincides with the separatrix and is given by $a = (\bar{\theta}/\widehat{u})/\widehat{\nu}_\sigma$ (6.25). At large τ_0, the separatrix occurs at an almost constant a, independent of σ (a horizontal line in the state space portrait), and runs close to the lower branch of the a-isocline, even for considerable

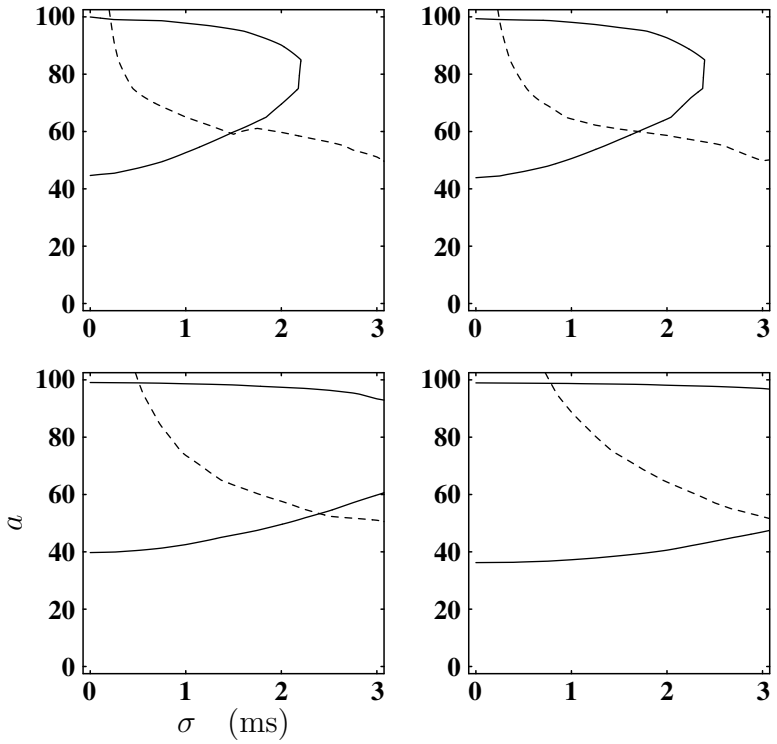

Figure 7.3 Dependence of isoclines on PSP rise time. The four panels correspond to the (a, σ) state space portraits shown in Fig. 7.2 (σ horizontal, a vertical). Rise time of the post-synaptic potential is increasing from left to right and from top to bottom $\tau_0 = 1.7, 2.0, 4.0, 6.0$ ms. The solid curve represents the a-isocline, the set of points in state space for which in the next iteration the number of spikes does not change (the loci of horizontal flow). The dashed curve is the σ-isocline, the set of points in state space for which in the next iteration the temporal spread remains unchanged (the loci of vertical flow). Fixpoints occur at the intersections of the two isoclines (no flow). As for rise times 1.7, 2.0 ms (upper left and upper right) the a-isocline is a continuous curve at 4.0 ms (lower left) and 6.0 ms (lower right); the maximal extent of the latter two curves in σ direction is not visible, due to the arbitrary restriction of the displayed region of state space to $\sigma \leq 3$ ms.

σ_V. Thus, in both cases, small σ_V and large τ_0, the lower branch of the isocline coincides with the separatrix. In the first case the activation curve $a_{\text{out}}(a_{\text{in}})$ crosses the diagonal $a_{\text{out}} = a_{\text{in}}$ at different values for a_{in}, depending on the input spread σ_{in} (isocline). If an input packet (a, σ) crosses the diagonal, the activity reaches the attractor because the temporal spread immediately vanishes (separatrix). In the second case, the activation curve crosses the diagonal at an a_{in} independent of σ_{in} (isocline). If an input packet crosses the diagonal, the activity reaches the attractor independent of the initial σ. The latter case shows that the effect of the parameter σ_V –finite, σ_{in}-dependent output spread– is rendered ineffective at large τ_0 by removing the σ-dependence of the activation curve. This is the reason why the relation between the lower branch of the a-isocline and the separatrix is the same as in the case of vanishing membrane potential fluctuations.

The σ-isocline loses its τ_0-dependence for large temporal spread (dashed curves in Fig. 7.3 have comparable values at $\sigma = 3$ ms). Here, the width of the Gaussian spike packet becomes dominant, and only the area of the post-synaptic potential enters the up-slope of the packet

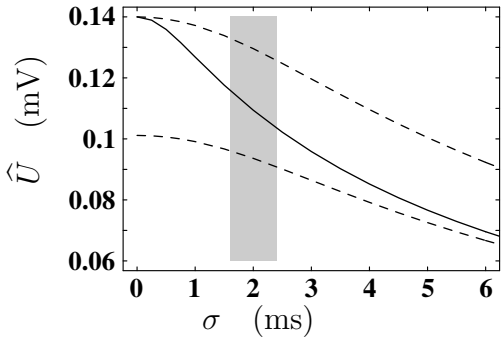

Figure 7.4 Comparison of the differential effects of normalization of amplitude and area of the post-synaptic potential on the packet potential amplitude. Packet potential amplitude as a function of input spread σ, here for an input packet of area 1. Solid curve is the result for a PSP of rise time 1.7 ms and amplitude 0.14 mV, the upper dashed curve for a rise time of 6.0 ms and identical amplitude, the lower dashed curve for rise time 6.0 ms and area identical to the case with 1.7 ms rise time. The origin of the graph is located at about half the initial amplitude (0 ms, 0.06 mV). The area shaded in gray marks the regime where the a-isocline reaches maximal extent in σ-direction at rise time 1.7 ms (Fig. 7.3, upper left panel).

potential. Compare $\sigma_{\text{out}}(\sigma_{\text{in}})$-curves for different τ_0 at large σ_{in} in Fig. 7.1. However, the spike time precision which can be reached in the attractor is strongly determined by τ_0. The invariant σ at maximal activation ($a = 100$ in Fig. 7.3) moves to larger σ for increasing τ_0.

Again, the dependence of the σ-isocline on the parameter τ_0 is qualitatively different from its dependence on the parameter σ_V (cf. Fig. 5.4). We have seen in Chap. 5 that at membrane potential fluctuations which cover a considerable portion of the up-slope, the σ-isocline depends only weakly on σ_V (compare σ-isocline between panels in Fig. 5.4). For small σ_{in}, the temporal spread of the response spikes is limited by the rise time of the post-synaptic potential. At small σ_V the σ-isocline bends strongly downwards to much smaller σ (upper left panel in Fig. 5.4) compared to our standard value $\sigma_V = 2.5$ mV.

From the comparison of Fig. 7.3 and Fig. 5.4 we can conclude that the two parameters of the dynamics τ_0, and σ_V, play different roles in different parts of the isocline. The behavior at small σ is determined by the rise time of the post-synaptic potential τ_0, the dependence on membrane potential fluctuations σ_V in this regime is comparatively small. By contrast, in the large σ regime, the position of the σ-isocline is determined by the membrane potential fluctuations, whereas the dependence on the rise time τ_0 of the PSP is comparatively small.

7.4 Normalization of PSP

In the preceding sections, the rise time of the post-synaptic potential τ_0 was treated as a parameter of the dynamics. Thus, τ_0 was varied, while holding the amplitude of the PSP constant. Using this parameterization, the area of the PSP necessarily increases with increasing rise time.

Ultimately, the rise time of the packet potential and its amplitude determine the response to an incoming pulse packet. At small σ, the amplitude of the packet potential is mainly determined by the amplitude of the PSP. However, at large σ the amplitude of the packet potential is determined by the area of the PSP. In the convolution of the PSP with the broad

Gaussian input packet, the shape of the PSP becomes irrelevant, and only its "mass" enters the resulting membrane potential time course.

To disentangle the role of the rise time of the post-synaptic potential and the PSP area, we have to study the effects of rise time under normalization of PSP area, and compare the resulting state space structure with the results obtained earlier under normalization of PSP amplitude.

Fig. 7.4 shows the decline of packet potential amplitude with increasing temporal spread of the input packet. The solid curve represents the result for our standard PSP with rise time 1.7 ms. The upper dashed curve shows the result for a PSP with $\tau_0 = 6$ ms normalized to the same amplitude (0.14 mV). Here we assumed that the packet potential is a deterministic function, resulting from the convolution of a single PSP with a Gaussian pulse density distribution (see Chap. 6 and Fig. 6.3 **A**). The area of the pulse density was assumed to be unity for this graph. For large σ, the PSP with larger rise time maintains a considerably larger amplitude of the packet potential. By contrast, the lower dashed curve shows the result for a PSP with rise time 6 ms (identical to upper dashed curve) with an area identical to the area of the PSP with rise time 1.7 ms (solid curve). Thus, area normalization forces the amplitude of the PSP to be lower when the rise time (temporal extent) is increased, most prominently at $\sigma = 0$ ms. As expected, at large σ the amplitudes of the packet potentials for $\tau_0 = 1.7$ ms and $\tau_0 = 6$ ms approach each other (solid curve and lower dashed curve). Fig. 7.4 exemplifies that amplitude normalization of the PSP renders the packet potentials comparable at small σ, whereas area normalization allows comparison at large σ.

The task now is to investigate the change in state space structure for area normalized PSPs. Fortunately, it turns out that the transmission function can be obtained by appropriate scaling of the transmission function for amplitude normalized PSPs.

Let $u_1(t)$, $u_2(t)$ be PSP shapes for two different rise times (τ_{10} and τ_{20}) and identical amplitudes ($\widehat{u}_1 = \widehat{u}_2$). From (6.9) we know that we can write the packet potential as

$$U_2(t) = a \cdot (g_\sigma * u_2)(t). \tag{7.3}$$

In Chap. 2 we denoted the area of the PSP by a form factor F^1

$$F_i^1 = \int_{-\infty}^{\infty} u_i(t)\, dt. \tag{7.4}$$

Therefore, the packet potential for rise time τ_{20} with PSP area identical to the case τ_{10} is

$$U_2(t) = a \cdot (g_\sigma * \frac{F_1^1}{F_2^1} u_2)(t) \tag{7.5}$$

$$= \frac{F_1^1}{F_2^1} a \cdot (g_\sigma * u_2)(t). \tag{7.6}$$

Obviously, PSP area can be compensated by the number of input spikes a. Let $T_2(a, \sigma)$ be the transmission function for an amplitude normalized PSP of rise time τ_{20}, as obtained in Sec. 7.1. The corresponding mapping for an area normalized PSP then is

$$(a_{\text{out}}, \sigma_{\text{out}}) = T_{2w}(\frac{F_1^1}{F_2^1} \cdot a_{\text{in}}, \sigma_{\text{in}}), \tag{7.7}$$

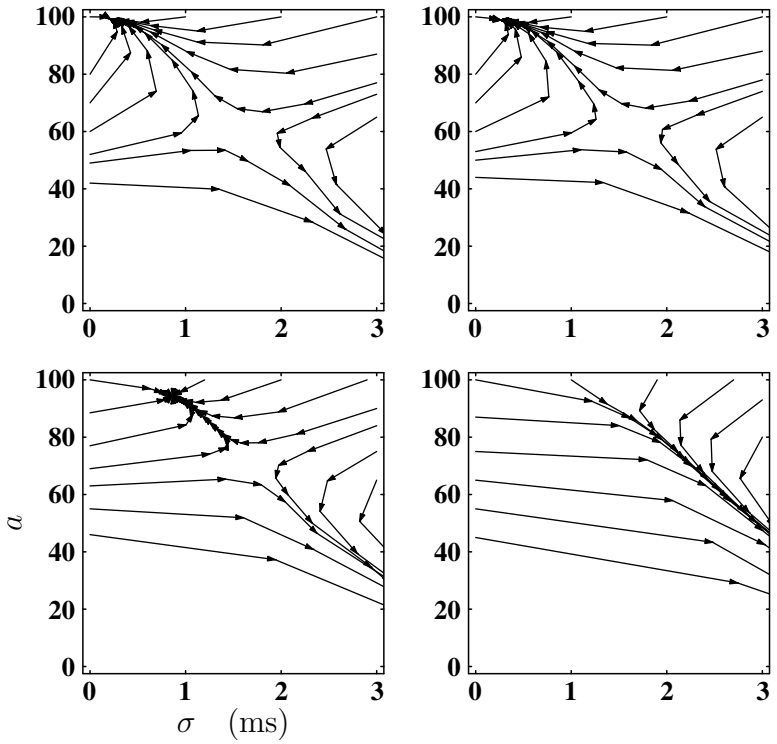

Figure 7.5 Dependence of state space structure on PSP rise time for PSPs with identical area. Four portraits of (a, σ) state space (σ horizontal, a vertical). The number of neurons per group is identical in all four cases ($w = 100$). Rise time of the post-synaptic potential is increasing from left to right and from top to bottom $\tau_0 = 1.7, 2.0, 4.0, 6.0$ ms. Selected trajectories starting at the border of the displayed region of state space indicate the position of fixpoints. Arrows depict the development of activity along a chain from one neuron group to the next. A structural change occurs between rise times 4.0 ms and 6.0 mV: the two fixpoints, present in the first three portraits, disappear.

with $F_1^1/F_2^1 < 1$ if $\tau_{10} < \tau_{20}$. Note, that in contrast to the w-scaling (Sec. 4.1), which operates on the α component i.e. the output of the transmission function, the present scaling operates on one of the arguments of the transmission function. Thus, it affects both the $a_{\text{out}}(a_{\text{in}})$ and the $\sigma_{\text{out}}(\sigma_{\text{in}})$ section of the transmission function.

Fig. 7.5 displays the state space portraits resulting from the area normalized transmission function (7.7). Other parameters are identical to the amplitude normalized version (Fig. 7.2). Observe that the development of the state space structure with increasing rise time has changed qualitatively. Now, the two fixpoints approach each other with increasing rise time of the PSP. The saddle point remains approximately stationary, while the attractor moves to larger temporal spread and lower activity levels. Between $\tau_0 = 4$ ms (lower left) and $\tau_0 = 6$ ms (lower right) the two fixpoints disappear and stable propagation of synchronous activity is no longer possible. The overall picture is similar to the σ_V-bifurcation Fig. 5.3. However, the trench along which the (a, σ)-packets travel towards extinction is now located at larger temporal spread, particularly for high values of a. As already observed in Fig. 7.2, the development of activity in (a, σ)-space appears to be more rapid at larger rise times, because larger distances in σ-direction are covered by one iteration step. In terms of the number of iteration steps needed to reach equivalent regions in state space, the situation is

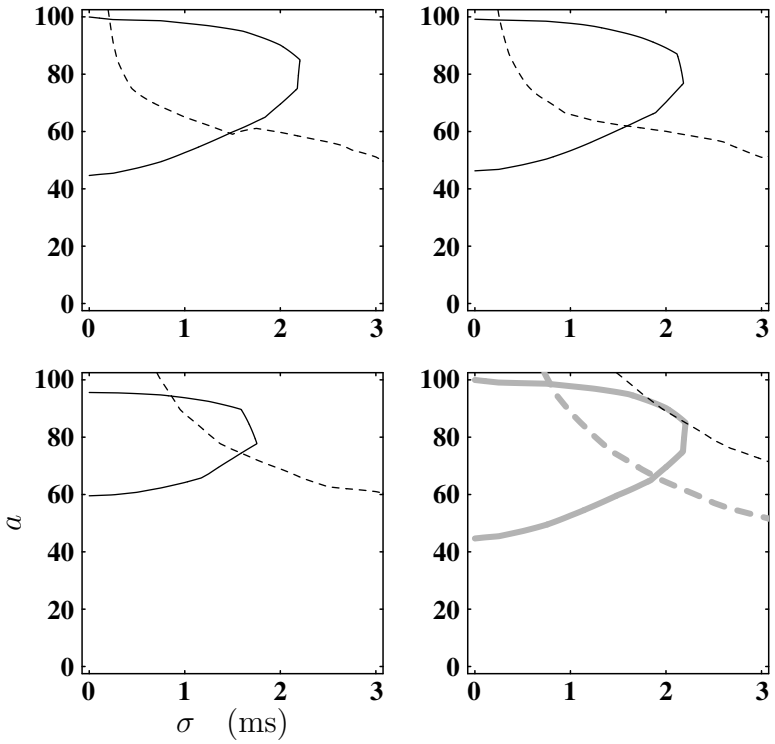

Figure 7.6 Dependence of isoclines on PSP rise time for PSPs with identical area. The four panels correspond to the (a, σ) state space portraits shown in Fig. 7.2 (σ horizontal, a vertical). Rise time of the post-synaptic potential is increasing from left to right and from top to bottom $\tau_0 = 1.7, 2.0, 4.0, 6.0$ ms. The solid curve represents the a-isocline, the dashed curve is the σ-isocline. Fixpoints occur at the intersections of the two isoclines (no flow). At rise time 6.0 ms (lower right) the number of response spikes a_{out} is always smaller than a_{in}, therefore no a-isocline exists. The solid gray curve is the a-isocline for unchanged packet potential amplitude, compared to a rise time of 1.7 ms (copied from upper left panel). The dashed gray curve is the σ-isocline obtained under normalization of PSP amplitude (copied from Fig. 7.3, lower right panel).

comparable to the w-bifurcation at the same magnitude of membrane potential fluctuations Fig. 4.7.

Comparison of the isoclines between the two normalization schemes (Fig. 7.6 and Fig. 7.3) confirms that the behavior of the system under variation of parameter τ_0 has changed dramatically. The additional factor in the transmission function (7.7) leads to a relabeling of the curves for constant a in the $\sigma_{\text{out}}(\sigma_{\text{in}})$ sections of the transmission functions in Fig. 7.1 (right column). A $\sigma_{\text{out}}(\sigma_{\text{in}})$ curve for a specific constant $a_{\text{in}\widehat{u}}$ under amplitude normalization now describes the system for an $a_{\text{in}F^1}$ under area normalization

$$a_{\text{in}F^1} = \left(\frac{F_1^1}{F_2^1}\right)^{-1} \cdot a_{\text{in}\widehat{u}}. \tag{7.8}$$

Note that $a_{\text{in}F^1}$ is increasing with increasing rise time of the PSP. Thus, the σ-isoclines under area normalization result from the σ-isoclines under amplitude normalization by a scaling with $(F_1^1/F_2^1)^{-1}$ in a-direction (compare dashed curves in Fig. 7.6 and Fig. 7.3, lower rows). As a result the σ-isocline is located at larger values of a. For the $a_{\text{out}}(a_{\text{in}})$ section of the iterative mapping (Fig. 7.1, left column with w-scaled ordinate $a_{\text{out}} = w\alpha$), area

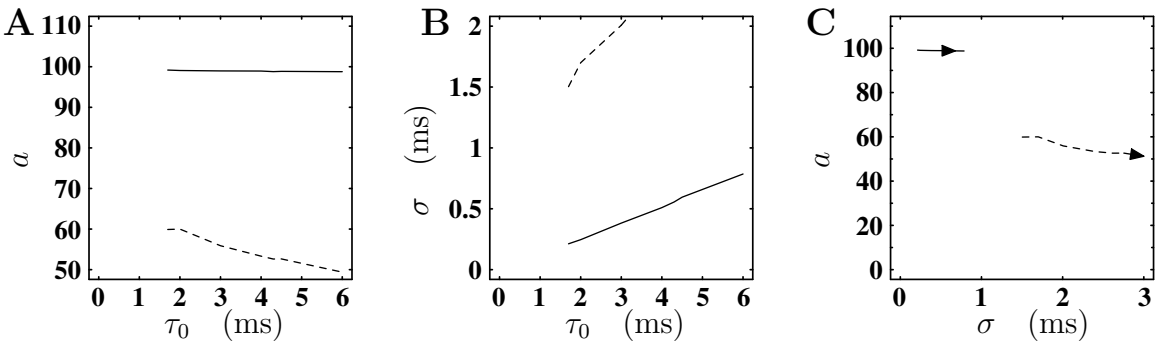

Figure 7.7 Bifurcation diagram for the parameter PSP rise time τ_0 under amplitude normalization of the PSP (attractor: solid line, saddle: dashed line). **A** a-projection of the τ_0-bifurcation. **B** σ-projection of the τ_0-bifurcation. **C** Trace of the two fixpoints in state space in τ_0-bifurcation. While the a coordinate of the fixpoints remains approximately constant, both move to larger temporal spread (horizontally, left to right).

normalization results in a scaling of the a_{in}-axis. High response probabilities are reached only for a larger number of input spikes. Consequently, for a given number of neurons w available, a smaller part of the activation curve lies above the diagonal in the $a_{\text{out}}(a_{\text{in}})$ representation. It is important to point out that the above statement also holds for full synchronization of the input ($\sigma_{\text{in}} = 0\,\text{ms}$). The scaling of the argument in $a_{\text{out}}(a_{\text{in}})$ translates to a change in the a-isocline (Fig. 7.6, solid curves). The onsets of the two branches of the a-isocline at $\sigma = 0\,\text{ms}$ are given by the intersections of $a_{\text{out}}(a_{\text{in}})$ with the diagonal at $\sigma = 0\,\text{ms}$. Thus, for increasing rise time the two onsets approach each other, the lower bound moving upwards, the upper bound moving downwards. Under amplitude normalization, the onsets of the a-isocline remained approximately unchanged. For large σ, the shrinkage of the a-isocline compared to the situation obtained under amplitude normalization is most prominent. However, at large σ the amplitude of the packet potential becomes independent of PSP rise time, if area normalization is applied (compare Fig. 7.4 solid and lower dashed curves). Therefore, for large σ we expect the a-isocline to remain unchanged, compared to the original rise time (upper left panel in Fig. 7.6). Fig. 7.6 clearly demonstrates that this is not the case. In the critical σ-regime, where the maximal extent of the a-isocline into σ direction is located (at original τ_0), the decline in packet potential amplitude is still considerable (gray shaded regime in Fig. 7.4). At those σ values where the packet potential amplitude for $\tau_0 = 6\,\text{ms}$ becomes indistinguishable from the corresponding value for $\tau_0 = 1.7\,\text{ms}$, the a-isocline has already vanished. Thus, the a-isocline shrinks with increasing τ_0 to lower σ, also in comparison to the original rise time. The bifurcation observed in Fig. 7.5 is caused by both effects: shrinkage of the a-isocline with respect to σ, and movement of the σ-isocline to larger a. The contribution of the change in σ-isocline to the τ_0-bifurcation is more pronounced than in the σ_V-bifurcation (Fig. 5.4).

The bifurcation scenarios of the two normalization schemes are summarized in Fig. 7.7 and Fig. 7.8. The construction of the diagrams is the same as we used for the w-bifurcation (Fig. 4.8).

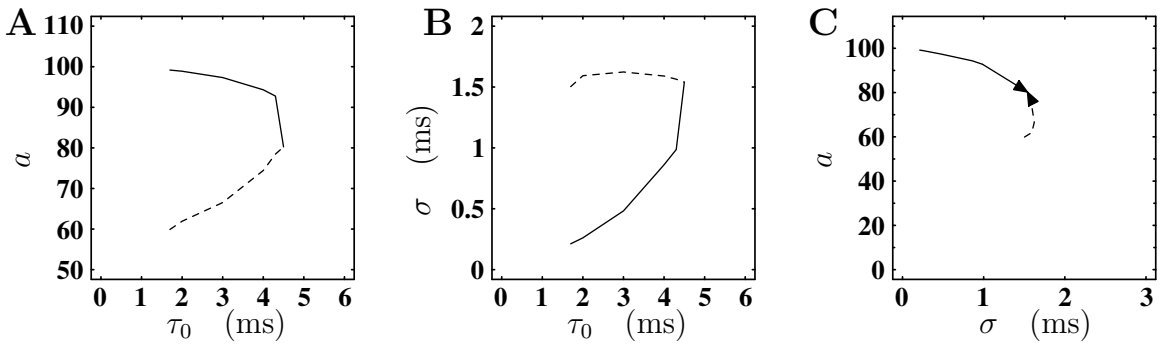

Figure 7.8 Bifurcation diagram for the parameter PSP rise time τ_0 under area normalization of the PSP (attractor: solid line, saddle: dashed line). **A** a-projection of the τ_0-bifurcation. **B** σ-projection of the τ_0-bifurcation. **C** Trace of the two fixpoints in state space in τ_0-bifurcation. Attractor and saddle approach an intermediate a. The temporal spread σ of the saddle remains approximately constant, whereas the temporal spread in the attractor grows, until the two fixpoints collide and vanish.

7.5 Packet Potential Normalization

We have shown above that the activation curves $a_{\text{out}}(a_{\text{in}})$ primarily depend on the development of the packet potential amplitude. Thus, in an ideal compensation for an increased rise time, the amplitude of the packet potential remains identical to the amplitude at the original rise time τ_{10} for all σ_{in} the a-isocline should remain unchanged under variation of τ_0. In this situation, the τ_0-bifurcation is purely caused by the change in the σ-isocline (influence on output spread). This is in contrast to the w-bifurcation, where the change in state space structure is caused purely by a change in the a-isocline.

Similar to (7.6), we can obtain appropriate packet potentials by the following normalization

$$U_2(t) = \frac{\widehat{U}_1(\sigma)}{\widehat{U}_2(\sigma)} a \cdot (g_\sigma * u_2)(t), \tag{7.9}$$

with $\widehat{U}_i(\sigma)$ representing the maximum of the packet potential for rise time τ_{i0}. Again rescaling of one argument is sufficient to obtain the corresponding mapping from the transmission function computed for amplitude normalized PSPs:

$$(a_{\text{out}}, \sigma_{\text{out}}) = T_{2w}(\frac{\widehat{U}_1(\sigma_{\text{in}})}{\widehat{U}_2(\sigma_{\text{in}})} \cdot a_{\text{in}}, \sigma_{\text{in}}). \tag{7.10}$$

The lower right panel in Fig. 7.6 includes the a-isocline at the original rise time as the solid gray curve. This is the a-isocline as it would be maintained under normalization of the amplitude of the packet potential. The dashed gray curve in the same panel is the σ-isocline obtained under normalization of PSP amplitude at the corresponding rise time ($\tau_0 = 6\,\text{ms}$). Because the solid curve in Fig. 7.4 ($\tau_0 = 1.7\,\text{ms}$) runs between the two dashed curves ($\tau_0 = 6\,\text{ms}$), the σ-isocline for (7.10) would run between the dashed black curve and the dashed gray curve in Fig. 7.6, lower right panel. Thus, under normalization of the packet potential amplitude, the fixpoints still exist at $\tau_0 = 6\,\text{ms}$. The σ-isocline intersects the a-isocline (solid gray curve) somewhere between the dashed black curve and the dashed gray

curve. However, at larger τ_0 the bifurcation will occur (not shown), because the σ-isocline moves upwards and the a-isocline remains stationary. The scaling introduced in (7.10) is qualitatively different from the scaling used in (7.7), since in (7.10) the scaling factor itself depends on the temporal spread of the input packet σ_{in}.

A biophysical interpretation of such scaling would be that the amplitude of individual post-synaptic potentials depends on the temporal spread in the input packet. Large amplitude for high synchronization, and low amplitude at large dispersion. In order to explain (7.10) the magnitude of the effect would have to increase with the rise time of the PSP. Spikes in a pulse packet are arriving at individual synapses of the (post-synaptic) target neuron. Hence, a specific type of interaction between synaptic currents, outside the scope of the model discussed in the present work, would be necessary. A simple example for the presence of such interaction is the fact that synaptic conductances affect the integration properties of the membrane (e.g. Wilson, 1995; Contreras, Timofeev, & Steriade, 1996) and thus, the resulting membrane potential excursions. However, the primary motivation to consider a dynamic normalization (7.10) is not to provide a realistic setting for comparison of PSPs with different rise times, but to disentangle the effects of PSP rise time and packet potential amplitude.

In summary: the PSP rise time governs the spike timing precision reached in the attractor. τ_0 controls the magnitude of the temporal spread of the response spikes in $\sigma_{\text{out}}(\sigma_{\text{in}})$ and operates on the σ-isocline, whereas w controls the number of response spikes in $a_{\text{out}}(a_{\text{in}})$ and operates on the a-isocline. σ_V controls the shape of $a_{\text{out}}(a_{\text{in}})$ and $\sigma_{\text{out}}(\sigma_{\text{in}})$, determining the curvature of the a-isocline and the σ-isocline. The alternative approach of using packet potential amplitude and rise time instead of (a, σ) as variables to describe pulse packet dynamics is discussed in Chap. 10.

Chapter 8

Amplitude of the Post-Synaptic Potential

In Chap. 4 we constructed a deterministic iterative mapping to describe the propagation of synchronous spiking activity in a feed-forward network. The analysis is based on the idea of treating the expected number of spikes emitted by each neuron group as a dynamic variable, defining the state of the system. In Chap. 6 we argued that at full synchronization the packet potential is simply given by the shape of a single post-synaptic potential (PSP) multiplied by a factor $w\alpha$. Thus, in our parameterization of the PSP, the amplitude of the packet potential depends on the product of the expected number of spikes and the unit PSP amplitude $(w\alpha) \cdot \widehat{u}$. Here, a smaller number of neurons per group can be compensated for by a larger amplitude of the individual PSP. This property is of relevance because for a fixed $\widehat{u}$, the group size w is a bifurcation parameter of the system (Chap. 4) and anatomical considerations may restrict the available range of w (Chap. 10).

Using the above scaling property, the relative contribution of individual synapses to the total membrane potential excursion increases with decreasing group size. In the present chapter we investigate the effect of PSP amplitude on the propagation of synchronous activity. It turns out that fluctuations in the activity of a neuron group increase with increasing PSP amplitude. While the system behaves deterministically for small PSP amplitudes, justifying the deterministic iterative mapping, increasing variability is exhibited at larger amplitudes. However, reliable transmission of synchronous activity is possible even if PSP amplitudes need to be increased by an order of magnitude compared to our standard situation (Chap. 4). Thus, PSP amplitudes suitable for stable propagation of synchronous spiking largely cover the physiologically available range.

The methods, developed in the present chapter for the analysis of PSP amplitude, allow for an extension of the deterministic iterative mapping to a stochastic mapping which may be utilized to describe the variability observed in simulations of the corresponding neuronal network structures.

8.1 Relative Group Activation

Given an input configuration $(a_{\text{in}}, \sigma_{\text{in}})$, the probability α for each neuron in a group receiving that input to generate a response spike is, as defined in (3.3), given by

$$(\alpha, \sigma_{\text{out}}) = (\alpha(a_{\text{in}}, \sigma_{\text{in}}), \sigma_{\text{out}}(a_{\text{in}}, \sigma_{\text{in}})) = T(a_{\text{in}}, \sigma_{\text{in}}). \tag{8.1}$$

Considering a group of w neurons, the probability that exactly k response spikes are generated is $\alpha^k(1-\alpha)^{w-k}$ times the number of ways to choose a subset of k elements out of a set of w elements. This is the binomial distribution

$$\mathcal{B}_{w,\alpha}(k) = \binom{w}{k}\alpha^k(1-\alpha)^{w-k}. \tag{8.2}$$

Thus, the number of response spikes is a random variable

$$B_w[\alpha] \sim \mathcal{B}_{w,\alpha}(k). \tag{8.3}$$

The expectation value of (8.2) is $w\alpha$. Use of this expectation value allowed us in Chap. 4 to transform the single neuron transmission function into an iterative mapping (4.1) for the entire group $T \to T_w$:

$$(a_{i+1}, \sigma_{i+1}) = (w\alpha(a_i, \sigma_i), \sigma_{\text{out}}(a_i, \sigma_i)) = T_w(a_i, \sigma_i). \tag{8.4}$$

This mapping describes the dynamics of mean activity along a chain.

Exploiting the scaling property of packet potentials (6.9), let us now assume that the transmission function T_1 obtained for a specific PSP amplitude $\widehat{u}_1$ can be used to construct the transmission function T_2 valid for a new PSP amplitude $\widehat{u}_2$

$$T_2(a_{\text{in}}, \sigma_{\text{in}}) = T_1(\frac{\widehat{u}_2}{\widehat{u}_1}a_{\text{in}}, \sigma_{\text{in}}). \tag{8.5}$$

Consequently, the response obtained in the mean for an input packet (a_2, σ) with PSP amplitude $\widehat{u}_2$ is identical to the response to (a_1, σ) with amplitude $\widehat{u}_1$ if we have the following relation

$$a_2\widehat{u}_2 = a_1\widehat{u}_1. \tag{8.6}$$

Thus, in two synfire chains constructed with PSP amplitudes $\widehat{u}_1$ and $\widehat{u}_2$, respectively, we expect according to the above scaling-law the same dynamic behavior if

$$w_2\widehat{u}_2 = w_1\widehat{u}_1. \tag{8.7}$$

In order to be able to compare the variable a of the dynamics in both cases, we introduce the relative group activation

$$\tilde{a} = \frac{1}{w}a. \tag{8.8}$$

Relating (8.8) and (8.4), we observe that the expectation value of $\tilde{a}$ is nothing but the single neuron spike probability α.

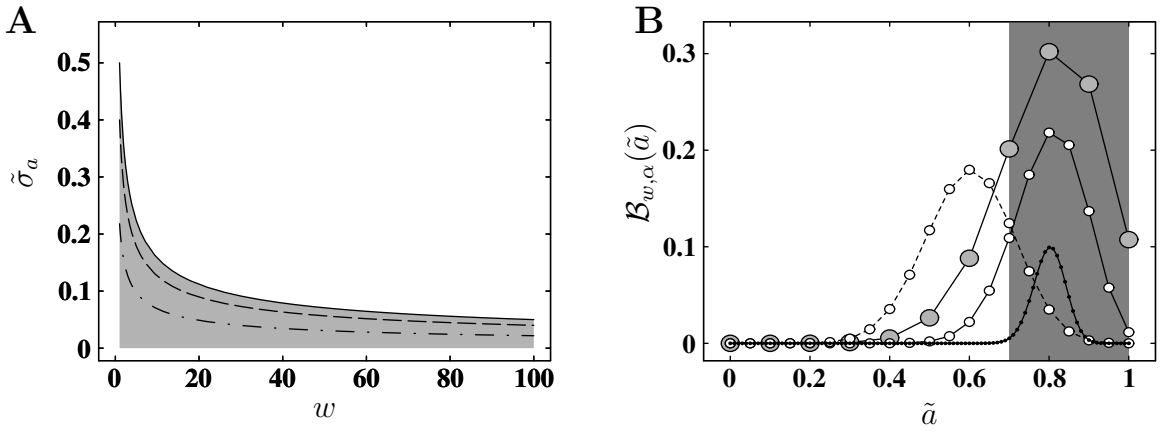

Figure 8.1 Variability in the number of response spikes of a neuron group. **A** Relative variability $\tilde{\sigma}_a$ as a function of the number of neurons per group (group size) w for different response probabilities α (solid 0.5, dashed 0.8, dot-dashed 0.95). $\tilde{\sigma}_a$ is the standard deviation of the number of spikes divided by the maximal number of spikes w. Maximum variability occurs at a response probability α of 0.5 (gray area indicates allowed values of $\tilde{\sigma}_a$). **B** Distribution of relative group activation $\mathcal{B}_{w,\alpha}(\tilde{a})$ for different group sizes w. $\tilde{a}$ is the number of response spikes divided by the maximal number of response spikes w. For a given response probability ($\alpha = 0.8$, disks connected by solid lines) distributions for different w (black disks 100, white disks 20, gray disks 10) have identical expectation values equal to α. The number of support points $w + 1$ decreases with group size. Distribution for $w = 20$ and $\alpha = 0.6$ (disks connected by dashed lines) shown for comparison. Assuming a threshold activation of $\tilde{\theta} = 0.7$, the dark gray region indicates the part of the distributions in which the number of spikes suffices for the survival of activity. Whereas for $w = 100$ the full distribution is in this regime, for $w = 20$ and $w = 10$ considerable parts are outside.

The variance of the number of response spikes from realization to realization is then given by the variance of the binomial distribution (8.2)

$$\sigma_a^2 = w\alpha(1-\alpha). \tag{8.9}$$

The standard deviation σ_a is a measure for the uncertainty in the number of response spikes. Hence, for a fixed spike probability α, the uncertainty in the number of response spikes increases with $\sqrt{w}$.

However, σ_a is still expressed in the absolute number of response spikes. Therefore, we define $\tilde{\sigma}_a = \frac{1}{w}\sigma_a$ as the standard deviation of the relative group activation

$$\tilde{\sigma}_a = \frac{1}{w}\sqrt{w} \cdot \sqrt{\alpha(1-\alpha)} \tag{8.10}$$

$$= \frac{1}{\sqrt{w}} \cdot \sqrt{\alpha(1-\alpha)}. \tag{8.11}$$

Although the variability measured in absolute spike number increases with $\sqrt{w}$, the variability of the relative group activation decreases with $1/\sqrt{w}$. Thus, (8.11) resolves the apparent contradiction between the fact that the variance of the binomial distribution increases with the size of the set, and the intuition that the response of a larger group of neurons, with each unit carrying only little weight, should show less variability than a smaller group.

We can restate this surprising result as a general property of the binomial distribution. Given n bins with individual occupation probability p. The number of bins occupied in the

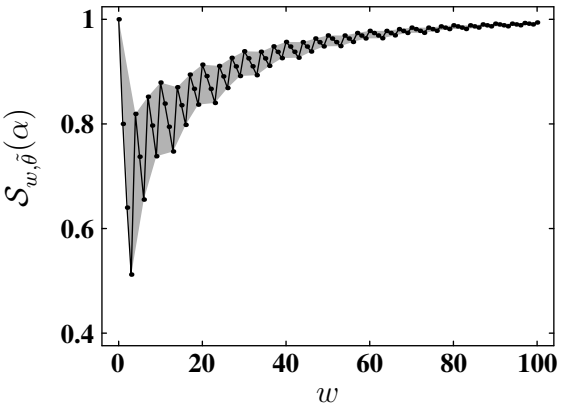

Figure 8.2 Survival probability as a function of group size w for a given response probability $\alpha = 0.8$ and threshold $\tilde{\theta} = 0.7$. The survival probability at a particular w is indicated by a dot. In addition values for consecutive w are connected by a black line, demonstrating a saw-tooth like pattern. The upper boundary of the gray area connects the local maxima in survival probability, the lower boundary connects the local minima.

mean is np, and the variance of this number is $np(1-p)$. However, if the n bins are viewed as partitioning the unit interval $[0, 1]$, the fraction of the interval occupied in the mean is p and the variance of this number is $\frac{1}{n}p(1-p)$.

Fig. 8.1 **A** shows the variability of the relative group activation as a function of the number of neurons per group for three different response probabilities. The hyperbolic decline of variability with increasing group size is clearly visible. Note that for a given group size w, there is an upper bound on relative variability given by $1/(2\sqrt{w})$. Since the distribution of relative group activation is defined on a finite carrier $[0, 1]$, variability vanishes for $\alpha \to 0$ as well as for $\alpha \to 1$ and reaches a maximum at $\alpha = 1/2$. The gray area in Fig. 8.1 **A** indicates the regime of values $\tilde{\sigma}_a$ can obtain. For a response probability α above 0.8, relative variability falls below 10% for all group sizes larger than 10. The quantitative analysis of Fig. 8.1 **A** is illustrated in Fig. 8.1 **B**, where the distribution of relative group activation for three different group sizes is compared at a fixed response probability. The broadening of the discrete distribution, and the reduction in the number of support points, can clearly be observed.

8.2 Reliability of Transmission

The broadening of the distribution of relative group activation with decreasing w described in the preceding section suggests that narrow chains are more susceptible to failures in the propagation of synchronous activity. In the present section we investigate how the limited number of neurons in a group restricts the reliability of the system. The next section connects these considerations to the dynamics of the system. Let us assume the existence of a threshold $\tilde{\theta}$ in relative group activation above which the activity is known to be still in the basin of attraction. For a threshold value of 0.7 the situation is illustrated in Fig. 8.1 **B**. In the case of $w = 100$ practically the whole distribution is located to the right of the threshold, therefore there is a high probability that synchronous activity is sustained. The distribution is narrow

compared to the unit interval on which $\tilde{a}$ is defined and, therefore, we expect only small deviations between different realizations. For groups with a lower number of neurons, but with the same expectation value, however, the distributions show contributions to the left of the threshold. This indicates that realizations can occur, in which synchronous activity is not sustained. On the other hand, with low number of neurons per group there is a finite probability at sub-threshold expectation values (see Fig. 8.1 **B**, dashed curve) that activity spontaneously jumps into the basin of attraction.

Let us temporarily give a definition of survival probability which only depends on network structure and an assumed threshold $\tilde{\theta}$,

$$\mathcal{S}_{w,\tilde{\theta}}(\alpha) = \sum_{k=\lceil w\tilde{\theta}\rceil}^{w} \mathcal{B}_{w,\alpha}(k)\,. \tag{8.12}$$

This static picture allows us to investigate the properties of survival probability due to the discrete nature of the distribution of response spikes in the absence of effects introduced by the dynamics T_w of the system. The model is completed in the next section by using T_w to relate α and $\tilde{\theta}$ to the dynamic state of the system (a, σ).

Fig. 8.2 shows the dependence of $\mathcal{S}_{w,\tilde{\theta}}(\alpha)$ on group size. As expected, generally, survival probability decreases with decreasing w. However, if we take a detailed look and decrease the group size neuron by neuron, a saw-tooth pattern emerges. Starting at a group size corresponding to a local peak in $\mathcal{S}_{w,\tilde{\theta}}(\alpha)$, survival probability drops into a local minimum when w is decreased by a single neuron, but climbs up again with further decreasing w until the next peak is reached. The saw-toothed shape occurs because of the competition of two effects. With decreasing w each possible outcome of $\tilde{a}$ (support points in Fig. 8.1 **B**) gains more weight. At the same time, however, the first support point in the distribution to the right of the threshold moves closer to the threshold. At a certain $w \to (w-1)$ this support point transits from the right to the left side of the threshold, thus $\mathcal{S}_{w,\tilde{\theta}}(\alpha)$ abruptly drops. Because the loss of a support point is a $1/w$-type process, the size of the tooths is increasing with decreasing w. We can distinguish a set of group sizes generating particularly large survival probabilities and a set of group sizes generating particularly low survival probabilities

$$L_{\uparrow}(\tilde{\theta}) = \left\{ w\colon \lceil (w-1)\tilde{\theta}\,\rceil = \lceil w\tilde{\theta}\,\rceil \right\} \tag{8.13}$$

$$L_{\downarrow}(\tilde{\theta}) = \left\{ w\colon \lceil w\tilde{\theta}\,\rceil = \lceil (w+1)\tilde{\theta}\,\rceil \right\}. \tag{8.14}$$

The upper boundary of the gray area in Fig. 8.2 connects the elements of $L_{\uparrow}(\tilde{\theta})$, the lower boundary the elements of $L_{\downarrow}(\tilde{\theta})$.

With increasing expectation value α, the bell-shaped binomial distribution shifts to the right (cf. Fig. 8.1 **A**, distributions marked by white disks) passing the threshold. Therefore, $\mathcal{S}_{w,\tilde{\theta}}(\alpha)$ depends on α in a sigmoidal fashion, with the point of inflection at threshold value (Fig. 8.3 **A**). The sigmoid is a smooth function of α and becomes less steep with decreasing w. This is because under variation of α, in contrast to the w-dependence of survival probability (cf. Fig. 8.2), the location of support points relative to $\tilde{\theta}$ remains unchanged. Only the

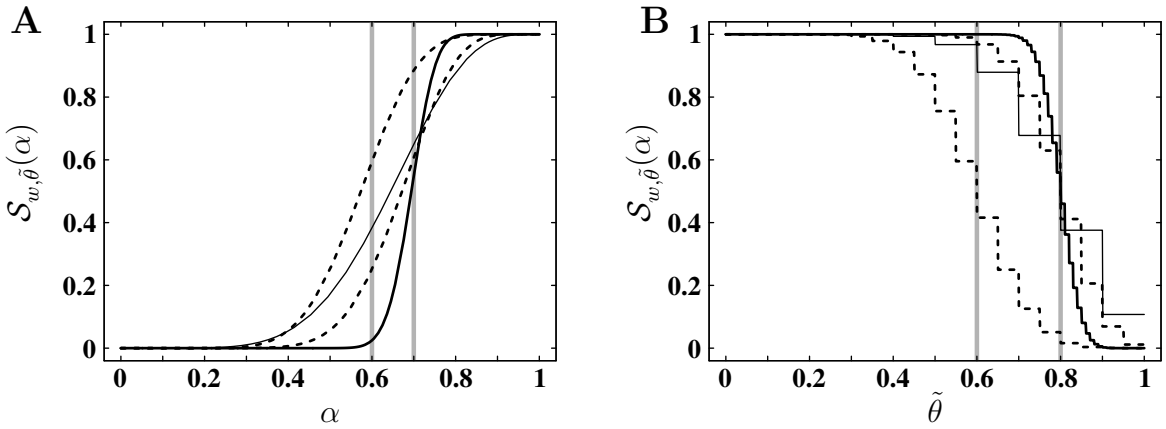

Figure 8.3 Survival probability as a function of spike probability α (**A**) and threshold activation $\tilde{\theta}$ (**B**) for three group sizes $w = 100$ (thick solid), 20 (dashed), and 10 (thin solid). **A** The gray vertical lines indicate threshold values $\tilde{\theta} = 0.7$ and 0.6. Survival probability smoothly increases with α in sigmoidal fashion. Curves computed for 0.7 intersect approximately at threshold value. Curve for $\tilde{\theta} = 0.6$ and $w = 20$ shown for comparison. **B** The gray vertical lines indicate spike probability values $\alpha = 0.8$ and 0.6. With increasing $\tilde{\theta}$ survival probability declines in staircase like manner. Curves for $\alpha = 0.8$ have largest step at corresponding $\tilde{\theta}$. Curve for $\alpha = 0.6$ and $w = 20$ shown for comparison.

relative weight of the support points changes. At activation threshold $\tilde{\theta}$, the survival probability is larger than 0.5 because the distribution of spike counts is discrete and, according to our definition (8.12), a relative group activation equal to $\tilde{\theta}$ is sufficient for survival.

The last parameter of (8.12) we need to look at is the threshold value $\tilde{\theta}$. With increasing threshold, $\mathcal{S}_{w,\tilde{\theta}}(\alpha)$ decreases in staircase like manner where the width of the steps is $\frac{1}{w}$ (Fig. 8.3 **B**). This is because the distribution is given only at discrete support points and hence, for intermediate values of $\tilde{\theta}$ the sum over all probabilities to the right of the threshold remains unchanged. The decline in survival probability becomes less steep, however more discrete, with decreasing w.

8.3 Survival Probability

Let us utilize the results of the last section to construct a model of survival probability for the propagation of synchronous activity. The single neuron spike probability $\alpha(w\tilde{a}, \sigma_{\text{in}})$ considered in Fig. 8.3 is a function of relative input activity $\tilde{a}$ and temporal input spread σ_{in}. Thus, for the probability that synchronous activity survives the transmission by the neuron group we can write

$$\mathcal{S}_{w,\tilde{\theta}}(\alpha, \sigma) = \mathcal{S}_{w,\tilde{\theta}}(\alpha(w\tilde{a}, \sigma)) . \tag{8.15}$$

The dependence of survival probability on relative input activity $\tilde{a}$ is shown in Fig. 8.4. Here, we still assume an arbitrary threshold $\tilde{\theta}$. The slope of $\alpha(\tilde{a}, \sigma_{\text{in}})$ is less steep than the slope of $\mathcal{S}_{w,\tilde{\theta}}(\alpha)$. Therefore, the slope of $\mathcal{S}_{w,\tilde{\theta}}(\alpha(\tilde{a}, \sigma_{\text{in}}))$ is governed by $\mathcal{S}_{w,\tilde{\theta}}$. Now, the temporal spread of the input spikes σ_{in} has entered survival probability via the α-section (cf. Fig. 3.4) of the transmission function T. The relative input activity where the survival probability rises abruptly from 0 to 1 strongly depends on input spread σ_{in}.

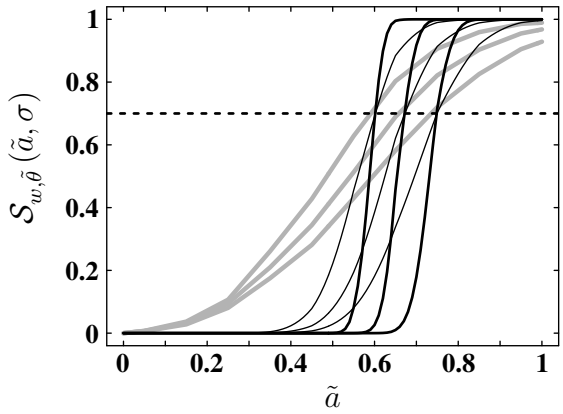

Figure 8.4 Survival probability predicted by performing a single iteration step. Black solid curves (thick: $w = 100$, thin: $w = 10$) show survival probability as a function of relative input activity $\tilde{a}$ for different temporal input spread (from left to right $\sigma_{\text{in}} = 0.5, 1.5, 2.5\,\text{ms}$). Response probability α (see Fig. 8.3) is computed using the α-component of the transmission function $\alpha(w\tilde{a}, \sigma_{\text{in}})$ (shown as gray curves for comparison). Activation threshold $\tilde{\theta}$ is 0.7 (dashed horizontal line). The point of inflection of survival probability occurs where $\alpha(w\tilde{a}, \sigma_{\text{in}})$ reaches $\tilde{\theta}$ (intersections of gray curves with dashed horizontal line).

The next task is to replace the arbitrary threshold $\tilde{\theta}$ by a meaningful measure derived from the dynamics of the system. In the deterministic case (Chap. 4) a separatrix (see Fig. 4.3) divides the state space into a regime where all initial activity reaches the attractor for synchronous activity and a regime in which all initial activity eventually vanishes. The state variable a is the expected number of response spikes $w\alpha$, no transition from one regime to the other is possible. At a given temporal spread σ, comparison of a with the location of the separatrix $a^{\text{s}}(\sigma)$ determines whether activity survives or dies out. However, for the purposes of the present chapter we treat the number of response spikes as a random variable $B_w[\alpha]$ (8.3). Thus, activity (a_i, σ_i) initially above the separatrix can leave the basin of attraction if the number of spikes in the next iteration step $B_w[\alpha(a_i, \sigma_i)]$ falls below the location of the separatrix $a^{\text{s}}(\sigma_{i+1})$ at the resulting temporal spread. Conversely, activity initially below the separatrix can jump into the basin of attraction. We can conclude that for the response pair $(\alpha, \sigma_{\text{out}})$ the appropriate threshold value $\tilde{\theta}$ is given by

$$\tilde{\theta}(\sigma_{\text{out}}) = \frac{1}{w} a^{\text{s}}(\sigma_{\text{out}}), \tag{8.16}$$

where the factor $1/w$ occurs because $\tilde{\theta}$ is defined in terms of relative group activation.

In the preceding two paragraphs we have discussed how our abstract ansatz for survival probability (8.12) can be related to the dynamics of the system. The arbitrary value of the threshold is removed by identification with the separatrix, and effects of the dynamical variable σ on the response probability as well as on the threshold value are considered. The refined model of survival probability now reads

$$\mathcal{S}_w(\tilde{a}, \sigma) = \mathcal{S}_{w,\tilde{\theta}(\sigma_{\text{out}}(w\tilde{a},\sigma))}(\alpha(w\tilde{a}, \sigma)). \tag{8.17}$$

There are two critical assumptions inherent in this model. First, it is assumed that for all possible configurations of initial activity $(\tilde{a}, \sigma)$, the probability of survival can be estimated

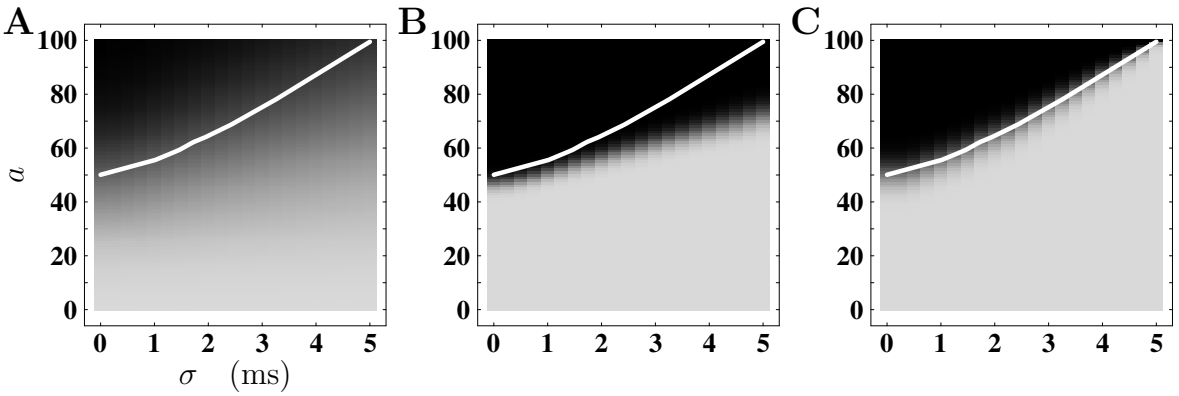

Figure 8.5 Survival probability considering a single iteration step. **A** Response probability $\alpha(a, \sigma)$ as a function of the number of spikes a (vertical) and the temporal spread of the input packet σ (horizontal). The number of neurons per group $w = 100$ and the amplitude of the post-synaptic potential (PSP) $\widehat{u} = 0.14\,\mathrm{mV}$ correspond to the standard situation used throughout the study (cf. Fig. 3.4 **A**). α is represented by a density plot with linear dependence of gray level on the response probability (black: 1, lightest gray: 0). The separatrix of the deterministic dynamics (cf. Fig. 4.3) is shown for orientation (white curve). Parameters and representation identical in all panels. **B** Survival probability for each location in state space assuming a fixed relative threshold activity of $\tilde{\theta} = 0.5$ (here, 50 spikes). The gray level indicates the probability that activity in the next iteration step is larger or equal to $\tilde{\theta}$. **C** Survival probability for each (a, σ) configuration assuming that activity survives if in the next iteration step the system is found in the basin of attraction of the deterministic case (white curve: border of basin). The observed discretization in gray levels comes from the natural restriction of a to integer numbers and the arbitrary restriction of the resolution to 0.25 ms in σ-direction.

by considering only a single iteration step. Second, it is required that the temporal spread of the response spikes σ_{out} can be treated as a deterministic variable.

Fig. 8.5 **C** illustrates the dependence of the survival probability resulting from (8.17) on the state-space coordinates. There is a steep increase of survival probability precisely at the location of the separatrix. The steepness of the slope justifies our deterministic treatment of the dynamics. The probability that activity starting below the separatrix will enter the basin of attraction is practically zero, and the probability that activity starting in the basin reaches the attractor approaches unity. Only in the vicinity of the separatrix some variability is exhibited. Note that we have exploited knowledge of the location of separatrix in our model of survival probability. Therefore, we cannot draw strong conclusions about the fact that the position in state space where survival probability has peak derivative coincides with the position of the separatrix.

The influence of the presence of the separatrix can be judged by comparing Fig. 8.5 **C** with Fig. 8.5 **B**. Here, the σ dependent threshold in (8.17) represented by the separatrix is replaced by a constant value. Clearly, the location of the up-slope in survival probability exhibits σ-dependence and is not predefined by the threshold value. In the latter case, the up-slope would appear in the state-space portrait along a horizontal line, parallel to the σ-axis. The observed bending of iso-$\mathcal{S}_w(\tilde{a}, \sigma)$ curves towards larger spike numbers with increasing σ stems from the σ-dependence of response probability α, displayed in Fig. 8.5 **A**. The σ-dependence of the separatrix enhances the effect. In addition, the increase in slope from $\alpha(w\tilde{a}, \sigma)$ to $\mathcal{S}_w(\tilde{a}, \sigma)$, we already discussed using Fig. 8.4, can easily be seen by comparing

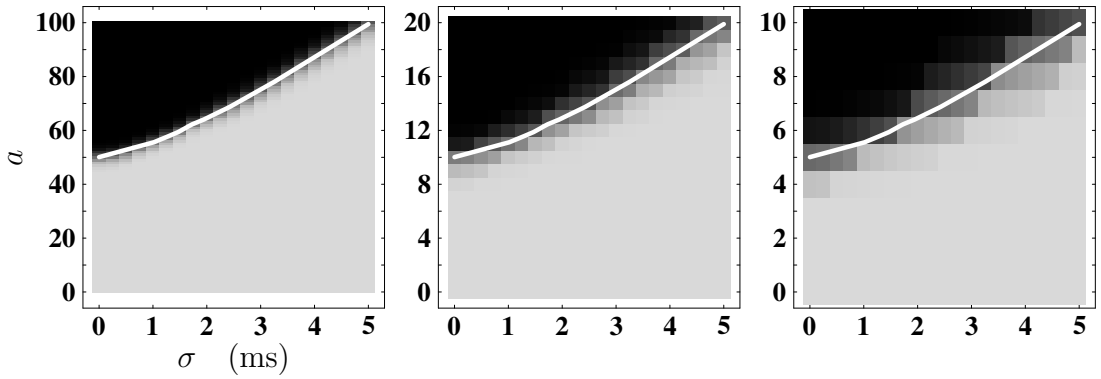

Figure 8.6 Survival probability in networks of different group sizes on the basis of the variability of a in a single iteration step and the location of the separatrix. The number of neurons per group w is decreasing from left to right ($w = 100$, 20, 10) while the amplitude of the post-synaptic potential $\widehat{u}$ is up-scaled leaving the product $w\widehat{u}$ invariant. Same representation as in Fig. 8.5 **C**, the left panel is identical to Fig. 8.5 **C**. In vertical direction, survival probability is evaluated on the natural grid (integer spike numbers). The area covered by the density plot increases with decreasing w to keep rectangles representing survival probability of (a, σ) centered at the grid coordinate.

Fig. 8.5 **A** and Fig. 8.5 **B**.

Now, the tools are at hand to investigate the reliability of the system when the scaling law (8.7) is used to construct networks with fewer neurons per group but appropriately increased PSP amplitudes. Fig. 8.6 shows the survival probability for three different group sizes, with the number of neurons decreasing from left to right. Despite the fact that the PSP amplitude changes by an order of magnitude, a considerable regime where survival probability is practically unity remains. As expected (cf. Fig. 8.3 **A**), the slope of survival probability declines with decreasing w. Consequently, the regime close to the separatrix where variability allows the system to spontaneously enter or leave the basin of attraction enlarges.

We conclude that with enough neurons available there is no advantage for the propagation of synchronous activity in using a few, specifically strong synapses. On the other hand, the physiologically relevant range of post-synaptic amplitudes, say from 0.1 mV to 1 mV (e.g. Matsumura et al., 1996), does not impose severe constraints on the reliable transmission of synchronous activity. Before we discuss some limitations of the transmission function at large PSP amplitudes at the end of the chapter, let us first evaluate the major assumption in the above analysis. Central to the arguments is knowledge of the location of the separatrix in the deterministic case. No independent information is available that in the presence of variability in the number of response spikes, the separatrix still characterizes the initial number of spikes required to reach the attractor with high probability. However, the next section demonstrates that when a stochastic mapping is constructed which does not make use of the separatrix, results are consistent with the analysis of the present section considering only a single iteration step.

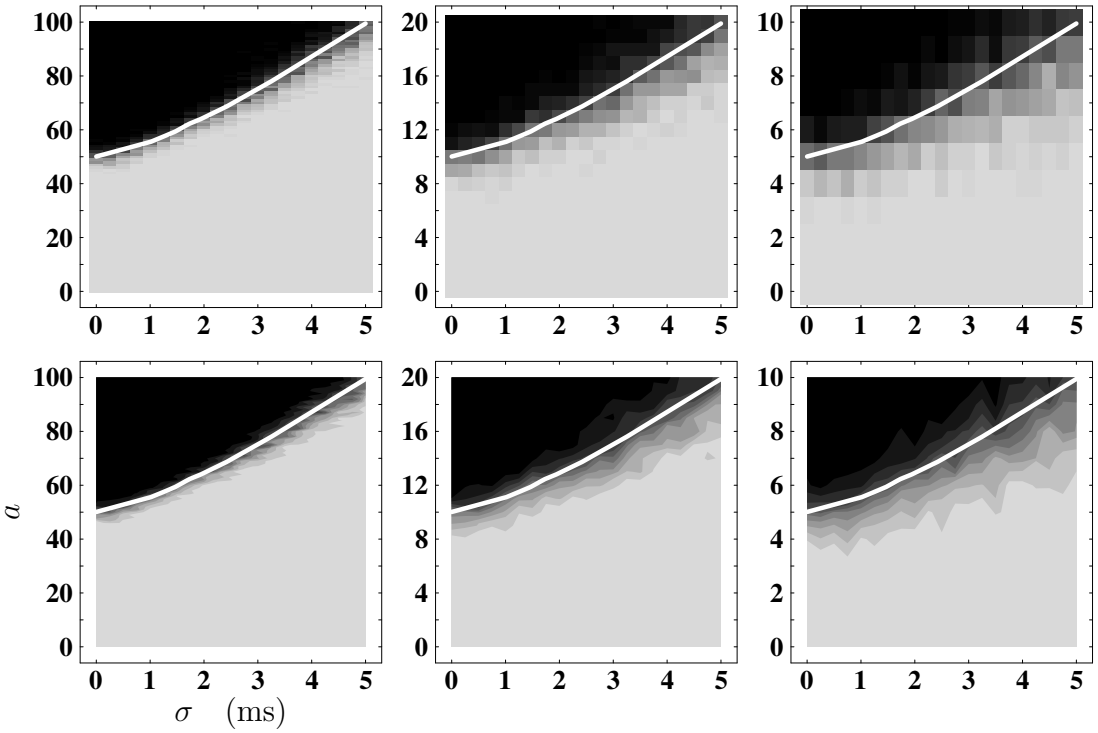

Figure 8.7 Survival probability taking into account variability of a and σ, computed at the natural resolution of integer spike counts (vertical). Columns from left to right show results for group sizes $w = 100$, 20, and 10 with invariant $w\widehat{u}$. Resolution for σ (horizontal) is 0.25 ms. For each initial condition on the grid, survival probability is estimated on the basis of 50 realizations. Activity is assumed to decay if it falls below $a^\dagger$ (20, 4, 3) within the first $l = 7$ iteration steps. The upper row uses the same representation of survival probability as in Fig. 8.6 (black: 1, lightest gray: 0). The lower row shows the same data as the upper row as contour plots with 10 iso-survival-probability curves (contours) to enhance the structure of the slope. Area between contours indicates magnitude of survival probability, same gray coding as in upper row. In all panels the separatrix of the deterministic system is shown superimposed (white curve) for comparison.

8.4 Monte-Carlo Approach to Survival Probability

In Chap. 4 the transmission function T was used to construct the deterministic iterative mapping T_w (4.1):

$$\begin{array}{ccc} (a_i, \sigma_i) & \xrightarrow{\quad T \quad} & (\alpha, \sigma_{i+1}) \\ & \searrow^{T_w} & \Big\downarrow a_{i+1} = w\alpha \cdot \\ & & (a_{i+1}, \sigma_{i+1}) \end{array} \tag{8.18}$$

Here, the mean spike count of (8.2) $w\alpha$ is used to specify the number of spikes a_{i+1} in the next iteration step. In order to incorporate the variability in spike count into the dynamics we can introduce a new operator

$$A_w(\alpha, \sigma) = (B_w[\alpha], \sigma) \tag{8.19}$$

which replaces the mean spike count by the appropriate random variable (8.3)

$$(a_i, \sigma_i) \xrightarrow{T} (\alpha, \sigma_{i+1}) \xrightarrow{A_w} (a_{i+1}, \sigma_{i+1}) \quad . \tag{8.20}$$

This is a stochastic mapping, generating random trajectories in state space. If activity is repeatedly started at some initial (a_0, σ_0), a certain fraction of the trajectories ends up in the vicinity of the attractor while the remaining ones eventually decay. Survival probability $\mathcal{S}(a, \sigma)$ is now naturally given by the fraction of trajectories reaching the attractor, and, generally, depends on the location of the initial activity (a, σ) in state space. Knowledge of the behavior of the deterministic system is no longer required for the definition of survival probability.

Even if there is a location in state space which serves as an attractor for synchronous activity, the system exhibits ongoing random fluctuations in its vicinity due to the stochastic nature of the mapping. Therefore, it seems to be better suited to identify the fraction of trajectories on which activity eventually vanishes and to use the complement of this fraction as the survival probability. When the number of spikes in a packet has reached a low value, say 10 in the case of $w = 100$, synchronous activity dies out with a probability of practically 1. Thus, we can introduce a threshold $a^\dagger$ to stop the iteration process once a_i falls below this value. Obviously, this threshold needs to be chosen far away from the location of the separatrix of the deterministic dynamics not to predetermine an outcome of the analysis trivially compatible with the results of the previous section (cf. Fig. 8.5). The lower limit of the threshold value is given by the limited precision of the transmission function for low numbers of input spikes. In this regime response probability is low. Thus, an increasing number of simulation runs (Chap. 3) would be required to determine a and σ_{out} with appropriate accuracy. The termination condition introduced above is not sufficient to enable determination of $\mathcal{S}(a, \sigma)$ by Monte-Carlo simulations. A maximum number of iteration steps needs to be introduced to stop the iteration process when the system has reached a regime where it is unlikely that activity will vanish in future iterations. Strictly, survival probability can only be defined for a given number of iteration steps. Because α is always below unity, some residual variability remains. Consequently, with an infinite number of iteration steps, any initial activity will eventually die out. However, we have seen in Chap. 4 that the development into the neighborhood of the attractor and the decay of activity occur within a few iteration steps. Once activity has reached the vicinity of the attractor, the magnitude of response probability and the size of the basin of attraction guarantee that activity does not leave this area of state space again. Thus, we can expect that evaluation for a number of iteration steps large enough to capture the transient behavior of the system provides an adequate measure of survival probability, meaningful also for larger numbers of iteration steps. Note the fundamental asymmetry in our model: initial full activation ($a = w$) can, in principle, decay but non-vanishing activity cannot develop from the silent state ($a = 0$). The asymmetry results from the fact that the spontaneous formation of pulse packets is not considered in the transmission function (Chap. 3). Only the neuronal self-inhibition caused by spontaneous activity (see also Fig. 5.6) is taken into account. Preliminary results (Tetzlaff, Geisel, & Diesmann, 2002) indicate that, in the parameter regime investigated here, the probability that synchronous activity develops spontaneously is exceedingly low.

In conclusion, survival probability is defined as the fraction of trajectories starting at (a, σ) for which in l iteration steps a_i has not fallen below $a^\dagger$.

In the above framework we restrict ourselves to a numerical evaluation of survival probability. However, up to now variability was considered only for variable a, as in Sec. 8.3 temporal spread σ is still considered to be a deterministic variable. When a neuron receives a packet of spikes, the temporal spread of spike times determines the neuronal response. In the deterministic dynamics, temporal spread is described by the standard deviation σ of the temporal distribution individual spike times are drawn from. Nevertheless, the temporal spread of a particular realization of spike times can considerably deviate from σ. Hence, the transmission function $T(a, \sigma)$ may over- or underestimate the effectiveness of an input packet, depending on the actual configuration of spike times in the packet. We can obtain a better estimate of the relevant temporal spread by recomputing σ on the basis of the set of spike times in each realization. From this point of view, spike time is a random variable $G[\sigma]$ drawn from a Gaussian distribution with standard deviation σ

$$G[\sigma] \sim \frac{1}{\sigma\sqrt{2\pi}}\, e^{-\dfrac{t^2}{2\sigma^2}}. \tag{8.21}$$

Time zero is the expected response time of the preceding neuron group emitting the pulse packet. The delay between the emission of the packet and the time of impact is of no importance because we assume synaptic delays to be homogeneous and non-fluctuating. Similar to (8.19) we introduce a new operator $S(a, \sigma)$ estimating the temporal spread of the a random spike times in the packet

$$S(a, \sigma) = (a, \sqrt{\frac{1}{a}\sum_{k=1}^{a} G_k^2[\sigma]}). \tag{8.22}$$

This time, the operator leaves the first component unchanged and operates exclusively on the second component. The sequence of operations in one iteration step now reads

$$(a_i, \sigma_i) \xrightarrow{T} (\alpha, \sigma) \xrightarrow{A_w} (a_{i+1}, \sigma) \xrightarrow{S} (a_{i+1}, \sigma_{i+1}) \quad . \tag{8.23}$$

The formal expression of survival probability taking into account variability in a and σ finally is

$$\delta_l(a, \sigma) = \begin{cases} 0\,; & \exists\, a_i < a^\dagger \quad \text{with} \quad (a_i, \sigma_i) = \left[S \circ A_w \circ T\right]^i (a, \sigma),\ i \in 0 \ldots l \\ 1\,; & \text{else} \end{cases} \tag{8.24}$$

$$\mathcal{S}_{w,l}(a, \sigma) = \left\langle \delta_l(a, \sigma) \right\rangle_{\text{trials}}. \tag{8.25}$$

Fig. 8.7 and Fig. 8.8 are computed with the newly defined stochastic process. Comparison of the upper row of Fig. 8.8 with Fig. 8.6 shows that the variability of a in the vicinity of the separatrix (8.17) already explains most of the variability of the system. The contour plots (Fig. 8.8, lower row) represent a smoothed version of the original data highlighting the broadening of the up-slope in survival probability with decreasing w. Comparison of

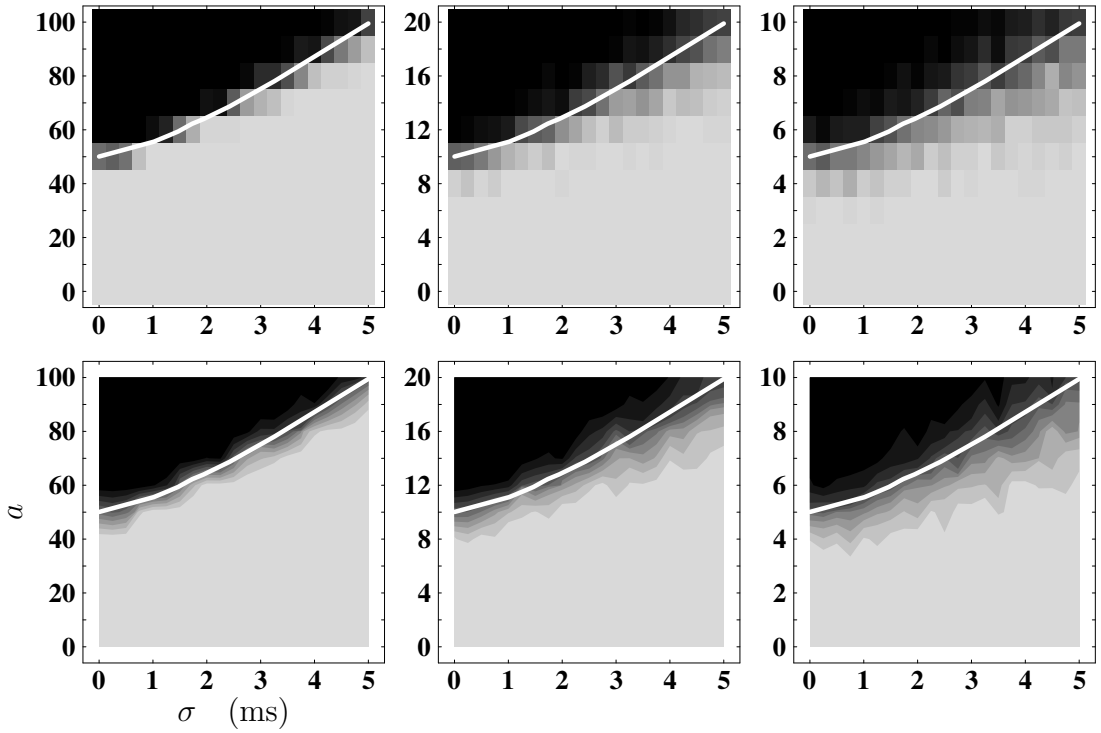

Figure 8.8 Effect of discretization by possible spike counts $1 \ldots w$ on the slope of survival probability. Same arrangement and representation as in Fig. 8.7. For comparison the state space is sampled using the same relative spacing of the grid in all cases (columns from left to right: $w = 100$, 20, 10). Horizontal resolution is 0.25 ms as in Fig. 8.7. 10 steps are used to sample the range of spike counts (vertical). This is the maximal number of steps available at a group size of $w = 10$ (right column identical to right column in Fig. 8.7).

corresponding panels in the upper and the lower row convinces us that the arbitrary selection of contours has not distorted the visual impression of the raw data at a given w. Note, that in contrast to the approach taken in (8.17), the separatrix of the deterministic mapping does not enter the computation of survival probability in (8.25). It is therefore reassuring that the curve in state space where survival probability abruptly increases, coincides with the separatrix of the deterministic mapping (Chap. 4). A sharp transition in survival probability defines the basin of attraction for synchronous activity.

With decreasing group size w, the number of support points at which for a given σ survival probability can be computed naturally decreases because of the restriction of spike counts to integer values $1 \ldots w$. The question arises whether the w-dependence of the slope of survival probability observed in Fig. 8.6 and Fig. 8.7 is trivially due to this choice of initial conditions. In Fig. 8.8, the number of support points is artificially restricted to 10 for all 3 group sizes. While the discretization is now clearly visible also for $w = 100$ (compare upper left panels of Fig. 8.8 and Fig. 8.7), it does not explain the changes in the slope of survival probability. Thus, we have confirmed that the increase in variability with decreasing group size is an inherent property of the system

The results on survival probability are in good correspondence with results from network simulations (Gewaltig, Diesmann, & Aertsen, 2001b). Now, in principle, also the variability of individual trajectories (cf. Gewaltig, Diesmann, & Aertsen, 2001b) can be investigated.

However, a detailed comparison of our stochastic mapping with results from network simulations is outside the scope of the present study.

Let us end the chapter with a discussion of the limitations of our analysis of PSP amplitude. The comparison of different PSP amplitudes is based on the scaling property (8.7). The transmission function obtained for a particular PSP amplitude can be rescaled to describe the dynamics for systems with different PSP amplitudes. The procedure by which the transmission function is obtained (Chap. 3) assumes that all input packets (a, σ) cause a statistically equivalent neuronal response. In the limit of small PSP amplitudes, this condition is fulfilled because the packet potential does no longer depend on the detailed spike time configuration. We have exploited this property in Chap. 6, where the packet potential is expressed by the convolution of the PSP and the Gaussian spike time distribution. The situation changes when group size is reduced to a few neurons and PSP amplitudes are large. In the absence of membrane potential fluctuations, the timing of the response spike is completely determined by the timing of the input spikes. Thus, the distribution of response spikes as measured by the transmission function originates from differences in the packet potentials caused by individual spike time configurations. However, the situation in the feed-forward network is dramatically different. Every neuron in a group receives exactly the same configuration of input spikes (the effect is washed out for randomly diluted chains, Hehl, Aertsen, & Diesmann, 2001a). Thus, all neurons generate a response spike at the same point in time. In other words, on the ms time scale, the transmission function ignores the fact that the neurons of a group receive correlated spike input. The average over trials entering the transmission function overestimates the distribution of response spikes. The difference increases with decreasing group size. Here, the contribution of individual PSPs to the packet potential increases. Therefore, we have to expect deviations from our predictions at small group sizes even if the scaling property (8.7) is fulfilled. In the presence of membrane potential fluctuations, the transmission function captures the combined effect of the different spike time configurations and the different membrane potential time courses in different trials. Indeed, in the network the membrane potential is different for every neuron in the group. The configuration of input spikes, however, is identical. Nevertheless, the transmission function successfully describes the neuronal response at moderate group sizes because the temporal spread of the input spikes is small compared to the time constants of the PSP. Details of the spike time configuration are smoothed by convolution with the PSP. In addition, the temporal spread of response spikes caused by realistic membrane potential fluctuations is much larger than the temporal spread caused by different input spike configurations rendering the latter irrelevant.

A more elaborate procedure for constructing the transmission function should first determine response parameters for individual input spike configurations and only in a second step average response parameters over input spike configurations to arrive at $(\alpha, \sigma_{\text{out}})$. The effect of PSP amplitude (subject to the scaling law) on the locking of synchronous activity is discussed in Sec. 10.1.2.

Chapter 9

Slow Fluctuations Model

The transmission function for synchronous input introduced in Chap. 3 allowed us to investigate the dependence of the synchronization dynamics on several physiologically relevant measures. Parameters describing network structure like the number of neurons per group w (Chap. 4, see also Chap. 8 for the role of PSP amplitude) are relevant for network dynamics (4.2) but do not alter the transmission function itself. In contrast, the magnitude of membrane potential fluctuations σ_V (Chap. 5) and the rise time of the PSP τ_0 (Chap. 7) determine the shape of the transmission function. The limit of vanishing membrane potential fluctuations (Chap. 6) allowed us to derive that the shape of the PSP controls the border of the basin of attraction for synchronous activity. In addition, the basic dependence of the activation curves on input spread and the potentially constructive effect of background activity are uncovered in the limit of vanishing σ_V. However, in this limit no statements can be made about the temporal spread of response spikes, and also the detailed shape of the activation curves remains unexplained. In order to gain some insight into the origin of the transmission function, an analytical description is desired that is parameterized by physiologically interpretable parameters σ_V and τ_0. In his 1991 monograph Abeles states that for a large number of synchronized input spikes, the temporal spread of the response spike σ_δ should be governed by

$$\sigma_\delta = \frac{1}{\bar{D}}\sigma_V, \tag{9.1}$$

where $\bar{D}$ is the average derivative of the up-slope of the packet potential. The model is based on the assumption that on the time-scale of the rise time of the PSP the (background) membrane potential is only slowly fluctuating. The input packet is assumed to cause a suprathreshold response (say, packet potential amplitude being twice the distance from membrane potential mean to spike threshold), independent of the initial value of the membrane potential. Under these conditions, spikes occur on the up-slope of the packet potential and, thus, the random variable spike time δ is a function of the random variable V. If the up-slope is sufficiently well described by $\bar{D}$, the distribution of V is linearly mapped to the distribution of δ, and therefore we obtain (9.1). The present chapter generalizes this model to arbitrary input packets. The distribution of spike times, and therefore the temporal spread as well as the response probability can be computed. While the model explains important aspects of the transmission function, especially the interaction between membrane potential fluctuations and PSP rise time, significant deviations from the transmission function obtained in

simulations of the full I&F model (Chap. 3) remain. A comparison of the two models using the concept of spike intensity (Sec. 9.5) allows us to discuss the model components which a complete theory of pulse packet transmission needs to include.

9.1 Spike Generation on Packet Potential Up-slope

Consider the membrane potential V caused by background activity to be a random variable which varies much slower in time than the membrane potential excursion caused by an incoming pulse packet. The threshold condition reads

$$\theta = V + U(t), \tag{9.2}$$

where $U(t)$ denotes the packet potential. The origin of time t can be defined as the point in time where the mean of the pulse density causing the packet potential reaches the target neuron (in Chap. 6 there was no need to specify the origin, because we were only interested in the maximum of the packet potential, not in its timing). Because we assumed the pulse density to be a Gaussian distribution, $U(t)$ deviates from zero for arbitrary times before $t = 0$. In practice, however, the limited number of spikes in a pulse packet and the membrane potential noise restricts $U(t)$ to some finite time interval. At the point in time where the neuron first experiences an appreciable increase in membrane potential caused by an incoming pulse packet, the membrane potential due to background activity has some random value V. V is considered to be constant over the time course of $U(t)$. In this situation, (9.2) determines the time of threshold crossing δ (if $V + U(t)$ becomes supra-threshold at all)

$$\delta = U^{-1}(\theta - V) \quad \text{for} \quad \widehat{U} \geq \theta - V. \tag{9.3}$$

Thus, the time of threshold crossing δ is a function of the random variable V and, therefore, by itself a random variable. Note that as a consequence of our assumption that V is constant over the time course of $U(t)$, spikes can occur only on the rising phase of the packet potential. Following the impact of a pulse packet, the membrane potential covers a limited interval of membrane potential values $V, V + \widehat{U}$. Each value is visited twice: first on the rising phase of the packet potential and later during the decay of the potential. If, and only if, the threshold value is included in the interval, a response spike is generated. The threshold is reached first on the rising phase, and therefore it is here where the spike will be generated. If we assume that the refractoriness of the neuron is longer than the time span over which $V + U(t)$ is above threshold, no further spike is generated. Under this condition, the spike time δ is a function of the value of the membrane potential. The task now is to compute the probability density of spike times $\rho(\delta)$ from the probability density of membrane potential values V. The two densities are connected by the fundamental theorem on functions of a random variable (Papoulis, 1991; Chap. 5).

$$\rho_\delta(\delta) = \frac{\rho_V(V)}{\left|\frac{d}{dV} U^{-1}(\theta - V)\right|}. \tag{9.4}$$

Due to the presence of the spike threshold, $\rho_V(V)$ is not a Gaussian distribution as predicted from a free shot-noise process (Sec. 2.3). We compensate for the presence of the boundary

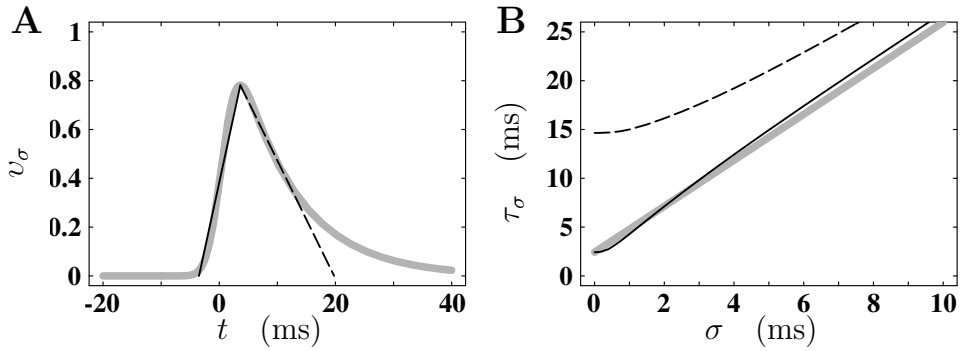

Figure 9.1 Rise time approximation for packet potential. **A** The gray curve shows the characteristic membrane potential excursion v_σ, caused by an incoming pulse packet (here, $\sigma = 2\,\mathrm{ms}$ for a post-synaptic potential with rise time $\tau_0 = 1.7\,\mathrm{ms}$). Rise time of a packet potential is defined by a straight line (solid) starting at the peak of $v_\sigma(t)$ and intersecting the up-slope at half height. The temporal distance between the point in time where the line intersects the abscissa and the point in time at which the peak is reached is called rise time τ_σ, (9.5). **B** Dependence of packet potential rise time on input spread σ (solid curve). Applying the definition of rise time used in **A** to a Gaussian yields $2\sqrt{2\ln 2}\sigma$. An explicit expression approximating τ_σ (gray curve) is given by $2\sqrt{2\ln 2}\sigma + \tau_0$, (9.24). For comparison, the definition used in **A** is also applied to the down-slope of v_σ (dashed curves in both panels).

by renormalizing the truncated Gaussian on the interval $(-\infty, \theta)$. In the following the normalization factor is omitted from the equations for clarity. In addition the Gaussian is distorted by the AHP following a spike, the distortion depending on the details of the AHP model (e.g. reset to V_0, cf. Fig. 2.6) and on the spike rate. Exploiting the assumption we made throughout the present work that we are operating in a regime of low spontaneous firing rates, this distortion is neglected. With the same argument, the normalization factor described above is close to unity.

To obtain insight in the properties of (9.4) and to avoid the complication that we have to relate the time of threshold crossing to the origin of the incoming pulse packet, we introduce a linear approximation of the rising phase of the packet potential. However, expressions for $(\alpha, \sigma_{\mathrm{out}})$ can also be derived for arbitrary shapes of the rising phase (Sec. 9.5). The requirement is that a suitable expression for the root of $(\theta - V) - U(t)$ (9.3) can be found. We define the rise time of the packet potential τ_σ as twice the temporal distance of the maximum of the characteristic membrane potential excursion v_σ (6.10) to its half height in the rising phase:

$$v_\sigma(\widehat{t} - \frac{1}{2}\tau_\sigma) = \frac{1}{2}\widehat{v}_\sigma, \quad \tau_\sigma > 0. \tag{9.5}$$

Here, $\widehat{t}$ denotes the position of the maximum of $v_\sigma(t)$. The approximation of the rising phase is

$$U(t) \approx a\widehat{u}\widehat{v}_\sigma \cdot \frac{1}{\tau_\sigma} t, \tag{9.6}$$

where we have made the variable substitution $t + (\tau_\sigma - \widehat{t}) \to t$, such that the maximum is reached at τ_σ and the origin is at the onset of the approximated packet potential (9.6). By solving (9.6) for t and inserting into (9.3) we obtain

$$\delta(V) = \frac{\tau_\sigma}{a\widehat{u}\widehat{v}_\sigma}\,(\theta - V)\,, \tag{9.7}$$

and

$$\left|\frac{d}{dV}U^{-1}(\theta - V)\right| = \frac{\tau_\sigma}{a\widehat{u}\widehat{v}_\sigma}. \tag{9.8}$$

Therefore, the corresponding probability density for δ is

$$\rho_\delta(\delta) = \frac{a\widehat{u}\widehat{v}_\sigma}{\tau_\sigma} \cdot \rho_V\left(\theta - \frac{a\widehat{u}\widehat{v}_\sigma}{\tau_\sigma}\delta\right), \quad 0 \le \delta \le \tau_\sigma. \tag{9.9}$$

The argument of ρ_V is only a scaling, followed by shifting of δ. Moreover, the factor of ρ_V does not depend on δ. Thus, if the rising phase of the packet potential can be approximated by a linear slope, ρ_δ is a Gaussian. Within our simplified model, ρ_δ describes the spike density in response to an incoming pulse packet. The fact that the Gaussian input packet results in a Gaussian response density justifies our interpretation of the transmission function as an iterative mapping, and the description of the pulse packet by just two parameters: area and standard deviation (we return to this point in Chap. 10). Note that the Gaussian shape of the response packet does not stem from the Gaussian shape of the input packet. The input packet only enters with the linear slope of the packet potential. It is the Gaussian nature of the membrane potential fluctuations which causes the response packet to be Gaussian. The mechanism controlling the transmission of synchronous activity has an intrinsic tendency to generate Gaussian shaped pulse packets.

However, in general we can not assume that a packet potential reaches threshold for arbitrarily low values of V. Only under this condition the response density would indeed be a complete Gaussian and the response probability would be unity. The lowest membrane potential value V_{τ_σ} at which a spike can be generated at all is given by the maximum of the packet potential

$$\theta - V_{\tau_\sigma} = a\widehat{u}\widehat{v}_\sigma. \tag{9.10}$$

Here, the spike occurs at the latest possible point in time τ_σ. If $V_{\tau_\sigma} \ll \eta$, V_{τ_σ} is already in the lower tail of the distribution of membrane potential values, and the response probability is close to 1. If not, however, only part of the membrane potential distribution is accessible for the packet potential, and, hence, the response probability (using (9.9)) is

$$\alpha = \int_0^{\tau_\sigma} \rho_\delta(\delta)\, d\delta = \int_{\theta - a\widehat{u}\widehat{v}_\sigma}^{\theta} \rho_V(V)\, dV \tag{9.11}$$

$$= \operatorname{erf}\left[\frac{\theta - \eta}{\sigma_V}\right] - \operatorname{erf}\left[\frac{\theta - \eta - a\widehat{u}\widehat{v}_\sigma}{\sigma_V}\right], \tag{9.12}$$

with erf denoting the error function (e.g. Papoulis, 1991). Likewise, we compute the mean response time η_δ

$$\eta_\delta = \frac{1}{\alpha}\int_0^{\tau_\sigma} \delta\rho_\delta(\delta)\, d\delta \tag{9.13}$$

$$= \left(\frac{\tau_\sigma}{a\widehat{u}\widehat{v}_\sigma}\right)\left[\theta - \frac{1}{\alpha}\int_{\theta - a\widehat{u}\widehat{v}_\sigma}^{\theta} V\rho_V(V)\, dV\right] \tag{9.14}$$

$$= \left(\frac{\tau_\sigma}{a\widehat{u}\widehat{v}_\sigma}\right)\left[(\theta - \eta) - \frac{\sigma_V}{\alpha\sqrt{2\pi}}\left(e^{-\frac{(\theta - \eta - a\widehat{u}\widehat{v}_\sigma)^2}{2\sigma_V^2}} - e^{-\frac{(\theta-\eta)^2}{2\sigma_V^2}}\right)\right] \tag{9.15}$$

and the standard deviation σ_δ of the truncated Gaussian

$$\sigma_\delta^2 = \frac{1}{\alpha}\int_0^{\tau_\sigma} (\delta-\eta_\delta)^2 \rho_\delta(\delta)\, d\delta \tag{9.16}$$

$$= \left(\frac{\tau_\sigma}{a\widehat{u}\widehat{v}_\sigma}\right)^2 \Bigg[-\left((\theta-\eta) - \left(\frac{a\widehat{u}\widehat{v}_\sigma}{\tau_\sigma}\right)\eta_\delta\right)^2 + \frac{1}{\alpha}\int_{\theta-a\widehat{u}\widehat{v}_\sigma}^{\theta} (V-\eta)^2 \rho_V(V)\, dV \Bigg] \tag{9.17}$$

$$= \left(\frac{\tau_\sigma}{a\widehat{u}\widehat{v}_\sigma}\right)^2 \Bigg[-\left((\theta-\eta) - \left(\frac{a\widehat{u}\widehat{v}_\sigma}{\tau_\sigma}\right)\eta_\delta\right)^2 + \sigma_V^2\left(1 + \frac{1}{\alpha\sqrt{2\pi}}\left(\frac{\theta-\eta-a\widehat{u}\widehat{v}_\sigma}{\sigma_V} e^{-\frac{(\theta-\eta-a\widehat{u}\widehat{v}_\sigma)^2}{2\sigma_V^2}} - \frac{\theta-\eta}{\sigma_V} e^{-\frac{(\theta-\eta)^2}{2\sigma_V^2}}\right)\right)\Bigg]. \tag{9.18}$$

Thus, within our simplified model we now have expressions to compute the output pair $\left(\alpha,\ \sigma_{\text{out}} = \sigma_\delta\right)$ as a function of the input pair $\left(a_{\text{in}} = a,\ \sigma_{\text{in}} = \sigma\right)$ on the basis of the shape of the post-synaptic potential and the membrane potential statistics.

9.2 Activation Curves

Let us now compare the resulting transmission function (Fig. 9.2) with the transmission function we obtain in simulations of the I&F model (Fig. 5.2). The activation curves (left column) are in good agreement with the simulation results. Using (9.12) it can easily be shown that the point of inflection occurs at

$$\frac{d^2\,\alpha}{d\,a^2} = 0 \quad \Rightarrow \quad a = \frac{\theta-\eta}{\widehat{u}\widehat{v}_\sigma}. \tag{9.19}$$

A larger input spread σ_{in} leads to a smaller characteristic amplitude $\widehat{v}_\sigma$. Thus, with increasing σ_{in} the point of inflection occurs at larger values of input activity a. At the point of inflection, the response probability is 0.5. We now understand the origin of this value (see Sec. 6.5). Here, the amplitude of the packet potential just covers the distance from spike threshold to the mean of the membrane potential. Thus, if the distribution of membrane potential values is not considerably truncated by the threshold, a response spike is generated for 50% of all possible membrane potential values. The input spread determines the characteristic amplitude and, thereby, effectively scales the input activity axis. At a given a, the response probability declines with increasing σ_{in} because the amplitude of the packet potential drops and, consequently, the fraction of all membrane potential values which allow for a response spike. The rows in Fig. 9.2 illustrate how the activation curves (left column) depend on the amount of membrane potential fluctuations. For small (amplitude below $\theta-\eta$) input packets, increased fluctuations σ_V have a constructive effect: at a given a the probability to hit a membrane potential value close enough to threshold is increased. The situation is

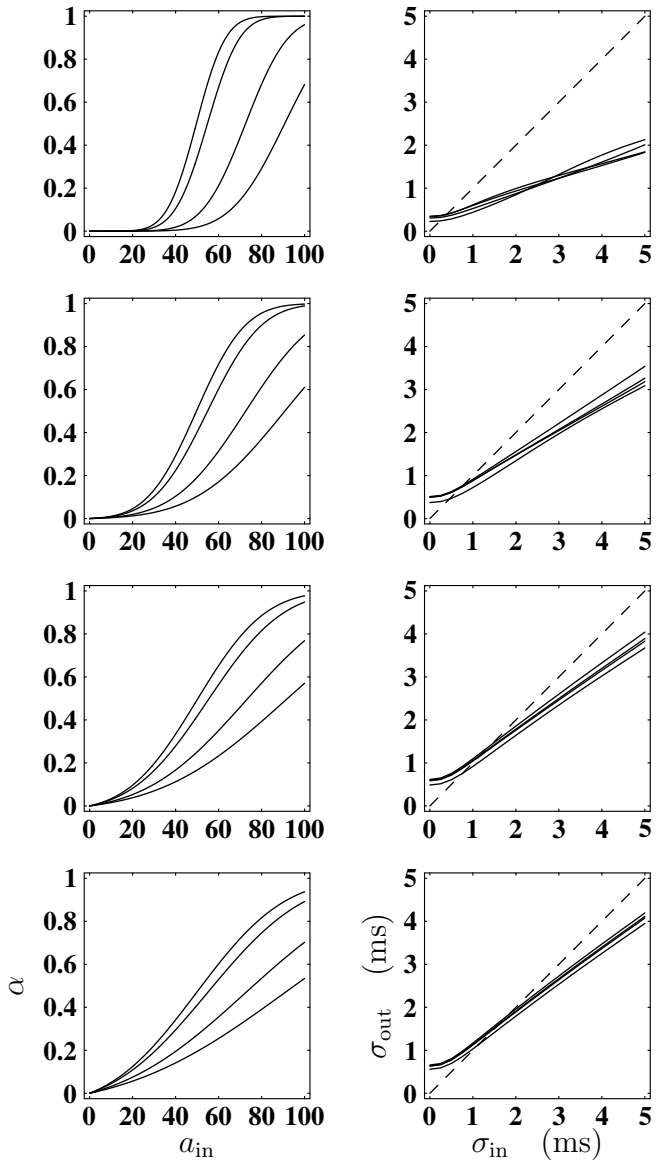

Figure 9.2 Dependence of transmission function on membrane potential fluctuations in the slow fluctuations model. Same parameters and arrangement as in the corresponding figure for the I&F model (Fig. 5.2). The standard deviation of the fluctuations is increasing from top to bottom $\sigma_V = 1.5, 2.5, 3.5, 4.5\,\mathrm{mV}$ (four rows). The left column displays the $\alpha(a_{\mathrm{in}})$ section of the transmission function. The four curves represent different constant input spread $\sigma_{\mathrm{in}} = 0, 1, 3, 5\,\mathrm{ms}$ (from left to right). The right column displays the $\sigma_{\mathrm{out}}(\sigma_{\mathrm{in}})$ section of the transmission function. The four curves represent different constant input activity $a_{\mathrm{in}} = 45, 65, 75, 115$ (from top to bottom). The dashed line indicates the diagonal.

reversed for large (amplitude above $\theta - \eta$) input packets. Here, an increase in fluctuations increases the probability that the membrane potential is far away from the threshold. Thus, the probability that for a given input packet the membrane potential is close enough to threshold to cause a response spike is decreased.

9.3 Output Spread

The overall shape of the σ_{out}-curves (Fig. 9.2, right column) has many characteristics of the curves obtained for the full I&F model. For sufficiently strong input packets, the integral (9.17) extends over most of the Gaussian membrane potential distribution and we have

$$\sigma_\delta = \left(\frac{\tau_\sigma}{\widehat{a}\widehat{u}\widehat{\upsilon}_\sigma}\right)\sigma_V. \tag{9.20}$$

The σ_{out}-curves show a finite spread, even at full input synchronization. This is caused by the finite rise time of the post-synaptic potential τ_0. At $\sigma_{\text{in}} = 0\,\text{ms}$, (9.20) reduces to

$$\sigma_\delta = \left(\frac{\tau_0}{\widehat{a}\widehat{u}}\right)\sigma_V. \tag{9.21}$$

Thus, the finite slope of the packet potential at full input synchronization determines the output spread. We have recomputed Abeles' approximation (9.1), verified in Sec. 7.1 on page 75. Output spread is smaller for a larger number of input spikes, and increases with membrane potential fluctuations. Above a certain value, however, the input spread is no longer larger than the output spread

$$\sigma_\delta < \sigma_{\text{in}}. \tag{9.22}$$

With (9.20) this leads to:

$$\frac{\tau_\sigma}{\sigma_{\text{in}}} < \frac{\widehat{a}\widehat{u}\widehat{\upsilon}_\sigma}{\sigma_V}. \tag{9.23}$$

This inequality is the condition under which strong input packets exhibit a synchronizing behavior. It relates the temporal domain (l.h.s.) to the membrane potential domain (r.h.s.). Synchronization occurs if the ratio of rise time and temporal spread of the input packet is smaller than the ratio of the maximum of the membrane potential excursion and the membrane potential fluctuations.

At vanishing input spread, the rise time of the packet potential equals the rise time of the post-synaptic potential τ_0. At large σ_{in}, the rise time of the packet potential is dominated by the rise time of the Gaussian. Thus, we can use the sum of the two rise times (that of the PSP and that of the Gaussian) as an approximation for the rise time of the packet potential. The rise time of the Gaussian we define by the half height approximation we already introduced for the packet potential above (see (9.5), Fig. 9.1 **B** for illustration)

$$\tau_\sigma \approx 2\sqrt{2\ln 2}\sigma + \tau_0. \tag{9.24}$$

By inserting the approximations for $\widehat{v}_\sigma$ (6.17) and τ_σ into (9.20) we obtain

$$\sigma_\delta = \frac{\sigma_V\sqrt{2\pi}}{aF^1}\left(2\sqrt{2\ln 2}\sigma_{\text{in}} + \tau_0\right)\sigma_{\text{in}}. \tag{9.25}$$

Thus, the strong packet approximation (9.25) predicts that σ_δ depends on σ_{in} in a quadratic manner. For large enough input spread, the output spread eventually surpasses the input spread. The condition for synchronization (9.22) reads

$$\sigma_{\text{in}} < \left(\frac{aF^1}{\sigma_V\sqrt{2\pi}} - \tau_0\right)\frac{1}{2\sqrt{2\ln 2}}. \tag{9.26}$$

(9.23) is valid for strong input packets. In this regime, the r.h.s. of (9.26) is positive. With all other parameters held constant, synchronization is only possible for an input spread below a critical value. However, for a given input spread σ_{in}, the condition for synchronization can always be met by adopting a large enough number of input spikes a.

In contrast to the strong packet approximation (9.20), both simulations (Fig. 5.2) and the slow fluctuations model (Fig. 9.2) show that for large σ_{in}, the output spread does *not* quadratically increase with input spread. For larger input spread, σ_δ increases linearly with σ_{in}, the slope depending on the membrane potential fluctuations. Interestingly, the slope is less than unity, with the result that for large σ_{in} the system exhibits a synchronizing behavior even for weak (low a, large σ_{in}) input packets. Here, the strong packet approximation breaks down, because a new mechanism limiting the output spread comes into play. By the construction of our process, spikes can only be generated on the up-slope of the packet potential. Therefore, the maximal spread occurs when the response spikes are evenly distributed over the time span of the up-slope (rise time):

$$\sigma_{\text{out}} = \frac{1}{2\sqrt{3}}\tau_\sigma. \tag{9.27}$$

The factor $1/(2\sqrt{3})$ is the standard deviation of a rectangular distribution extending over the unit interval (e.g. $[-1/2, +1/2]$, Nawrot, Aertsen, & Rotter, 1999). Using the rise time approximation (9.24) we see that

$$\sigma_{\text{out}} = \frac{1}{2\sqrt{3}}\left(2\sqrt{2\ln 2}\sigma_{\text{in}} + \tau_0\right). \tag{9.28}$$

Thus, the upper limit for the output spread is a linear function of the input spread. The slope is well below 1, ensuring the synchronizing property of the system

$$\sigma_{\text{out}} \propto \sqrt{\frac{2\ln 2}{3}} \cdot \sigma_{\text{in}} \tag{9.29}$$

$$\propto 0.68 \cdot \sigma_{\text{in}}. \tag{9.30}$$

Comparison of (9.28) with the synchronization condition (9.22) leads to the relationship

$$\sigma_{\text{out}} < \sigma_{\text{in}} \quad \text{for} \quad \sigma_{\text{in}} > \frac{1}{2(\sqrt{3} - \sqrt{2\ln 2})} \cdot \tau_0 \tag{9.31}$$

$$> 1.11 \cdot \tau_0. \tag{9.32}$$

According to this result, we expect the output spread to be smaller than the input spread when the input spread is somewhat (by 11%) larger than the rise time of the post-synaptic potential. Note that it is the rise time of the post-synaptic potential τ_0 which appears in the inequality, *not* the σ_{in}-dependent rise time of the packet potential τ_σ. Fig. 9.2 shows that the inequality indeed holds for the slow fluctuations model. Simulation results of the full model (Fig. 5.2) show that for packets with a low number of spikes and at large membrane potential fluctuations, the intersection with the ($\sigma_{\text{out}} = \sigma_{\text{in}}$)-diagonal occurs at a temporal spread considerably larger than τ_0. However, the general property following from our considerations that for large membrane potential fluctuations output spread saturates can also be observed in the simulation results (cf. Fig. 5.2). The effects leading to further broadening not captured by the slow fluctuations model are discussed below in Sec. 9.5.

9.4 Vanishing Fluctuations

We have seen so far that generally the output spread increases with increasing input spread. However, for a given input spread there is always an input activity which leads to an output spread smaller than the input spread (9.26). In addition, the maximal output spread for our process is limited by the rise time of the PSP (9.27). Above a certain σ_{in}, σ_{out} is always smaller than σ_{in}. For small membrane potential fluctuations we can observe additional effects. First, output spread is low in general, well below our maximal spread estimation (9.28). Second, for weak input packets (low a) we observe that after the initial increase, output spread can reach a maximum and decrease again. The effect visible at $\sigma_V = 1.5\,\text{mV}$ in the I&F simulation (see Fig. 5.2) is also clearly present in the simplified model (Fig. 9.2). Curves for different constant numbers of input spikes cross each other. At a certain σ_{in} a curve for a large number of spikes may have a larger output spread than a curve for a lower number of input spikes.

The complex picture arises because at low membrane potential fluctuations we have a competition of several mechanisms. An increase in input spread increases the rise time of the packet potential and simultaneously causes a drop in amplitude. Both measures control the factor connecting ρ_V with ρ_δ in (9.9). The effects on the standard deviation of ρ_δ (output spread σ_δ) are studied above (9.20) using the assumption that the full shape of the membrane potential distribution is accessible by the packet potential. To understand the behavior of σ_δ at low membrane potential fluctuations we have to study changes in the accessible shape of ρ_V itself.

Let us consider packet potentials with amplitudes comparable to the distance from membrane potential mean to spike threshold $\theta - \eta$. At small membrane potential fluctuations the distribution of membrane potential values does not evenly fill the space between membrane potential mean and threshold. Thus, an incoming pulse packet has a low probability to hit a membrane potential value V close to threshold and, consequently, to generate a response spike close to the onset of the packet potential. The probability to hit a membrane potential value around the mean of the membrane potential, hence in the peak region of the membrane potential distribution, is much larger. If a spike is generated at all, it is in this case generated late in the rising phase of the packet potential. Going downwards from a membrane potential value close to threshold, the slope of the Gaussian membrane potential

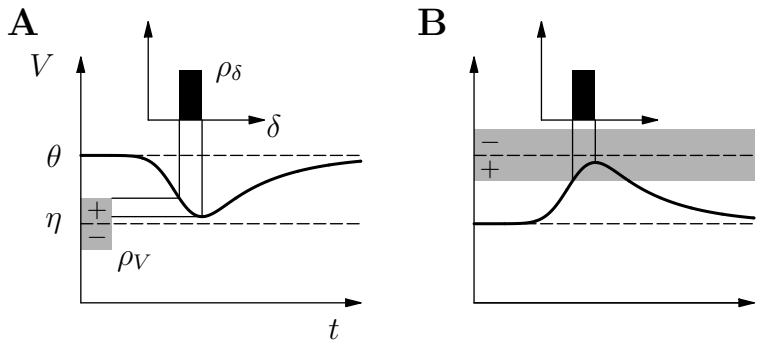

Figure 9.3 Model for the interaction of small membrane potential fluctuations and packet potentials of moderate amplitude. **A** The rectangular distribution ρ_V (gray) of membrane potential V (vertical) is centered around the mean η (lower dashed line). The part of the distribution having a smaller distance to spike threshold θ (upper dashed line) than η is labeld "+", the part having a larger distance "-". The width of ρ_V is small compared to $\theta - \eta$. The packet potential (thick curve) is drawn upside down with an offset of θ (minimum of thick curve represents peak of packet potential). The projection (thin lines) of the part of ρ_V accessible by the packet potential onto the temporal axis (horizontal) defines the distribution of response spikes ρ_δ (black rectangle). The highest existing V results in the earliest response time δ (thin line starting at upper margin of gray rectangle and ending at left margin of black rectangle). The lowest reachable V results in the latest response time (thin line connecting the gray rectangle with the right margin of the black rectangle via the peak of the packet potential). **B** Different representation of the situation in **A**. Membrane potential is constant at η (lower dashed line), spike threshold is a random variable (distribution indicated by gray rectangle) centered at θ (upper dashed line). The packet potential (thick curve) is added to the mean membrane potential η. A low threshold in **B** corresponds to a high membrane potential in **A** ("+"). An increase in σ_{in} has two competing effects: broadening of ρ_δ because of increased rise time of the packet potential, narrowing of ρ_δ because of decreased amplitude.

probability density is small first, increases rapidly until the point of inflection is reached and declines again until the maximum of the probability density is reached at η. ρ_δ is only a linear transformation of the part of ρ_V accessible by the packet potential. Thus, ρ_δ has a regime of low response probability and a regime of high response probability. Again we can introduce an approximation valid in a specific parameter regime to gain insight into the behavior of the full equation (9.18).

Consider the membrane potential probability density to be of a rectangular shape centered at η. In terms of its standard deviation it extends $\sqrt{3}\sigma_V$ into the direction of the threshold value with equal magnitude into the direction of resting potential. The situation is illustrated in Fig. 9.3 **A**. We construct the firing probability density by first drawing the packet potential upside down with the origin at threshold value. Let us assume that the amplitude of the packet potential does not extend into the tail of the membrane potential distribution below $\eta - \sqrt{3}\sigma_V$. In this case the latest point in time (and lowest membrane potential value) at which a spike occurs is given by τ_σ. The first point in time δ_l is determined by the largest existing membrane potential value $\eta + \sqrt{3}\sigma_V$ and the slope of the packet potential

$$\theta - (\eta + \sqrt{3}\sigma_V) = \frac{a\widehat{u}\widehat{v}_\sigma}{\tau_\sigma}\delta_l. \tag{9.33}$$

Thus, the standard deviation of the response probability density is given by

$$\sigma_\delta = \frac{1}{2\sqrt{3}} (\tau_\sigma - \delta_l) \tag{9.34}$$

$$= \frac{1}{2\sqrt{3}} \left(1 - \frac{(\theta - \eta) - \sqrt{3}\sigma_V}{a\widehat{u}\widehat{v}_\sigma} \right) \tau_\sigma. \tag{9.35}$$

Here, the region of low probability density for large membrane potential values is approximated by 0 and the region of high probability density by a constant value. Only the region of high probability density contributes to the standard deviation.

In the expression for maximal output spread (9.27) σ_δ is determined by the rise time of the packet potential τ_σ. This dependency reoccurs as the first term in the parenthesized expression of (9.35). The second term is controlled by the characteristic amplitude $\widehat{v}_\sigma$; it reduces the rise time to the range effectively available for the generation of response spikes. (9.35) is a manifestation of the competing effects determining the development of output spread with increasing σ_{in}. Increasing rise time increases the output spread. The declining characteristic amplitude, however, decreases the output spread. Insertion of the approximations for τ_σ (9.24) and $\widehat{v}_\sigma$ (6.17) into (9.35) exhibits the quadratic dependence of σ_{out} on σ_{in} with the leading coefficient being negative. At small σ_{in} the increase in rise time dominates and the output spread increases until it reaches a maximum. At larger σ_{in} the effect of the declining amplitude dominates and output spread decreases again.

A different way to visualize the model of background fluctuations appropriate in this parameter regime is shown in Fig. 9.3 **B**. Here, the rectangular distribution of membrane potential values is shown as a gray "band" centered at the threshold θ. The packet potential is now drawn in its natural orientation with the origin at mean membrane potential η. Only the part of the packet potential extending into the noise band can cause a response spike and consequently its temporal spread is restricted to the time interval which the up-slope of the packet potential spends in the noise band.

The above approximation was constructed for packet potentials of moderate amplitude which reach well into the peak region of the membrane potential distribution. The model cannot be valid for small packet potentials which live in the tail of the membrane potential distribution. Here, a new approximation needs to be developed. However, the regime of small packet potentials is of no importance for the stability of synchronous activity and the synchronization dynamics, and is therefore outside the scope of the present study. Outside the basin of attraction for synchronous activity (Fig. 4.3), any initial activity (a, σ) eventually reaches the regime where pulse packets contain, in the above sense, only a low number of spikes a. For the completion of the description of our system it is an interesting question where the attractor for vanishing activity, suggested by our limited data (cf. Fig. 5.3), is located and how its location depends on the membrane potential fluctuations σ_V. The dependence of the trajectories leading toward vanishing activity on σ_V in Fig. 5.3 clearly demonstrates the role of membrane potential fluctuations. In the next and final section of this chapter we discuss limitations of the slow fluctuations model, which turn out to be particularly relevant at low activity.

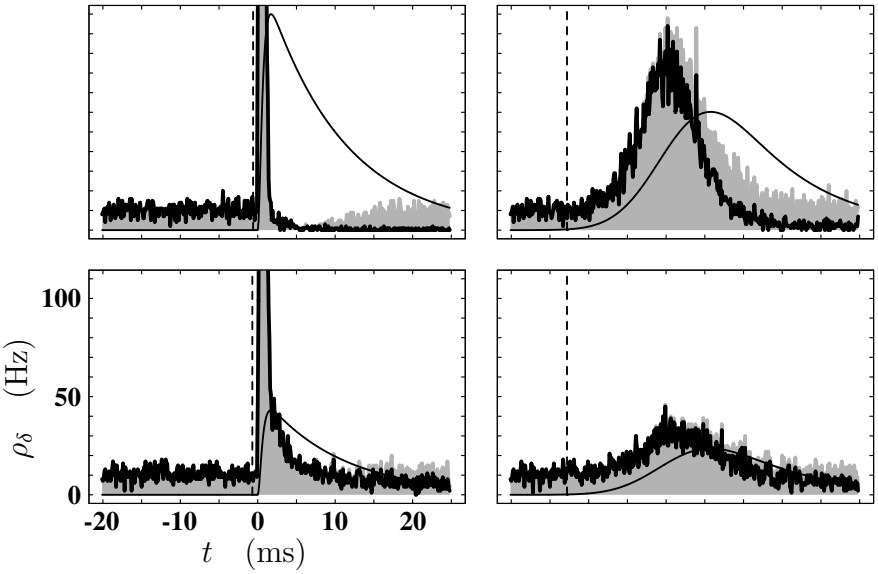

Figure 9.4 Comparison of the time course of the packet potential and the resulting spike response of the integrate-and-fire model. Panels showing data for extreme input packets (a, σ) are arranged as the variables of (a, σ)-space (cf. Fig. 4.3): a vertical, bottom (45) to top (115) and σ horizontal, left (0 ms) to right (5 ms). Thin black curve is the membrane potential excursion (packet potential) U caused by the incoming pulse packet (a, σ). The origin of the temporal axes is defined by the center of mass of the distribution the input spikes are drawn from. The gray area represents the time course of the neuronal spike response averaged over 10,000 repetitions as a histogram with temporal resolution 0.1 ms. The histogram is normalized by the number of repetitions and temporal resolution, expressing the response (vertical axes) in units of spike rate. The dashed vertical line indicates the onset of the response (see Fig. 3.3 for definition). To the left of the onset the gray histogram and the thick black curve are identical, demonstrating a spontaneous firing rate of 10.3 Hz (caused by membrane potential fluctuations $\sigma_V = 4.5$ mV). To the right of the onset, the thick black curve represents a histogram ρ_δ of the first spike in the response. The peaks of the histograms for perfectly synchronized input (left column) are truncated, peak values are: 350 Hz (bottom) and 1700 Hz (top). Maximal U ($115 \cdot 0.14$ mV, upper left) is scaled to fit displayed range of ρ_δ (16.1 mV corresponds to 110 Hz). Identical scaling for ρ_δ and U in all panels. The case of large σ_V is chosen to highlight the occurrence of second spikes (cf. Fig. 3.3).

9.5 Relation to Intensity Models

The slow fluctuations model described above explains important features of the response of the full integrate-and-fire system to synchronous input. The model allows us to express the probability density of the response spike directly in terms of the parameters of the I&F system. No adjustment of arbitrary parameters is required. Being restricted to the up-slope of the packet potential, the model underestimates the temporal spread of response spikes especially for weak (small a) input packets (cf. Fig. 9.2). There is another class of models of spike response which we will call *intensity models*. Here, the instantaneous probability density to emit a spike is described by an intensity $f(\delta) = f(U(\delta))$ depending only on the contribution U to the total membrane potential caused by the input under consideration. The effects of the unobserved background activity on membrane potential and, potentially, also other sources of noise are summarized in the shape of f.

Let us now assume that before the input packet arrives the neuron is in a state of low

spontaneous firing rate. The probability density of the first response spike ρ_δ, as it would be observed by averaging over many repetitions of the experiment, is then given by

$$\rho_\delta(\delta) = f(\delta)(1 - \int_0^\delta \rho_\delta(t)dt). \tag{9.36}$$

Thus, the probability density of a response spike at time δ is given by the intensity f at that point in time provided that the neuron has not already emitted a spike before. Relation (9.36) clarifies why f is sometimes also called *free intensity* for better distinction of ρ_δ and f. The term

$$Q(\delta) = 1 - \int_0^\delta \rho_\delta(t)dt \tag{9.37}$$

is called survival probability or *survivor function*. It is a standard result of renewal theory (Cox, 1967) that ρ_δ can also be written as

$$\rho_\delta(\delta) = f(\delta) \exp(- \int_0^\delta f(t)dt) \tag{9.38}$$

removing the recursion in (9.36). The theory sketched above is developed in (Cox, 1967) and generalized for application to neuronal processes in (Rotter, 1994). Gewaltig (2000) was able to remove the restriction to the first spike and to consistently incorporate an equilibrium probability density by introducing a finite refractory kernel.

The concept of an intensity $f(U)$ raises two questions, regarding the nature of spike generation and the relationship between the different types of models. First, the slow noise model is based on the observation that spikes are much more likely to occur on the up-slope than on the down-slope of the packet potential. Slow fluctuations naturally introduces this asymmetry: threshold cannot be crossed on the down-slope because the required random membrane potential V implies that θ would already have been crossed on the up-slope. In the intensity model a unique intensity f is assigned to a particular U independent of its occurrence on the up-slope or on the down-slope. However, our observable is spike density ρ_δ, and here asymmetry is introduced by the effect of the survivor function (9.36). The fact that spikes do occur on the down-slope requires us to ask whether the observed asymmetry can be explained by (9.36), and, consequently, $f(U)$ constitutes a more complete model of spike generation than the slow fluctuations approach. The second question is to what extent far the two models are compatible. Whereas in the case of the slow fluctuations model we can derive ρ_δ directly from the assumptions, we do not have a direct route to construct an appropriate f (see Abeles, 1991; Gewaltig, Diesmann, Rotter, & Aertsen, 1997; Gewaltig, 2000; Plesser & Gerstner, 2000 for discussion). If the slow fluctuations approach can mathematically be mapped to an intensity model this gives us insight into the relevant ingredients of f.

Fig. 9.4 illustrates four characteristic spike probability densities in comparison to the time course of the packet potential. For a strong and well synchronized input packet (upper left) spikes occur on the narrow up-slope of the packet potential. Following the high spike density and synchronization on the up-slope, spike density drops below the spontaneous level because here the neuron is refractory in most of the trials. After the neuron recovers

from refractoriness, activity does not exceed the spontaneous level and is composed of second spikes. A few first spike responses occur on the down-slope in the peak region of the packet potential. For a weaker input packet with identical synchronization (lower left) a trough caused by refractoriness cannot be observed. Now, a considerable percentage of the response spikes occurs on the down-slope of the packet potential. Again, second spikes do not contribute to the shape of the peak in spike density. A strong but dispersed input packet (upper right) results in an almost symmetric probability density. The peak in probability density occurs on the up-slope of the packet potential, close to the point of inflection of the voltage excursion. Second spikes occur on the down-slope of the packet potential. While at full synchronization of the input (upper left) the synchronization of the first response spikes causes a clear separation of the distributions of first and second spikes, the two distributions merge in the case of large input jitter (upper right). Note that the presence of second spikes does not explain the deviations of the slow fluctuations model from the I&F simulations. Only first spikes enter the transmission function for synchronous input (Chap. 3). Thus, deviations must be explained in terms of the probability density for first spikes. Weak and dispersed input packets (Fig. 9.4, lower right) cause only a small excursion in probability. At the same voltage, the spike probability density on the down-slope of the packet potential is of the same order as on the up-slope. In Fig. 9.4 the origin of the temporal axes is defined by the time of impact of the center of mass of the input packet. Therefore input packets with large temporal spread (right column) can cause deviations of ρ_δ from the spontaneous level at negative times.

Having made the above observations, let us now try to interpret the histograms of Fig. 9.4 in terms of our simple intensity model (9.36). Given the histogram of the first spikes ρ_δ we can write (9.36) as

$$f(\delta) = \frac{\rho_\delta(\delta)}{Q(\delta)}. \tag{9.39}$$

Here, the origin of δ is defined as the point in time where the collection of the first response spikes starts. In principle, it is sufficient to place the origin of δ at an arbitrary point in time where the input packet has not already affected the probability density. In the regime of spontaneous spiking, intensity f is a constant, with (9.38) leading to an exponentially decaying probability density. Thus, locating $\delta = 0\,\mathrm{ms}$ at a point in time long before the response to the input packet occurs reduces the probability to observe the first spike in the regime of interest. With a finite amount of data (repetitions) available, f can still be computed, however, the accuracy of the estimate may considerably be degraded. Therefore, we position the origin at the onset of the response. This onset was already introduced in Chap. 3 to extract response probability α and temporal spread of the response σ_{out}.

In the histograms for large input spread (Fig. 9.4, right column) the selected point in time of the onset seems to be somewhat arbitrary. However, one should be reminded that the histogram shows the raw simulation data. In contrast, the onset is estimated from a smoothed version of the histogram to improve robustness.

Fig. 9.5 **A** shows the survivor functions $Q(\delta)$ computed from the histograms in Fig. 9.4. The steep decline in the left column reflects the narrowness of the excitation at full synchronization of the input spikes. For a strong input packet (large a, upper left) the probability that the neuron has not emitted a spike drops to zero after a few ms. For a weaker input

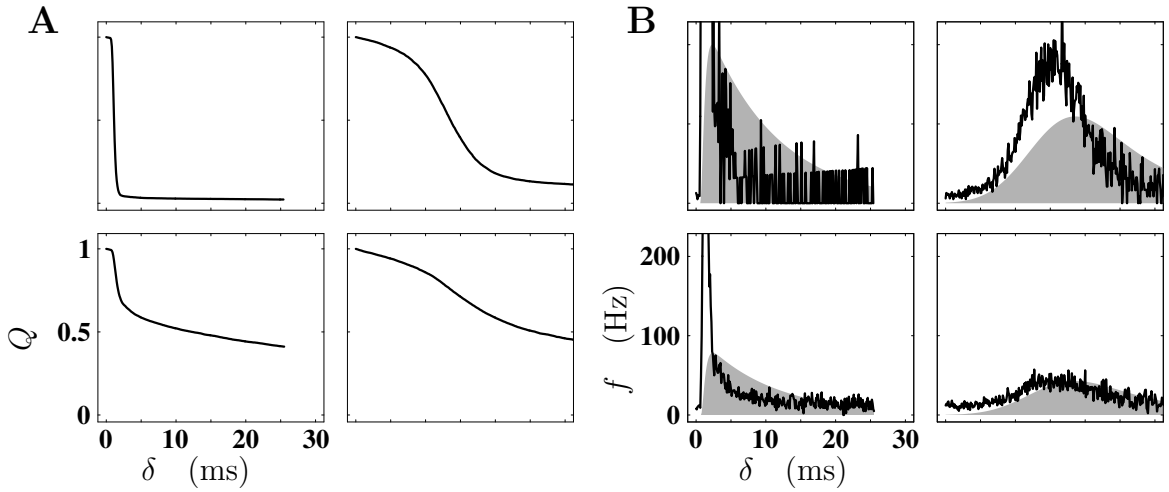

Figure 9.5 Survivor function $Q(\delta)$ and intensity $f(\delta)$. **A** Probability to have not generated a response spike until time δ measured from the onset of the response (computed from data shown in Fig. 9.4). Same arrangement of graphs as in Fig. 9.4, number of input spikes a increases vertically, temporal spread σ horizontally. Right endpoints of curves in left column indicate limit of data set (cf. shift of temporal axes Fig. 9.4). In the first 30 ms following the onset of the response the total drop in Q is determined by a and the steepness of the decline by σ. **B** Intensity (black curve) compared to shape of packet potential U (gray area). Data and arrangement of graphs correspond to **A** and Fig. 9.4. The peaks of f for perfectly synchronized input (left column) are truncated, peak values are: 400 Hz (bottom) and 3000 Hz (top). Maximal U ($115 \cdot 0.14$ mV, upper left) is scaled to fit displayed range of f (16.1 mV corresponds to 200 Hz). Identical scaling for f and U in all panels. Fluctuations in f are due to the limited amount of data in the histograms determining ρ_δ (cf. Fig. 9.4). Discretization by spike counts 0, 1, 2 (0.1 ms bin-width) clearly visible for $\delta > 10$ ms in upper left graph.

packet (small a, lower left) the initial decline is as rapid. However, there is a considerable probability to survive the peak region of the packet potential. The picture is similar for large input spread (right column). Here, the decline in Q is less steep. Independent of the input packet, $Q(\delta)$ eventually goes to zero (not shown) because of the spontaneous spikes resulting from background activity.

Having constructed probability density (Fig. 9.4) and survival probability (Fig. 9.5 **A**) we are now in a position to compute spike intensity $f(\delta)$ using (9.39). Results are shown in Fig. 9.5 **B**. The time course of f is surprisingly similar to the time course of ρ_δ. f represents the instantaneous excitability of the neuron, all effects of refractoriness entering ρ_δ are removed. Thus, we can already conclude that refractoriness is not the main mechanism limiting the temporal spread of the neuronal response to an incoming pulse packet. Furthermore, qualitative comparison of $f(\delta)$ with the time course of the packet potential reveals that spike intensity cannot be represented as function of $U(\delta)$. At the same membrane potential U, intensity is clearly larger on the up-slope of the packet potential than on the down-slope.

In Fig. 9.5 **B** we have compared intensity $f(\delta)$ and membrane potential excursion $U(\delta)$ by superposition of the two graphs involving arbitrary scaling of the relative amplitudes. In order to get a more quantitative understanding of the dependence of f on the properties of $U(\delta)$ we can eliminate time from the pair $(f(\delta), U(\delta))$ and study the implicitly defined graph

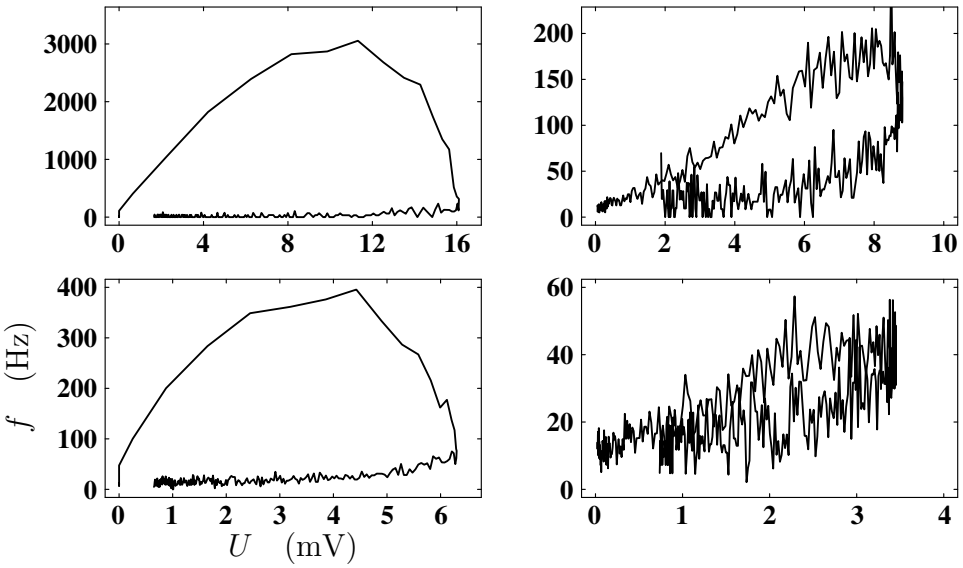

Figure 9.6 Spike intensity f versus membrane potential excursion U. Same data and arrangement as in Fig. 9.5 **B**. Time is eliminated from the combination of $f(\delta)$ and $U(\delta)$ in Fig. 9.5 **B** using the implicit representation $(f(\delta), U(\delta))$. Starting at $U = 0$, intensity continuously increases on the up-slope of the packet potential (ignoring fluctuations in f, see Fig. 9.5 **B**), reaches a maximum before the peak in U is reached, and continues to decline on the down-slope (on curve (f, U), time proceeds in clockwise fashion). For the same value of U, f obtains larger values on the up-slope than on the down-slope of the packet potential (f is not a function of U). On the up-slope, f obtains identical values for different values of U (f is not monotonous in U). Curve for low number of input spikes and perfect synchronization (bottom left) gains higher peak intensity but lower peak voltage as curve for large a and large σ (top right). Graphs are individually scaled to show full extend of the hysteresis of (f, U) for each pair of input parameters (a, σ).

$$(f, U)_{a_{\text{in}}, \sigma_{\text{in}}}. \tag{9.40}$$

Results for our four parameter sets are shown in Fig. 9.6. While the range of values covered by (f, U) varies by more than an order of magnitude in f and a factor of 5 in U, a pronounced hysteresis is observable in all four cases. Given an intensity function $f(U)$, no hysteresis should occur. Once the system has reached the peak amplitude in U, it should return on the same path (f, U) it had taken on the up-slope of the packet potential. Compared to the up-slope, intensity is much reduced on the down-slope of the packet potential. In addition, for a given value of U the intensity on the up-slope is different for the different input packets. Intensity is much higher for packet potentials with a rapid increase in membrane potential (Fig. 9.6, left column). For packet potentials with a gentle increase in packet potential (Fig. 9.6, right column), intensity increases with increasing membrane potential. However, for packet potentials with a steep up-slope a clear derivative dependence is observable. Intensity reaches its maximum in the region where the slope of the membrane potential is maximal and returns to low values in the peak region of the packet potential. It is instructive to compare the two cases for perfectly synchronized input packets (Fig. 9.6, left column). With 45 input spikes (lower left panel) the packet potential reaches a maximum value of about 6 mV. At the peak, intensity has already dropped off to 50 Hz. A strong

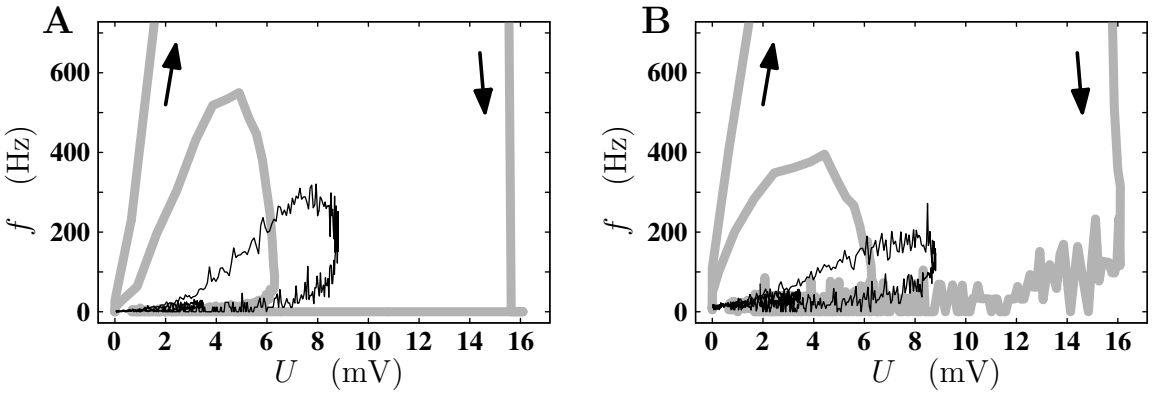

Figure 9.7 Development of spike intensity in response to pulse packet input at different levels of membrane potential fluctuations σ_V. **B** (f, U) curves of Fig. 9.6 combined into a single graph. Gray curves show data for $\sigma = 0\,\text{ms}$ (left column in Fig. 9.6, intensity of upper graph truncated), black curves for large σ (right column in Fig. 9.6). Arrows indicate direction of time. At this scale, intensity on up- and down-slope caused by $(45, 5\,\text{ms})$ (bottom right graph in Fig. 9.6) cannot be differentiated (blackening between $U = 0 \ldots 4\,\text{mV}$). **A** Same analysis and input parameters as in **B** for smaller σ_V $(= 2.5\,\text{mV})$. Intensity is lower at small U but reaches larger peak values (6000 Hz on truncated curve) compared to the corresponding curves in **B** $(\sigma_V = 4.5\,\text{mV})$ on the down-slope intensity is reduced. The figure illustrates the limited predictive power of U concerning f.

packet with 115 spikes (upper left panel) causes an intensity of about 2000 Hz at 6 mV and is still on its way to peak intensity.

Let us summarize our results for the intensity describing the response of the integrate-and-fire model to pulse packet input by displaying the graphs for different input parameters (a, σ) in a single diagram. Fig. 9.7 **B** corresponds to the data shown in Fig. 9.6. The range of different intensity values available at a single value of U now becomes apparent. A well synchronized input packet with low packet potential amplitude $(45, 0\,\text{ms})$ can generate a larger peak intensity than an input packet causing a larger packet potential amplitude but being less synchronized $(115, 5\,\text{ms})$. There is intensity on the down-slope of the packet potential, albeit on a much smaller scale than on the up-slope. Fig. 9.7 **A** displays the results for the same sets of input parameters but for our standard value for membrane potential fluctuations $\sigma_V = 2.5\,\text{mV}$. The most prominent difference between the two levels of membrane potential fluctuations is the reduction in intensity on the down-slope for the smaller σ_V. A possible explanation of the effect would be that larger fluctuations ($\sigma_V = 4.5\,\text{mV}$ compared to $\sigma_V = 2.5\,\text{mV}$) increase the probability that threshold is reached on the down-slope if the neuron failed to reach threshold on the up-slope. The response to input packet $(115, 5\,\text{ms})$ reaches a larger peak intensity at $\sigma_V = 2.5\,\text{mV}$ than at $\sigma_V = 4.5\,\text{mV}$. We already argued in Sec. 5.2 that the broader distribution of membrane potential values at $\sigma_V = 4.5\,\text{mV}$ increases the probability that the input packet impinges on the neuron in a state too polarized to reach threshold. The observed narrowing of $f(U)$ for $\sigma_V = 2.5\,\text{mV}$ compared to $\sigma_V = 4.5\,\text{mV}$ may be explained by the stronger concentration of membrane potential values around the mean at $\sigma_V = 2.5\,\text{mV}$.

We should reiterate that the effects summarized above are based on an analysis of the free intensity and, therefore, cannot be explained by refractoriness. An intensity model based only on the instantaneous value of membrane potential would collapse the observed

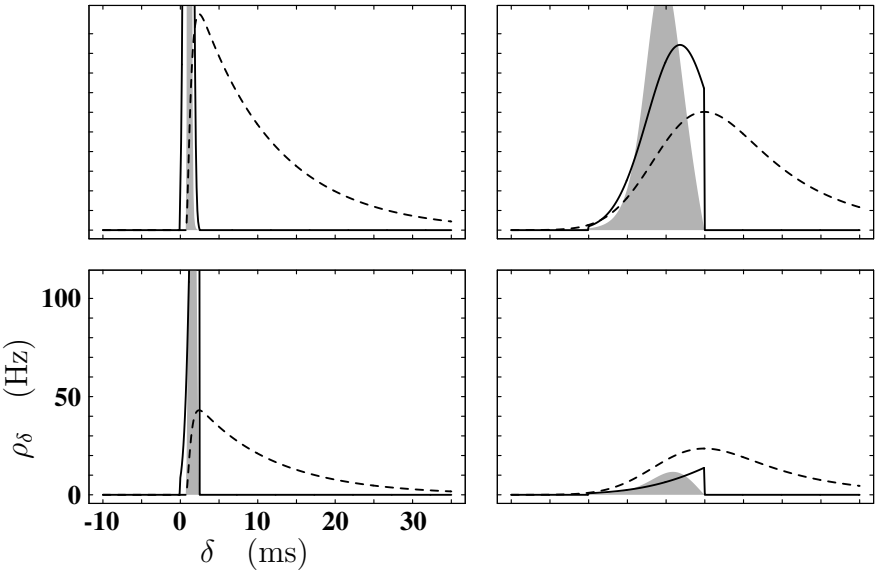

Figure 9.8 Comparison of the time course of the packet potential and the resulting spike response of the slow fluctuations model. Same input parameters and arrangement of panels as in Fig. 9.4, $\sigma_V = 2.5\,\mathrm{mV}$. Dashed black curve is the membrane potential excursion (packet potential) $U(\delta)$ caused by the incoming pulse packet (a, σ). The origin of the temporal axes is defined by the onset of packet potential up-slope in linear approximation (9.5). Solid black curve is the spike probability density ρ_δ computed for the linear up-slope, peak values (not shown) in left column are: 400 Hz (bottom) and 1100 Hz (top). Scaling of ρ_δ-axis and relative scaling of ρ_δ and U identical to Fig. 9.4. For a large number of input spikes (top row), ρ_δ exhibits a maximum on the up-slope. At the peak of the packet potential, ρ_δ obtains a non-zero value and discontinuously drops to zero (by definition) for later times. The gray area represents the time course of the spike probability density taking into account the detailed shape of the up-slope, peak values (not shown) are: 500 Hz (bottom left), 3100 Hz (top left), and 130 Hz (top right). After reaching a maximum on the up-slope of U, ρ_δ continuously declines before it vanishes at the peak of the packet potential in all cases.

complexity of Fig. 9.7 to a single curve (function) without hysteresis.

Intensity in the Slow Fluctuations Model

The slow fluctuations model yields an expression for spike probability density ρ_δ not involving the concept of an intensity. One may ask the question if an analysis of this model in terms of intensity gives us insight into the ingredients of a successful intensity function and aspects of the integrate-and-fire dynamics that cannot be explained in the slow fluctuations model.

Let us start by comparing the time course of ρ_δ to the time course of the packet potential as we have done for the I&F dynamics in Fig. 9.4. In the linear approximation of the up-slope of the packet potential (9.6), the onset of the voltage and spike response is well defined. Therefore, $\delta = 0\,\mathrm{ms}$ is immediately used as the origin of the temporal axes in Fig. 9.8. At negative times ρ_δ is zero because spontaneous activity is not included in the model. Also by definition, probability density is zero on the down-slope of the packet potential. ρ_δ reaches a peak on the up-slope if the amplitude of the packet potential is large enough to drive the membrane potential to threshold starting from initial values below the mean of the membrane potential distribution. The two cases for large spread of input spikes (Fig. 9.8,

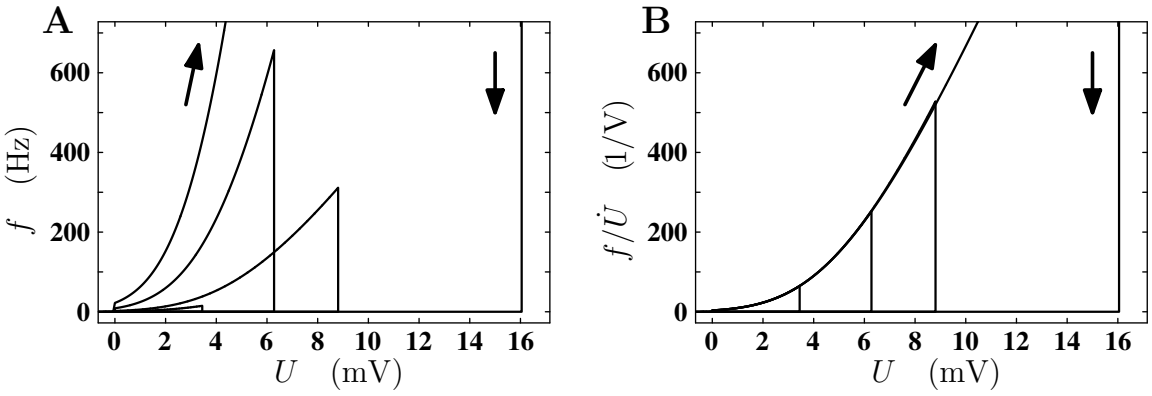

Figure 9.9 Dependence of spike intensity f on membrane potential excursion U in the slow fluctuations model assuming a linear up-slope of the packet potential. **A** (f, U)-representation with scaling and input parameters identical to Fig. 9.7 **A** showing corresponding curves for the integrate-and-fire model. f exhibits an expansive dependence on U. At a given U, however, intensity still depends on input parameters (a, σ) (cf. Fig. 9.7 **A**). The peak intensity occurs at peak voltage, no saturation in peak region is observed (data not shown for curve closest to arrows). **B** Ambiguity of f with respect to U is completely removed if the quotient $f/\dot{U}$ is considered. Same input parameters as in **A**. $\dot{U} = a\widehat{u}\widehat{v}_\sigma/\tau_\sigma$ depends on (a, σ) and is constant on the up-slope. Small deviations between $f/\dot{U}$ for different (a, σ) are due to limited precision of the numerics.

right column) exemplify the fact that in the linear up-slope approximation the probability density obtains a finite value at the peak of the packet potential and is truncated to zero for later times. This is in contrast to the probability density of I&F dynamics which exhibits a smooth decline in the peak region of the packet potential. The formal expression for ρ_δ (9.4) shows that spike probability vanishes when the derivative of the packet potential is zero. Thus, the linear approximation of the up-slope causes an overestimation of probability density in the peak region of the packet potential. The finite slope at $\delta = 0\,\mathrm{ms}$ is of minor importance because in this regime ρ_V is negligible.

The behavior of the intensity in the peak region of the packet potential is of interest in the comparison to I&F dynamics (see Fig. 9.4). To distinguish general properties of the slow fluctuations model from effects introduced by the linear approximation we will for the remainder of the chapter consider the exact shape of the up-slope in parallel to the approximation. According to (9.4) ρ_δ can also be solved for the exact shape of the up-slope. For convenience we define $\delta = 0\,\mathrm{ms}$ as the onset of the response, using the rise time of the linear approximation τ_σ for the coordinate transformation as in (9.6). The resulting probability density is shown in Fig. 9.8 as the gray area. As expected from the above discussion the exact shape leads to a narrowing of the density, approaching zero at the peak of the packet potential and at the onset.

Inserting ρ_δ for the linear up-slope (9.9) into (9.39) yields a surprisingly simple expression for the intensity

$$f(\delta) = \frac{a\widehat{u}\widehat{v}_\sigma}{\tau_\sigma} \cdot \frac{\rho_V(\theta - \frac{a\widehat{u}\widehat{v}_\sigma}{\tau_\sigma}\delta)}{1 - \int_{\theta - \frac{a\widehat{u}\widehat{v}_\sigma}{\tau_\sigma}\delta}^{\theta} \rho_V(V)\,dV}. \tag{9.41}$$

Results for our four typical input packets corresponding to the graphs in Fig. 9.7 **A** are shown in Fig. 9.9 **A**. The qualitative and quantitative correspondence of the two figures is

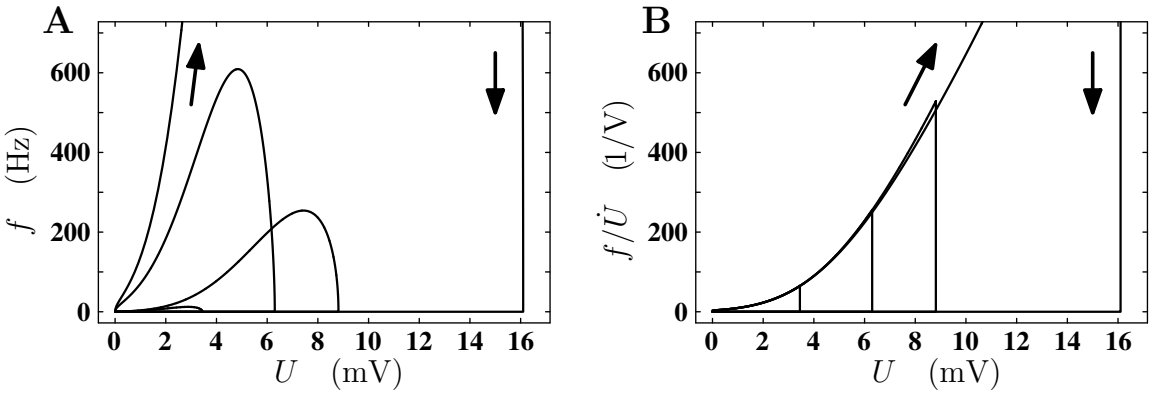

Figure 9.10 Dependence of spike intensity f on membrane potential excursion U in the slow fluctuations model assuming the detailed shape of packet potential up-slope. Graphs and input parameters identical to Fig. 9.9. **A** For a given pair (a, σ), f is not a monotonous function of U. Intensity reaches a maximum on the up-slope, decays, and vanishes at the peak voltage. Collection of (f, U)-curves is in agreement with the results for the integrate-and-fire model (Fig. 9.7 **A**), see Fig. 9.11. **B** As in Fig. 9.9 **B**, ambiguity of f with respect to U is completely removed if the quotient $f/\dot{U}$ is considered. In contrast to Fig. 9.9 **B**, $\dot{U}$ is a function of time. $f/\dot{U}$ recovers the expansive dependence on U and is identical for the linear and the detailed model of the up-slope of the packet potential. Small deviations between $f/\dot{U}$ for different (a, σ) are due to limited precision of the numerics.

immediately apparent. The hysteresis is trivially introduced by defining probability density to be zero on the down-slope of the packet potential. However, the fact that a steeper up-slope results in a larger intensity is an inherent property of the model. The intensity is not an instantaneous function of membrane potential only. Indeed (9.41) is a product of the (constant) slope of the membrane potential excursion and a term depending only on the instantaneous value of the packet potential U

$$f/\left(\frac{a\widehat{u}\widehat{v}_\sigma}{\tau_\sigma}\right) = \frac{\rho_V(\theta - U)}{1 - \int_{\theta-U}^{\theta} \rho_V(V)\, dV}. \tag{9.42}$$

Fig. 9.9 **B** illustrates how, in the parameter regime of interest, (9.42) maps the complex dependence of intensity on the input parameters a and σ to a single expansive function of U.

Repeating the calculation which led to (9.41) for the exact shape of the up-slope demonstrates that a relation of the type (9.42) holds for arbitrary (monotonous) up-slopes of the packet potential

$$f(U, \dot{U}) = \dot{U} \cdot \frac{\rho_V(\theta - U)}{1 - \int_{\theta-U}^{\theta} \rho_V(V)\, dV}. \tag{9.43}$$

In our formal expression for the intensity (9.39) f carries the argument δ because it may be an explicit function of time. However, (9.43) demonstrates that the intensity we constructed fully qualifies as a component of an intensity model in the sense that it only depends on the instantaneous properties of the membrane potential excursion. In contrast to earlier models, the instantaneous value of the packet potential and its derivative determine spike intensity. f is an expansive function of U (cf. Fig. 9.10 **B**) and proportional to $\dot{U}$.

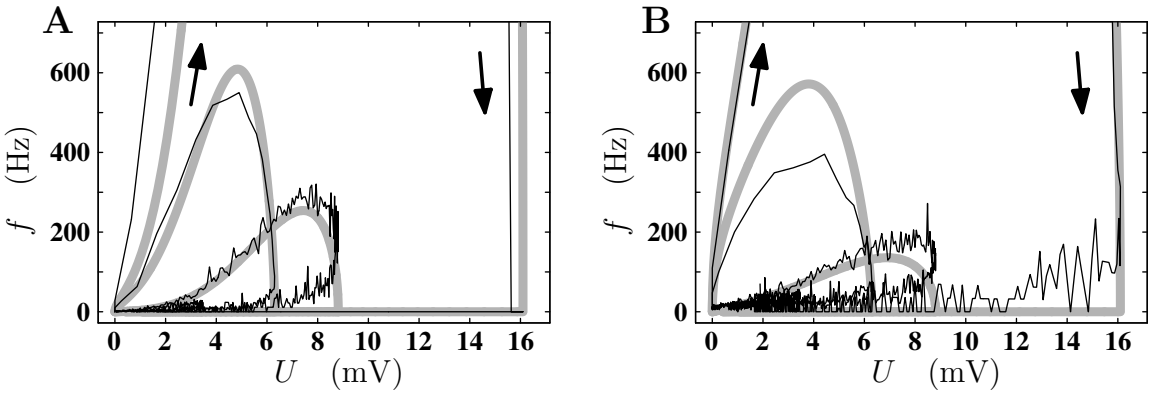

Figure 9.11 Comparison of spike intensity in the integrate-and-fire model and the slow fluctuations model at different levels of membrane potential fluctuations σ_V. Same graphs and input parameters as in Fig. 9.7. The black curves show simulation results for the integrate-and-fire model (same data as in Fig. 9.7). Gray curves show corresponding results for the slow fluctuations model. **A** $\sigma_V = 2.5\,\mathrm{mV}$, gray curves are the redisplayed curves of Fig. 9.10. The two models are qualitatively and quantitatively in good agreement. The slow fluctuations model does not make predictions for the intensity on the down-slope. **B** $\sigma_V = 4.5\,\mathrm{mV}$, gray curves computed as in Fig. 9.8. Deviations are more pronounced than in **A**.

Fig. 9.10 displays the results for the same situation as in Fig. 9.9 for the exact up-slope of the packet potential. Similar to the results for the probability density (Fig. 9.8) intensity now exhibits a maximum before the packet potential reaches its maximum and drops to zero at the peak of the voltage excursion. Fig. 9.10 **B** verifies that voltage and derivative dependence of f can be separated.

Finally, we can directly compare the intensity computed for the slow fluctuations model to the results for I&F dynamics. Fig. 9.11 shows the two sets of curves superimposed for two different levels of membrane potential fluctuations. The intensity model captures the details of the I&F dynamics. In particular also the regime shortly before the peak of the packet potential is reached is well described. The deformation in the shape of intensity curves caused by an increase in membrane potential fluctuations is well captured. The intensity model slightly overestimates the responsiveness of the neuron in the peak region of intensity. The effect is more pronounced at large σ_V. This may be due to the presence of spontaneous activity which we have neglected in our intensity model. Spontaneous spikes occurring before the pulse packet arrives render the neuron refractory and thereby reduce the intensity f as defined here. The fact that spontaneous activity increases with membrane potential fluctuations is consistent with the observed reduction in intensity (compare panels **A** and **B** in Fig. 9.11).

Note that we derived an expression for intensity in terms of the parameters of the I&F model without the need of adjusting model parameters or introducing arbitrary free parameters. Interestingly, in (9.43) the conversion of units from V^{-1} to s^{-1} is naturally provided by the derivative of the packet potential. In an early ansatz of Abeles (1982b) the integral $\int_{\theta-U}^{\theta} \rho_V(V)\,dV$ is used to model the excitability of the neuron. It is argued that the conversion of this quantity to units of spike probability density should be provided by the inverse of a time constant related to the refractoriness of the neuron. While the model was successfully applied (Boven & Aertsen, 1990) to study the response to a single synaptic event

in dependence of background activity, it fails to give results consistent with I&F dynamics for input packets with varying number of spikes. For a different number of input spikes a different constant is required to give accurate results, a fact which in the light of $\dot{U}$ is now easy to interpret.

The study of the relationship between the slow fluctuations model and an intensity model enabled us to gain insight into the origin of the spikes occurring on the down-slope of the packet potential and to differentiate the roles of model components like refractoriness, membrane potential fluctuations, and the derivative of the packet potential. The construction of a full intensity model incorporating spontaneous activity, the down-slope, and finite refractoriness is outside the scope of the present study and may require more advanced methods as discussed in the works of Rotter (1994), Gewaltig (2000), Plesser and Gerstner (2000), and Câteau and Fukai (2001). However, we are now in possession of considerable constraints a successful intensity model is required to fulfill.

Chapter 10

Discussion

10.1 Results and Interpretation

10.1.1 Summary of Results

At the outset of the present study we asked the question in which sense a propagating volley of synchronous spikes represents a stable state (attractor) of the network. It turns out that it is sufficient to characterize volleys of synchronous spikes ("pulse packets") by two variables: the number of spikes in the packet a, and a measure for their temporal spread σ. Propagation of synchronous activity in the network is then described by the sequence of (a_i, σ_i) pairs, occurring in consecutive neuron groups, consisting of w neurons each. For an analysis of the synchronization dynamics in the network, the equations describing network activity should be expressed in terms of the variables a and σ. The iterative nature of the network structure suggests the construction of an iterative mapping T_w, defining the transformation a pulse packet undergoes while propagating from group i to group $i + 1$. A stationary state is reached if the packet (a, σ) traveling from group to group is no longer changing, neither in the number of spikes, nor in its temporal dispersion. In this sense network activity has reached a fixpoint. If the fixpoint is surrounded by a basin within which all initial activity ultimately reaches the fixpoint, it is an attractor of the system. It should be pointed out that this attractor is different from the well known Hopfield-attractor (Hopfield, 1982) of network activity in two important aspects. First, the Hopfield-attractor describes a state of stationary spike rates, whereas in our case transients in activity are considered. Second, the Hopfield-attractor describes a stationary rate configuration in neuron space, whereas in the case of pulse packet activity, it describes a propagating spike volley, transmitted from one neuron group to the next, each neuron typically participating with one spike per volley.

Chap. 3 defines a new single neuron transmission function T, describing the neuron's response to transient input. The next chapter (Chap. 4) shows that knowledge of T is sufficient to construct the propagator for pulse packets T_w. This iterative mapping describes network activity in the mean-field picture. It provides the expected number of response spikes and the width of the distribution that the individual spike times are drawn from. In turn, it is constructed under the assumption that a input spikes drawn from a distribution with temporal spread σ affect the target neuron, irrespective of the detailed configuration of spike times in the input packet. In addition, we assume that the distribution of response spikes can

be approximated by a Gaussian. This assumptions seems critical, because in the mapping T_w, the variables (a, σ) are in each iteration step assumed to describe a Gaussian packet. If the group response is not Gaussian one can imagine a scenario where T_w predicts the decay of synchronous activity in the mean whereas the activity in actual network simulations stabilizes. This could, for example, be the case if the distribution of the response spike has a considerable tail, which leads to a large estimate of σ and, at the same time, the peak region of the distribution, which effectively drives the neuron in the succeeding group, is quite narrow. Also the reverse situation is conceivable. In order to exclude these possibilities, a model was desired in which the full shape of the pulse packet can be iterated, and the invariant pulse packet shape can directly be observed (Gewaltig, Diesmann, Rotter, & Aertsen, 1997).

Gewaltig (2000) developed such a continuous model for a neuron group, transforming an incoming pulse density to an outgoing pulse density. The model is based on a stochastic description of the single neuron, in which the spike "intensity" (see also Rotter, 1994) is a function of the deterministic membrane potential caused by the incoming pulse density. All stochasticity is captured in the dependence of the intensity f on the instantaneous membrane potential: $f(U(t))$. Independence of stochastic effects influencing the system at times t_1 and t_2 is assumed. The resulting dynamics of the pulse density indeed reproduces the four characteristic routes of network activity shown in Fig. 1.3. Pulse density propagations mapped into the (a, σ)-space reproduce the state space structure of T_w. There is an invariant pulse density corresponding to the (a, σ)-attractor. Hence, we can be confident that the (a, σ) description of pulse packet propagation captures the network dynamics in sufficient detail. A different approach to test the validity of the (a, σ) description is to reconstruct the state-space portrait from network simulations (like the examples in Chap. 1). This allowed us to verify that network simulations correspond well to the predictions of the iterative mapping, and to characterize the variability in individual realizations of network activity (Gewaltig, 2000; Gewaltig, Diesmann, & Aertsen, 2001a; Gewaltig, Diesmann, & Aertsen, 2001b, see also Chap. 8). Thus, the results of Chap. 4 enable us to reduce the detailed dynamics of the spiking neural network to a deterministic two-dimensional iterative mapping, describing the dynamics in the mean.

Robustness is demonstrated by an analysis of the (a, σ) state space. For realistic parameter values, an attractor close to full activation and at some residual temporal spread is surrounded by a basin of attraction. A separatrix divides the state space into a regime where activity synchronizes and reaches the attractor, and a regime where activity eventually vanishes. The propagator comprises two classes of parameters. First, single neuron properties such as membrane time constant, rise time of the post-synaptic current, and spike threshold. Second, network properties like the number of neurons in a group and the amount of fluctuations of the membrane potential due to background activity. Single neuron parameters and the statistics of membrane potential fluctuations are experimentally accessible. However, the experimental literature shows that these parameters are not universal. Instead, it appears that for each parameter there is a plausible range, the specific value being dependent on the type of neuron, the type of synapse, or even on the state of the unit. The number of neurons per group cannot directly be determined experimentally, and is a central parameter in anatomical considerations about the plausibility of feed-forward subnetworks. Therefore, the parameter dependence of the dynamics is an important aspect of the present study. The

dependence of the dynamics on the group size w is studied in Chap. 4. It turns out that w is a bifurcation parameter of the system. The attractor for synchronous activity requires a certain minimal group size. The effect of membrane potential fluctuations σ_V is studied in Chap. 5. Here, the bifurcation scenario is more complex and, in addition, exhibits a characteristic dependence on the parameter w. At small group sizes, increasing fluctuations rapidly destroy the attractor, while for large group sizes moderate fluctuations actually increase the basin of attraction before it shrinks again at even larger fluctuations. The discussion of the noise-free case (Chap. 6) provides insight into several aspects of the synchronization dynamics. We can define the packet potential as the membrane potential excursion, caused by an incoming pulse packet (a, σ). The minimal number of spikes required for the packet potential to reach spike threshold at a given σ defines the separatrix in the noise-free case.

At finite levels of membrane potential fluctuations, position and curvature of the separatrix deviate from the noise-free case. However, the shape of the separatrix observed in the noise free case remains the dominant feature of the state space structure. Therefore, the shape of the post-synaptic potential, which is experimentally accessible, determines the structure of state space (Chap. 6). In the framework of the noise-free case, a simple estimate is derived for the minimal group size. One would expect that the magnitude of the effect a single neuron in group i exerts on a single neuron in group $i + 1$ should enter this minimal group size. Indeed, the minimal group size is proportional to the ratio of the amplitude of the post-synaptic potential and the distance from membrane potential mean to spike threshold. The constructive effect of the membrane potential fluctuations (background activity) on the propagation of synchronous activity can be understood by analyzing how the a-sections of the iterative mapping (i.e. the activation curves) develop under the transition to finite background activity.

A parameter summarizing many details of the single neuron model is the rise time of the post-synaptic potential τ_0. Chap. 7 shows that the rise time controls the residual temporal spread in the attractor. This effect can be explained by a simple model (Chap. 9) for the interaction of the packet potential and the membrane potential fluctuations. In this model, the resulting temporal spread of the response spike is proportional to the magnitude of the fluctuations and inversely proportional to the slope of the packet potential.

The study of the rise time of the post-synaptic potential also reveals another important property of the packet potential. In Chap. 6 we have seen that the separatrix is determined by the dependence of the packet potential amplitude on the temporal spread of the input packet. For vanishing temporal dispersion of the input, the amplitude of the packet potential is determined by the amplitude of the post-synaptic potential. Here, the rise time of the post-synaptic potential does not affect the position of the separatrix. However, at large temporal dispersion the amplitude of the packet potential is determined by the area of the post-synaptic potential. Thus, the effect of the rise time on the position of the separatrix depends on the normalization of the post-synaptic potential. If the rise time is increased under conservation of PSP amplitude, the area of the post-synaptic potential increases with rise time. Consequently, we expect the separatrix to bend to lower values of a when the input spread becomes comparable to the temporal extent of the post-synaptic potential. If, however, the rise time is increased under conservation of PSP area, the amplitude of the packet potential remains unaffected, except for low temporal dispersion. Therefore, the increased

rise time now mainly affects the temporal dispersion of the response. The two conservation schemes lead to different bifurcation scenarios. Under amplitude normalization the attractor moves to larger temporal spread and the basin of attraction extends to lower values of a. The situation is dramatically different under area normalization. Here, the attractor also moves to larger temporal spread. However, the separatrix rapidly moves upwards to larger a, and eventually destroys the attractor. This destruction of the attractor due to an increase in rise time with practically invariant activation curves is a further confirmation that both variables a and σ are required to describe the synchronization dynamics, and that any single one does not suffice.

Fig. 10.1 summarizes the effect of the neuron and network parameters on the synchronization dynamics. The three bifurcation parameters distinctly operate on the position of the fixpoints. w controls the activity in the attractor and the temporal spread reached in the saddle point. The bifurcation is governed by the movement of the saddle point to the smaller temporal spread reached in the attractor. For the bifurcation parameter τ_0, the situation is reversed (under area normalization). τ_0 controls the residual temporal spread in the attractor and the activity at the saddle point. The bifurcation is governed by the movement of the attractor to the larger temporal spread reached at the saddle point. The influence of σ_V on the position of the attractor is small. While increasing σ_V monotonically shifts the saddle point to larger a, the temporal spread at the saddle point exhibits a non-monotonic movement. Initially, it shifts to larger temporal spread, reaches a maximum, and consecutively approaches the small temporal spread in the attractor. The extent of the excursion of the saddle point into the regime of large temporal spread is controlled by w. Non-monotonicity of the development is reflected in the dependence of the size of the basin of attraction on the various bifurcation parameters. Under variation of w, the basin is continuously increasing or decreasing, respectively. Variation of σ_V results in a clear maximum of basin size, where two opposing changes in the distribution of membrane potential values compensate each other (Chap. 5).

10.1.2 Spatio-Temporal Spike Patterns

Having successfully answered the methodological questions posed in the introduction, we can now turn to the question whether locally feed-forward structures as studied here are plausible generators of spatio-temporal spike patterns in the light of the available experimental data (Sec. 1.5). One of the prominent features in experimentally observed spike patterns is the precision of spike timing in different realizations of the same pattern (Abeles, Bergman, Margalit, & Vaadia, 1993; Prut et al., 1998). The reported patterns have a precision of ± 1 ms. For data obtained with a temporal resolution $h = 1$ ms, this translates to the statement that most of the realizations of a specific spike in a pattern fall into a time window of $\Delta = 3$ ms width. In some studies in the motor cortex spike synchronization appears to be somewhat less precise (Riehle, Grün, Diesmann, & Aertsen, 1997; however see Riehle, Grammont, Diesmann, & Grün, 2000). Let us reconsider the relation of the precision of spike timing observed in the attractor of the iterative mapping and the temporal spread observed in physiological spike patterns. In the context of the synfire model, the repeated occurrence of simultaneous spikes (coincidences) above chance level (Grün, Diesmann, & Aertsen, 2002a) is interpreted as activity recorded from units of the same neuron group.

Parameter	Bifurcation Diagram	Condition
w	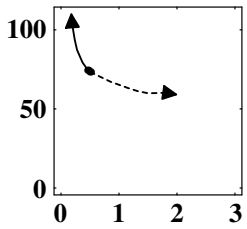	$\widehat{u} = \text{const}$
σ_V	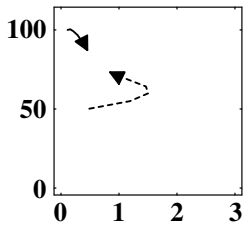	$w \approx w_*$
	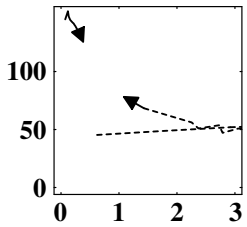	$w > w_*$
τ_0	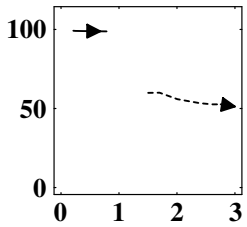	$\widehat{u} = \text{const}$
	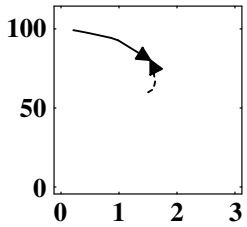	$F^1 = \text{const}$

Figure 10.1 Summary of parameters determining the synchronization dynamics. w specifies the number of neurons in each group of the feed-forward network. With decreasing w, the attractor (solid) moves to a lower number of spikes (vertical) and the saddle point (dashed) to smaller temporal spread (horizontal in ms). Here, a constant amplitude ($\widehat{u}$) of the post-synaptic potential (PSP) is assumed. Increasing w increases the basin of attraction. σ_V describes the membrane potential fluctuations. Movement of the saddle point is non-monotonic, it undergoes an excursion to large temporal spread. The size of the basin reaches a maximum, the effect being stronger for w well above w_* characterizing the number of neurons required for stable propagation. Under amplitude normalization of the PSP, increasing the rise time of the PSP τ_0 shifts the attractor and the saddle to larger temporal spread. Under area (F^1) normalization, the situation is reversed, compared to the w-bifurcation. The attractor now moves to larger temporal spread, and the saddle point moves to a larger number of spikes.

Thus, the temporal spread in the attractor should be directly comparable to the precision of spike coincidences. Because of the Gaussian nature of the spike time distribution, the observation that most of the spikes are found within a 3 ms time window would result in the requirement that the temporal spread in the attractor is

$$\sigma \approx \frac{1}{\sqrt{2}} \cdot \frac{1}{6}\Delta = 0.35\,\mathrm{ms}. \tag{10.1}$$

The parameter of our model most effectively controlling the temporal spread is the rise time of the post-synaptic potential (Chap. 7). The experimentally observed temporal spread is in good agreement with PSP rise times of about 2 ms (Fig. 7.7). The factor $1/\sqrt{2}$ in (10.1) takes into account that we are observing the difference of two spike time realizations, and not a spike time realization with respect to the origin of the underlying distribution.

The iterative mapping is constructed on the basis of single neuron response properties. It does not contain direct information about the build-up of temporal jitter in the network with respect to some external reference. In other words, in the iterative mapping, the time variable is eliminated from the dynamics. In a temporal spike pattern, spikes may occur at intervals of up to a few hundred ms. Assuming a synaptic delay of 2 ms, tens of neuron groups may need to be passed to transport activity from the neuron group emitting the first spike in the pattern to the neuron group emitting the second spike. In the framework of the iterative mapping, the locking of a spike in the lth group to a spike in the 0th group (cf. Fig. 1.3) can be estimated as follows. Let us assume that the 0th group is ignited at time 0 (center of the Gaussian spike time distribution). With a synaptic delay τ_d, the expected arrival time of the packet at the 1st group is τ_d with a jitter of arrival time $\sigma_0/\sqrt{w}$ (standard deviation of the mean). Here, we assume that we are in the attractor (invariant spread σ_0), and that practically all neurons are emitting a spike (invariant number of spikes $a_0 \approx w$). With respect to the origin, a response in the 1st group has a variance of $(\sigma_0/\sqrt{w})^2 + \sigma_0^2$. Triggering on a spike of the 0th group we have $(\sigma_0/\sqrt{w})^2 + 2\sigma_0^2$. Thus, for the temporal spread of a spike in the lth group with respect to a spike in the 0th group we have

$$\sigma_l = \sigma_0\sqrt{\frac{l}{w} + 2}. \tag{10.2}$$

The temporal jitter in spike locking σ_l is twice the intrinsic jitter σ_0 when the activity has passed $l = 2w$ groups. For our default group size of $w = 100$, this occurs in a group distance of 200 or, equivalently, in a spike distance of $200\tau_\mathrm{d} = 400$ ms. The effect is stronger in narrow groups (see the discussion of narrow groups below). In principle, analysis of the dependence of the variance σ_l^2 on the temporal distance of spikes in the patterns $l\tau_\mathrm{d}$ can be used to test the relationship predicted by the model. Assuming a fixed synaptic delay τ_d, estimations of w and σ_0 can be obtained from the coefficients of the fitting line. Fig. 10.2 illustrates such an analysis. However, variability in w and contributions to temporal jitter not considered in the model may require more advanced data analysis, or may even prohibit conclusive results. It is interesting, though, that we have derived here a relationship that enables us to use the electrophysiological data (spike patterns) to draw conclusions about anatomical structure (w). We were recently able to verify in network simulations (Gewaltig, Diesmann, & Aertsen, 2001b) that the build-up of temporal jitter in the locking of activity in feed-forward chains to

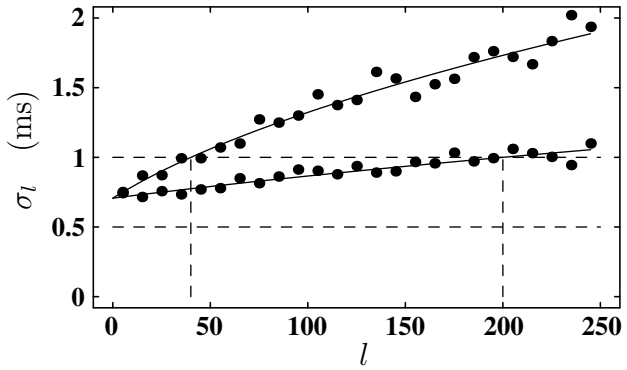

Figure 10.2 Illustration of possible analysis of temporal jitter in spatio-temporal spike patterns. Temporal jitter of two consecutive spikes in a pattern as a function of the number of intermediate neuron groups ($\propto$ temporal distance). Data points (dots) are obtained from simulations in which spike times of a neuron group are drawn from a Gaussian distribution of width σ_0, centered at the mean time of impact of the incoming pulse packet. Full activation of the neuron groups is assumed ($a_0 = w$). Number of groups l varied from 5 to 245 in steps of 10, intrinsic temporal jitter $\sigma_0 = 0.5\,\text{ms}$ (lower dashed horizontal line), 400 occurrences of each pattern are considered. Upper dots $w = 20$ neurons per group, lower dots $w = 100$. Solid curves represent the theoretical relationship. Vertical dashed lines mark the number of groups required (40, 200) for the temporal jitter in the pattern to equal twice the intrinsic jitter ($\sigma_l = 1\,\text{ms}$, upper dashed horizontal line). Minimal jitter observed at $l = 0$ independent of w is $\sqrt{2}\sigma_0$.

an initial stimulating pulse packet is indeed small, as predicted by (10.2). Considerable jitter occurs if the stimulating pulse packet is weak and, therefore, on its way to the attractor the standard deviation of impact time is still large. The model of spike synchronization predicts a residual temporal spread (σ in the attractor). Hence, experimental multiple single unit data analyzed for spatio-temporal spike patterns (including coincidences) with a gradually increasing measure of the allowed temporal spread should exhibit a characteristic dependence of the number of patterns on the allowed jitter width. A strong initial increase in the number of patterns should reduce to the expected increase when the allowed jitter width has passed the natural precision in the attractor (assuming comparable measures for jitter width and precision in the attractor). An increase in the number of patterns is expected even in the absence of correlated activity, due to the increased probability to find random (background) spikes at the appropriate distances. The significance of the number of patterns, however, should show a maximum at the point where jitter width corresponds to temporal precision in the attractor. First results (Prut, 1995; Grün et al., 1999) indicate that a preferred synchronization width indeed exists and can be measured. The latter study provides a clear example where the significance of the number of coincidences found in a data set exhibits a global maximum at particular jitter width. However, appropriate tools are still under development (Grün & Diesmann, 2000) and no systematic study has been carried out yet.

10.1.3 Connection to Subthreshold Dynamics

From the above discussion we can conclude that our model of spike synchronization consistently connects experimental measurements at two levels of description: temporal precision of spike patterns observed in multiple single unit recordings and rise time of the post-synaptic

potential as observed in spike triggered averaging (STA) of intracellular recordings. Rise times of individual post-synaptic potentials reported in the literature range from fractions of a ms to several ms (Fetz, Toyama, & Smith, 1991; Mason, Nicoll, & Stratford, 1991; Matsumura et al., 1996). Fig. 10.1 shows that a large rise time alone does not prevent the occurrence of spike synchronization, it merely limits the temporal spread reached in the attractor. If the amplitude of the post-synaptic potential and the number of neurons per group allow for it, synchronous activity can be stabilized at large temporal spread. The range of stable temporal spreads illustrated in Fig. 10.1 well covers the range observed in electrophysiological data. Recently, the technology is becoming available to record intracellularly from neurons in the mammalian cortex *in vivo* (e.g. Azouz & Gray, 1999; Bringuier et al., 1997; Matsumura et al., 1996; Lampl, Reichova, & Ferster, 1999; Heck, Léger, Stern, & Aertsen, 2000). Combination of this technology with extracellular multiple single unit recordings will greatly enhance testability of model predictions. Requiring simultaneous consistency of the model on both, the network level (spike patterns) and the level of subthreshold processes in individual neurons (e.g. PSP rise time, PSP amplitude, also see discussion of membrane potential fluctuations below) would equip us with more stringent constraints than can be imposed today. As an example, being able to correlate pattern precision with the rise time of the typical post-synaptic potential in different preparations (brain region, species) will provide a test of such multiple level spanning predictions. Amplitudes of post-synaptic potentials reported in the experimental literature span an order of magnitude from below 0.1 mV to the multiple mV scale (e.g. Fetz, Toyama, & Smith, 1991; Thomson, Deuchars, & West, 1993; Markram & Tsodyks, 1996). This range probably reflects the natural inter-synaptic variability and possibly also differences with age of the preparation (newborn vs. mature). It should be noted that measurements are mostly obtained *in vitro* (see Léger, Stern, Aertsen, & Heck, 2002 for differences of factor 2 or more between down-state ($\sim$ *in vitro*) and up-state ($\sim$ *in vivo*)). In addition the PSP amplitude is subject to plasticity. In the present study, PSP amplitude was held constant at a value closer to the lower end of the plausible regime. We were able to demonstrate that for the attractor to exist, synaptic potentials in a feed-forward subnetwork are not required to be of larger amplitude than the synaptic potentials assumed for the background activity. We also showed that a scaling law connects the PSP amplitude $\widehat{u}$ and the number of neurons in a group w. Network dynamics as described by the iterative mapping is invariant under changes in $\widehat{u}$, provided the product $w\widehat{u}$ remains unchanged (Chap. 8). In contrast, the locking between spikes from different neuron groups discussed above (10.2) directly depends on w. In a network where w is reduced from 100 to 25, and amplitudes of intra-chain synapses are scaled up accordingly, the state space portrait is practically unchanged. However, the locking of synchronous activity to the stimulus now degrades two times faster ($2/\sqrt{100} = 1/\sqrt{25}$). Thus, with knowledge about PSP amplitude independent estimates of $\widehat{u}$ and w can be obtained.

10.1.4 Existence of Feed-Forward Subnetworks

The iterative mapping describes the development of spiking activity in feed-forward structures as a deterministic system. The last paragraphs showed that the finite number of spikes has to be taken into account to understand the effects of time locking. With the dynamics of the mean unchanged, locking deteriorates faster in narrow chains. This raises the

question how useful the deterministic description is to characterize the stochastic spiking activity in the network. Chap. 8 extends the model by a stochastic component to study the survival probability of activity on its way into the attractor. Analytical considerations and Monte-Carlo simulations show that the system indeed behaves quasi-deterministically. At the location of the separatrix, computed for the deterministic case, the survival probability shows a sharp transition from vanishing survival probability outside the basin of attraction to a survival probability approaching unity inside the basin of attraction. Only close to the separatrix may the activity be driven out of or into the basin of attraction by random fluctuations. Results are in good agreement with network simulations (Gewaltig, 2000; Gewaltig, Diesmann, & Aertsen, 2001b). The slope of the survival probability at the separatrix becomes less steep with decreasing numbers of neurons per group w (under $\widehat{u}$ compensation). An intuitive explanation is that in a group of size w, each spike contributes a weight of $1/w$ to the group's activity. Thus, if a neuron fails to emit a response spike in a narrow chain, a larger fraction of the total activity is missing. In the context of locking, the effect shows up in the temporal domain. Here, the main effect is on the variability of the group activity.

Minimal group size is an important parameter for anatomical considerations. Using arguments from random graph theory (Palmer, 1985; Janson, Rucinski, Luczak, & Uczak, 2000) and anatomical data on cortical connectivity (e.g. Braitenberg & Schüz, 1998; Hellwig, 2000) Abeles (1991) has shown for globally random networks and Hehl et al. (2001) for random networks with a space constant that completely connected feed-forward subnetworks are very unlikely to exist in the neocortex. At the same time, both studies show that "incomplete" or "diluted" chains are certain to exist. The effect can be traced back to the well known threshold-like appearance of subnetwork structures in random graphs. The above findings are critical in the light of the common assumption that in the adult cortex new synapses cannot be formed (however, recent studies (Matus, 1999; Maletic-Savatic, Malinow, & Svoboda, 1999; Engert & Bonhoeffer, 1999) indicate that the network may be more plastic than hitherto thought). Moreover, synaptic plasticity can strengthen the synapses of a chain, thereby reducing the required number of neurons per group. In fact, plasticity which depends on the relative timing of the pre- an the post-synaptic spike (Markram, Lübke, Frotscher, & Sakmann, 1997; Zhang et al., 1998) has recently attracted much interest (Song, Miller, & Abbott, 2000; Rubin, Lee, & Sompolinsky, 2001; Gütig et al., 2001) and seems to be suited to strengthen synchronous activity in feed-forward subnetworks. However, classical synaptic plasticity requires that the neuronal substrate, the graph, is already installed. Furthermore, plasticity can strengthen individual synapses only within certain limits, and we have seen above that too narrow chains should be avoided because of their increased susceptibility to noise. The charm of weak intra-chain synapses would be that individual neurons can be members of a large number of chains, allowing for the superposition of chains and potentially richer combinatorics, which might be of functional relevance (Bienenstock, 1991b; Bienenstock, 1996).

Thus, if complete chains do exist in the cortex, they are probably generated by a specific growth process during development. It is possible that the global picture of a cortical column still retains many properties of a random graph, because of the superposition of many locally feed-forward subnetworks with other subnetworks. Therefore, deviations from randomness may so far have been overlooked (we come back to this point in the outlook section). Note

that the above process is to be distinguished from the development of chains in a random network with initially homogenous distribution of synaptic weights (Bienenstock, 1991a; Bienenstock, 1995; Herrmann, Hertz, & Prügel-Bennett, 1995; Hertz & Prügel-Bennet, 1996), which is sometimes termed a "growth" process.

Because of the above considerations it seems useful to study diluted feed-forward networks as structures which do exist in random networks and at the same time do not require specifically strong synapses. Preliminary results indicate that diluted chains can sustain synchronous activity, and that their main features can well be described within the framework developed in the present study (Hehl, Aertsen, & Diesmann, 2001a). Their detailed dynamics is the subject of ongoing research (Hehl, Aertsen, & Diesmann, 2001b). As the simplest example, let us consider a chain where each neuron projects to dw' neurons in the consecutive group, and each neuron receives input from dw' neurons of the preceding group. Here, d is called the dilution factor ($0 \leq d \leq 1$). In this case, the dynamics in the chain is equivalent to the dynamics of a complete chain with group size $w = dw'$. The argument can be reversed: if the dynamics requires a minimal group size w_* and a dilution factor d is required by anatomy, then the minimal group size of an operational diluted chain is $w' = w_*/d$ (e.g. $w_* = 100$, $d = 0.3$: $w' = 300$). One may speculate that the main task of a structuring mechanism ("learning") would not be to strengthen connections in diluted feed-forward subnetworks, but to degrade connections to neurons receiving some, but insufficient ($< dw$), convergence from neurons of a preceding group. Thereby, activity would be focused on pathways that successfully transmit synchronous activity. Diffusive spread of activity triggering the inhibitory subnetwork is prevented. Neurons that by their anatomical connectivity do not qualify as members of a particular feed-forward subnetwork are left undisturbed by the subnetwork's activity, and may become members of other feed-forward subnetworks, to which they have better connectivity. Thus, the structuring mechanism reorganizes the initially random network into a network of (overlapping) diluted feed-forward subnetworks by drawing neurons into one or the other subnetwork. Figuratively speaking, the contrast between different subnetworks is enhanced and activity to some extent decoupled (see the remark about the potential functional relevance of coupling below).

10.1.5 Background Activity

Having discussed the consequences and predictions of our results for the parameters rise time τ_0 and group width w, and their interaction with the amplitude of the post-synaptic potential $\widehat{u}$, let us now come back to the discussion of membrane potential fluctuations σ_V which we have left in Sec. 10.1.1. The range of membrane potential fluctuations investigated in the present study well covers the physiologically plausible range. The lower bound, the noise-free case, is approximately realized in neurons in the *in vitro* preparation. Remaining fluctuations in this preparation are due to few synaptic inputs, spontaneous releases, and thermal fluctuations. The use of studying the noise-free case is that basic mechanisms determining the structure of state space can be uncovered. The upper bound is determined by the available regime between spike threshold and resting potential. The large membrane potential fluctuations studied practically fill this regime. We demonstrated that the temporal spread introduced by membrane potential fluctuations is limited when the membrane potential fluctuations are large enough to distribute the response spike over the rise time

of the packet potential (Chap. 9). The relationship between the parameters τ_0 and σ_V can be summarized as follows: τ_0 determines the time window over which response spikes can be distributed, and σ_V determines the fraction of this time window exploited. Membrane potential fluctuations control the spontaneous spike rate of the neurons. The model achieves consistency with the spontaneous spike rates observed *in vivo*, thus providing evidence independent from the model of subthreshold activity that the appropriate range of fluctuations is studied. However, a high level of spontaneous activity may introduce additional effects, not captured by our model of pulse packet propagation (see discussion below). At large σ_V, the voltage excursions driving the membrane potential away from spike threshold (hyperpolarizing direction) already reach unrealistically large (negative) values. In our model, synaptic currents are independent of membrane potential, and can therefore drive the potential to arbitrarily negative values. However, in real neurons, inhibitory synapses cannot drive membrane potential below the reversal potential of the respective currents. Thus, at large fluctuations our model may underestimate the neuron's ability to respond to an incoming pulse packet. The physiological range of membrane potential fluctuations σ_V is limited, and we have seen (Chap. 5) that within this range a moderate increase in w can compensate for the effect of fluctuations on the existence of the attractor for synchronous activity. We can conclude that the large membrane potential fluctuations observed *in vivo* do not prohibit the existence of the attractor and, hence, propagation of synchronous activity. This is in contrast to the conclusion of earlier studies (Shadlen & Newsome, 1994; Shadlen & Newsome, 1995; Shadlen & Newsome, 1998) claiming the reverse; that cortical neurons would not be able to reliably respond to input spike constellations. These studies basically demonstrated that under conditions of uncorrelated excitatory input to a neuron, there is no considerable correlation of output spikes with excitatory input spike constellations. However, this finding is perfectly consistent with our findings. The argument involves two steps. First, the argument that uncorrelated input spike trains do not contain spike constellations able to reliably elicit response spikes does not exclude that correlated input spike trains can do so. The neural transmission function for transient input we introduced (Chap. 3) precisely quantifies the required relationship: the dependence of the reliability of neural response on the correlation of input spikes. Let us assume for the sake of argument that the term "reliable neuronal response" is defined by having, say, 80% response probability within a time window of 3 ms. The shape of the transmission function shows that a large enough number of spikes arriving in a short enough time interval can reliably drive a neuron. Thus, uncorrelated activity cannot reliably drive a neuron whereas correlated activity can. Second, the finding that uncorrelated input spike trains do not contain spike constellations able to reliably drive a neuron is in fact a requirement for synchronous activity to be a meaningful mode of operation. Synchronous activity in a feed-forward network can only transmit information if it is not elicited spontaneously from random fluctuations. A stable ground state of uncorrelated spontaneous activity is required.

It has now become clear why the question whether the cortical neuron can support precise spike timing, a question raised many years ago (Abeles, 1982b) and revived recently (Shadlen & Newsome, 1994; Shadlen & Newsome, 1995; Shadlen & Newsome, 1998; König, Engel, & Singer, 1996), could not be resolved in earlier studies. Several studies found that neuronal response is more reliable if input spikes are correlated (Abeles, 1982b; Murthy &

Fetz, 1993; Murthy & Fetz, 1994; Bernander, Koch, & Usher, 1994). Others (Abeles, 1991; Marsalek, Koch, & Maunsel, 1997; Kisley & Gerstein, 1999) found that the temporal jitter of the spike response (precision) of a neuron can be smaller than the temporal jitter in input spikes. However, because of the presence of background activity, the reliability is not 100% and temporal spread is not vanishing. Therefore, no definitive answer to the question could be provided. Our study showed that the two variables have to be treated simultaneously. Whether the temporal precision in a packet of spikes is large enough depends on the number of spikes available, and –vice versa– whether the number of spikes is sufficient depends on their temporal precision. Furthermore, it turns out that the question cannot be answered independently of the network structure. A single neuron converts the number of spikes at its input into a response probability. Knowledge about the network structure (w in our case) is required to obtain comparable measures on the input and the output side. The basic result is inherent in the discussion of synfire activity by Abeles (1991), and formalized in the construction and analysis of the iterative (a, σ)-mapping (Diesmann, Gewaltig, & Aertsen, 1996b; Diesmann, Gewaltig, & Aertsen, 1997).

In fact, we have seen that moderate membrane potential fluctuations consistent with low spontaneous activity have a constructive effect on the size of the basin of attraction (Chap. 6). The effect can be compared to aperiodic stochastic resonance (Collins, Chow, & Imhoff, 1995; Collins, Chow, Capela, & Imhoff, 1996; Heneghan et al., 1996). In aperiodic stochastic resonance, the ability of a system to respond to an aperiodic signal is measured by the cross-correlation. Postma and Hudson (1996) observed the effect in a discrete-time feed-forward network, ignoring temporal spread, and they related the effect to stochastic resonance. Unaware of the work on stochastic resonance, Boven and Aertsen (1990) noted the constructive effect of excitatory background activity on the coupling strength of a single synapse. Different from the standard situation for stochastic resonance, the elevated background activity increases both: membrane potential fluctuations σ_V and the mean of the membrane potential η_V. The conceptual framework to study the dynamics of the coupling between neurons in experimental data and the notion of "effective connectivity" was introduced by Aertsen, Gerstein, Habib, and Palm (1989), extending earlier work by Gerstein and Perkel (1969). First examples for the fact that the cross-correlation of two neurons cannot simply be interpreted in terms of anatomical connection, but may change in dependence of stimulus context and behavioral state are presented in (Aertsen et al., 1991). Background activity exploits stochastic resonance and enhances the effect by controlling the distance between membrane potential mean and spike threshold. Boven and Aertsen (1990) speculated that neural systems could use background activity as "gating" mechanism for synaptic pathways (see also Aertsen, Erb, & Palm, 1994). The potential role of background activity as a gating mechanism becomes exceptionally clear in the synfire model. Especially for weak pulse packets close to the separatrix, the level of background activity can determine whether synchronous activity decays or propagates through the network in stable fashion. By contrast, pulse packets which have already reached the vicinity of the attractor are not affected by the precise position of the separatrix and thus, the level of background activity. This introduces a hysteresis, not present in stochastic resonance itself. Once an elevation in background activity has stabilized a pulse packet, the network can sustain the propagating synchronous activity, even if background activity falls back to its original level. Background

activity may need to drop to considerably lower levels to switch off synchronous activity again. Here we have described an interaction between the asynchronous general excitation level in the network and synchronous spiking activity. The fact that such interaction can be achieved in the absence of changes in mean membrane potential may be relevant in the context of balanced neural networks (van Vreeswijk & Sompolinsky, 1996; Amit & Brunel, 1997; van Vreeswijk & Sompolinsky, 1998).

Both types of activity, incoming pulse packets and background activity, may be temporally modulated allowing for rich dynamics, potentially relevant for neural computation. Let us illustrate the possible network architectures by an example. Consider a local network with several embedded feed-forward subnetworks, each one able to sustain synchronous activity. Modulated background activity can sequentially "load" independent entities of synchronous activity into the network. The entities are weak pulse packets, received by particular feed-forward subnetworks from outside the local network, when background activity has entered a high rate regime. Because synchronous activity rapidly reaches the attractor, it is not destroyed when the overall activity level goes down again. However, in this state the local network is decoupled from the rest of the brain with respect to pulse packet input. Note, that there is again a form of hysteresis here. To kick the pulse packet out of the basin of attraction, background activity has to fall below the level required to drive a "weak" packet into the basin. In the general context of cell assemblies, background activity is not restricted to two states and may rather form a continuum. The level of activity controls sensitivity and selectivity of the system. The idea of using threshold control in neuronal processing by cell assemblies was introduced by Braitenberg (1978) and elaborated in (Palm, 1982; Braitenberg, 1984; Braitenberg & Schüz, 1998). In the above example, we have connected the concept of a temporally modulated threshold to the stabilization of synchronous activity in a specific type of subnetwork. In our picture, threshold modulation is implemented by the dynamics of background activity. Remember that the discussion of membrane potential fluctuations has shown that threshold modulation does not require a change in the distance from membrane potential mean to spike threshold. A change in membrane potential fluctuations generated by balanced network activity is sufficient. Thus, we have described two extreme mechanisms leading to dynamic changes in the correlation of neuronal spike trains. In the first, a neuron which is part of several feed-forward subnetworks contributes to different spatio-temporal spike patterns, depending on the activated subnetwork. In the second, uncorrelated background activity controls the effective or functional coupling between neurons. The example above illustrates how the two mechanisms may cooperate.

10.1.6 Subthreshold Oscillations

In the cortical network, the membrane potential time course of a single neuron will not be completely unstructured. Likewise, the membrane potential time courses of two arbitrary neurons will not always be completely uncorrelated. Especially subthreshold oscillations (SOs) of membrane potential in the γ-range have gained a considerable amount of attention (e.g. Lampl & Yarom, 1993; Lampl & Yarom, 1997; Volgushev, Christakova, & Singer, 1998). Interestingly, γ-range oscillations and the membrane potential excursions caused by an incoming pulse packet are on a comparable time scale, allowing for an interaction of the two processes. Thus, now that we have understood the interaction of pulse packet input

with unstructured membrane potential fluctuations, we can address the question how pulse packets interact with other types of ongoing activity in the brain. It turns out that the interaction between pulse packet input and SOs can be visualized and quantified with a two-dimensional timing diagram (the "BiPSTH") similar to the JPSTH (Aertsen, Gerstein, Habib, & Palm, 1989). Whereas the JPSTH compares the position of two spikes in reference to a single trigger event, the BiPSTH relates the timing of a single response spike to two independent trigger events (Mohns, Diesmann, Grün, & Aertsen, 1999; Mohns, 2000). Also in this setting, relevant conclusions cannot be made without taking into account the amount of fluctuations caused by random background activity. For example, because of classical stochastic resonance, the integrate-and-fire model in the presence of noise (fluctuations) is sensitive to subthreshold oscillations. The range of SO amplitudes for which the output spike train does not become periodic itself is limited by the magnitude of the membrane potential fluctuations. This constraint is relevant, because the strength of the interaction between pulse packet input and SOs depends on the amplitude of the oscillations and hence, on the expected amount of fluctuations. Depending on the shape and amplitude of the two signals, the response spike can be locked to either one of the signals, or to both of them. The results can be interpreted in terms of two possible network effects of subthreshold oscillations. First, weak input packets may be kicked in or out of the basin of attraction for synchronous activity, depending on their time of impact relative to the phase of the SO. Thus, subthreshold oscillations are able to control the propagation of synchronous spiking activity. Second, the cross-correlation between the response spike and a spike of the input packet ("external") is weaker than the correlation between different realizations of the response spike at constant phase ("internal"). The terms "external" and "internal" are used here because from the point of view of a neuron group in a feed-forward subnetwork, the former is measured between a neuron in the group and a source outside the group, whereas the latter is measured between two members of the group. If neurons of one group take part in the same SO and neurons of other groups are not taking part in this SO, an asymmetry is introduced between delayed and zero-delay cross-correlations. Although synchronous activity propagates with low internal temporal spread, the presence of subthreshold oscillations can degrade the delayed correlation between neurons from different groups while enhancing the correlation between neurons from the same group. This effect might explain why many of the observed tight correlations between single neurons are centered on zero (Vaadia & Aertsen, 1992). Here we used subthreshold oscillations as a toy model to discuss possible interactions of pulse packet input with other, more structured, types of ongoing activity. The timing diagram is not restricted to periodic processes, however, e.g. engagement of neurons in multiple synfire chains, "pulse packet – pulse packet" interactions may also be of interest. In Sec. 10.1.7 we work out in some detail a research plan to measure the neuronal transmission for transient input *in vitro*. With the technology developed in this project, also the interaction of pulse packet input with subthreshold oscillations can be investigated (Chakalova, 1998). Using extracellular stimulation and intracellularly applied sinusoidal current, earlier studies (Volgushev, Christakova, & Singer, 1998) already indicated that, at least in the absence of background activity, effects not captured by the integrate-and-fire model do occur. Wennekers (1998a) discusses integrative scenarios of γ-oscillations and synfire activity. The two dimensional BiPSTH timing diagram does not depend on a

particular neuron model and can, therefore, be used to analyze experimental data and to directly compare experimental results with model predictions.

The combination of intracellular recording from a single neuron (or some other appropriate technique measuring the trans-membrane potential) and multiple single neuron recordings *in vivo* will help us to uncover the origin of the dynamics of correlations between neuronal spike trains. If phases of high correlation in neuronal spike trains are by themself correlated with increased membrane potential fluctuations, this indicates that background activity is controlling effective connectivity. Assuming that all neurons in the local volume receive the same level of background activity, the analysis can be performed for all simultaneously recorded neurons. Unfortunately, not much can be learned from a comparison of fluctuations with temporal jitter in spike patterns. In Chap. 5, we have seen that in the realistic regime of large membrane potential fluctuations, the temporal jitter is insensitive to changes in the magnitude of fluctuations. Immediately the question arises what the statistical properties of the membrane potential can tell us about the ongoing processes. If spikes are elicited in response to incoming pulse packets, the action potentials should "ride" on characteristic membrane potential excursions (packet potentials) which may be distinguishable from the fluctuations causing a spike under spontaneous conditions. Kisley and Gerstein (1999) suggest to compare the slope of the membrane potential preceding a spike with predictions for spikes, generated under spontaneous conditions and as the result of pulse packet input. Packet potentials should also affect the distribution of membrane potential values. The occurrence of packet potentials should distort the Gaussian membrane potential distribution predicted by shot noise theory towards close to threshold values. If convergent synchronous input would be a prominent feature of subthreshold activity, spike triggered averaging (STA) of the membrane potential of a post-synaptic neuron should often exhibit residual potentials, deviating from an individual post-synaptic potential. Such compound PSPs are generated if the triggering pre-synaptic neuron spikes in synchrony with a group of other pre-synaptic neurons. The resulting packet potential is the superposition of the individual post-synaptic potentials. Using the spikes from a single pre-synaptic neuron as the trigger, the observed potential is the packet potential, convolved again with the (Gaussian) spike time distribution. Therefore it is typical for packet potentials as observed in STA that the potential starts to deviate from baseline already before the trigger spike has reached the target neuron (Matsumura et al., 1996). Knowledge of the shape of an individual post-synaptic potential allows for an estimate of the shape of the spike time distribution, and of the number of spikes involved by deconvolution of the packet potential (Aertsen, 1995). The development of detailed predictions remains for future work (see also Heck, Léger, Stern, & Aertsen, 2000).

10.1.7 Experimental Determination of the Transmission Function

The experimental tests proposed in the preceding paragraphs are concerned with passive observation of activity in the brain. The main purpose is to check the consistency of the model by observing different measures (e.g. temporal jitter of spikes and rise time of the PSP) in the same system. Certain relationships between these measures predicted by the model can be tested. The advantage of these studies is that they can be performed on almost arbitrary data sets, because we are only interested in statistical results. The details

of the experimental protocol are of limited importance. However, the framework developed in the present study allows for a more direct test in which the system is not only passively observed, but also actively manipulated. The analysis of the state space for synchronous spiking activity is based on the definition of a new transmission function for the single neuron (Chap. 3). The definition essentially is model free. It only assumes a system interacting with its environment by receiving point events (spikes) and emitting point events. We have developed a protocol and the data processing tools that allow for the reconstruction of the transmission function from a series of single neuron experiments. This protocol was used to obtain the transmission function for the specific neuron model used in the present study (Chap. 2). Obviously, the details of the transmission function will be different for different neuron models. The integrate-and-fire model is known to describe the properties of a cortical neuron under DC current injection in the regime of low membrane potential fluctuations. Although experiments show that a neuron responds to fluctuating input current with highly reproducible spike trains (Bryant & Segundo, 1976; Mainen & Sejnowski, 1995; Nowak, Sanchez-Vives, & McCormick, 1997; Warzecha, Kretzberg, & Egelhaaf, 2000), little is known about the details of the neuronal response to highly transient, supra-threshold input currents. Thus, the present study draws conclusions from a model which is operated in a parameter regime it originally was not constructed for. It is therefore essential to be able to directly measure the transmission function of cortical neurons. The purpose is twofold. First, since only a numerical representation of the transmission function is required for state space analysis, results of the present study can immediately be recomputed for the experimental data. Second, deviations of the experimentally obtained transmission function from the transmission function computed for the integrate-and-fire model can be used to develop a neuron model which better describes neuronal responses to transient stimuli. For example, likely candidates for such deviations from the model are two competing effects. Spike generation may not only depend on a voltage threshold but also on a component depending on the slope of the membrane potential (Ebbinghaus, Diesmann, Rotter, & Aertsen, 1997; Ebbinghaus, 1997; Rotter, Diesmann, Frégnac, & Aertsen, 2001; Azouz & Gray, 1999; Azouz & Gray, 2000). At fast transients, the efficiency of spike generation may be reduced, due to the limited time the membrane potential spends at particular membrane potential values.

The protocol requires that for a given neuron a specific number of synapses can be supplied with input spikes of a pre-determined temporal relationship. With current technology it seems infeasible to orchestrate the activation of synapses in such well defined manner. We have stated in Chap. 2 that in an *in vitro* slice preparation of cortical tissue, the membrane potential can be recorded by an intracellular electrode. Simultaneous to the observation of the membrane potential, a current can be injected into the soma of the neuron. This is the setup in which the classical λ-I curves (Chap. 2) are obtained. As an approximation to the original protocol we suggest (Kampa, 1998; Kampa et al., 1999) to inject a current into a neuron as it would be generated by the impact of a pulse packet (a, σ). In each trial, the required current is computed by convolving the specific realization of spike times with the shape of a post-synaptic current as measured at the soma. This procedure is justified by the fact that experimentally, post-synaptic potentials (PSPs) or post-synaptic currents (PSCs) are usually measured at the soma. Thus, as in our model neuron, we assume deterministic synapses and linear superposition of PSCs (cf. Heck, Léger, Stern, & Aertsen, 2000). Conse-

quently, results of the proposed experiment do not allow for conclusions about the influence of the stochastic nature of synapse, voltage dependence of synaptic currents, and nonlinear processes in the dendrite. Basically we have reduced the neuron to a system with passive spread of current from the recording site into the cell, and a spike generation mechanism. In Chap. 2 we described that in the *in vitro* preparation, most of the inputs to a neuron are missing and, therefore, the mean membrane potential is close to resting level and exhibits little fluctuations. As in the noise-free case studied in Chap. 6, the membrane potential needs to be elevated to reach a dynamical regime, comparable to the *in vivo* situation. This can be achieved by injection of an appropriate constant current in addition to the currents mimicking pulse packet input.

The protocol has to sample the (a, σ) space with some resolution $(\Delta a, \Delta\sigma)$. The preparation is likely to only remain stable for up to a few hours, and intervals of a few hundred ms are required between individual stimuli to allow for full recovery of the neuron. This allows for in the order of $10,000$ stimulations. Note that in the case of the model neuron, we performed $10,000$ realizations at each location in (a, σ) input space. If we regard 100 spikes as the minimal number of response spikes required for reliable estimation of the response parameters α and σ_{out} of the output density, a grid of 10 by 10 data points seems to be available to map (a, σ) space. However, not every input packet elicits a response spike. In the region of interest where the packet potential reaches spike threshold the response probability is only 0.5. Therefore, a grid of 5 by 5 data points is more realistic. With current technology it seems to be unavoidable to select a few σ values, and to concentrate a values in a region where the transition from low to high response probability is expected. Stimuli should be presented in random sequence to minimize systematic effects, and to leave the experimenter with a complete as possible data set when at some point the recording becomes unstable.

The stimulus protocol developed so far does not require feed-back from the outcome of the experiment. The sequence of stimulating currents can be computed prior to the experiment and e.g. stored on CD. When the outcome of a trial (spike or no spike) becomes available to the stimulus generator, a number of optimizations are possible. First, the stimulation software can count the performed number of trials and the number of response spikes individually for each point in stimulus space. As soon as the required number of response spikes (say 100) is obtained, the corresponding (a, σ) pair is excluded from the stimulation procedure, reserving more time for the less successful parameter sets. Second, the recovery period may be shortened to some minimal value when no response spike occurred because most of the recovery effects are assumed to originate from action potential generation (time constant of the passive membrane versus time constants of the after hyper-polarization, AHP). Still, the procedure requires preselection of a few points in the (a, σ) space at which the experiment is performed. More support points are needed in regions where the slope of the transmission function is steep than in regions where the response probability is either very low or close to unity. Whether the efficacy of neuronal response will closely follow the theoretical predictions in the region of interest is unknown prior to the experiment. With the help of some online analysis, it should be possible to develop an algorithm that optimizes the positioning of stimulus parameters according to the actual neuronal responses. In the present simulation study, no attempt was made to implement such optimization. In any case, online optimization should be developed and tested in a simulated environment. It will

be important to compare the noise in the experimentally obtained transmission function to the variability of the transmission functions across neurons. If this variability is low, one may finally decide to average the transmission function over neurons to reduce noise. It is a dilemma that in the simplest experiment, where the membrane potential fluctuations are left at their negligible level, the determination of the transmission function is most difficult because of the steepness of the slopes.

The next step in bringing the experimental protocol closer to the dynamic regime of the intact brain is to restore background activity. Much in the same way as we introduced background activity in the model neuron, a shotnoise current can be injected into the neuron to generate realistic membrane potential fluctuations (Stevens & Zador, 1998; Nawrot et al., 2001b). This allows us to verify if integrate-and-fire dynamics presents a valid model for the interaction of membrane potential fluctuations and pulse packet input. Since the slopes in the transmission decrease with increasing fluctuations, the experimental determination of the transmission function is now less difficult than in the case of vanishing fluctuations. The injection of shotnoise current cannot simulate the changes in conductance caused by the synaptic bombardment *in vivo* (see e.g. Paré et al., 1998) . Conductance changes may be important for the transmission of synchronous activity, because of its effect on the neuron's ability to integrate currents. In the integrate-and-fire model this corresponds to the fact that the coefficient termed membrane time constant becomes time dependent. The "dynamic clamp" procedure (Sharp, O'Neil, Abbott, & Marder, 1993a; Sharp, O'Neil, Abbott, & Marder, 1993b; O'Neil et al., 1995) can replace the time-dependent current injected into the neuron by an imposed time-dependent conductance. In this setup, a current described by an equation like $I(t) = g(t)(E-V(t))$ is injected into the neuron, where E is an arbitrary reversal potential, $V(t)$ the membrane potential of the neuron, and $g(t)$ the desired conductance time course. By rapidly switching between current injection and voltage measurement, such dynamic clamp can be achieved using a single electrode. Thus, the protocol for measuring the transmission function changes only in so far that now a synaptic conductance time course (and a corresponding reversal potential) has to be supplied, instead of a current time course. In fact, in a different context the developers of the dynamic clamp recently proposed its use to mimic effects of (balanced) background activity *in vitro* (Chance & Abbott, 2000; Abbott & Nelson, 2000). A completely different approach to the problem of generating realistic membrane potential fluctuations is the attempt to directly activate the remaining network in the slice. To this end, the cortical slice is loaded with a caged version of the excitatory transmitter glutamate, which can be activated by a UV-laser beam. By sequentially stimulating randomly chosen sites in the slice, the spike rates of neurons are increased and *in vivo* like membrane potential fluctuations can be observed (Kampa et al., 2000; Nawrot et al., 2001a).

Experimental determination of the transmission function is an ongoing project which has already inspired more general methodological work (Mehring et al., 2001). Although preliminary results in the regime of vanishing fluctuations have been obtained (Kampa et al., 1999; Rodriguez et al., 2001), demonstrating the principal feasibility of the approach, more work is needed to carry out the research program as described above. As we have already noted in Sec. 10.1.6, the protocol being developed in this project can also be used to obtain first insights into the interaction of pulse packet input and other types of ongoing activity.

10.2 Open Questions and Outlook

After having interpreted the results of the present work and discussed its immediate predictions, let us now summarize some of the questions generated by the study. In addition to questions directly related to the analysis in the present work, we shall also discuss the next and medium-term steps that can be taken to further investigate the origin of synchronous spiking activity in cortical networks. It turns out that the next target would be to simulate a small volume of cortex. Within this model, theoretical results about the existence of a stable state at low spike rates in a cortical network (Amit & Brunel, 1997; van Vreeswijk & Sompolinsky, 1996; Brunel, 2000) and results about the propagation of synchronous activity (Abeles, 1991; Diesmann, Gewaltig, & Aertsen, 1999) can be reintegrated. Most importantly, virtual multiple single-neuron recordings will provide us with better predictions for the occurrence of spike patterns than are available to the present day (Grün, Diesmann, & Aertsen, 2002b; Grün, Riehle, & Diesmann, 2001).

We have discussed in Sec. 10.1.7 that an important next step is an experimental one. For further theoretical work on network dynamics it is essential to establish whether the integrate-and-fire model is appropriate under conditions of transient stimuli. The relationship of the neuronal transmission function to the development of synchronous activity in the network allows us to judge the significance of experimentally observed deviations from model predictions. In case of relevant deviations, it will be interesting to explore possible biophysical mechanisms, to modify the neuron model accordingly, and to propose new experiments to validate the model. Compartmental modeling (see e.g. Segev, Burke, & Hines, 1998) can be used to check whether the potentially observed deviations are due to the specific simplifications in the integrate-and-fire model. Possible candidates are the reduction of the passive electrical properties to a point-neuron model and the reduction of Hodgkin-Huxley (Cronin, 1987) dynamics to a voltage threshold (e.g. Azouz & Gray, 1999).

Several technical questions arise within the framework of the present study, which are presented here in listed form:

- a and σ seem to be natural variables for the characterization of a volley of spikes. However, the results of Chap. 6 suggest that with respect to the threshold process of the integrate-and-fire model, the amplitude and rise time (or slope, compare Kisley & Gerstein, 1999) of the packet potential could lead to a simpler structure of the state space. Thus, it appears worthwhile to investigate whether there are better suited variables than a and σ.

- The state space portraits suggest that for decaying trajectories there is also an attractor at vanishing activity and finite temporal spread. This regime is, unfortunately, numerically extremely difficult to study. Two effects compete: whereas the broadening of the packet potential increases the spread of the response spikes, the decrease in amplitude leads to a decrease in temporal spread because spikes can only be created in a narrowing peak region. In addition the position of the attractor for vanishing activity depends on background activity because the shape of the part of the membrane potential distribution interacting with the packet potential determines temporal spread (cf. Chap. 9). Investigation of the regime of vanishing activity may lead to deeper insights into the threshold process.

- A spike intensity model would be better suited for analysis than the integrate-and-fire model because of the connection to the mathematical framework of point processes (see e.g. Rotter, 1994). If we regard the integrate-and-fire model as an accurate description of neuronal dynamics, a mapping to an intensity description valid in the desired dynamical regime needs to be constructed. The database of response spike distributions for individual input parameter sets (a, σ) can be used to compute the spike intensity, and to study its dependence on the input. Such investigation may clarify the interesting observation that the slow fluctuation model presented in Chap. 9, as well as an intensity model assuming arbitrarily fast fluctuations (Gewaltig, 2000), capture essential aspects of the synchronization dynamics (see also Plesser & Gerstner, 2000 and references therein). First steps are undertaken in Sec. 9.5.

- In the construction of the transmission function, we averaged over many realizations of input packets with identical parameters (a, σ). By contrast, in a completely connected feed-forward network each neuron in a group receives the identical configuration of input spikes. At large membrane potential fluctuations this difference is irrelevant. The situation might change in a regime of small fluctuations, and in networks with a low number of neurons per group but large post-synaptic potentials.

- The ad hoc procedure applied in the present study to estimate a and σ from the response spike distributions in the presence of background activity leads to consistent results. However, it is conceptually not satisfying, one should look for a better integration into the framework of stochastic point processes.

10.2.1 Ground State of Synfire Activity

The (a, σ) state space picture implicitly assumes that there is a stable ground state of the system. Only when excited by an incoming pulse packet, synchronous activity travels through the network. The ground state is characterized by independent activity of the neurons at a low spike rate. In Chap. 4 we have shown that increasing the group size extends the basin of attraction to pulse packets with lower number of input spikes. This was interpreted as stabilizing synchronous activity, because also initially weak packets can reach the attractor, and synchronous activity becomes more robust against fluctuations in the number of spikes and their temporal spread. However, we have recently shown (Tetzlaff, Geisel, & Diesmann, 2001) that at large group sizes, the ground state can lose its stability. Above a critical w, synchronous activity forms spontaneously and repetitively, destroying the possible functional relevance of the excited state. While the process is clearly mediated by an instability in spike rate in the feed-forward network, the details of the transition from uncorrelated spike rate to synchronous activity remain for further investigation. One option is that in a situation where the basin of attraction for synchronous activity extends to the regime of packets with only a few spikes, these packets could form spontaneously for a certain spike rate. Thus, because of fluctuations in the number of spikes arriving from the previous group in a certain time interval, activity can spontaneously jump into the basin of attraction. It seems that there is not only a lower limit for the number of neurons in a group but also an upper one, providing us with a further constraint.

10.2.2 High Rate Limit of Synfire Activity

The finding of a possible upper bound for synfire chain width is related to another important question, the high rate limit of synchronous activity. In different cortical areas the mean spike rates differ. In the prefrontal cortex, spike rates are at the level of a few Hz (Abeles, Vaadia, & Bergman, 1990), they seem to be of the order of a few 10 Hz (e.g. Taira & Georgopoulos, 1993) in the motor cortex. If spatio-temporal patterns would be observed in neurons with mean spike rates incompatible with the existence of a stable ground state, this would clearly indicate that the occurrence of the patterns cannot be explained by the synfire model. For a given group size several scenarios are possible how spontaneous spiking activity can destroy the functionality of synchronous activity. For example, the spike rate in the ground state could be large enough to spontaneously create pulse packets which can reach the attractor. In a different scenario, the spike rate reduces the ability of the neurons to respond to an incoming pulse packet, due to an increased probability to be refractory (absolute or relative), to a degree that the network cannot sustain synchronous activity. In yet another scenario, the high spike rate has decreased the critical group size, above which the ground state becomes instable, down to a value where the network cannot sustain synchronous activity. One of the strongest assumptions made in the present study is that we can investigate the dynamics of a feed-forward subnetwork, without considering its feed-back connections to the embedding network. This assumption allowed us to assume that background activity composed of excitatory and inhibitory inputs is stationary. The assumption is valid in a large random network, where the propagating pulse packet represents only a negligible fraction of the total excitatory activity. Apart from the feed-forward connections, neurons of a particular group have little overlap in their target neurons (convergence). Therefore, activity changes induced outside the feed-forward subnetwork are practically absent and, consequently, no feed-back can be observed. Consistent with the above assumptions is the further requirement that background activity received by any two neurons is independent. Once the rate instability occurs, the above assumptions may no longer hold. Neurons in the feed-forward subnetwork exhibit a sustained high spike rate, inconsistent with the balanced state of the entire network. Thus, the network will counteract the increase by inhibitory activity. Thereby, a coupling is introduced between the background activity of neurons in different groups. Complicated network dynamics may arise, depending on the fraction which the feed-forward subnetwork contributes to the total number of neurons in the network, and the details of the excitatory and inhibitory single neuron dynamics (time constants). Thus, the investigation of large group sizes and the high rate limit requires consideration of recurrent networks. As a rate model proven to be useful to understand instability of the ground state in the feed-forward subnetwork (Tetzlaff, Geisel, & Diesmann, 2001), it will be interesting to see if the approach (Amit & Brunel, 1997; Dayan & Abbott, 2001) can successfully be applied to describe the recurrent network, and to explore how the rate description and spike synchronization interact.

10.2.3 Spatial Constraints of Embedding

The consideration of large group sizes and inhibitory feed-back immediately raises the question on the details of the embedding of a feed-forward structure in the cortical network.

Obviously, the cortical network cannot be described by an random graph on arbitrary spatial scales. Considering only local connections, it is known that the probability of synaptic contact between two arbitrary neurons decreases with the spatial distance between the neurons' somata. In an elegant study, Hellwig (2000) showed quantitatively that the probability of synaptic contact falls off with spatial distance in a Gaussian manner. The reconstructed arborization of arbitrary cortical pyramidal cells was used to compute statistics of the number of synaptic contacts as a function of the horizontal distance of the two neurons. Based on anatomical observations, the algorithm assumes that synapses are formed wherever axon and dendrite approach each other within the resolution of some minimal volume element. As a first step towards a more realistic model of the cortical network, this knowledge can be used to construct random networks with a space constant.

Surprisingly, it turns out that in such networks, feed-forward subnetworks are confined to a cortical volume on the order of the axono-dendritic connectivity radius of two neurons (Hehl et al., 2001). Thus, assuming localized random connectivity, in the order of $1\,\mathrm{mm}^3$ of cortex is available for a feed-forward subnetwork. This clearly constrains the effective size of the embedding network which plays a role in the stabilization of network activity as described in this study. Furthermore, we can safely assume that also inhibitory neurons collect and distribute activity on a local scale. Their spatial structure cannot be neglected in the study of network dynamics. One should be reminded though, that the studies by Hellwig (2000) and Hehl et al. (2001) only considered the local connections of a cortical neuron, which make up about 50% of the total number of inputs to a neuron. Further studies will have to address the question whether synchronous activity is possibly propagated through the patchy connectivity (Amir, Harel, & Malach, 1993) surrounding the local volume, or by global convergence of termination sites in long range connections (Schüz, 1994; Schüz & Liewald, 2001).

We have discussed above that in random networks as well as in random networks with a space constant, network connectivity plays the role of a threshold variable for the occurrence of feed-forward subnetworks. In both types of networks, the available connectivity does not support the existence of completely connected chains, analyzed in the present study. Only feed-forward subnetworks with small group sizes have non-vanishing probability of existence. It would be plausible that the large amplitudes of post-synaptic potentials required by small group sizes are created by suitable mechanisms of synaptic potentiation (e.g. Song, Miller, & Abbott, 2000; Abbott & Nelson, 2000). However, large PSP amplitudes limit the reliability of transmission (Chap. 8) and reduce the combinatorial possibilities to arrange neurons into different functional groups. By contrast, incomplete or diluted feed-forward subnetworks can exist, given a certain network connectivity and dilution parameter. The detailed dynamics of diluted chains and the dependence on the dilution scheme still need to be investigated. Preliminary results of graph theoretical considerations (Hehl et al., 2001) and network simulations (Mehring et al., 2003) suggest that, once the existence of subnetworks with a certain inter-group connectivity becomes likely, more than the required number of target neurons is available. In addition, a number of neurons exist that do not receive sufficient convergent input from a neuron group to qualify as members of a successive group. However, the convergence at these "halo" neurons can still be large enough to lead to an undesired unspecific spread of activity into the remainder of the network. In this light we have

speculated above, that the task of a potentiation mechanism stabilizing the propagation of synchronous activity would not so much be to strengthen intergroup connections, but rather to degrade connections from the chain into the embedding network, leading to unspecific spread of activity. At the same time, some explicit or implicit normalization is desired to limit the group size to values not considerably larger than that required to sustain synchronous activity. Such normalization schemes were discussed by Bienenstock (1995) and Doursat (1991). Earlier results on the 'growth' of feed-forward subnetworks (Hertz & Prügel-Bennet, 1996) may have to be reviewed in the light of spike time dependent plasticity (Markram, Lübke, Frotscher, & Sakmann, 1997; Zhang et al., 1998). If such growth rules, combined with local inhibition, provide a mechanism to increase the probability that neuron groups are formed in some distance to the preceding group, and thereby the strong localization suggested by the random placement of neurons in succeeding groups can be overcome, needs to be investigated.

10.2.4 From Random Graphs to Cortical Anatomy

Taken together, our findings suggest a plan for future research in which the dynamics of a small volume (about $1\,\mathrm{mm}^3$) of cortex is the next strategic target. This will require the simulation of a minimum of 10^5 model neurons of the type discussed in the present work. This is within the reach of today's computer systems. In these networks, neurons can be simulated with a realistic number of synapses and PSP amplitudes. It is no longer required to speculate how effects observed in the dynamics scale with network size. Artificially large overlap in the input of two arbitrary neurons can be avoided. In the same way as the simulation of isolated feed-forward structures has guided our research in recent years in terms of the development of abstract descriptions of network dynamics and comparability of simulation results with experimental data, the small volume of cortex can now take that role. The minimal volume is determined by the connectivity radius of an individual neuron. The network size should be large enough to allow neurons with sufficient spatial distance to receive non-overlapping inputs. The immediate task is twofold. On the one hand, results obtained for the isolated chain should be checked in simulations of the full network. The first step towards a realistic network structure is to move from a random graph to the local connectivity rule. On the other hand, simulations should be used to perform virtual multiple single-unit recordings, combined with a realistic number of intracellular recordings. Analysis of these data will provide better predictions for the occurrence of spatio-temporal patterns in neuronal spike data. The typical cross- and higher order correlations occurring in such networks can be compared to effects observed in experimental data (Vaadia & Aertsen, 1992; Vaadia et al., 1995; Grün, Diesmann, & Aertsen, 2002b). Comparison of the results in different parameter regimes (Brunel, 2000) may give insight into the nature of the cortical network. As discussed above, especially the comparison of multiple single-unit spiking activity and intracellularly recorded subthreshold activity will provide us with valuable information and constraints for the network models. Simple hypotheses like the one that spatio-temporal patterns naturally occur in a random network in response to some unspecific excitation remote from the recording site can then easily be tested in the model. Having understood the basic properties of the network model now enables us to implement several feed-forward subnetworks within the global network to investigate their interaction with the inhibitory subnetwork and the interactions between

the feed-forward subnetworks. The synfire chain model, which has formerly been treated as a graph with arbitrary spatial arrangement, is now embedded into the space constrained by cortical connectivity and by the inhibitory subnetwork. In principle, measures relevant for the interpretation of data like the probability to observe the activity of a feed-forward subnetwork with a given number of electrodes and given electrode distance can be tackled. Another example is the relationship between the number of spatio-temporal and purely temporal (auto-) patterns expected to be found in neuronal data.

In the above discussion, the cortex was essentially treated as a two-dimensional sheet of neurons, the vertical structure (Braitenberg & Schüz, 1998; Nicholls, Martin, Wallace, & Fuchs, 2001) has been ignored. Neurons in different layers of the cortex have different properties. Also, the number of inputs into a local column and the number of outputs from a local column differ between layers. In addition, there are indications for a specific wiring pattern between layers (e.g. Douglas & Martin, 1991a; Lübke, Markram, Frotscher, & Sakmann, 1996; Lübke, Egger, Sakmann, & Feldmeyer, 2000). Thus, on a longer time scale the three-dimensional structure of the cortex should be considered. In this strategy, we use the occurrence of synchronous activity and other cooperative phenomena on the level of spike times as a guideline, while constructing a model of the cortex.

10.2.5 Functional Relevance

In the present work we have purposely avoided to discuss the potential functional role of synfire chains. Instead, we have concentrated on the detailed dynamics of such subnetworks, and their dependence on experimentally accessible parameters. It is plausible that the cortical network can support synchronous spiking activity, and many constraints are now known. The dynamics was discussed in the framework of a single synfire chain. However, the dynamics neither prohibits that an individual neuron recurs at different locations in a single chain, nor that an individual neuron takes part in multiple chains. Thus, each neuron may participate –spike by spike– in multiple volleys with different neuron compositions, provided its engagements differ by more than the refractory period. Several such volleys may propagate through the network simultaneously, allowing multiple synchronous processes to coexist while maintaining their identities. Therefore, one should probably rephrase the main result of the present study as follows: A group of neurons can reproduce synchronous activity in its input at its output. Hence, to support synchronous spiking activity, the network only needs to be *locally feed-forward*.

Some of our results, such as the transmission function for transient input, the discussion of the temporal precision of neuronal response, and the role of background activity, may be useful beyond the framework of feed-forward subnetworks. Others have discussed the potential functional role of synfire activity. The literature ranges from abstract considerations (Bienenstock, 1991a; Bienenstock, 1991b; Bienenstock, 1995; Herrmann, Hertz, & Prügel-Bennett, 1995; Arnoldi & Brauer, 1996) to detailed implementations (Abeles et al., 1993a; Arnoldi, 1996; Arnoldi, Englmaier, & Brauer, 1999; Wennekers, 1998b). These researchers argue that the combinatorial possibilities of synfire chains, together with a mechanism to dynamically bind activity between chains, make them an ideal substrate for neuronal processing. Whether the brain uses feed-forward subnetworks to carry out its tasks, and how these operations are performed, is outside the scope of the present study and remains for further investigation.

Appendix A

Exact Integration

Here we briefly describe the numerical methods used to solve the neuron and network model introduced in Chap. 2. It turns out that by restricting all spikes in the system to an evenly spaced temporal grid, the subthreshold dynamics can efficiently be integrated without further approximation. Hence, the name "Exact Integration". A detailed description of the general approach and its application to integrate-and-fire dynamics can be found in (Rotter & Diesmann, 1999). The first section shows that the subthreshold dynamics of a model neuron is captured by a three-dimensional state vector, an appropriate propagator is constructed. The next section specifies the mechanism of spike generation and the interaction between model neurons.

Subthreshold Dynamics

The membrane properties are described by a first order linear differential equation (2.1). The α-function (2.2), describing the time course of a post-synaptic current, is a solution of a time-invariant two-dimensional system of first order linear differential equations (cf. Wilson & Bower, 1989; Bernard et al., 1994). Therefore, a post-synaptic potential (2.3) can be generated by

$$\dot{y} = Ay + x, \tag{A.1}$$

where $y(t)$ is the time-dependent state of the system, $x(t)$ is the time-dependent input to the system, and A is a matrix of constants characterizing the system. Identifying $y_3 = V$ and using the substitutions $y_2 = \iota$, $y_1 = \frac{1}{\tau_\alpha}\iota + \frac{d}{dt}\iota$ we have

$$A = \begin{bmatrix} -\frac{1}{\tau_\alpha} & 0 & 0 \\ 1 & -\frac{1}{\tau_\alpha} & 0 \\ 0 & \frac{1}{C} & -\frac{1}{\tau_\mathrm{m}} \end{bmatrix}. \tag{A.2}$$

A single PSP (2.3) is generated at time t^k for

$$x(t) = \begin{bmatrix} \widehat{\iota}\frac{e}{\tau_\alpha} \\ 0 \\ 0 \end{bmatrix} \delta(t - t^k). \tag{A.3}$$

Let us now assume that we are interested in the response $y(t)$ of the system (A.1) to more general input $x(t)$ on an evenly spaced temporal grid $t^k = kh$, where h is a fixed time step (here 0.1 ms). We write $y^k \equiv y(t^k)$ for brevity. If the input is a "pulse train" restricted to the temporal grid

$$x(t) = \sum_k x^k \delta(t - t^k) \tag{A.4}$$

the system can be integrated using

$$y^{k+1} = e^{Ah} y^k + x^{k+1}, \tag{A.5}$$

where we have exploited the general solution (Hirsch & Smale, 1974; Arnol'd, 1992; Bronstein et al., 1996)

$$y(t) = e^{A(t-s)} y(s) + \int_{s^+}^{t} e^{A(t-t')} x(t') dt' \tag{A.6}$$

of (A.1), $y(s)$ representing the initial conditions. Having an exact solution available for our system is of interest because with time constants differing by more than an order of magnitude it already represents a moderately stiff system (Mascagni, 1989; Press, Teukolsky, Vetterling, & Flannery, 1992). The matrix exponential e^{Ah} is time-independent and is called the *propagator* of the system

$$P(h) = e^{Ah} \tag{A.7}$$

$$= \begin{bmatrix} e^{-\frac{h}{\tau_\alpha}} & 0 & 0 \\ h e^{-\frac{h}{\tau_\alpha}} & e^{-\frac{h}{\tau_\alpha}} & 0 \\ \frac{1}{C}\left(\frac{e^{-\frac{h}{\tau_m}} - e^{-\frac{h}{\tau_\alpha}}}{(\frac{1}{\tau_\alpha} - \frac{1}{\tau_m})^2} - \frac{h e^{-\frac{h}{\tau_\alpha}}}{(\frac{1}{\tau_\alpha} - \frac{1}{\tau_m})} \right) & \frac{1}{C} \frac{e^{-\frac{h}{\tau_m}} - e^{-\frac{h}{\tau_\alpha}}}{(\frac{1}{\tau_\alpha} - \frac{1}{\tau_m})} & e^{-\frac{h}{\tau_m}} \end{bmatrix}. \tag{A.8}$$

The analytic calculation of the matrix e^{Ah} can be performed either by hand (Hirsch & Smale, 1974; Colquhoun & Hawkes, 1995; Leonard, 1996) or with the help of a software package such as Mathematica (Wolfram, 1996). Algorithms for the numerical computation of the matrix exponential are available (Moler & van Loan, 1978; Golub & van Loan, 1996; Druskin, Greenbaum, & Knizhnerman, 1998; Kenny & Laub, 1998) and implemented (e.g. MathWorks, 1998).

Because of the linearity of (A.1), the effects of the input spikes arriving at the excitatory and inhibitory synapses of the neuron can be summarized in a single input pulse train (A.4). The x^k represent the sums of the initial conditions (A.3) of all synaptic events elicited by spikes arriving at the neuron at t^k. The dynamics of an arbitrary number of synapses is captured by just three state variables. Note that amplitude and sign of the PSP can be different for different synapses, only the time constant is required to be identical. The state vector $y(t)$ reflects the history of all input spikes that have occurred up to time t. There is no need to keep a list of input events. The propagator matrix (A.8) is lower triangular. Therefore, the iteration step (A.5) does not require a full matrix multiplication. In addition, the update of y from one time step to the next can be carried out "in place", starting at the bottom row and working upwards. Consequently, the overhead in computational costs compared to other integration methods is negligible.

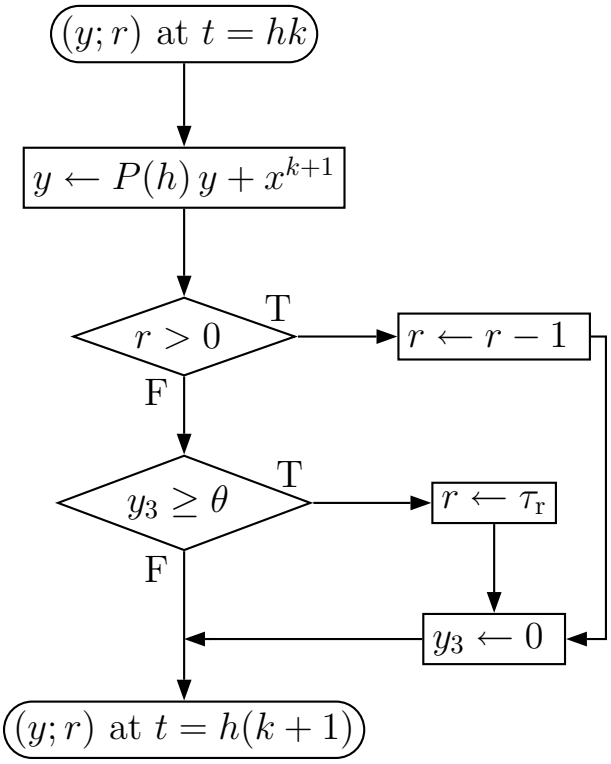

Figure A.1 Propagator of the integrate-and-fire neuron model. The state of the system $(y; r)$ is described by the state vector y of the subthreshold dynamics and integer r, counting the remaining time steps the neuron has to spend in the absolute refractory period. The sequence of Exact Integration of the subthreshold dynamics and algorithmic components for spike generation propagate the state of the system from time hk to time $h(k+1)$. x^{k+1} is the input to the neuron arriving at time $h(k+1)$.

The above described approach can be extended to a larger class of input functions $x(t)$ by adding equations to the system (Rotter & Diesmann, 1999), e.g. DC or sinusoidal input currents.

Integration Scheme

The neuron model is defined by the subthreshold dynamics discussed in the previous section and an algorithmic threshold operation (cf. Fig. 2.2). Following threshold crossing, the membrane potential is clamped to resting level for an absolute refractory period τ_{r}. Fig. A.1 illustrates the complete propagator of the neuron model. The membrane potential is checked for threshold crossing on the temporal grid. If the membrane potential is above threshold, a spike is immediately reported with the help of an additonal state variable r. At the time of spike generation we have $r = \tau_{\mathrm{r}}$. The neuron is able to emit a new spike if $r = 0$. At spike generation the membrane potential is immediately reset. In the state vector supra-threshold values can never be observed. The sequence of operations specified by Fig. A.1 ensures that the effect of an incoming spike is directly observable in the state of the system. Compatible with the restriction on input spikes, output spikes are bound to the temporal grid.

In networks of such units a minimal delay of one time step for synaptic interactions enforces causality of the system and is required by a parallel update scheme. Each neuron receives pulse train input, and is itself the generator of a pulse train. Since pulse train inputs are well suited for Exact Integration, the method constitutes a natural choice for integrate-and-fire type models. If the value of the membrane potential represented in the state vector is of no concern, the propagator can be further simplified by resetting the membrane potential at the end of the refractory period only.

The threshold operation on a fixed temporal grid introduces two types of integration errors. First, spikes can only be reported on the temporal grid. This effect can partially be overcome by determining the precise time of threshold crossing using linear interpolation (Hansel, Mato, Meunier, & Neltner, 1998). Second, threshold crossings can be completely overlooked, if the integration step is to large and the membrane potential returns to sub-threshold values within one iteration step. In (Rotter & Diesmann, 1999) Exact Integration is compared to a number of integration methods routinely used in neuronal modeling. It turns out that Exact Integration generally yields reliable simulations and more accurate results. The neuron model as described above is implemented in the simulation tool SYNOD (Diesmann, Gewaltig, & Aertsen, 1995).

Appendix B

List of Symbols

Symbol	Description
a	number of spikes in a pulse packet
σ	temporal spread of a pulse packet
α	response probability
w	number of neurons per group
T	$(a_{\text{in}}, \sigma_{\text{in}}) \rightarrow (\alpha, \sigma_{\text{out}})$, transmission function
T_w	$(a_{\text{in}}, \sigma_{\text{in}}) \rightarrow (a_{\text{out}}, \sigma_{\text{out}})$, iterative mapping
$a^{\text{s}}(\sigma)$	separatrix
R	membrane resistance
C	membrane capacitance
I	membrane current
τ_{m}	membrane time constant
V	membrane potential
V_0	resting potential
θ	$V_0 + \theta$ is threshold potential
τ_{r}	absolute refractory period
λ	spike rate
$\iota(t)$	post-synaptic current (PSC)
τ_α	rise time of PSC
$u(t)$	post-synaptic potential (PSP)
$\upsilon_0(t)$	PSP of unit amplitude
τ_0	rise time of PSP
F^1	form factor PSP area
F^2	form factor PSP peakedness

continued

Symbol	Description
η_V	$V_0 + \eta_V$ is membranepotential mean
σ_V	standard deviation of membrane potential
$\rho_V(V)$	probability density of V
$\bar{\theta}$	$\theta - \eta_V$
g_σ	Gaussian with standard deviation σ
$U(t)$	packet potential
$\upsilon_\sigma(t)$	characteristic membrane potential excursion
$\widehat{\upsilon}(\sigma)$	characteristic amplitude
τ_σ	rise time of packet potential
$\tilde{a}$	relative group activation
$\tilde{\sigma}_a$	standard deviation of $\tilde{a}$
$\mathcal{B}_{w,\alpha}(\tilde{a})$	distribution of $\tilde{a}$
$A_w(\alpha, \sigma)$	operator, generates (a, σ) with random a
$S(a, \sigma)$	operator, generates (a, σ) with random σ
$\mathcal{S}_w(a, \sigma)$	survival probability
$\rho_\delta(\delta)$	spike probability density
$Q(\delta)$	survivor function
$f(\delta)$	spike intensity
h	step size of simulation
$P(h)$	propagator of subthreshold dynamics

- $\widehat{x}$ denotes the peak value of a function $x(t)$ with a single and well defined maximum
- x_+ and x_- specify x for excitatory and inhibitory processes, respectively

Bibliography

Abbott, L. F., & Nelson, S. B. (2000). Synaptic plasticity: taming the beast. *Nat. Neurosci. 3*(Supplement), 1178–1183.

Abeles, M. (1982a). *Local Cortical Circuits: An Electrophysiological Study.* Studies of Brain Function. Berlin, Heidelberg, New York: Springer-Verlag.

Abeles, M. (1982b). Role of cortical neuron: integrator or coincidence detector? *Israel J. Med. Sci. 18*, 83–92.

Abeles, M. (1991). *Corticonics: Neural Circuits of the Cerebral Cortex* (1 ed.). Cambridge: Cambridge University Press.

Abeles, M., Bergman, H., Margalit, E., & Vaadia, E. (1993). Spatiotemporal firing patterns in the frontal cortex of behaving monkeys. *J. Neurophysiol. 70*(4), 1629–1638.

Abeles, M., & Gerstein, G. L. (1988). Detecting spatiotemporal firing patterns among simultaneously recorded single neurons. *J. Neurophysiol. 60*(3), 909–924.

Abeles, M., Prut, Y., Bergman, H., & Vaadia, E. (1994). Synchronization in neuronal transmission and its importance for information processing. In G. Buzsaki et al. (Eds.), *Temporal Coding in the Brain*, pp. 39–50. Berlin, Heidelberg: Springer-Verlag.

Abeles, M., Prut, Y., Bergman, H., Vaadia, E., & Aertsen, A. (1993a). Integration, synchronicity and periodicity. In A. Aertsen (Ed.), *Brain Theory. Spatio-temporal Aspects of Brain Function*, pp. 149–181. Amsterdam: Elsevier.

Abeles, M., Vaadia, E., & Bergman, H. (1990). Firing patterns of single units in the prefrontal cortex and neural network models. *Network: Comput. Neural Systems 1*, 13–25.

Abeles, M., Vaadia, E., Bergman, H., Prut, Y., Haalman, I., & Slovin, H. (1993b). Dynamics of neuronal interactions in the frontal cortex of behaving monkeys. *Conc. Neurosci. 4*(2), 131–158.

Adrian, E. D. (1928). *The Basis of Sensation.* London: Christophers.

Aertsen, A. (1995). Do insights and insides coincide? Some observations on spike correlations. Talk held at the Center for Neural Computation, Hebrew University, Jerusalem.

Aertsen, A., & Arndt, M. (1993). Response synchronization in the visual cortex. *Curr. Opin. Neurobiol. 3*, 586–594.

Aertsen, A., Diesmann, M., & Gewaltig, M.-O. (1996). Propagation of synchronous spiking activity in feedforward neural networks. *J. Physiol. (Paris) 90*, 243–247.

Aertsen, A., Erb, M., & Palm, G. (1994). Dynamics of functional coupling in the cerebral cortex: an attempt at a model-based interpretation. *Physica D 75*, 103–128.

Aertsen, A., Gerstein, G., Habib, M., & Palm, G. (1989). Dynamics of neuronal firing correlation: Modulation of 'effective connectivity'. *J. Neurophysiol. 61*(5), 900–917.

Aertsen, A., Vaadia, E., Abeles, M., Ahissar, E., Bergman, H., Karmon, B., Lavner, Y., Margalit, E., Nelken, I., & Rotter, S. (1991). Neural interactions in the frontal cortex of a behaving monkey: Signs of dependence on stimulus context and behavioral state. *J. Hirnf. 32*(6), 735–743.

Agin, D. (1964). Hodgkin-Huxley equations: Logarithmic relation between membrane current and frequency of repetitive activity. *Nature 201*, 625–626.

Ahissar, M., Ahissar, E., Bergman, H., & Vaadia, E. (1992). Encoding of sound-source location and movement: Activity of single neurons and interactions between adjacent neurons in the monkey auditory cortex. *J. Neurophysiol. 67*, 203–215.

Amir, Y., Harel, M., & Malach, R. (1993). Cortical hierarchy reflected in the organization of intrinsic connections in macaque monkey visual cortex. *J. Compar. Neurol. 334*, 19–46.

Amit, D. J. (1989). *Modeling Brain Function*. Cambridge, New York: Cambridge University Press.

Amit, D. J., & Brunel, N. (1997). Model of global spontaneous activity and local structured activity during delay periods in the cerebral cortex. *Cereb. Cortex 7*, 237–252.

Arnol'd, V. I. (1992). *Ordinary Differential Equations* (3 ed.). Berlin, New York: Springer.

Arnoldi, H. M., & Brauer, W. (1996). Synchronization without oscillatory neurons. *Biol. Cybern. 74*(3), 209–223.

Arnoldi, H. M., Englmaier, K. H., & Brauer, W. (1999). Translation-invariant pattern recognition based on synfire chains. *Biol. Cybern. 80*(6), 433–447.

Arnoldi, H.-M. R. (1996). Korrelationsbedingte Informationsverarbeitung in neuronalen Systemen. Technical Report GSF-Bericht 8/96, Institut für Medizinische Informatik und Systemforschung, GSF-Forschungszentrum, Neuherberg.

Azouz, R., & Gray, C. M. (1999). Cellular mechanisms contributing to response variability of cortical neurons *in vivo*. *J. Neurosci. 19*(6), 2209–2223.

Azouz, R., & Gray, C. M. (2000). Dynamic spike threshold reveals a mechanism for synaptic coincidence detection in cortical neurons in vivo. *Proc. Natl. Acad. Sci. USA 97*(14), 8110–8115.

Baker, S. N., & Gerstein, G. L. (2000). Improvements to the sensitivity of gravitational clustering for multiple neuron recordings. *Neural Comput. 12*, 2597–2620.

Baker, S. N., & Gerstein, G. L. (2001). Determination of response latency and its application to normalization of cross-correlation measures. *Neural Comput. 13*(6), 1351–1377.

Barlow, H. (1992). The biological role of neocortex. In A. Aertsen & V. Braitenberg (Eds.), *Information Processing in the Cortex*, pp. 53–80. Berlin, Heidelberg, New York: Springer-Verlag.

Barlow, H. B. (1972). Single units and sensation: a neuron doctrine for perceptual psychology? *Perception 1*, 371–394.

Bernander, Ö., Koch, C., & Usher, M. (1994). The effect of synchronized inputs at the single neuron level. *Neural Comput. 6*, 622–641.

Bernard, C., Ge, Y. C., Stockley, E., Willis, J. B., & Wheal, H. V. (1994). Synaptic integration of NMDA and non-NMDA receptors in large neuronal network models solved by means of differential equations. *Biol. Cybern. 70*, 267–273.

Beurle, R. L. (1956). Properties of a mass of cells capable of regenerating pulses. *Philos. Trans. Roy. Soc. London B240*, 55–94. reprinted in (Shaw & Palm, 1988).

Bienenstock, E. (1991a). Notes on the growth of a "composition machine". In D. Andler, E. Bienenstock, & B. Laks (Eds.), *Proceedings of the Royaumont Interdisciplinary Workshop on Compositionality in Cognition and Neural Models*, Abbaye de Royaumont, Asniere s. Oise (Fr), pp. 1–19.

Bienenstock, E. (1991b). Suggestions for a neurobiological approach to syntax. In D. Andler, E. Bienenstock, & B. Laks (Eds.), *Proceedings of the Royaumont Interdisciplinary Workshop on Compositionality in Cognition and Neural Networks – II*, Abbaye de Royaumont, Asniere s. Oise (Fr), pp. 13–21.

Bienenstock, E. (1995). A model of neocortex. *Network: Comput. Neural Systems 6*, 179–224.

Bienenstock, E. (1996). Composition. In A. Aertsen & V. Braitenberg (Eds.), *Brain Theory – Biological Basis and Computational Principles*, Amsterdam, pp. 269–300. Elsevier.

Boven, K.-H., & Aertsen, A. (1990). Dynamics of activity in neuronal networks give rise to fast modulations of functional connectivity. In R. Eckmiller, G. Hartmann, & G. Hauske (Eds.), *Parallel Processing in Neural Systems and Computers*, pp. 53–56. Amsterdam: Elsevier.

Braitenberg, V. (1978). Cell assemblies in the cerebral cortex. In R. Heim & G. Palm (Eds.), *Theoretical Approaches to Complex Systems*, Volume 21 of *Lecture Notes in Biomathematics*, pp. 171–188. Berlin, Heidelberg, New York: Springer-Verlag.

Braitenberg, V. (1984). *Vehicles, Experiments in Synthetic Psychology.* Cambridge, Mass.: MIT Press.

Braitenberg, V., & Schüz, A. (1991). *Anatomy of the Cortex: Statistics and Geometry.* Berlin, Heidelberg, New York: Springer-Verlag.

Braitenberg, V., & Schüz, A. (1998). *Cortex: Statistics and Geometry of Neuronal Connectivity* (2nd ed.). Berlin: Springer-Verlag.

Bringuier, V., Chavane, F., Glaeser, L., & Frégnac, Y. (1999). Horizontal propagation of visual activity in the synaptic integration field of area 17 neurons. *Science 283*(5402), 695–699.

Bringuier, V., Frégnac, Y., Baranyi, A., Debanne, D., & Shulz, D. E. (1997). Synaptic origin and stimulus dependency of neuronal oscillatory activity in the primary visual cortex of the cat. *J. Physiol. (Lond.) 500.3*, 751–774.

Brody, C. D. (1999a). Correlations without synchrony. *Neural Comput. 11*, 1537–1551.

Brody, C. D. (1999b). Disambiguating different covariation types. *Neural Comput. 11*, 1527–1535.

Bronstein, I. N., Semendjajew, K. A., Grosche, G., Ziegler, V., Ziegler, D., & Zeidler, E. (1996). *Teubner-Taschenbuch der Mathematik* (25th ed.). Teubner Verlag.

Brunel, N. (2000). Dynamics of sparsely connected networks of excitatory and inhibitory spiking neurons. *J. Comput. Neurosci. 8*(3), 183–208.

Brunel, N., & Hakim, V. (1999). Fast global oscillations in networks of integrate-and-fire neurons with low firing rates. *Neural Comput. 11*(7), 1621–1671.

Bryant, H. L., & Segundo, J. P. (1976). Spike initiation by transmembrane current: a white-noise analysis. *J. Physiol. (Lond.) 260*, 279–314.

Burns, B. D., & Webb, A. C. (1976). The spontaneous activity of neurones in the cat's visual cortex. *Proc. R. Soc. Lond. B. 194*, 211–223.

Calvin, W. H., & Stevens, C. F. (1968). Synaptic noise and other sources of randomness in motoneuron interspike intervals. *J. Neurophysiol. 31*, 574–587.

Campbell, N. (1909). The study of discontinuous phenomena. *Proc. Cambridge Phil. Soc. 15*, 117–136.

Câteau, H., & Fukai, T. (2001). Fokker-planck approach to the pulse packet propagation in synfire chain. *Neural Networks 14*, 675–685.

Chakalova, K. (1998). Influence of oscillatory network activity on the response of single neurones to synchronous input. *Futura 13*(4).

Chance, F. S., & Abbott, L. F. (2000). Multiplicative gain modulation through balanced syaptic input. In *Soc. Neurosci. Abstr.*, Volume 26, pp. 1064.

Collins, J. J., Chow, C. C., Capela, A. C., & Imhoff, T. T. (1996). Aperiodic stochastic resonance. *Phys. Rev. E 54*(5), 5575–5584.

Collins, J. J., Chow, C. C., & Imhoff, T. T. (1995). Aperiodic stochastic resonance in excitable systems. *Phys. Rev. E 52*, R3321–R3324.

Colquhoun, D., & Hawkes, A. G. (1995). A Q-matrix cookbook: How to write only one program to calculate the single-channel and macroscopic predictions for any kinetic mechanism. In B. Sakmann & E. Neher (Eds.), *Single-Channel Recording* (2 ed.)., Chapter 20, pp. 397–482. New York: Plenum Press.

Connors, B. W., & Gutnick, M. J. (1990). Intrinsic firing patterns of diverse neocortical neurons. *TINS 13*(3), 99–104.

Connors, B. W., Gutnick, M. J., & Prince, D. A. (1982). Electrophysiological properties of neocortical neurons in vitro. *J. Neurophysiol. 48*(6), 1302–1320.

Contreras, D., Timofeev, I., & Steriade, M. (1996). Mechanisms of long-lasting hyperpolarizations underlying slow sleep oscillations in cat corticothalamic networks. *J. Physiol. (Lond) 494.1*, 251–264.

Cox, D. R. (1967). *Renewal Theory*. Science Paperbacks. London: Chapman and Hall.

Cox, D. R., & Isham, V. (1980). *Point Processes*. Monographs on Applied Probability and Statistics. Chapman and Hall.

Cronin, J. (1987). *Mathematical aspects of Hodgkin-Huxley neural theory*, Volume 7 of *Cambridge Studies in Mathematical Biology*. Cambridge: Cambrige University Press.

Dayan, P., & Abbott, L. F. (2001). *Theoretical Neuroscience*. Cambridge: MIT Press.

deCharms, R. C., & Merzenich, M. M. (1996). Primary cortical representation of sounds by the coordination of action-potential timing. *Nature 381*, 610–613.

Diesmann, M., Gewaltig, M.-O., & Aertsen, A. (1995). SYNOD: An environment for neural systems simulations - language interface and tutorial. Technical report, The Weizmann Institute of Science, 76100 Rehovot, Israel. Technical Report GC-AA/95-3.

Diesmann, M., Gewaltig, M.-O., & Aertsen, A. (1996a). Characterization of synfire activity by propagating 'pulse packets'. In J. M. Bower (Ed.), *Computational Neuroscience: Trends in Research 1995*, Chapter 10, pp. 59–64. San Diego: Academic Press.

Diesmann, M., Gewaltig, M.-O., & Aertsen, A. (1996b). A two-dimensional state space analysis of cortical synfire activity. In *Israel Society for Neuroscience, Fifth Annual Meeting*, Volume 32, Eilat, pp. 22. Israel Society for Neuroscience.

Diesmann, M., Gewaltig, M.-O., & Aertsen, A. (1997). Cortical synfire activity – a two dimensional state space analysis. In H. Wässle & N. Elsner (Eds.), *From Membrane to Mind. Proc 25th Göttingen Neurobiol Conf*, pp. 62. Stuttgart, New York: Thieme.

Diesmann, M., Gewaltig, M.-O., & Aertsen, A. (1999). Stable propagation of synchronous spiking in cortical neural networks. *Nature 402*, 529–533.

Diesmann, M., Gewaltig, M.-O., Rotter, S., & Aertsen, A. (2001). State space analysis of synchronous spiking in cortical neural networks. *Neurocomputing 38–40*, 565–571.

Diesmann, M., Rotter, S., Gewaltig, M.-O., & Aertsen, A. (1996). Estimating the temporal accuracy of neural spike responses. In H. Schnitzler & N. Elsner (Eds.), *Brain and Evolution. Proc 24th Göttingen Neurobiol Conf*, Volume 2, pp. 474. Stuttgart, New York: Thieme.

Douglas, R. J., & Martin, K. A. C. (1991a). A functional microcircuit for cat visual cortex. *J. Physiol. (Lond.) 440*, 735–769.

Douglas, R. J., & Martin, K. A. C. (1991b). An intracellular analysis of the visual responses of neurones in cat visual cortex. *J. Physiol. (Lond.) 440*, 659–696.

Doursat, R. (1991). *Contribution à l'étude des représentations dans le systéme nerveaux et dans les réseaux de neurones formels*. Ph. D. thesis, Université Paris VI.

Druskin, V., Greenbaum, A., & Knizhnerman, L. (1998). Using nonorthogonal Lanczos vectors in the computation of matrix functions. *SIAM J. Appl. Math. 19*(1), 38–54.

Ebbinghaus, C. (1997). Charakterisierung der neuronalen Feuerschwelle. Master's thesis, Fak. f. Biologie der Universität Tübingen.

Ebbinghaus, C., Diesmann, M., Rotter, S., & Aertsen, A. (1997). The neural firing threshold: Can I help U? In H. Wässle & N. Elsner (Eds.), *From Membrane to Mind. Proc. 25th Göttingen Neurobiol Conf.*, Volume 2, pp. 624. Stuttgart, New York: Thieme.

Eccles, J. C. (1957). *The physiology of nerve cells*. Baltimore: Johns Hopkins Press.

Eckhorn, R., Bauer, R., Jordan, W., Brosch, M., Kruse, W., Munk, M., & Reitböck, H. J. (1988). Coherent oscillations: A mechanism of feature linking in the visual cortex? *Biol. Cybern. 60*, 121–130.

Eggermont, J. J. (1992). Neural interaction in cat primary auditory cortex. II. Effects of sound stimulation. *J. Neurophysiol. 71*, 246–270.

Elaydi, S. N. (1999). *Discrete Chaos*. Chapmann & Hall/CRC.

Engel, A. K., König, P., Schillen, T. B., & Singer, W. (1992). Temporal coding in the visual cortex: new vistas on integration in the nervous system. *TINS 15*(6), 218–226.

Engert, F., & Bonhoeffer, T. (1999). Dendritic spine changes associated with hippocampal long-term synaptic plasticity. *Nature 399*, 66–70.

Fetz, E., Toyama, K., & Smith, W. (1991). Synaptic interactions between cortical neurons. In A. Peters (Ed.), *Cerebral Cortex*, Volume 9, Chapter 1, pp. 1–47. New York: Plenum Publishing Corporation.

Fujii, H., Ito, H., Aihara, K., Ichinose, N., & Tsukada, M. (1996). Dynamical cell assembly hypothesis – theoretical possibility of spatio-temporal coding in the cortex. *Neural Networks 9*(8), 1303–1350. special issue.

Georgopoulos, A. P., Kettner, R. E., & Schwartz, A. B. (1988). Primate motor cortex and free arm movements to visual targets in three-dimensional space. II. Coding of the direction of movement by a neuronal population. *J. Neurosci. 8*(8), 2928–2937.

Georgopoulos, A. P., Lurito, J. T., Petrides, M., Schwartz, A. B., & Massey, J. T. (1989). Mental rotation of the neuronal population vector. *Science 243*, 234–236.

Gerstein, G., Bloom, M. J., Espinosa, I. E., & Evanczuk, S. (1983). Design of a laboratory for multiunit studies. *IEEE Trans. Sys. M. Cybern. 5*, 668–676.

Gerstein, G. L., & Aertsen, A. M. H. J. (1985). Representation of cooperative firing activity among simultaneously recorded neurons. *J. Neurophysiol. 54*(6), 1513–1528.

Gerstein, G. L., Bedenbaugh, P., & Aertsen, A. (1989). Neuronal assemblies. *IEEE Trans. Biomed. Eng. 36*, 4–14.

Gerstein, G. L., & Mandelbrot, B. (1964). Random walk models for the spike activity of a single neuron. *Biophys. J. 4*, 41–68.

Gerstein, G. L., & Perkel, D. H. (1969). Simultaneously recorded trains of action potentials: Analysis and functional interpretation. *Science 164*, 828–830.

Gerstein, G. L., & Perkel, D. H. (1972). Mutual temporal relationships among neuronal spike trains. *Biophys. J. 12*, 453–472.

Gewaltig, M.-O. (2000). *Evolution of Synchronous Spike Volleys in Cortical Networks – Network Simulations and Continuous Probabilistic Models*. Aachen, Germany: Shaker.

Gewaltig, M.-O., Diesmann, M., & Aertsen, A. (2001a). Cortical synfire-activity: Configuration space and survival probability. *Neurocomputing 38–40*, 621–626.

Gewaltig, M.-O., Diesmann, M., & Aertsen, A. (2001b). Propagation of cortical synfire activity: survival probability in single trials and stability in the mean. *Neural Networks 14*, 657–673.

Gewaltig, M.-O., Diesmann, M., Rotter, S., & Aertsen, A. (1997). Cortical synfire activity – stability in an analytical model. In H. Wässle & N. Elsner (Eds.), *From Membrane to Mind. Proc 25th Göttingen Neurobiol Conf*, Volume 2, pp. 620. Stuttgart, New York: Thieme.

Goldstein, M. H. (1960). A statistical model for interpreting neuroelectric responses. *Information and Control 3*, 1–17.

Golub, G. H., & van Loan, C. F. (1996). *Matrix Computations* (3 ed.). Johns Hopkins University Press.

Gray, C. M., König, P., Engel, A. K., & Singer, W. (1989). Oscillatory responses in cat visual cortex exhibit inter-columnar synchronization which reflects global stimulus properties. *Nature 338*, 334–337.

Gray, C. M., & Singer, W. (1987). Stimulus-specific neuronal oscillations in the cat visual cortex: A cortical functional. In *Soc. Neurosci. Abstr.*, Volume 13, pp. 404.3.

Gray, C. M., & Singer, W. (1989). Stimulus-specific neuronal oscillations in orientation columns of cat visual cortex. *Proc. Natl. Acad. Sci. USA 86*, 1698–1702.

Griffith, J. S. (1963). On the stability of brain-like structures. *Biophys. J. 3*, 299–308.

Grün, S. (1996). *Unitary Joint-Events in Multiple–Neuron Spiking Activity: Detection, Significance, and Interpretation*. Reihe Physik, Band 60. Thun, Frankfurt/Main: Verlag Harri Deutsch.

Grün, S., & Diesmann, M. (2000). Evaluation of higher-order coincidences in multiple parallel proceses. In *Soc. Neurosci. Abstr.*, Volume 26, pp. 828.3.

Grün, S., Diesmann, M., & Aertsen, A. (2002a). 'Unitary Events' in multiple single-neuron activity. I. Detection and significance. *Neural Comput. 14*(1), 43–80.

Grün, S., Diesmann, M., & Aertsen, A. (2002b). 'Unitary Events' in multiple single-neuron activity. II. Non-Stationary data. *Neural Comput. 14*(1), 81–119.

Grün, S., Diesmann, M., Grammont, F., Riehle, A., & Aertsen, A. (1999). Detecting unitary events without discretization of time. *J. Neurosci. Meth. 94*, 67–79.

Grün, S., Riehle, A., & Diesmann, M. (2001). Unitary events analysis on the basis of surrogates. In N. Elsner & G. Kreutzberg (Eds.), *Proceedings of the 28th Göttingen Neurobiology Conference*, Stuttgart, pp. 251. Thieme.

Gütig, R., Aertsen, A., & Rotter, S. (2002). Statistical significance of coincident spikes: Count-based versus rate-based statistics. *Neural Comput. 14*(1), 121–153.

Gütig, R., Aharanov-Barki, R., Rotter, S., Aertsen, A., & Sompolinsky, H. (2001). Generalized synaptic updating in temporally asymmetric hebbian learning. In *Proceedings of the 28th Göttingen Neurobiology Conference*, Stuttgart, pp. 254. Thieme.

Hansel, D., Mato, G., Meunier, C., & Neltner, L. (1998). On numerical simulations of integrate-and-fire neural networks. *Neural Comput. 10*(2), 467–483.

Hatsopoulos, N. G., Ojakangas, C. L., Paninski, L., & Donoghue, J. P. (1998). Information about movement direction obtained from synchronous activity of motor cortical areas. *Proc. Natl. Acad. Sci. USA 95*, 15706–15711.

Haykin, S. S. (1998). *Neural Networks: A Comprehensive Foundation* (2 ed.). Upper Saddle River: Prentice Hall.

Hebb, D. O. (1949). *Organization of behavior. A neurophysiological theory*. New York: John Wiley & Sons.

Heck, D., Léger, J. F., Stern, E. A., & Aertsen, A. (2000). Size and summation of synchronous and asynchronous population PSPs in rat neocortical neurons: Intracellular recording in vivo with dual intracortical microstimulation. In *Soc. Neurosci. Abstr.*, Volume 26, pp. 609.6.

Hehl, U., Aertsen, A., & Diesmann, M. (2001a). Dynamics of diluted synfire chains. In A. Aertsen, G. Hauske, & M. Tsudaka (Eds.), *6th Tamagawa Brain Forum*, Breisach, pp. P–18. Neurobiology & Biophysics, Albert-Ludwigs-Universität.

Hehl, U., Aertsen, A., & Diesmann, M. (2001b). Dynamics of diluted synfire chains.

Hehl, U., Hellwig, B., Rotter, S., Diesmann, M., & Aertsen, A. (2001). Localization of synchronous spiking as a result of anatomical connectivity. In *Soc. Neurosci. Abstr.*, Volume 27, pp. 64.1.

Hellwig, B. (2000). A quantitative analysis of the local connectivity between pyramidal neurons in layers 2/3 of the rat visual cortex. *Biol. Cybern. 82*, 111–121.

Heneghan, C., Chow, C. C., Collins, J. J., Imhoff, T. T., Lowen, S. B., & Teich, M. C. (1996). Information measures quantifying aperiodic stochastic resonance. *Phys. Rev. E 54*, R2228–R2231.

Hentschke, H., & Antkowiak, B. (1999). NMDA receptor-mediated changes of spontaneous activity patterns in thalamocortical slice cultures. *Brain Res. 830*, 123–137.

Herrmann, M., Hertz, J. A., & Prügel-Bennett, A. (1995). Analysis of synfire chains. *Network 6*, 403–414.

Hertz, J., & Prügel-Bennet, A. (1996). Learning synfire-chains by self-organization. *Network: Comput. Neural Systems 7*(2), 357–363.

Hirsch, M., & Smale, S. (1974). *Differential Equations, Dynamical Systems, and Linear Algebra*. San Diego: Academic Press.

Hodgkin, A. L., & Huxley, A. F. (1952). A quantitative description of membrane current and its application to conduction and excitation in nerve. *J. Physiol. (Lond.) 117*, 500–544.

Holt, G. R., Softky, W. R., Koch, C., & Douglas, R. J. (1996). Comparison of discharge variability *in vitro* and in *in vivo* in cat visual cortex neurons. *J. Neurophysiol. 75*(5), 1806–1814.

Hopfield, J. J. (1982). Neural networks and physical systems with emergent collective computational abilities. *Proc. Natl. Acad. Sci. USA 79*, 2554–2558.

Hopfield, J. J. (1984). Neurons with graded response have collective computational properties like those of two-state neurons. *Proc. Natl. Acad. Sci. USA 81*, 3088–3092.

Hubel, D. H., & Wiesel, T. N. (1968). Receptive fields and functional architecture of monkey striate cortex. *J. Neurophysiol. 195*(1), 215–243.

Jack, J. J. B., Noble, D., & Tsien, R. W. (1983). *Electric Current Flow in Excitable Cells*. Oxford: Oxford University Press.

Janson, S., Rucinski, A., Luczak, T., & Uczak, T. (2000). *Theory of Random Graphs*. Wiley.

Johnston, D., & Wu, S. M.-S. (1995). *Foundations of Cellular Neurophysiology*. Cambridge, Massachusetts: MIT Press.

Kampa, B. (1998). Untersuchung der dynamischen Übertragunseigenschaft cortikaler Neuronen: Ein Vergleich von Simulation und Experiment. Master's thesis, Fakultät für Biologie, Albert-Ludwigs-Universität Freiburg, Germany.

Kampa, B., Chakalova, K., Heck, D., Diesmann, M., & Aertsen, A. (1999). Transmission of synchronous spiking activity by cortical neurons *in vitro*. In *Proceedings of the 27th Göttingen Neurobiology Conference*, Stuttgart, pp. 99. Thieme.

Kampa, B., Nawrot, M. P., Aertsen, A., Rotter, S., & Heck, D. (2000). Cortical dynamics in vivo: A new in vitro approach. In *Soc. Neurosci. Abstr.*, Volume 26, pp. 609.4.

Kandel, E. R., Schwartz, J. H., & Jessel, T. M. (1991). *Principles of neural science* (3 ed.). New York: Elsevier.

Kaplan, D., & Glass, L. (1995). *Understanding Nonlinear Dynamics*. Springer.

Katz, B. (1966). *Nerve, Muscle and Synapse*. New York: McGraw-Hill.

Kenny, C. S., & Laub, A. J. (1998). A Schur-Fréchet algorithm for computing the logarithm and exponential of a matrix. *SIAM J. Matrix Anal. Appl. 19*(3), 640–663.

Kisley, M. A., & Gerstein, G. L. (1999). The continuum of operating modes for a passive model neuron. *Neural Comput. 11*, 1139 – 1154.

Knight, B. W. (1972). Dynamics of encoding in a population of neurons. *J. Gen. Physiol. 59*, 734–766.

Koch, C. (1999). *Biophysics of Computation. Information Processing in Single Neurons*. New York, Oxford: Oxford University Press.

König, P., Engel, A. K., & Singer, W. (1996). Integrator or coincidence detector? The role of the cortical neuron revisited. *TINS 19*(4), 130–137.

Kuhn, A., Rotter, S., & Aertsen, A. (2002). Correlated input spike trains and their effects on the leaky integrate-and-fire neuron. *Neurocomputing 44–46*, 121–126.

Lampl, I., Reichova, I., & Ferster, D. (1999). Synchronous membrane potential fluctuations in neurons of the cat visual cortex. *Neuron 22*, 361–374.

Lampl, I., & Yarom, Y. (1993). Subthreshold oscillations of the membrane potential: A functional synchronizing and timing device. *J. Neurophysiol. 70*(5), 2181–2186.

Lampl, I., & Yarom, Y. (1997). Subthreshold oscillations and resonant behavior – two manifestations of the same mechanism. *Neuroscience 78*(2), 325–341.

Lapicque, L. (1907). Recherches quantitatives sur l'excitation electrique des nerfs traitee comme une polarization. *J. Physiol. Pathol. Gen. 9*, 620–635.

Laubach, M., Wessberg, J., & Nicolelis, M. A. (2000). Cortical ensemble activity increasingly predicts behaviour outcomes during learning of a motor task. *Nature 405*(6786), 567–571.

Léger, J.-F., Stern, E. A., Aertsen, A., & Heck, D. (2002). Synaptic integration in the cortex shaped by network activity. (submitted).

Leonard, I. E. (1996). The matrix exponential. *SIAM Rev. 38*(3), 507–512.

Lettvin, J. Y., Maturana, H. R., McCulloch, W. S., & Pitts, W. R. (1959). What the frog's eye tells the frog's brain. *Proc. I. R. E. 47*, 1940–1951.

Levitan, H., Segundo, J. P., Moore, G. P., & Perkel, D. H. (1968). Statistical analysis of membrane potential fluctuations. *Biophys. J. 8*(2), 1256–1274.

Lewicki, M. (1998). A review of methods for spike sorting: the detection and classification of neural action potentials. *Network: Computation in Neural Systems 9*, R53–R78.

Lübke, J., Egger, V., Sakmann, B., & Feldmeyer, D. (2000). Columnar organization of dendrites and axons of single and synaptically coupled excitatory spiny neurons in layer 4 of the rat barrel cortex. *J. Neurosci. 20*, 5300–5311.

Lübke, J., Markram, H., Frotscher, M., & Sakmann, B. (1996). Frequency, number and dendritic distribution of autapses established by layer 5 pyramidal neurons in the neocortex: Comparison with synaptic innervation of neighboring neurons of the same class. *J. Neurosci. 16*(10), 3209–3218.

MacGregor, R. J. (1987). *Neural and Brain Modeling*. San Diego: Academic Press.

Mainen, Z. F., & Sejnowski, T. J. (1995). Reliability of spike timing in neocortical neurons. *Science 268*, 1503–1506.

Maletic-Savatic, M., Malinow, R., & Svoboda, K. (1999). Rapid dendritic morphogenesis in ca1 hippocampal dendrites induces by synaptic activity. *Science 283*, 1923–1927.

Markram, H., Lübke, J., Frotscher, M., & Sakmann, B. (1997). Regulation of synaptic efficacy by coincidence of postsynaptic APs and EPSPs. *Science 275*, 213–215.

Markram, H., & Tsodyks, M. (1996). Redistribution of synaptic efficacy between neocortical pyramidal neurons. *Nature 382*(6594), 807–810.

Marsalek, P., Koch, C., & Maunsel, J. (1997). On the relationship between synaptic input and spike output jitter in individual neurons. *Proc. Natl. Acad. Sci. USA 94*, 735–740.

Martin, K. A. C. (1994). A brief history of the "feature detector". *Cereb. Cortex 4*, 1–7.

Martin, K. A. C. (2000). The pope and grandmother– a frog's-eye view of theory. *Nat. Neurosci. 3*, 1169.

Mascagni, M. V. (1989). Numerical methods for neuronal modeling. In C. Koch & I. Segev (Eds.), *Methods in Neuronal Modeling: From Synapses to Networks*, Chapter 13, pp. 439–484. Cambridge, Massachusetts: A Bradford Book, The MIT Press.

Mason, A., Nicoll, A., & Stratford, K. (1991). Synaptic transmission between individual pyramidal neurons of the rat visual cortex in vitro. *J. Neurosci. 11*(1), 72–84.

MathWorks (1998). *MATLAB The Language of Technical Computing: Using MATLAB*. Natick, MA. 24 Prime park Way, Natick, Mass. 01760-1500.

Matsumura, M., Chen, D., Sawaguchi, T., Kubota, K., & Fetz, E. E. (1996). Synaptic interactions between primate precentral cortex neurons revealed by spike-triggered averaging of intracellular membrane potentials *in vivo*. *J. Neurosci. 16*(23), 7757–7767.

Matus, A. (1999). Postsynaptic actin and neuronal plasticity. *Curr. Opin. Neurobiol. 9*, 561–565.

McCormick, D. A., Connors, B. W., Lighthall, J. W., & Prince, D. A. (1985). Comparative electrophysiology of pyramidal and sparsely spiny neurons of the neocortex. *J. Neurophysiol. 54*(4), 782–806.

McCulloch, W. S., & Pitts, W. (1943). A logical calculus of the ideas immanent in neural nets. *Bull. Math. Biophys. 5*, 115–137.

Mehring, C., Hehl, U., Kubo, M., Diesmann, M., & Aertsen, A. (2003). Activity dynamics and propagation of synchronous spiking in locally connected random networks. *Biol. Cybern. 88*(5), 395–408.

Mehring, C., Kümmell, F., Rodriguez, V., Nawrot, M., Aertsen, A., & Heck, D. (2001). Non-linear electrical properties of sharp microelectrodes and patch pipettes: relevance for experiments using intracellular current injection. In N. Elsner & G. W. Kreutzberg (Eds.), *Proceedings of the 28th Göttingen Neurobiology Conference*, Stuttgart, pp. 618. Thieme.

Minsky, M. L., & Papert, S. (1988). *Perceptrons: An introduction to computational geometry* (expanded ed.). Cambridge, Massachusetts: MIT Press.

Mohns, M. (2000). Interaction of synchronous spiking and ongoing activity in cortical networks – a model study. Master's thesis, Fakultät für Biologie, Albert-Ludwigs-Universität Freiburg, Germany.

Mohns, M., Diesmann, M., Grün, S., & Aertsen, A. (1999). Interaction of synchronous input activity and subthreshold oscillatons of membrane potential. In *Proceedings of the 27th Göttingen Neurobiology Conference*, Stuttgart, pp. 100. Thieme.

Moler, C., & van Loan, C. (1978). Nineteen dubious ways to compute the exponent of a matrix. *SIAM Rev. 20*(4), 801–836.

Murthy, V. N., & Fetz, E. E. (1992). Coherent 25 to 35 Hz oscillations in the sensorimotor cortex of awake behaving monkeys. *Proc. Natl. Acad. Sci. USA 89*, 5670–5674.

Murthy, V. N., & Fetz, E. E. (1993). Effects of input synchrony on the response of a model neuron. In F. H. Eeckman & J. M. Bower (Eds.), *Computation and Neural Systems*, pp. 475–479. Boston: Kluwer Academic Publishers.

Murthy, V. N., & Fetz, E. E. (1994). Effects of input synchrony on the firing rate of a three-conductance cortical neuron model. *Neural Comput. 6*, 1111–1126.

Nawrot, M. P., Aertsen, A., & Rotter, S. (1999). Single-trial estimation of neuronal firing rates: From single-neuron spike trains to population activity. *J. Neurosci. Meth. 94*(2), 81–92.

Nawrot, M. P., Kampa, B., Aertsen, A., Rotter, S., & Heck, D. (2001a). Network activity in vitro induced by dynamic photostimulation. In *Proceedings of the 28th Göttingen Neurobiology Conference*, Stuttgart, pp. 617. Thieme.

Nawrot, M. P., Rodriguez, V., Aertsen, A., Rotter, S., & Heck, D. (2001b). Variability and irregularity of firing in cortical neurons. In *Proceedings of the 28th Göttingen Neurobiology Conference*, pp. 619.

Nicholls, J. G., Martin, R. A., Wallace, B. G., & Fuchs, P. A. (2001). *From neuron to brain* (4 ed.). Sunderland, MA: Sinauer Associates.

Nicolelis, M. A. L. (Ed.) (1998). *Methods for Neural Ensemble Recordings*. Boca Raton, Florida: CRC Press.

Nicolelis, M. A. L., Baccala, L. A., Lin, R. C. S., & Chapin, J. K. (1995). Sensorimotor encoding by synchronous neural assembly activity at multiple levels in the somatosensory system. *Science 268*, 1353–1358.

Nowak, L. G., Sanchez-Vives, M. V., & McCormick, D. A. (1997). Influence of Low and High Frequency Inputs on Spike Timing in Visual Cortical Neurons. *Cereb. Cortex 7*, 487–501.

O'Neil, M., Abbott, L., Sharp, A., Turrigiano, G., & Marder, E. (1995). The dynamic clamp: Using neurons as simulators. In M. Arbib (Ed.), *The Handbook of Brain Theory and Neural Networks*, pp. 326–328. Cambridge: MIT Press.

Palm, G. (1982). *Neural Assemblies. An Alternative Approach to Artificial Intelligence*, Volume 7 of *Studies of Brain Function*. Berlin: Springer-Verlag.

Palm, G. (1990). Cell assemblies as a guidline for brain reseach. *Conc. Neurosci. 1*, 133–148.

Palmer, E. M. (1985). *Graphical Evolution*. Wiley.

Papoulis, A. (1991). *Probability, Random Variables, and Stochastic Processes* (3rd ed.). New York: McGraw-Hill, Inc.

Paré, D., Shink, E., Gaudreau, H., Destexhe, A., & Lang, E. (1998). Impact of spontaneous synaptic activity on the resting properties of cat neocortical pyramidal neurons in vivo. *J. Neurophysiol. 79*, 1450–1460.

Pauluis, Q., & Baker, S. N. (2000). An accurate measure of the instantaneous discharge probability, with application to unitary joint-event analysis. *Neural Comput. 12*(3), 647–669.

Perkel, D. H., & Bullock, T. H. (1968). Neural coding. *Neurosci. Res. Prog. Bull. 6*(3), 221–348.

Perkel, D. H., Gerstein, G. L., & Moore, G. P. (1967a). Neuronal spike trains and stochastic point processes. I. The single spike train. *Biophys. J. 7*(4), 391–418.

Perkel, D. H., Gerstein, G. L., & Moore, G. P. (1967b). Neuronal spike trains and stochastic point processes. II. Simultaneous spike trains. *Biophys. J. 7*(4), 419–440.

Perkel, D. H., Gerstein, G. L., Smith, M. S., & Tatton, W. G. (1975). Nerve-impulse patterns: a quantitative display technique for three neurons. *Brain Res. 100*, 271–296.

Plesser, H. E., & Gerstner, W. (2000). Noise in integrate-and-fire neurons: From stochastic input to escape rates. *Neural Comput. 12*, 367–384.

Postma, Eric O. van den Herik, H. J., & Hudson, P. T. W. (1996). Robust feedforward processing in synfire chains. *Int. J. Neural. Sys. 7*(4), 537–542.

Press, W. H., Teukolsky, S. A., Vetterling, W. T., & Flannery, B. P. (1992). *Numerical Recipes in C* (2 ed.). Cambridge University Press.

Prut, Y. (1995). *Firing Patterns as a sensitive estimator of cortical information processing*. PhD dissertation, Hebrew University of Jerusalem.

Prut, Y., Vaadia, E., Bergman, H., Haalman, I., Hamutal, S., & Abeles, M. (1998). Spatiotemporal structure of cortical activity: Properties and behavioral relevance. *J. Neurophysiol. 79*(6), 2857–2874.

Ricciardi, L. M., Di Crescenzo, A., Giorno, V., & Nobile, A. G. (1999). An outline of theoretical and algorithmic approaches to first passage time problems with applications to biological modeling. *Math. Japonica 50*(2), 247–322.

Rice, S. O. (1944). Mathematical analysis of random noise. *Bell System Tech. J. 23*, 282–332. reprinted in (Wax, 1954).

Riehle, A., Grammont, F., Diesmann, M., & Grün, S. (2000). Dynamical changes and temporal precision of synchronized spiking activity in motor cortex during movement preparation. *J. Physiol. (Paris) 94*(5–6), 569–582.

Riehle, A., Grün, S., Diesmann, M., & Aertsen, A. (1997). Spike synchronization and rate modulation differentially involved in motor cortical function. *Science 278*, 1950–1953.

Rodriguez, V. M., Diesmann, M., Kampa, B., Mehring, C., Aertsen, A., & Heck, D. (2001). Reliability and precision of cortical spike responses to synchronous input: Dependence on shape and temporal distribution of epscs. In *Soc. Neurosci. Abstr.*, Volume 27, pp. 501.8.

Roelfsema, P., Engel, A., König, P., & Singer, W. (1996). The role of neuronal synchronization in response selection: A biologically plausible theory of structured representations in the visual cortex. *J. Cogn. Neurosci. 8*(6), 603–625.

Rotter, S. (1994). *Wechselwirkende stochastische Punktprozesse als Modell für neuronale Aktivität im Neocortex der Säugetiere*. Number 21 in Reihe Physik. Frankfurt am Main: Verlag Harri Deutsch.

Rotter, S., & Diesmann, M. (1999). Exact digital simulation of time-invariant linear systems with applications to neuronal modeling. *Biol. Cybern. 81*(5/6), 381–402.

Rotter, S., Diesmann, M., Frégnac, Y., & Aertsen, A. (2001). The firing threshold of cortical neurons revealed from *in vivo* intracellular recordings. In N. Elsner & G. W. Kreutzberg (Eds.), *Proceedings of the 28th Göttingen Neurobiology Conference*, Stuttgart, pp. 256. Thieme.

Roy, A., Steinmetz, P. N., & Niebur, E. (2000). Rate limitations of unitary event analysis. *Neural Comput. 12*, 2063–2082.

Rubin, J., Lee, D., & Sompolinsky, H. (2001). Equilibrium properties of temporally asymmetric Hebbian plasticity. *Phys. Rev. Lett. 86*, 364–367.

Rummelhart, D. E., McClelland, J. L., & the PDP Research Group (1986). *Parallel Distributed Processing, Explorations in the Microstructure of Cognition: Foundations*, Volume 1. Cambridge, Massachusetts: MIT Press.

Sakurai, Y. (1996). Population coding by cell assemblies - what it really is in the brain. *Neuroscience Research 26*, 1–16.

Salinas, E., & Sejnowski, T. J. (2001). Correlated neuronal activity and the flow of neural information. *Nat. Rev. Neurosci. 2*(8), 539–550.

Sanes, J. N., & Donoghue, J. P. (1993). Oscillations in local field potentials of the primate motor cortex during voluntary movement. *Proc. Natl. Acad. Sci. USA 90*, 4470–4474.

Savitzky, A., & Golay, M. J. E. (1964). Smoothing and differentiation of data by simplified least squares procedures. *Analytical Chemistry 36*(8), 1627–1639.

Schüz, A. (1994). Patchiness as a means to get a message across. *TINS 17*(9), 365.

Schüz, A., & Liewald, D. (2001). Patterns of cortico-cortical connections in the mouse. In *Proceedings of the 28th Göttingen Neurobiology Conference*, Stuttgart, pp. 624. Thieme.

Segev, I., Burke, R. E., & Hines, M. (1998). Compartmental models of complex neurons. In C. Koch & I. Segev (Eds.), *Methods in neuronal modeling: from ions to networks* (2 ed.)., Chapter 3, pp. 93–136. Cambridge: A Bradford Book, MIT Press.

Shadlen, M. N., & Movshon, A. J. (1999). Synchrony unbound: A critical evaluation of the temporal binding hypothesis. *Neuron 24*, 67–77.

Shadlen, M. N., & Newsome, W. T. (1994). Noise, neural codes and cortical organization. *Curr. Opin. Neurobiol. 4*(4), 569–579.

Shadlen, M. N., & Newsome, W. T. (1995). Is there a signal in the noise? *Curr. Opin. Neurobiol. 5*, 248–250.

Shadlen, M. N., & Newsome, W. T. (1998). The variable discharge of cortical neurons: Implications for connectivity, computation, and information coding. *J. Neurosci. 18*(10), 3870–3896.

Sharp, A., O'Neil, M. B., Abbott, L. F., & Marder, E. (1993a). The dynamic clamp: Artificial conductances in biological neurons. *TINS 16*, 389–394.

Sharp, A. A., O'Neil, M. B., Abbott, L. F., & Marder, E. (1993b). The dynamic clamp: Computer-generated conductances in real neurons. *J. Neurophysiol. 69*, 992–995.

Shaw, G. L., & Palm, G. (Eds.) (1988). *Brain Theory*, Volume 1 of *Advanced Series in Neuroscience*. Singapore: World Scientific.

Sherman-Gold, R. (1993). *The axon guide for electrophysiology and biophysics laboratory techniques*. Axon Instruments, Inc.

Sherrington, C. S. (1906). *Integrative action of the nervous system*. New Haven: Yale University Press.

Singer, W. (1993). Synchronization of cortical activity and its putative role in information processing and learning. *Annu. Rev. Physiol. 55*, 349–374.

Singer, W. (1999a). Neural synchrony: a versatile code for the definition of relations. *Neuron 24*, 49–65.

Singer, W. (1999b). Striving for coherence. *Nature 397*, 391–393.

Singer, W., Engel, A. K., Kreiter, A. K., Munk, M. H. J., Neuenschwander, S., & Roelfsema, P. R. (1997). Neuronal assemblies: necessity, signature and detectability. *Trends in Cognitive Sciences 1*(7), 252–261.

Singer, W., & Gray, C. (1995). Visual feature integration and the temporal correlation hypothesis. *Annu. Rev. of Neurosci. 18*, 555–586.

Softky, W. R., & Koch, C. (1993). The highly irregular firing of cortical cells is inconsistent with temporal integration of random EPSPs. *J. Neurosci. 13*(1), 334–350.

Song, S., Miller, K. D., & Abbott, L. F. (2000). Competitive Hebbian learning through spike-timing-dependent synaptic plasticity. *Nat. Neurosci. 3*(9), 919–926.

Stein, R. B. (1965). A theoretical analysis of neuronal variability. *Biophys. J. 5*, 173–194.

Stein, R. B. (1967a). The frequency of nerve action potentials generated by applied currents. *Proc. R. Soc. Lond. B. 167*, 64–86.

Stein, R. B. (1967b). Some models of neuronal variability. *Biophys. J. 7*, 37–68.

Stein, R. B. (1972). The stochastic properties of spike trains recorded from nerve cells. In P. A. W. Lewis (Ed.), *Stochastic Point Processes – Statistical Analysis, Theory and Applications*, pp. 700–731. New York: Wiley.

Steinmetz, P., Roy, A., Fitzgerald, P., Hsiao, S., Johnson, K., & Niebur, E. (2000). Attention modulates synchronized neuronal firing in primate somatosensory cortex. *Nature 404*(6774), 187–190.

Stemmler, M. (1996). A single spike suffices: The simplest form of stochastic resonance in model neurons. *Network: Comput. Neural Systems 7*(4), 687–716.

Stevens, C. F., & Zador, A. M. (1998). Input synchrony and the irregular firing of cortical neurons. *Nature Neuroscience 1*(3), 210–217.

Strogatz, S. H. (1994). *Nonlinear Dynamics and Chaos: with Applications to Physics, Biology, Chemistry, and Engineering*. Reading, Massachusetts: Perseus Books.

Taira, M., & Georgopoulos, A. P. (1993). Cortical cell types from spike trains. *Neurosci. Res. 17*, 39–45.

Tetzlaff, T., Buschermöhle, M., Geisel, T., & Diesmann, M. (2003). The spread of rate and correlation in stationary cortical networks. *Neurocomputing 52–54*, 949–954.

Tetzlaff, T., Geisel, T., & Diesmann, M. (2001). The ground state of synfire structures. In N. Elsner & G. Kreutzberg (Eds.), *Proceedings of the 28th Göttingen Neurobiology Conference*, Stuttgart, pp. 260. Thieme.

Tetzlaff, T., Geisel, T., & Diesmann, M. (2002). The ground state of cortical feed-forward networks. *Neurocomputing 44–46*, 673–678.

Thomson, A. M., Deuchars, J., & West, D. C. (1993). Large, deep layer pyramid-pyramid single axon epsps in slices of rat motor cortex display paired pulse and freuquency-dependent depression, mediated presynaptically and self-facilitation mediated postsynaptically. *J. Neurophysiol. 70*(6), 2354–2369.

Tuckwell, H. C. (1988a). *Introduction to Theoretical Neurobiology*, Volume 1. Cambridge: Cambridge University Press.

Tuckwell, H. C. (1988b). *Introduction to Theoretical Neurobiology*, Volume 2. Cambridge: Cambridge University Press.

Vaadia, E., & Aertsen, A. (1992). Coding and computation in the cortex: Single-neuron activity and cooperative phenomena. In A. Aertsen & V. Braitenberg (Eds.), *Information Processing in the Cortex*, pp. 81–121. Berlin: Springer-Verlag.

Vaadia, E., Haalman, I., Abeles, M., Bergman, H., Prut, Y., Slovin, H., & Aertsen, A. (1995). Dynamics of neuronal interactions in monkey cortex in relation to behavioural events. *Nature 373*(6514), 515–518.

van Vreeswijk, C., & Sompolinsky, H. (1996). Chaos in neuronal networks with balanced excitatory and inhibitory activity. *Science 274*, 1724–1726.

van Vreeswijk, C., & Sompolinsky, H. (1998). Chaotic balanced state in a model of cortical circuits. *Neural Comput. 10*, 1321–1371.

Villa, A. E., & Abeles, M. (1990). Evidence for spatiotemporal firing patterns within the auditory thalamus of the cat. *Brain Res. 509*(2), 325–327.

Volgushev, M., Christakova, M., & Singer, W. (1998). Modification of discharge patterns of neocortical neurons by induced oscillations of the membrane potential. *Neuroscience 83*(1), 15–25.

von der Malsburg, C. (1981). The correlation theory of brain function. Internal report 81-2, Max-Planck-Institute for Biophysical Chemistry, Göttingen, FRG.

von der Malsburg, C. (1986a). Am I thinking assemblies? In G. Palm & A. Aertsen (Eds.), *Brain Theory*, pp. 161–176. Berlin: Springer-Verlag.

von der Malsburg, C. (1986b). Frank Rosenblatt: Principles of neurodynamics: Perceptrons and the theory of brain mechanisms. In G. Palm & A. Aertsen (Eds.), *Brain Theory*, pp. 245–248. Berlin: Springer-Verlag.

Warzecha, A.-K., Kretzberg, J., & Egelhaaf, M. (2000). Reliability of a fly motion-sensitive neuron depends on stimulus parameters. *J. Neurosci. 20*(23), 8886–8896.

Wax, N. (Ed.) (1954). *Selected papers on noise and stochastic processes.* New York: Dover Publications.

Wennekers, T. (1998a). *Synchronisation und Assoziation in Neuronalen Netzen.* Aachen, Germany: Shaker.

Wennekers, T. (1998b). Synfire graphs: from spike patterns to automata of spiking neurons. Ulmer Informatik-Berichte 98-08, Fakultät für Informatik, Universität Ulm.

Wennekers, T., & Palm, G. (1996). Controlling the speed of synfire chains. In C. von der Malsburg, W. von Seelen, J. C. Vorbrüggen, & B. Sendhoff (Eds.), *Artificial Neural Networks – ICANN 96*, Berlin, pp. 451–456. Springer.

Wiener, N. (1948). *Cybernetics.* New York: John Wiley & Sons.

Wilson, C. J. (1995). ¨In M. Kimura & G. A. M. (Eds.), *Functions of the cortico-basal ganglia loop*, pp. 50–72. New York: Springer.

Wilson, M. A., & Bower, J. M. (1989). The simulation of large-scale neural networks. In C. Koch & I. Segev (Eds.), *Methods in Neuronal Modeling: From Synapses to Networks*, Chapter 9, pp. 291–333. Cambridge, Massachusetts: A Bradford Book, The MIT Press.

Wolfram, S. (1996). *The Mathematica Book* (3 ed.). Cambridge, UK: Wolfram Media/Cambridge University Press.

Zhang, L. I., Tao, H. W., Holt, C. E., Harris, W. A., & Poo, M. M. (1998). A critical window for cooperation and competition among developing retinotectal synapses. *Nature 395*, 37–44.

Ziegler, H. (1981). Properties of digital smoothing polynomial (dispo) filters. *Applied Spectroscopy 35*(1), 88–92.

Lebenslauf

Name	Markus Diesmann
Geburtsdatum	25. 11. 1968
Geburtsort	Bochum
Nationalität	deutsch
Familienstand	verheiratet
1975 – 1979	Grundschule, Bochum
1979 – 1988	Gymnasium, Freiherr-vom-Stein-Schule, Bochum
1988	Abitur, Leistungskurse Mathematik und Physik
1987 – 1997	Ersatzdienst, Technisches Hilfswerk
1988 – 1994	Studium der Physik mit Nebenfach Informatik, Ruhr-Universität Bochum
1990/1991	Austauschjahr, University of Sussex, Brighton (Großbritannien), Studiengang Physik und Cognitive Science
März 1994	Diplom in Physik, Fakultät für Physik und Astronomie, Ruhr-Universität Bochum
Seit März 1994	Doktorand, Institut für Neuroinformatik, Ruhr-Universität Bochum
März 1994 – Juli 1996	Department of Neurobiology/Brain Research, Weizmann Institute of Science, Rehovot (Israel)
Aug. 1996 – Juli 1999	Abteilung Neurobiologie und Biophysik, Institut für Biologie III, Albert-Ludwigs Universität Freiburg
Seit Aug. 1999	wissenschaftlicher Mitarbeiter, Abteilung Nichtlineare Dynamik, Max-Planck-Institut für Strömungsforschung, Göttingen